

Friction, wear and tangential stiffness of metal
surfaces under fretting conditions

by

Daniela Propretner

A thesis submitted to Imperial College London for the degree of Doctor of Philosophy

and Diploma of Imperial College (D.I.C)

April 2012

Tribology Section

Department of Mechanical Engineering

Imperial College London

Abstract

Bladed disk vibrations in turbomachinery can lead to failure due to High Cycle Fatigue. One way in which vibration may be reduced is by dry friction damping. Frictional damping originates from micro and macro slip in the contacting interfaces (“joints”) and is controlled by the relationship of the applied load and tangential displacement. In order to predict the dynamic response of the structure, knowledge of the coefficient of friction and the tangential contact stiffness of the contact are crucial.

Vibration induced slip and the consequent damage in contacting surfaces has been widely studied and is usually called fretting. However, little is known about the effect of the changing interface during fretting on the coefficient of friction and the tangential contact stiffness, which is required when trying to predict these parameters.

This study seeks an improved understanding of the effects of surface topography, surface chemistry, and elastic and plastic material properties on the friction and damping performance of joints under fretting conditions.

In the present study experiments were conducted to measure the coefficient of friction and the tangential contact stiffness of different metals under different test conditions.

Fretting damage mechanisms were investigated using metallography, SEM, EBSD, TEM and XRD techniques.

The evolution of roughness and conformity was investigated by using interferometric profiling systems and image registration via cross correlation.

An infrared radiation measuring system was employed to measure the dissipated radiation and frictional power in fretting which was then compared with calculated energy dissipation maps.

Experimental results were used to validate models predicting contact stiffness which have been developed throughout the project by collaborating researchers. This study highlighted real contact conditions and their dependence on running time, which need to be taken into account when modelling friction contacts.

Preface

This thesis is a description of work carried out in the Department of Mechanical Engineering, Imperial College of Science, Technology and Medicine, London, under the supervision of Professor Andy Olver and Professor David Ewins. The work here presented was part of a project in collaboration with the University of Oxford where partners included Professor David A. Hills and Professor David Nowell. Except where acknowledged, the material presented is the original work of the author and no part has been submitted for a degree at this or any other university. The research was funded by the Engineering, Physics and Science Research Council (EPSRC) and supported by Rolls-Royce.

Acknowledgements

I would like to express the greatest thanks to my supervisor Professor Andrew V. Olver for his guidance and support throughout the project.

Special thanks must go to Dr Simon Medina for his continuous help, support and many inspiring discussions. Comparing my experimental results with his predictions was a great honour.

I would also like to thank Dr Christoph Schwingshackl who was immense guidance and help operating the friction rig used in Chapter 3-5.

My eternal gratitude and thanks are extended to the following people for without their help this work would not have been possible:

To Dr Tom Reddyhoff for his help and support with the infrared work described in Chapter 6 and 7.

To all other members of the PAMFJP project at Imperial College London as well as University of Oxford: Professor David Ewins, Dr Daniele Dini, Dr Evgeny Petrov, Professor David Hills, Professor David Nowell, Dr Mehmet Kartal and Daniel Mulvihill. Their work is referred to throughout this thesis and was essential for discussions.

To Dr Barbara Shollock, Dr John Druce and the final year project students Ben Hanson and Kisharn Thanalingham based in the Materials Department for their work on the project.

To Dr Jeff Green and Dr John Schofield for providing the material and arranging a visit to Intertek metallography facilities. Thanks also to all the helpful people at Intertek.

To all the academics in the Tribology section as well as Ms Chrissy Stevens and Paul Jobson who were great help throughout my time in the lab.

To Agnieszka, Ales, Amir, Angelos, Aswad, Connor, Ingrid, Jenn, Jess, Joslyn, Juliane, Marc, Maria, Robbie, Simon, Sophie, Savi and Tom and all other members of the lab. You made the lab a brilliant place to work at and a place to find friends.

Finally, I would like to thank my family for their unconditional love, support and encouragement. I would like to dedicate my thesis to my beloved ones – ‘Für Euch’.

Contents

Abstract	2
Preface	4
Acknowledgements	5
Contents	7
Nomenclature	13
List of figures	15
Chapter 1 Introduction	23
1.1 Background	23
1.2 Aims and objectives	25
1.3 Collaboration.....	25
1.4 Thesis structure	26
Chapter 2 Reciprocating sliding of rough surfaces – A literature review	27
2.1 Rough surfaces.....	27
2.1.1 Roughness	28
2.1.1.1 Amplitude parameters	28
2.1.1.2 Texture parameters.....	30
2.1.2 Constitution of metallic surfaces.....	31
2.2 Contact between two rough surfaces.....	32
2.2.1 Single asperity contact	32
2.2.1.1 Traction and displacements due to normal loading	33
2.2.1.2 Tangential loading and friction	34
2.2.1.3 Stiffness and compliance of loaded bodies	38
2.2.1.4 Energy dissipation and oscillating tangential forces	38
2.2.1.5 Elasto-plastic single asperity contact model	39
2.2.2 Multi-asperity contact models of rough surfaces	39

2.2.2.1	Statistical and random process models	41
2.2.2.2	Numerical contact models.....	43
2.2.2.3	Other contact models	44
2.3	Fretting.....	44
2.3.1	Fretting regimes	45
2.3.2	Fretting mechanisms	48
2.3.2.1	Fretting wear	48
2.3.3	Fretting fatigue.....	51
2.3.4	Observed fretting damage	51
2.3.5	Fretting tests.....	53
2.3.5.1	Friction coefficient.....	55
2.3.5.2	Tangential contact stiffness.....	55
2.3.5.3	Energy dissipation.....	57
2.3.5.4	Temperatures in fretting.....	58
2.4	Dry friction and friction damping	59
2.4.1	Friction mechanisms	60
2.4.1.1	Adhesion term of friction.....	61
2.4.1.2	The deformation term of friction.....	62
2.4.1.3	Other theories.....	63
2.4.2	Running-in	63
2.4.3	Friction damping.....	64
2.5	Discussion	66
Chapter 3	Friction tests – Materials and methods	68
3.1	Materials.....	68
3.1.1	Ti6Al4V	68
3.1.2	Udimet 720.....	70
3.1.3	Steel selection	71
3.1.3.1	EN24T.....	71
3.1.3.2	Stainless steel BS 970 303S31	72

3.2	Methods.....	72
3.2.1	Friction tests.....	72
3.2.1.1	1 mm ² contact friction rig	73
3.2.1.2	80 mm ² contact friction rig	77
3.2.1.3	Comparison between 1 mm ² and 80 mm ² contact rig	79
3.2.1.4	Sample preparation	79
3.2.2	Surface characterisation	81
3.2.2.1	Wyko NT9100 profiler.....	81
3.2.2.2	Alicona profiler.....	82
3.2.2.3	Comparison between Wyko and Alicona.....	83
3.2.2.4	Measurements	84
3.2.2.5	Surface wear.....	85
3.2.2.6	Profile correlation	87
3.2.3	Sample preparation for microscopy	91
3.2.3.1	Grinding and polishing.....	92
3.2.3.2	Etching	92
3.2.4	Scanning electron microscopy (SEM)	93
3.2.4.1	Electron back scattering diffraction (EBSD)	94
3.2.5	Focused ion beam imaging (FIB).....	94
3.2.6	Transmission electron microscopy (TEM).....	95
3.2.7	X-ray diffraction (XRD)	96
Chapter 4	Fretting tests – Results.....	97
4.1	Coefficient of friction and tangential contact stiffness results	97
4.1.1	Influence of the material	97
4.1.2	Influence of load	99
4.1.3	Influence of contact shape.....	104
4.1.4	Influence of test rig	106
4.1.5	Influence of the surface roughness.....	109
4.2	Surface degradation.....	110

4.2.1	Development of correlation	112
4.2.2	Development of friction loops	116
4.2.3	Change of surface constitution.....	118
4.2.3.1	Oxide scale on Udimet 720.....	119
4.2.3.2	Oxide scale on Ti6Al4V	121
4.2.3.3	Oxide scale on EN24T	122
4.2.3.4	Oxide scale on stainless steel	124
4.2.3.5	Oxide composition	124
4.2.4	Deformation	126
4.2.4.1	Sub-surface deformation in Udimet 720.....	127
4.2.4.2	Sub-surface deformation in Ti6Al4V.....	131
Chapter 5 Friction tests - Discussion		136
5.1	Tangential contact stiffness.....	136
5.1.1	Comparison of two friction rigs	136
5.1.1.1	Influence of the area of contact	137
5.1.1.2	Location of the stiffness measurements	138
5.1.2	Comparison of measured and predicted behaviour of the tangential contact stiffness ...	142
5.1.2.1	The effect of material and load on the tangential contact stiffness	145
5.1.2.2	Contributions to the compliance of the contact.....	150
5.2	The time dependent behaviour of friction properties	152
5.2.1	A wear scar interaction model	152
5.3	Nature of the surface degradation	161
5.3.1	Oxide layers	161
5.3.1.1	Thickness of oxide layer	161
5.3.1.2	Chemical composition.....	162
5.3.2	Formation of oxide layer.....	162
Chapter 6 Infrared energy dissipation		165
6.1	Introduction.....	165
6.1.1	Optical investigation of fretting wear	165

6.1.2	Infrared temperature mapping.....	166
6.1.3	Proposed combination of techniques	167
6.2	Methods.....	167
6.2.1	High frequency reciprocating rig	167
6.2.1.1	Modifications of HFR rig.....	169
6.2.2	Infrared measurement	171
6.2.2.1	Modifications of the infrared system	171
6.2.3	Testing methodology.....	172
6.2.4	Data processing.....	174
6.2.5	Specimen surface characterisation	175
Chapter 7	Infrared energy dissipation – Results and discussion.....	176
7.1	Adjustment of test settings.....	176
7.2	Test results from coated discs	180
7.3	Test results from an uncoated disc	185
7.4	Distribution of temperature rise – A comparison to contact models.....	188
7.5	Discussion of the technique	192
Chapter 8	Discussion.....	194
8.1	Review of conducted work and results	194
8.2	Initial objectives of the project.....	197
8.2.1	Experiments vs. predictions: Frictional properties.....	197
8.2.1.1	Contact area	198
8.2.1.2	Use of tangential contact stiffness in dynamic models	198
8.2.2	Experiments vs. predictions: Dissipated energy	200
8.2.3	Experiments vs. predictions: Summary of main differences.....	200
8.2.4	Time dependent behaviour of the contact	202
8.3	Application of findings to frictional joints.....	202
8.3.1	Evolution of contact area with wear.....	203
8.3.2	Hysteresis characteristics at mm scale	203
8.3.3	Chemical layers.....	204

8.3.4 Surface definition.....	204
8.3.5 Design/Analysis of jointed structures	204
8.4 Suggested improvements and future work.....	204
8.4.1 Friction test conditions.....	205
8.4.2 Further characterisation of the compliant layer	205
Chapter 9 Conclusions.....	206
9.1 Experimental results.....	206
9.2 Experimental results vs. theories.....	207
9.3 Considerations for development of contact models	208
References.....	209
Appendix.....	216

Nomenclature

a	Hertzian contact radius
A	Area of contact
\bar{A}	Mean area of contact
A_{tot}	Total area of contact
A_0	Nominal area of contact
c	Hertzian stick zone radius
c_0	Compliance
C	Influence matrix
d	Distance
E, E_1, E_2	Young's modulus
E^*	Combined Young's modulus
G	Shear modulus
H	Hardness
k	Stiffness
k_n	Normal contact stiffness
k_t	Tangential contact stiffness
L	Evaluation length
L_p	Peclet number
n	Contact pressure exponent
n_a	Number of asperities forming contact
N_a	Number of asperities in surface profile
p	Contact pressure
p_0	Maximum contact pressure
p_m	Mean real pressure
P	Normal load
P_y	Yield strength
P_{tot}	Total normal load

q	Shear tractions per unit area
q_0	Maximum shear tractions per unit area
Q	Friction force, tangential force
Q_a	Adhesion force
Q_d	Deformation force
R, R_1, R_2	Asperity radius
R_a	Average height roughness
R_q	Root mean square height roughness
R_t	Peak-to-valley height roughness
R_z	Ten-point height roughness
s	Slip displacement
T	Temperature
T_f	Average flash temperature
T_{fmax}	Maximum flash temperature
u	Displacement
U, U_1, U_2	Velocity
z	Roughness peak height
δ	Displacement of remote points
κ	Thermal diffusivity
k	Thermal conductivity
μ	Coefficient of friction
ν	Poisson's ratio
σ	Standard deviation of asperity heights
τ	Shear strength
τ_{lag}	Delay length
ϕ	Probability of the height distribution
ϕ^*	Standardised probability of the height distribution
Φ	Probability function of the height distribution
ψ	Plasticity index

List of figures

Figure 1-1: (a) Fan turbine blade and (b) selection of under-platform dampers [1].....	24
Figure 2-1: Height distribution ϕz and cumulative probability height distribution $\Phi(d)$ for a surface profile (adapted from [4]).	29
Figure 2-2: Effect of (a) skewness and (b) kurtosis on a Gaussian height distribution and exemplary surfaces, (c) and (d) [5].	29
Figure 2-3: Schematic illustration of typical surface layers on a metal surface (not to scale) [7].....	31
Figure 2-4: Displacements of two spheres which are loaded normally and tangentially.	35
Figure 2-5: Traction and displacement of a sphere-on-half-space contact.	36
Figure 2-6: Load displacement loop [4].....	39
Figure 2-7: Model by Archard [21] with superimposed asperities.	40
Figure 2-8: Contact between a rough and a smooth surface. The load is carried by the shaded asperities which are greater than the distance between the two reference planes [23].....	41
Figure 2-9: Stick, partial-slip and gross slip regime with corresponding fretting logs and contact areas for a ball-on-flat contact.	46
Figure 2-10: (a) Schematic fretting wear map which indicates the different fretting regimes depending on normal contact load, N , and sliding amplitude, Δ , and (b) wear and fatigue life versus sliding amplitude, Δ , [56].	47
Figure 2-11: Delamination wear as a process schematic as presented by [69].....	49

Figure 2-12: Wear scar formation in (a) and (b) gross slip [67] and (c) and (d) partial slip [46].	52
Figure 2-13: (a) Ideal schematic fretting loop and indication of important parameters. (b) Measured fretting logs.	53
Figure 2-14: Time dependent evolution of fretting loops: (a) Transition from gross slip to partial slip behaviour during fretting test [78]. (b) Development of ‘peak’ at the points of sliding direction change [50].	54
Figure 2-15: Typical running-in behaviour for dry on dry contacts [115].	64
Figure 2-16: Influence of different (a) friction coefficient [119] and (b) tangential contact stiffness [120] values on the dynamic response of a system.	66
Figure 3-1: Microstructure of (a) $\alpha + \beta$ Ti-alloy Ti6Al4V, (b) Ni-based superalloy Udimet 720, (c) Stainless steel 303S31 and (d) low alloy steel EN24T.	70
Figure 3-2: (a) 1 mm ² contact area rig, (b) schematic fretting specimen arrangements forming a 1 mm ² area of contact [130] and (c) specimens mounted in holders.	74
Figure 3-3: Friction hysteresis loop and definition of contact stiffness, kt , and coefficient of friction, μ .	76
Figure 3-4: Measurement variation of (a) friction coefficient and (b) contact stiffness.	77
Figure 3-5: Schematic fretting specimen arrangements: (a) 1 mm ² contact area specimens and (b) 80 mm ² contact area specimens [130].	78
Figure 3-6: Roughness measurements of a 1 mm ² area using a (a) Wyko system and (b) Alicona system.	84
Figure 3-7: Measurement areas for (a) 1 mm ² contact rig and (b) 80 mm ² contact rig.	84
Figure 3-8: Procedure of wear calculation. (a) Worn surface after test. (b) The worn area is set to zero and the grinding structure is extrapolated to give a (c) unworn surface which can be easily subtracted from the original worn surface from which (d) the wear volume can be calculated.	86

Figure 3-9: Flowchart showing the sequence of operation during image correlation between worn profiles.....	89
Figure 3-10: Cross correlation of two worn surfaces: (a) Search for best alignment, (b) cross correlation plot for best alignment angle, (c) Profile <i>A</i> and (d) Profile <i>B</i>	90
Figure 3-11: Cutting planes for cross sections on (a) 1 mm ² contact rig specimens and (b) 80 mm ² contact rig specimens. The direction of sliding is indicated by a double arrow.	91
Figure 3-12: Cutting plane for cross section on an 80 mm ² contact rig specimen for XRD measurement. (b) Approximate penetration position and area.....	96
Figure 4-1: Comparison of the coefficient of friction over time for different materials: Udimet 720, Ti6Al4V, EN24T and stainless steel.....	98
Figure 4-2: Comparison of the tangential contact stiffness over time for different materials: Udimet 720, Ti6Al4V, EN24T and stainless steel.....	99
Figure 4-3: Influence of load on the evolution of coefficient of friction and tangential contact stiffness on different materials: Udimet 720 (a) μ and (b) kt , Ti6Al4V (c) μ and (d) kt , EN24T (e) μ , and (f) kt and stainless steel (g) μ and (h) kt	103
Figure 4-4: Comparison of (a) friction of coefficient and (b) tangential contact stiffness values for different contact conditions: flat-on-flat, cylinder-on-cylinder and sphere-on-flat.	105
Figure 4-5: Coefficient of friction measured with two different rigs on (a) Udimet 720 specimen and (b) Ti6Al4V specimen.	107
Figure 4-6: Tangential contact stiffness normalised by the nominal contact area measured with two different rigs on (a) Udimet 720 specimen and (b) Ti6Al4V specimen.	108
Figure 4-7: Comparison of (a) μ and (b) kt results from tests performed on Ti6Al4V samples with smooth and rough surface profiles.....	109

Figure 4-8: Worn contact interface of a (a) bottom and (b) top Udimet 720 specimen after a test performed at 70 MPa with a maximum displacement amplitude of around 18 μm . The specimens in contact formed a 1 mm^2 nominal contact.	110
Figure 4-9: Worn contact interface of a (a) bottom and (b) top EN24T specimen of a cylinder-on-cylinder contact. The test was performed at 70MPa with a maximum displacement amplitude of around 18 μm	111
Figure 4-10: Worn contact interface of a (a) bottom and (b) top EN24T specimen of a sphere-on-flat contact. The test was performed at 70MPa with a maximum displacement amplitude of around 18 μm	112
Figure 4-11: Wear scars obtained after (a) 15 seconds, (b) 30 seconds, (c) 1, (d) 2, (e) 3, (f) 6, (g) 9 and (h) 15 minutes. Tests were performed at 70MPa with maximum displacement amplitudes around 30 μm	115
Figure 4-12: Cross correlation factors are assessed for a series of samples which were subjected to fretting for the following time intervals: 0.25, 0.5, 1, 2, 3, 6, 9 and 15 minutes for EN24T samples.....	116
Figure 4-13: Fretting loop at the beginning of a test and 15 minutes into the test for tests performed on the 1 mm^2 contact rig.	117
Figure 4-14: Fretting loop at (a) the beginning of a test and (b) after nearly 15 minutes testing time for tests performed on the 80 mm^2 contact rig.	118
Figure 4-15: Optical micrographs of fretting induced oxide scales on (a) Udimet 720 (small back scattered electron image), (b) Ti6Al4V, (c) EN24T and (d) stainless steel.	119
Figure 4-16: Back scattered electron image of fretting induced oxide scale on Udimet 720.....	120
Figure 4-17: Back scattered electron image of details of a partially detached particle on Udimet 720 specimen.	120
Figure 4-18: Optical micrograph of a fretting induced oxide scale on a Ti6Al4V sample.	121

Figure 4-19: Details of immediate interface zone on Ti6Al4V specimen.	122
Figure 4-20: Fretting induced oxide scale on an EN24T sample.....	123
Figure 4-21: Scale thickness observed on EN24T after fretting tests performed at room temperature and 200°C.	123
Figure 4-22: Cross section of worn stainless steel specimen.....	124
Figure 4-23: XRD spectra of Udimet 720 samples before and after the tests.	125
Figure 4-24: XRD spectra of Ti6Al4V samples before and after the tests.....	126
Figure 4-25: Deformation indicated by red lines on (a) Ti6Al4V, (b) EN24T and (c) stainless steel observed with optical microscopy (all images same scale).	127
Figure 4-26: Unworn Udimet 720. (a) map (b) subsurface and (c) bulk.	128
Figure 4-27: Unworn Udimet 720. (a) map, (b) subsurface in 0-50 μm depth and (c) bulk in 50-100 μm depth.....	130
Figure 4-28: Focused ion beam image of (a) bulge and (b) centre area of 80 mm^2 specimen.	131
Figure 4-29: Unworn Ti6Al4V specimen: (a) EBSD map, (b) pole figures of subsurface region (0-50 μm depth) and (c) pole figures of bulk region (50-100 μm depth).....	132
Figure 4-30: Worn Ti6Al4V specimen: (a) EBSD map, (b) pole figures of subsurface region (0-50 μm depth) and (c) pole figures of bulk region (50-100 μm depth).....	134
Figure 4-31: TEM investigation of a worn Ti6Al4V specimen.....	135
Figure 5-1: Comparison of tangential contact stiffness values for Udimet 720 normalised either by A_0 or by A_0	138
Figure 5-2: Comparison of measurement methods for the tangential contact stiffness for the 1 mm^2 and 80 mm^2 contact rig. (Schematic drawings not to scale).....	139
Figure 5-3: Predicted displacement and stiffness behaviour for a smooth, (a), (b) and (c), and a rough contact (d), (e) and (f) using a half-space model.	141

Figure 5-4: The relationship between the tangential contact stiffness and load, as predicted by analytical models (straight lines) and a numerical model (continuous curved lines). Roughness influences the tangential contact stiffness at low loads, whereas the Young's modulus affects it at high loads.....	145
Figure 5-5: Comparison of 1 mm ² experimental value with predicted curves for (a) Udimet 720, (b) Ti6Al4V, (c) EN24T and (d) stainless steel. At low loads two options are given for a main structure and for a fine structure of the surface as explained in the text.....	148
Figure 5-6: Comparison of 80 mm ² experimental values with predicted curves for (a) Udimet 720 and (b) Ti6Al4V.....	150
Figure 5-7: Components of the total compliance inside the contact [49].....	151
Figure 5-8: Schematic illustration of the wear scar interaction model.	153
Figure 5-9: Schematic equilibrium of the forces in the interaction model.	154
Figure 5-10: Friction loops produced by the interaction contact model, where (a) $n = 2$ and (b) $n = 6$	156
Figure 5-11: (a) Expected wear scar evolution in a 1 mm ² contact without controlled displacement, (b) predicted loops corresponding to wear scars at three different times.	157
Figure 5-12: (a) Measured initial and final loop of a 1 mm ² contact, (b) predicted initial and final loop based on the same changes in displacement amplitude and coefficient of friction. The initial slopes of the predicted loops were adjusted additionally to correspond to the measured tangential contact stiffness.....	158
Figure 5-13: (a) Expected wear scar evolution in a 80 mm ² contact with controlled displacement, (b) predicted loops corresponding to wear scars at three different times.	159
Figure 5-14: (a) Measured initial and final loop of a 80 mm ² contact, (b) predicted initial and final loop based on the same changes in displacement amplitude and coefficient of friction. The initial slopes of the predicted loops were adjusted additionally to correspond to the measured tangential contact stiffness.....	160

Figure 5-15: Effect of acceleration where m and $n = 4$	160
Figure 6-1: Infrared measurement as used by Reddyhoff [139].	166
Figure 6-2: Schematic drawing of general HFR rig set up [140].	168
Figure 6-3: Cross section of sapphire disc and steel ball mounted in new sample holders.	170
Figure 6-4: (a) Hertzian contact area, when loaded with 1 kg, with measuring grid, where one square equals one pixel of $6.3 \times 6.3 \mu\text{m}$	172
Figure 6-5: Testing arrangement.	173
Figure 6-6: Derivation of conversion parameter from kindly provided data [139].	174
Figure 7-1: Fretting damage as observed for different fretting regimes. (a) ball and (b) disc stuck, (c) ball and (d) disc in partial slip and (e) ball and (f) disc in gross slip.	178
Figure 7-2: Surface profiles of worn (a) ball and (b) disc and corresponding cross sections (c) and (d).	181
Figure 7-3: Temperature increase maps ΔT maps after (a) 30 seconds, (b) 40 seconds, (c) 1 minute and (d) 5 minutes after test has finished. The radius of contact is indicated in (a) and (c). The moving sickle shaped maxima of the contact in gross slip are indicated.	182
Figure 7-4: Comparison of fretting regime, frictional behaviour of contact and maximum temperature rise during a test. (PS – partial slip, GS – gross slip).	184
Figure 7-5: Surface profiles of (a) coated disc and (b) ball after test.	185
Figure 7-6: Radiation maps after 4 seconds, 34 seconds, 1 minute and 30 seconds after the test had finished.	186
Figure 7-7: Comparison of fretting regime, frictional behaviour of contact and maximum temperature rise during a test. (PS – partial slip, GS – gross slip).	188

Figure 7-8: (a) Solution by Mindlin for the distribution of dissipated energy within a Hertzian contact [92]. (b) Cross section at a random angle of Mindlin's solution.....	189
Figure 7-9: (a) Energy dissipation as predicted by an analytical model presented by Nowell and Hills [92]. (b) Variation of the Ruiz initiation parameter over a circular contact.....	190
Figure 7-10: (a) Predicted energy dissipation using a numerical contact model, for (a) a smooth and (b) a rough circular contact, as shown by Medina [93].....	191
Figure 8-1: (a) Predicted frequency response curves of (b) a single degree of freedom system [120], and friction loops for different stiffness and displacement conditions (b), (c) and (d).....	199
Figure 8-2: Roadmap for research for friction contact and wear in structures adapted from Ewins [146]. Topics to which the current work contributed are highlighted green.....	203

Chapter 1

Introduction

1.1 Background

Gas turbine technology can be found in aircraft, marine, and space propulsion as well as in power generation plants. Being used in such a wide range of areas, major research has been dedicated to increase efficiency and lifespan while lowering production costs.

Vibrations in turbomachinery have been identified as a major threat when dealing with engine safety and reliability because they can lead to failure due to high cycle fatigue which can initiate immediate malfunction. The vibrations of blades are caused by unsteady pressure fields on the blade surfaces which can originate from aerodynamic or mechanical disturbances. Other contributing factors can be external sources such as relative motion between rotating and non-rotating parts.

One way in which bladed disk vibration is reduced is dry friction damping. It occurs at several positions on a blade e.g. at the blade root, where a dovetail joint keeps the blade attached to the disc or at the under-platform where friction dampers are intentionally attached to the structure as shown in Figure 1-1.

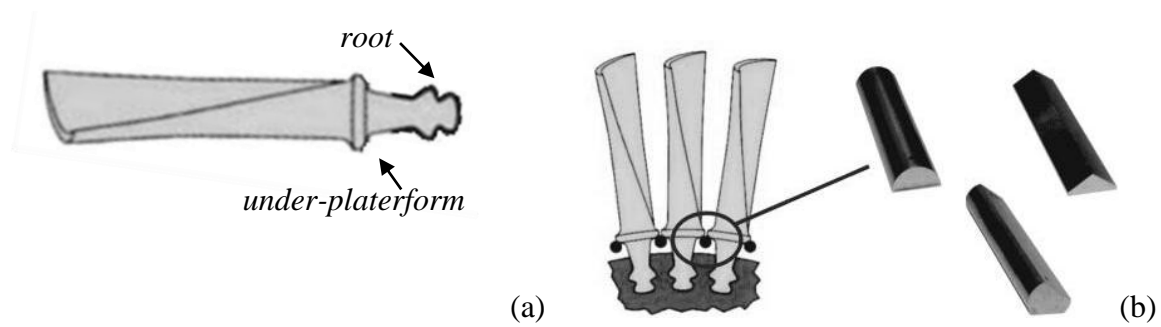


Figure 1-1: (a) Fan turbine blade and (b) selection of under-platform dampers [1].

Frictional damping originates from micro and macro slip in the contacting interfaces and is controlled by the relationship of the applied load and tangential displacement. In order to predict the joints damping performance and the overall dynamic response of the structure, knowledge about the resistance to tangential motion at the contact is crucial. This is described by two variables, the coefficient of friction and the tangential contact stiffness, both of which currently can only be obtained from experiments. No method has been presented yet to predict these values and to realise fully predictive dynamic response models.

Vibration induced micro-slip and the damage caused by it in joint surfaces has been widely studied under the name of fretting. The slip amplitude determines whether fretting wear or fretting fatigue is the predominant failure mode, later promoting the initiation of fatigue cracks which can drastically decrease the fatigue life of the connected parts. At present, a lot of work has been carried out to fully understand fretting and its failure regimes. A literature review which includes a large section on fretting is presented in Chapter 2. Even though the degradation of the surface, the subsurface, and debris formation due to fretting have been studied to some extent, the same cannot be said about the effect of the changing interface during fretting on the coefficient of friction and the tangential contact stiffness, which is required when trying to predict these parameters.

1.2 Aims and objectives

This study seeks an improved understanding of the effects of surface topography, surface chemistry, and elastic and plastic material properties on the friction and damping performance of joints under fretting conditions.

One objective is to deliver an experimental study of fretting and a comparison of different test conditions. The measurement of friction loops will provide data of coefficient of friction and tangential contact stiffness values. This will highlight to what extent different materials, roughness, contact area and loading conditions influence these properties.

Another primary objective is an investigation of the change which the contacting surfaces undergo when exposed to fretting conditions. At present, predictive models do not take into account any changes of surface topography or chemical nature.

One part of the work aims to measure the dissipated radiation in a reciprocating ball-on-flat contact and then to compare the measured radiation with calculated energy dissipation maps.

Experimental results will be used to validate models predicting contact stiffness which have been developed throughout the project by collaborating researchers. This study also aims to highlight real contact conditions and their dependence on running time, which need to be taken into account when modelling friction contacts.

1.3 Collaboration

This research has been carried out in close collaboration with several researchers at Imperial College London and at University of Oxford working on the EPSRC funded project ‘A Predictive Approach to Modelling Frictional Joint Performance (PAMFJP)’. One of the main objectives of the project is to provide the means to predict tangential stiffness and coefficient

of friction which then can be used in finite element models to predict the effect of frictional joints on the dynamic response. Analytical and numerical models developed concurrently by researchers of this collaboration will be validated through experimental results obtained by the author of this thesis. Friction and stiffness measurement results produced by the author are also compared with results reported by collaborators on a rig testing a frictional contact which is larger in scale. This information is used to highlight the effect of rigs and different nominal contact areas.

1.4 Thesis structure

This PhD thesis summarises the progress made by the author in the basic understanding of friction and damping behaviour of metal contacts under fretting conditions.

First Chapter 2 offers a literature review on the current understanding of contact modelling, fretting contacts and friction, in particular friction damping. Chapters 3 to 5 cover all details concerned with the performed friction tests. Chapter 3 presents materials and methods which were used to measure the coefficient of friction and tangential contact stiffness under various conditions. It also explains all other techniques which were employed to characterise the contact interface of the specimens before and after the tests. Chapter 4 presents all obtained results which are then discussed and compared with analytical and numerical models in Chapter 5. Chapter 6 introduces an infrared technique which enabled to measure radiation maps of reciprocating contacts. Results which were obtained with this method are presented in Chapter 7. A discussion of the results and a comparison with analytical and numerical derived radiation maps is presented at the end of the same chapter. A summarising discussion of the significance of the results follows in Chapter 8. Finally Chapter 9 summarises all relevant findings and points out the most important conclusions.

Chapter 2

Reciprocating sliding of rough surfaces –

A literature review

This literature review initially looks at rough surfaces, available parameters to describe roughness and the constitution of rough metallic surfaces. The next section deals with the fundamentals of contact models which have been developed to model the encounter of rough surfaces. As reciprocating sliding and especially fretting, is the main focus of this thesis, its mechanisms are described in the subsequent part. Reported fretting damage, fretting logs and from them derived friction properties are reviewed. This is followed by a brief section on friction and friction mechanisms and the relevance of friction parameters for friction damping. The chapter concludes with a discussion on the missing links between theory and the experimental work and provides a basis for this thesis.

2.1 Rough surfaces

The nature of a solid surface is highly complex and may depend on the material, machining process and the interaction with the environment. Both topography and physico-chemical properties of surfaces are of significant interest when studying interfacial phenomena such as friction and wear.

2.1.1 Roughness

Most real surfaces are rough and consist of a random arrangement of peaks and troughs, even if they appear macroscopically smooth. Topography measuring systems are either based on interferometry or the use of a stylus which scans the surface. A comprehensive review on rough surfaces was presented by Thomas [2].

2.1.1.1 *Amplitude parameters*

Statistical parameters are widely used to describe surfaces via their amplitude and texture characteristics. The extreme value parameters R_t (peak-to-valley height) and R_z (ten-point height) inform about the distance between the highest peak to the lowest valley within a sampling length L where R_z is the average of five R_t . Both of these values are often too inaccurate to describe a surface effectively, because their values vary too much from one sample to another. The average parameters R_a , or centre line average (CLA), and R_q , or root mean square (RMS), are alternatives and their definitions are shown by formulae (2.1) and (2.2). If the mean of the heights is zero, R_q is identical to the standard deviation σ [2].

$$R_a(x) = \frac{1}{L} \int_0^L |z| dx \quad \text{CLA} \quad (2.1)$$

$$R_q(x) = \sqrt{\frac{1}{L} \int_0^L z^2 dx} \quad \text{RMS} \quad (2.2)$$

The statistical variation of surface heights can be presented in a histogram which informs about the probability $\phi(z)$ that the height of a particular point on the surface lies between z and $z + dz$. The probability, as shown in (2.3), that the height of a point is greater than d is

predicted by the s-shaped cumulative probability height distribution $\Phi(d)$ which is also known as the bearing area curve [3].

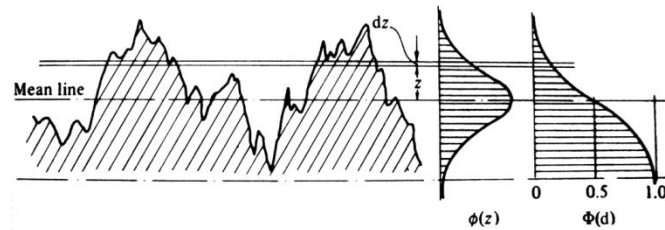


Figure 2-1: Height distribution $\phi(z)$ and cumulative probability height distribution $\Phi(d)$ for a surface profile (adapted from [4]).

$$\Phi(d) = \int_d^{\infty} \phi(z) dz \quad (2.3)$$

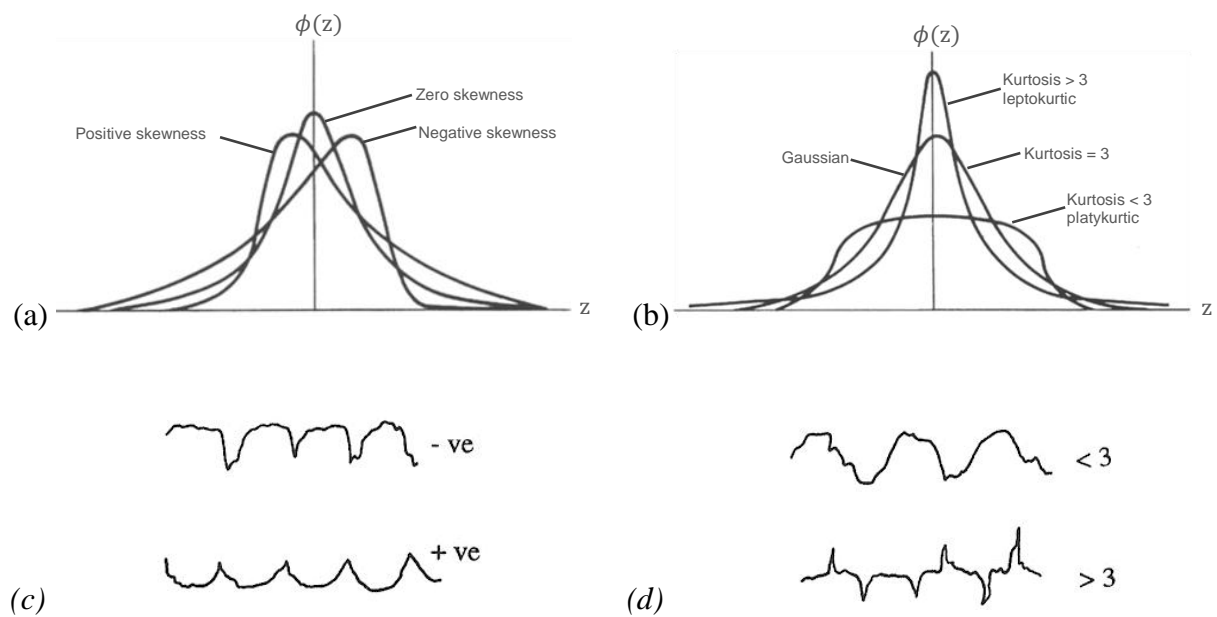


Figure 2-2: Effect of (a) skewness and (b) kurtosis on a Gaussian height distribution and exemplary surfaces, (c) and (d) [5].

Deviations from a symmetrical Gaussian height distribution can be described by the parameters skewness, R_{sk} , and kurtosis, R_k . The effect of these two parameters on a distribution of heights is shown in Figure 2-2. E.g. surfaces with a positive skewness can be observed after turning, shaping and electro discharge machining processes. Grooved surfaces produced due to abrasion processes, grinding, honing or milling often have a negative skewness and high kurtosis values [2].

2.1.1.2 Texture parameters

The spatial distribution of heights can be described by functions which have originally been developed for signal processing purposes. The autocovariance function (2.4) and the autocorrelation function (2.5) enable the prediction of the frequency of excursions above a certain height level and detect periodic structures of a surface. τ_{lag} is the separation of height data points. Equation (2.4) finds the average of the cross product $z(x)z(x + \tau_{lag})$ for all possible values of $z(x) \neq z(x + \tau_{lag})$ within the profile of length L . Performing the integral for many values of τ_{lag} creates a continuous function where some value of defined τ_{lag} can be interpreted from $R(\tau_{lag})$ as the delay length of a feature which reappears and where τ_{lag} marks the distance from the original position. The power spectral density function is the equivalent to the autocovariance function in the frequency domain and allows for quicker computing times. Sayles and Thomas [6] developed the structure function as an alternative to the autocorrelation function with the advantages of higher stability and easier computation.

$$R(\tau_{lag}) = \frac{1}{L} \int_0^L z(x)z(x + \tau_{lag})dx \quad \text{Autocovariance function} \quad (2.4)$$

$$\rho(\tau_{lag}) = \frac{R(\tau_{lag})}{R_q^2} \quad \text{Autocorrelation function} \quad (2.5)$$

Three-dimensional versions are available for both amplitude (S_a , S_q , S_z , S_{sk} , and S_k) and texture parameters ($AC(i, j)$ and $ACF(i, j)$). Their definitions are analogous to the two-dimensional parameters, but the domain of integration is now the area of measurement. Discrete forms of all parameters are used for computation [2].

2.1.2 Constitution of metallic surfaces

Surface films are omni-present on metallic surfaces as a result of machining processes and interaction with the environment. A schematic illustration of these layers is shown in Figure 2-3. Surface machining causes a heavily deformed zone which is about 1-2 μm in thickness. The deformation region underlying this work hardening layer reaches up to 100 μm into the bulk material. The Beilby layer, a microcrystalline or amorphous zone, lies on top of it. Most engineering surfaces are chemically reactive and form oxide layers. Adsorbed films are formed by either physisorption or chemisorption. Finally one can find contaminants such as traces of machining oil or lubricants [7].

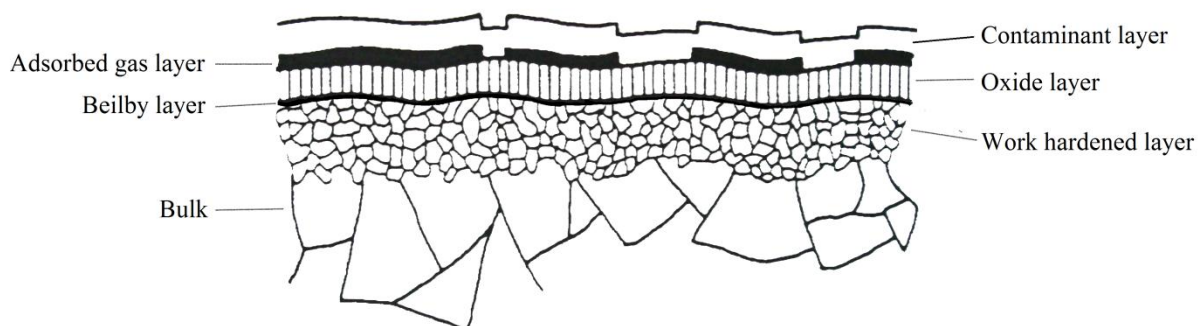


Figure 2-3: Schematic illustration of typical surface layers on a metal surface (not to scale) [7].

2.2 Contact between two rough surfaces

This section aims to review the means of contact mechanics to describe the encounter of rough surfaces. When two rough surfaces are placed together it is assumed that contacts are formed between the asperities. The first part of this section deals with an isolated single asperity contact whereas the second part reviews multiple asperity contact models. Comprehensive reviews on this topic can be found in the following references [2, 4, 8, 9].

2.2.1 Single asperity contact

An approximation of a single asperity contact is the encounter of two smooth spheres or even more simplified the contact of a sphere with a half-space. If perfectly elastic response of the bodies is expected, Hertzian [10] contact theory applies. The geometry of the two spheres is characterised by their individual radii R_1 and R_2 , where the radius of the half-space becomes infinitely large. When brought into contact a point contact is formed. Applying a normal load P forms a circular contact area of radius a . Hertz developed the means to calculate the contact area radius which is dependent on the elastic material properties, Young's modulus E and Poisson's ratio ν , of both bodies, the asperity geometry and applied load P . Hertzian formulae for the contact area radius a , the maximum pressure p_0 and the approach of two distant points δ are given in (2.6) to (2.8). Additional calculation parameters for the combined Young's modulus E^* and the combined radius R are given in (2.9) and (2.10) [4].

$$a = \left(\frac{3PR}{4E^*} \right)^{1/3} \quad \text{Contact radius} \quad (2.6)$$

$$p_0 = \frac{3P}{2\pi a^2} = \left(\frac{6PE^{*2}}{\pi^3 R^2} \right)^{1/3} \quad \text{Maximum contact pressure} \quad (2.7)$$

$$\delta = \frac{a^2}{R} = \left(\frac{9}{16} \frac{P^2}{RE^{*2}} \right)^{1/3} \quad \text{Approach of distant points} \quad (2.8)$$

Compliance

$$E^* \equiv \left(\frac{1 - \nu_1^2}{E_1} + \frac{1 - \nu_2^2}{E_2} \right)^{-1} \quad \text{Combined Young's modulus} \quad (2.9)$$

$$R \equiv (1/R_1 + 1/R_2)^{-1} \quad \text{Combined sphere radius} \quad (2.10)$$

2.2.1.1 *Tractions and displacements due to normal loading*

The loading of an elastic half-space with a concentrated force or a (non-)uniform pressure distribution p causes surface tractions. These tractions cause stresses and displacements which can be solved for by using the approach by Boussinesq [11] and Cerruti [12]. They employed the theory of potential and the results were presented by Love [13] and this method is now known as the classical and formal approach to the single contact problem. The main disadvantage of the method lies in the requirement of specifying the surface tractions, which are difficult to find. This can be overcome by starting from the stresses and displacements produced by concentrated normal and tangential forces and using superposition. For an axisymmetrical pressure applied on a circular region the solution is known and given by equation (2.11). Outside the contact area the pressure is zero.

$$p = p_0(1 - r^2/a^2)^n \quad (2.11)$$

If the pressure is distributed uniformly over the circular area, n needs to be equal to zero. For a uniform normal displacement, n is substituted by $-1/2$. Equation (2.12) shows the displacements for a Hertzian pressure distribution where n equals $1/2$. The pressure distribution of a Hertzian contact also causes radial displacements as given by (2.13).

$$\bar{u}_z(r) = \frac{(1 - \nu^2) \pi p_0}{E} \frac{1}{4a} (2a^2 - r^2), \quad r \leq a \quad (2.12)$$

$$\bar{u}_r(r) = \frac{(1 - 2\nu)(1 + \nu) a^2}{3E} \frac{1}{r} p_0 \{1 - (1 - r^2/a^2)^{3/2}\}, \quad r \leq a \quad (2.13)$$

2.2.1.2 Tangential loading and friction

A unidirectional tangential force Q applied to the normally loaded bodies gives rise to tangential tractions q which act in opposite directions within the contact. According to Amontons' law of friction, sliding of the whole contact does not occur as long as Q is smaller than the product of the normal load P and the coefficient of friction μ (see Section 2.4). If no slip occurs, the complete circular contact area is stuck. The tangential forces result in a distribution of tractions per unit area (2.14) which causes an elastic uniform displacement \bar{u} for all points inside the contact area (2.15). If the force is applied parallel to the x-axis then the tangential displacement must act in the same direction. The Young's modulus E is expressed by the shear modulus G in the form of $E = 2G(1 + \nu)$.

$$q = q_0(1 - r^2/a^2)^{-1/2} \quad (2.14)$$

$$\bar{u}_x = \frac{\pi(2 - \nu)}{4G} q_0 a = \text{constant} = \delta_x \quad (2.15)$$

The total displacement of the two bodies at a remote point is the sum of the purely elastic displacements for body 1 and 2 as shown in (2.16). The displacements \bar{u}_{x1} and \bar{u}_{x2} are equal if both bodies have the same elastic material properties.

$$\delta_x = |\bar{u}_{x1}| + |\bar{u}_{x2}| = \frac{Q_x}{8a} \left(\frac{2 - \nu_1}{G_1} + \frac{2 - \nu_2}{G_2} \right) \quad (2.16)$$

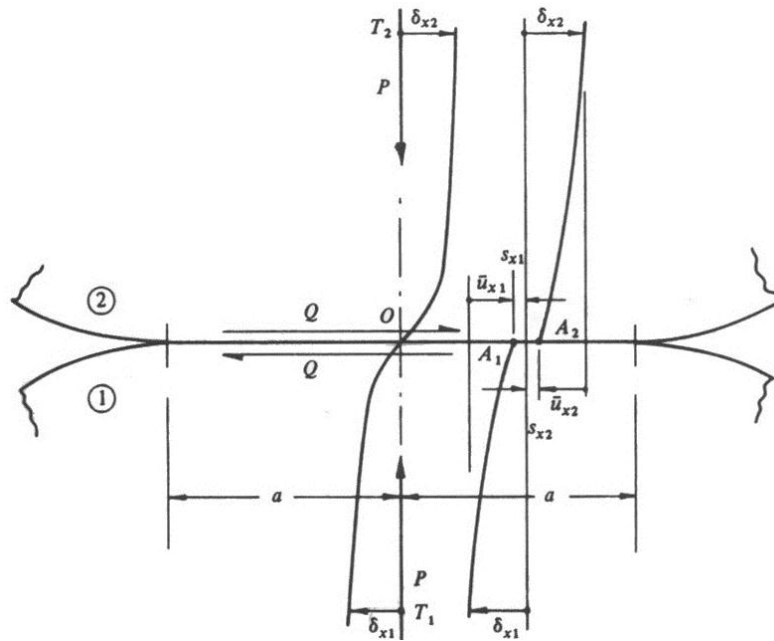


Figure 2-4: Displacements of two spheres which are loaded normally and tangentially.

The distribution of tractions as given by (2.14) would lead to infinitely high tangential tractions at the edges of the contact area. If the full contact remained stuck it would require an infinite coefficient of friction at the edges. Since this is impossible there must be some micro-slip at the edges as indicated in Figure 2-4. With increasing tangential force the micro-slip area starts growing as a concentric circle from the outside of the contact towards the centre.

The Cattaneo-Mindlin [14, 15] solution allows the calculation of the displacements within the slip area due to tangential traction. According results are shown in Figure 2-5.

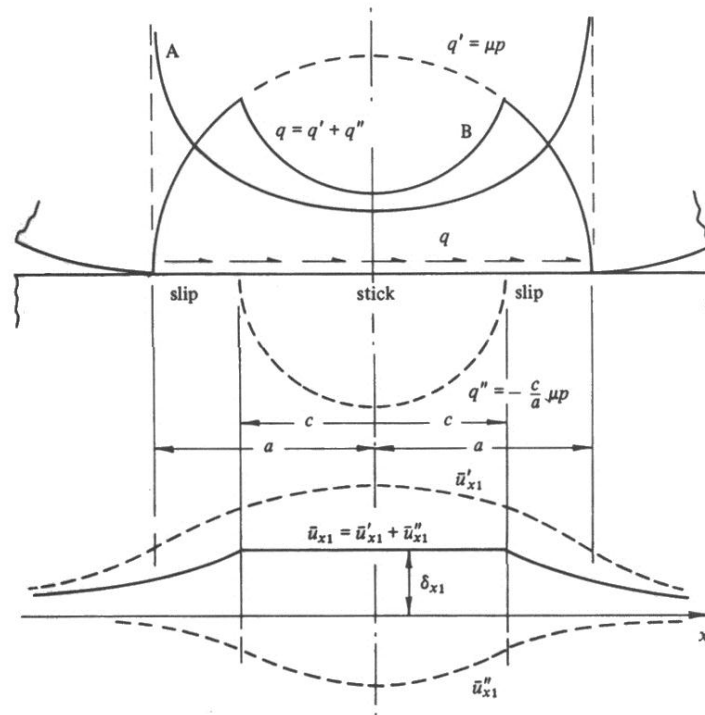


Figure 2-5: Traction and displacement of a sphere-on-half-space contact.

The inner area of the contact which sticks together deforms elastically and uniformly. It is limited by the radius c which is defined by the magnitude of the tangential force Q .

$$\frac{c}{a} = (1 - Q/\mu P)^{1/3} \quad (2.17)$$

Surface points in the outer region experience a rigid deformation and move apart. When only the centre point remains stuck the distribution of traction, which is defined by the force per unit area, is

$$q' = \mu p_0 (1 - r^2/a^2)^{1/2} \quad (2.18)$$

where p_0 is the maximum Hertz pressure. This traction causes displacements inside the contact in the direction of sliding as follows

$$\bar{u}'_x = \frac{\pi\mu p_0}{32Ga} \{4(2-v)a^2 - (4-3v)x^2 - (4-v)y^2\}, \quad r \leq a \quad (2.19)$$

To fulfil the requirement of a uniform normal displacement within the stick area the distribution of tractions q' needs to be corrected by

$$q'' = \mu p_0 (1 - r^2/a^2)^{-1/2} \quad (2.20)$$

To establish the displacements of the total contact one must first determine the displacements due to the tractions given by (2.20).

$$\bar{u}''_x = -\frac{c}{a} \frac{\pi\mu p_0}{32Gc} \{4(2-v)c^2 - (4-v)x^2 - (4-3v)y^2\}, \quad r \leq c \quad (2.21)$$

The displacements caused by q' and q'' are then added up and result in the overall distribution of displacements as follows

$$\bar{u}_x = \bar{u}'_x + \bar{u}''_x = \frac{\pi\mu p_0}{8Ga} (2-v)(a^2 - c^2) \quad (2.22)$$

The total relative tangential displacement of the two bodies is given by equation (2.23).

$$\delta_x = \frac{3\mu P}{16a} \left(\frac{2-v_1}{G_1} + \frac{2-v_2}{G_2} \right) \left\{ 1 - \left(1 - \frac{Q_x}{\mu P} \right)^{2/3} \right\} \quad (2.23)$$

The slip displacement can be found from equation (2.24) which relates the contributing parts of the total displacement. An approximation of the magnitude of slip at a radius r within the slip annulus is given by equation (2.25).

$$s_x = (\bar{u}'_{x1} + \bar{u}''_{x1}) + (\bar{u}'_{x2} + \bar{u}''_{x2}) - \delta_x \quad (2.24)$$

$$s_x(r) \approx \frac{3\mu P}{16Ga} (2 - \nu) \times \left\{ \left(1 - \frac{2}{\pi} \sin^{-1} \frac{c}{r}\right) \left(1 - 2 \frac{c^2}{r^2}\right) + \frac{2c}{\pi r} \left(1 - \frac{c^2}{r^2}\right)^{1/2} \right\} \quad (2.25)$$

2.2.1.3 Stiffness and compliance of loaded bodies

Assuming that both asperities have the same material properties, the normal k_n and tangential stiffness k_t can be found as follows.

$$k_n = \frac{dP}{d\delta_z} = \frac{2Ga}{(1 - \nu)} \quad (2.26)$$

$$k_t = \frac{dQ_x}{d\delta_x} = \frac{4Ga}{(2 - \nu)} \quad (2.27)$$

The normal and tangential compliance c_0 is the reciprocal of the corresponding contact stiffness. The magnitude of the compliance is approximately the same for both directions.

2.2.1.4 Energy dissipation and oscillating tangential forces

If the contact experiences an oscillating tangential force where the amplitude is too small to cause complete sliding, the relationship between force and displacement forms a closed hysteresis loop as shown in Figure 2-6 [16]. The displacement between the points O and A is given by (2.23). The tractions at point A are given by the sum of (2.18) and (2.20). Tractions at points B , C and D and the incremental tractions between these points as well as the displacements can be found in reference [4]. The area within the loop represents the dissipated energy due to the friction process and was first expressed by Mindlin [17].

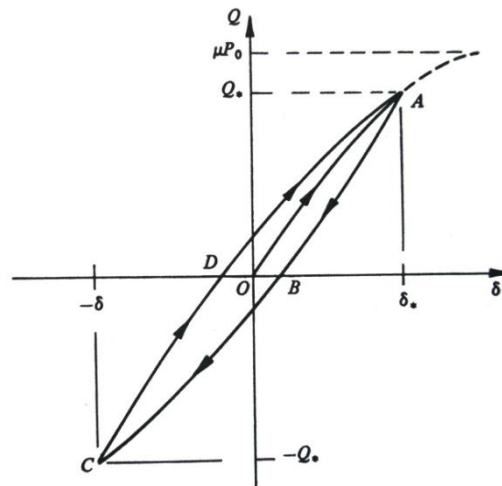


Figure 2-6: Load displacement loop [4].

2.2.1.5 Elasto-plastic single asperity contact model

Up to now only purely elastic contact has been assumed where the displacement is carried by the elastic deformation and the micro-slip between the surfaces. After experiments showed that contacts in partial slip could accommodate much higher displacements than expected by elastic theory, Ödfalk and Vingbo [18] proposed an elasto-plastic contact model. A concentric area of yield is introduced between the stick and the slip area.

2.2.2 Multi-asperity contact models of rough surfaces

Moving on from a single asperity contact to a multiple asperity contact, Bowden and Tabor [19] pointed out that when two nominally flat surfaces are put into contact only a small fraction of the nominal area of contact A_0 is actually in contact. This is called the true area of contact A . The easiest step from a single asperity model to a multi-asperity model is an arrangement of equal asperities. However the requirement imposed by Amontons' law of friction that the area of contact must be linearly proportional to the normal load would not be obeyed for an elastically deforming surface of equal asperities. Hence, heavy plastic

deformation and only a small amount of elastic deformation was expected which follows the above requirement as follows

$$A = P/H \quad (2.28)$$

where H is the hardness of the softer of the two materials in contact [20]. Even though plastic deformation is likely in the first few deformation cycles, an elastic steady state is eventually reached. The proportionality could finally be explained for an elastically deforming surface when Archard [21] introduced a surface model where hemispherical asperities are superimposed by smaller asperities, which are again covered in smaller asperities. When such a rough surface is pressed against a smooth rigid surface, as depicted in Figure 2-7, a simplification which was later justified by Greenwood and Tripp [22], the area of contact becomes close to being proportional to the load. The number of contacts becomes proportional to the area of contact and the number of individual areas becomes nearly proportional to the load and their sizes less dependent on it. Archard [21] concluded that plastic as well as elastic contact models were reasonable and obey Amontons' law of friction.

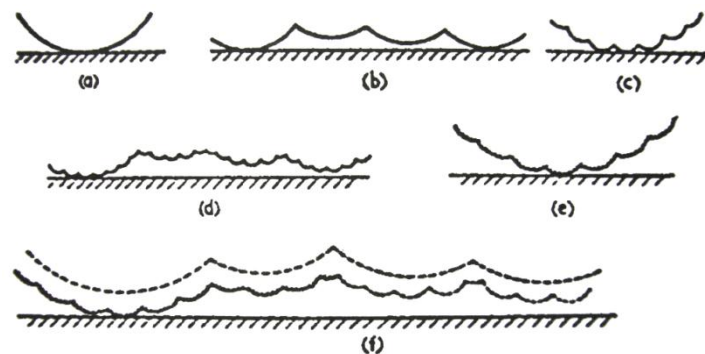


Figure 2-7: Model by Archard [21] with superimposed asperities.

2.2.2.1 Statistical and random process models

Greenwood and Williamson [23] combined Archard's representation of a rough surface with a statistical distribution of heights and proposed an elastic contact model with the following requirements.

- The rough surface is isotropic.
- The summits of the asperities are spherical and have the same radius of curvature.
- The heights of the asperities follow a Gaussian random distribution with a standard deviation of σ .
- No interaction between neighbouring asperities is allowed.
- The model is restricted to low loads which result in asperity deformation but not bulk deformation.

An example surface is shown in Figure 2-8.

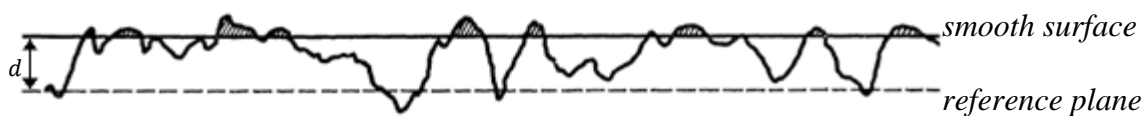


Figure 2-8: Contact between a rough and a smooth surface. The load is carried by the shaded asperities which are greater in height than the distance between the two reference planes [23].

If the surfaces come in contact each of the asperities whose height is greater than the distance d between the two reference planes forms a contact circle with the radius a and can be treated as an isolated Hertzian contact. The probability for an asperity of the height z to form a contact is given by the cumulative probability of the height distribution, see Equation (2.3). An exponential distribution, which does not require numerical integration in subsequent analysis, is commonly used to approximate the top end of a Gaussian distribution, since only the uppermost asperities are thought to be in contact. The model predicts a real area of

contact which is nearly proportional to the load and therefore obeys Amontons' law of friction.

This model has been extensively refined and extended as follows. E.g. curved surfaces [24] and misaligned asperities [22] were taken into account. Whitehouse and Archard [25] refined the properties of the surfaces such as decreasing the radii of curvature and introducing a statistical distribution of curvatures. Nayak et al. [26] used three spectral moments of the profile to fully describe random, isotropic, Gaussian surface profiles: variance of the distributions of profile heights, slopes and curvatures. The restriction of low loads to ensure no interaction was lifted to some extent by the introduction of paraboloidal asperities [27].

The prediction of the contact area with elastic contact models is only accurate up to a certain loading. At high loads elastic models underestimate the area of contact. Greenwood and Williamson [23] also introduced the 'plasticity index' for spherical asperities which provides a criterion whether a contact behaves elastically or plastically. The index, given by (2.29), represents the ratio of the nominal elastic contact pressure to the hardness, where H is the hardness of the material. Elastic behaviour is expected, when the index is low.

$$\psi = \frac{E^*}{H} \left(\frac{\sigma}{R} \right)^{1/2} \quad (2.29)$$

Pullen and Willimason [28] considered a plastic contact model which in contrast to previous plastic models took volume conservation into account. The displaced material would not be cut off but rise uniformly in the non-contacting surface areas. The resulting model showed that interaction between asperities starts already at very low loads and that the maximum real area of contact was predicted to be half the nominal area of contact.

Combined elastic-plastic models were presented by e.g. Chang et al. [29] who first took volume conservation into account and introduced a critical interference parameter which was

based on the plasticity index. Abdo and Farhang [30] further developed the concept of critical interference and combined elastic and plastic deformation within one asperity. First an asperity deforms elastically until a second layer at the depth of the critical interference is reached and the material deforms purely plastic.

2.2.2.2 Numerical contact models

The later random process models are not restricted anymore to a constant radius of asperity curvature like the original Greenwood and Williamson [23] model but they still require height and spatial parameters to describe a rough surface. The advance of computer technologies enabled the digitisation of measured surface profiles and the introduction of numerical models. The analysis could now be done directly on measured surfaces and there was no more need to model a surface based on simplifying assumptions.

The area of the contact is discretised into a mesh of small elements, which can be of the same size as the sampling interval of the measured surface. Webster and Sayles [31] employed the theory of Boussinesq-Cerruti (see section 2.2.1.1) to find the normal displacement within each element due to a concentrated force, applied at a different point of the surface. The position where the concentrated force is applied is where a contact is formed. If there are numerous contact spots their effect is added up to a total displacement for each element. The displacement u is then related to the contact pressure p via the so called influence matrix C . Initially the elemental pressures are not known but an iteration process can be employed to solve this problem. When two surfaces profiles approach each other in a rigid fashion, they overlap in the regions where the true area of contact is formed. The depth of the geometrical interference corresponds to the displacement and can be implemented to calculate the pressures distribution. An element with a negative contact pressure (tensile) is treated as invalid and the particular element is excluded from the next iteration until only elements with

a positive contact pressure are left. These elements correspond to the real area of contact. A comparison shows that the Hertzian model underestimates the local contact pressures for a rough surface. Local pressure peaks which are caused by the roughness and the contact of distributed asperities, are much higher than the pressure distribution proposed by the Hertzian contact model.

West and Sayles [32] extended the model to predict pressure distributions for three-dimensional surfaces. When allowing plastic deformation their method was also able to predict topography of a recovered surface after plastic deformation. Ren and Lee [33] introduced a moving grid method which reduced the high computational times for three-dimensional problem significantly.

2.2.2.3 Other contact models

Finite elements contact models have been developed by e.g. Francis [34] and Komvopoulos and Choi [35] but they are limited by the number of mesh elements of which a gigantic number is needed for three dimensional rough surface modelling.

The self-affinity of surfaces is used in the fractal analysis of contacts by e.g. Majumdar and Bhushan [36]. One of the main arguments for the use of fractal models is the limitation of every measurement technique by its resolution and the sensitivity of surface roughness parameters to filtering.

2.3 Fretting

Several tribological problems can result from the relative motion of two rough surfaces in contact. Those of interest to this work are caused by small sliding motion, which the term fretting is often applied to.

Fretting describes the surface damage of the surfaces which experience a tangential small amplitude loading over a large number of cycles, often caused by vibrations. Fretting was first observed on steel samples, where it leads to the production of red and brown iron oxides. Hence, the process was initially called fretting corrosion, a term which is still used [37]. Several extensive reviews on the subject have been compiled by Waterhouse [38-40].

The observed surface damage is caused by shear stresses and strains and can be divided into fretting wear and fretting fatigue. Both can lead to failure of the components. Fretting damage has been observed e.g. in dovetail joints [41], spline couplings [42] and riveted lap joints [43]. However fretting damage can occur in any loaded joint which is subject to vibrations. Equally, many different bulk materials and coatings have been studied under fretting conditions: e.g. steels [44, 45], titanium alloys [46, 47], aluminium alloys [48] nickel based alloys [49] and more. In order to simplify the contact conditions of applications scientists study often simplified systems such as ball-on-flat [44, 45, 50], cylinder-on-flat [51] or flat-on-flat [52, 53] geometries.

2.3.1 Fretting regimes

Fretting may be divided into fretting regimes where either fretting wear or fretting fatigue is the predominant damaging process. The regimes correspond to the stick-slip conditions introduced earlier by the Cattaneo-Mindlin theory (see Section 2.2.1.2) and are dependent on the slip amplitude as shown in Figure 2-9.

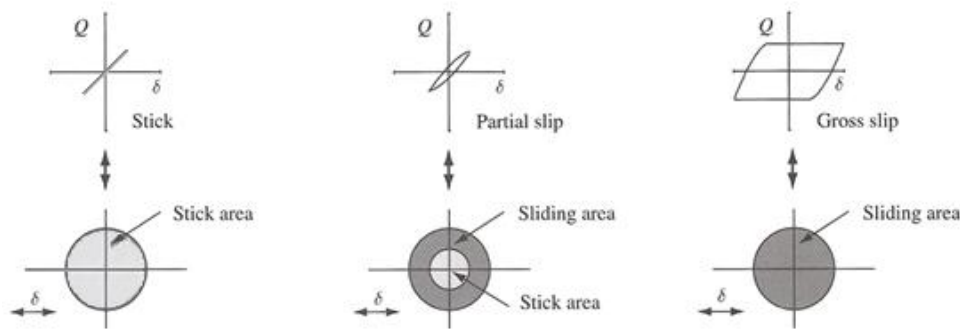


Figure 2-9: Stick, partial-slip and gross slip regime with corresponding fretting logs and contact areas for a ball-on-flat contact.

Whether a contact remains stuck or experiences partial slip or gross slip is controlled by normal and tangential loading. At low tangential excitation forces the whole contact remains stuck and only limited surface damage and no crack formation takes place. An increase of excitation forces results in a mixed partial regime where for a circular contact the outer annulus of the contact area starts sliding and the centre remains stuck. Damage appears only within the slip area and the stuck inner circle can be clearly distinguished from an outer worn circular annular [54]. Fretting fatigue is the main failure mechanism under partial slip conditions and crack nucleation is very likely in this regime. With further increase of the excitation forces, the sliding annulus grows into the centre of the contact until the full sliding of the contact is reached and fretting wear becomes predominant. Zhou and Vincent [55] further established the mixed fretting regime which marks the transition from partial slip to gross slip. In this regime a competition between crack nucleation and wear takes place

Vingsbo and Söderberg [45] introduced fretting maps to distinguish the different fretting regimes. Figure 2-10 (a) depicts the contact regimes in relationship with contact load and slip amplitude. Fretting maps are useful tools to locate the different fretting regimes or to present the material response due to the fretting loading. Material response fretting maps, which are

based on literature data and extremely time dependent, have been compiled as well, and an example is shown in Figure 2-10 (b).

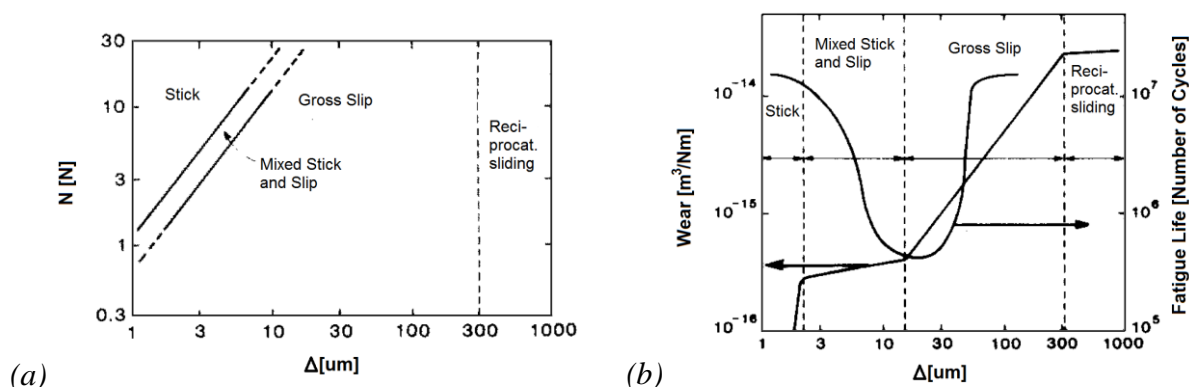


Figure 2-10: (a) Schematic fretting wear map which indicates the different fretting regimes depending on normal contact load, N , and sliding amplitude, Δ , and (b) wear and fatigue life versus sliding amplitude, Δ , [56].

Mindlin's [15] elastic theory can be used to predict the boundary between stick and slip and partial and gross slip for given loading conditions. However, Brygman and Söderberg [57] state that an elastic analysis underestimates the amplitude boundary as a significant amount of the displacement can be accommodated by plastic deformation. The transition from gross slip to reciprocating sliding is rather vague but a general rule claims that gross slip experiences sliding amplitudes which are much smaller than the diameter of the contact. Baker and Olver [58] reported a change of wear mechanism at approximately $200 \mu\text{m}$ stroke length associated with a large increase in the rate of removal of debris from the contact. Others reported displacement amplitude ranges for reciprocal sliding between 50 to $300 \mu\text{m}$ [45]. Varenberg et al. [59] proposed the concept of a slip index to find the transitions between the fretting regimes.

2.3.2 Fretting mechanisms

Fretting wear and fretting fatigue have been widely recognized as the source of fretting damage. Overstraining of the contact surface causes material changes and a subsequent loss in toughness leads to cracking and debris formation. Overstressing of the contact at the border between stick and slip zone leads to fatigue cracks. Even though wear and fatigue are often attributed to different fretting regimes their separation is not clear [60].

2.3.2.1 *Fretting wear*

Based on the early work of Tomlinson [61], Hurricks [62] reviewed the mechanisms of fretting wear and identified three stages: (1) Establishment of metal-metal contact, (2) debris production and (3) steady state. Various mechanisms and their combinations have been suggested to contribute to the debris production.

The first stage lasts only for a few strokes. Superficial oxide layers, present at any material, are removed and metal to metal contact is increased which initiates debris production [62].

Adhesion and material transfer play important roles at the initial stage of debris production. High pressures at the asperities weld the freshly formed metal-metal junctions together, tangential movement rip them apart and transfers material from one surface to the other. Further strokes break this material from the surface and metallic loose particles oxidise between the two surfaces. The oxidised materials are harder and promotes abrasive wear [62].

Suh [63] proposed the delamination mechanism as a process contributing to debris production. After the surface is smoothed by adhesion the surface is continuously stressed due to the fretting conditions, similar to a hard-working process. Dislocations pile up and form voids. Sub-surface crack initiate from these voids due to shear stresses and spread out, leading to the detachment of plate like particles of oxide coated metal. The thickness of these

primary flakes ranges from 1 to 10 μm , depending on the material [64, 65]. The oxide layer on the flakes can only be thin, but further breaking down of the flakes into smaller particles enhances the oxidation of the debris. Vingsbo and Söderberg [45] reported sliding marks in the direction of sliding which result in a scale-like topography and superficial plastic deformation which lead to extruded, elongated wear debris. Kapoor and Johnson [66] introduced the ratchetting mechanism in order to explain the formation of delamination. The accumulation of plastic strain in the contacts lead to fatigue of the material and wear debris is formed after reaching a plastic shakedown limit.

A different process leading to the degradation of the surface was observed by Sauger et al. [67]. The authors suggest that ductile materials form a nanocrystalline tribologically transformed structure (TTS) which is initiated by recrystallisation due to high plastic yielding. The weaker layer cannot resist the imposed displacement and breaks. Fragmentation of the parts continues. A threshold for the activation energy is suggested which must be exceeded to plastically transform the material [68].

Mohd-Tobi et al. [69] saw the above mechanisms as a stepwise process, as shown in Figure 2-11, leading up to wear.

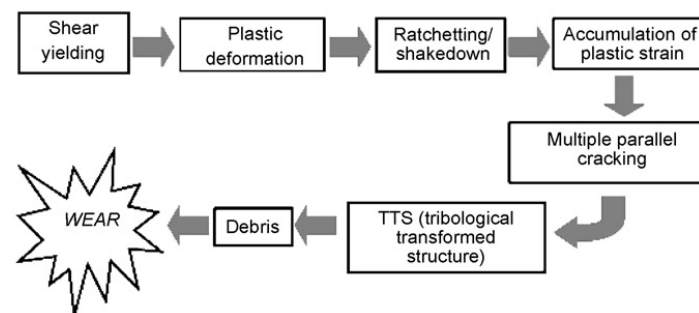


Figure 2-11: Delamination wear as a process schematic as presented by [69].

Kalin and Vizintin [70] observed phase transformation in steel samples which they attributed to local temperature rise. The phenomenon was observed under selected fretting conditions, where load and velocity were severe enough. The study does not clarify if the severe plastic strain alone could result in a phase change.

An abrasive wear mechanism takes place when material is removed from the surface by a harder material sliding across the surface under pressure. The harder material can be the counterface, when it is called ‘two-body abrasive wear’, or when loose particles which are moving and rolling around between the two surfaces, ‘three-body abrasive wear’. In the latter case, roughness, hardness and the motion path of the particles play an important role. If, for example, the particles are significantly harder than the surface, then the particles can embed into the soft surfaces and the mechanism returns to a two-body case. Abrasion decreases as the debris layer increases and a steady state is reached. Metallic debris is crushed into smaller metallic particles which start oxidising. The newly formed free surfaces and the defect rich subsurface promote the adsorption of gaseous oxygen. Further contributing mechanisms to oxidation are thought to be oxidation through flash temperature effects or oxidation through mechanical deformation [62]. One of the first wear models, proposed by Uhlig [71], incorporated the abrasive wear mechanism and assumed a repeated scraping off of oxide films by the asperities in combination with ploughing processes. However a purely abrasive wear mechanism during fretting conditions is unlikely, because the wear rates would be too high.

All above mentioned processes are contributing wear mechanisms but the third body theory by Godet et. al [72, 73] regards these processes only as particle detachment mechanisms. When reaching a steady state regime the wear process continues but is now governed by the dynamics of the third body. The formed debris, which is called the third body, is accumulated

in the fretting contact and cannot be ejected. The two surfaces are labelled first bodies. The powder bed, formed of trapped particles, can stop the bulk degradation and absorbs the cyclic loading. The wear rate is controlled by the quantity of debris within the contact. The dissipated energy due to friction can be connected to the formation of debris and tangential displacement.

2.3.3 Fretting fatigue

Waterhouse [74] reported that the initiation of a fatigue crack by fretting is associated with the progressive reduction in adhesion and the development of a slip region which is promoted by the presence of loose debris. The fatigue crack is initiated in the boundary between the slip and the non-slip areas. If the system shows continuously partial slip behaviour and therefore stays in the partial slip regime, initiated cracks propagate and damage is eventually initiated by a decrease in contact stiffness. In the transition from partial to gross sliding the two damaging processes, fretting wear and fretting fatigue, are acting in competition. For example, debris powder can seal small superficial cracks. Slip amplitude and therefore the formation of debris can be minimized if opening cracks take over a majority of the imposed displacement [75]. Immense research has gone into crack nucleation and propagation theories and prediction models but their content will not be part of this thesis.

2.3.4 Observed fretting damage

Cross-sections of fretting specimens reveal the damage to the surface which includes a list of changes: roughness, surface constitution and topography changes, transgranular cracking, phase changes, changes in grain size and shape, changes in composition, such as oxide formation, and changes in mechanical properties, such as microhardness [76].

A u-shaped wear scar is expected for gross-slip conditions of a ball-on-flat geometry as shown in Figure 2-12 (a) and (b). Everitt et al. [51] reported for a Ti-alloy that the thickness of the compacted debris layer is thicker in the centre of the contact. A highly oxidised debris layer is formed which lies on top of a less oxidised debris sub-layer. Deformation is observed in the plastic area. An attempt to characterise the deformation in titanium alloy Ti6Al4V was presented by Swalla et al. [76]. The authors showed that the hexagonal material developed a strong basal texture and which responds to the cyclic softened material.

A w-shaped worn cross section is typical for a surface which experienced partial slip conditions of a ball-on-flat geometry, as shown in Figure 2-12 (c) and (d). A wear annulus can be distinguished as the slip zone from which fatigue cracks propagated [46].

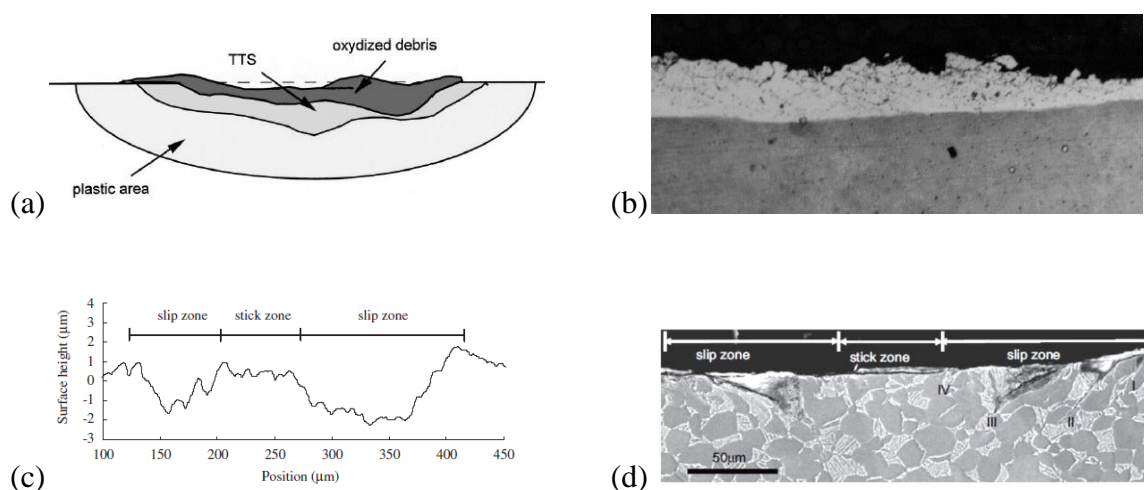


Figure 2-12: Wear scar formation in (a) and (b) gross slip [67] and (c) and (d) partial slip [46].

Fouvry et al. [44] showed that for smaller slip amplitudes, but still in the gross slip regime, the re-distribution of the third body leads to an annular ring of wear similar to the one in partial slip. The maximum stress position is moved from the inside of the contact to the outside towards the contact borders.

2.3.5 Fretting tests

Various rigs have been developed to reproduce and study fretting and record tangential force and displacement. The relationship of these two parameters is plotted as hysteresis loops also called fretting loops or fretting logs. Important parameters such as the friction coefficient μ , the tangential contact stiffness k_t and the dissipated energy E_d can be extracted from the loop as shown in Figure 2-13. The initial slope of the loop is governed by the elastic compliance of the contact, while the width of the loop is controlled by the non-elastic component of the displacement. Johnson [54] represents an elastic contact of two surfaces by two rigid bodies linked by a spring which has internal damping. If the displacement is completely non-elastic, the spring would be infinitely stiff and hypothetical ‘Coulomb damping’ would take place. This would lead to a rectangular fretting loop. As the initial slope in the partial slip area of measured loops appears to be always curved, energy dissipation is also expected during partial slip. An often observed characteristic of measured fretting loops is also an inclined horizontal line opposed to a flat top as shown in Figure 2-13 (a). An analysis by Mulvihill et al. [77] related this inclination to wear scar interaction effects.

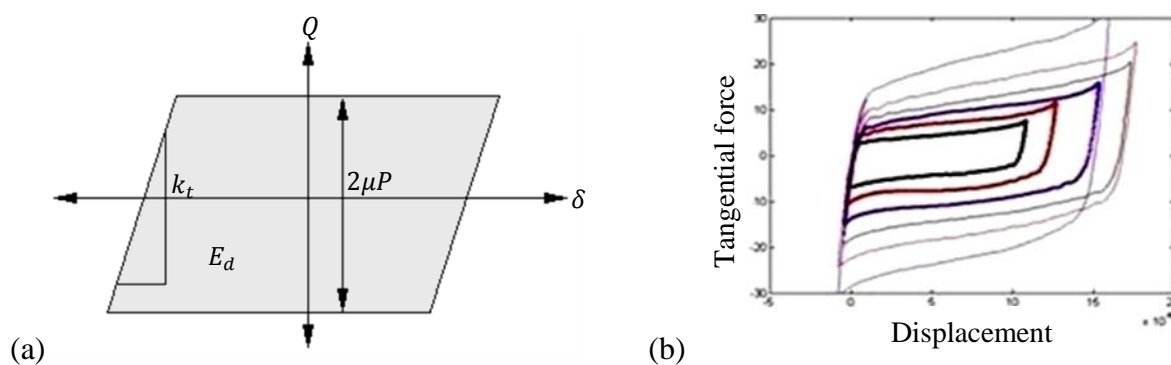


Figure 2-13: (a) Ideal schematic fretting loop and indication of important parameters. (b) Measured fretting logs for different sliding amplitudes and different applied tangential forces.

When recorded over time fretting logs display a running-in behaviour. Along with others, Dini [78] reported a transition from parallelepipedic (gross slip regime) to elliptic (partial slip regime) as shown in Figure 2-14 (a).

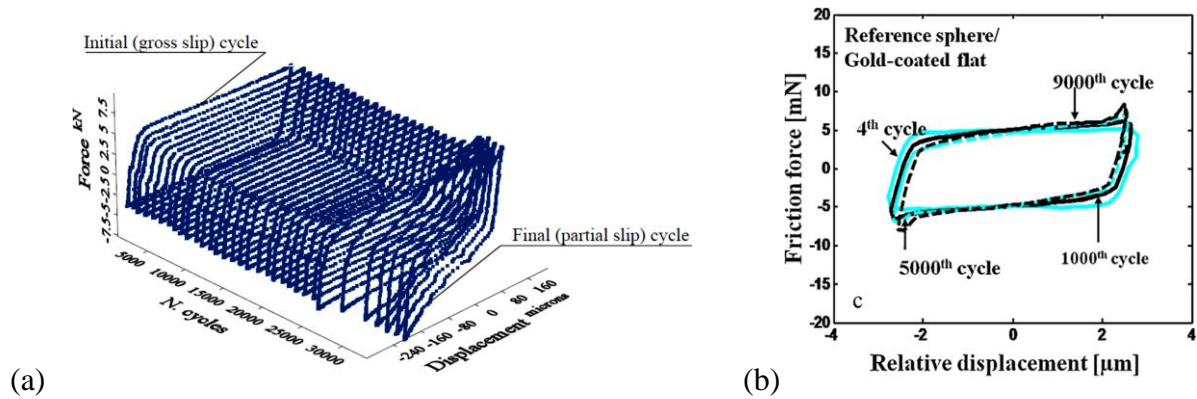


Figure 2-14: Time dependent evolution of fretting loops: (a) Transition from gross slip to partial slip behaviour during fretting test [78]. (b) Development of ‘peak’ at the points of sliding direction change [50].

Yoon [50] reported a similar behaviour, but also showed that this distinctive trend was not observed for a sphere in contact with a gold-coated disc. In this case, where one surface was significantly softer than the other, the fretting loops developed a more pronounced turning point as shown in Figure 2-14 (b). Yoon explained both trends by the evolvement of the contact and the establishment of a third body layer, but did not further quantify the evolvement by a parameter.

Based on the analytical and numerical tools presented in Chapter 0 many contact models have been proposed to produce fretting loops. Some of the earliest fretting tests date back to Mindlin [17] who wanted to validate his elastic contact model. The experimental validation process is crucial for every new model.

2.3.5.1 Friction coefficient

The coefficient of friction μ is derived from the distance of the horizontal lines of the loop and shows a running-in behaviour. The measurement of the limiting coefficient of friction is only possible in gross slip conditions as there is no defining plateau reached in partial slip conditions. Friction and friction mechanisms are discussed in more detail in section 2.4.

2.3.5.2 Tangential contact stiffness

The initial elastic slope of a friction loop determines the tangential contact stiffness k_t which is a measure of the frictionless accommodation of the tangential tractions in the interface. Convenient units to quantify the stiffness are $\text{N}/\mu\text{m}$, but some researchers suggested that a normalisation by the nominal area of contact is a valid procedure which leads to units such as kN/mm^3 [49]. Others [79] suggested a normalisation by the square root of the area, resulting in units kN/mm^2 , but it is unclear at the present which normalisation is most appropriate. The tangential contact stiffness evolves similar to the coefficient of friction and shows a running-in behaviour. Filippi et al. [80] emphasised that great care must be taken when designing a rig for stiffness measurements as the measurement of the stiffness of the structure itself must be avoided.

Berthoud and Baumberger [81] showed that the tangential contact stiffness behaves proportional to the applied normal load and did not show a strong dependence on the Young's Modulus of the contacting materials.

Olofsson and Hagman [82, 83] introduced an elastic contact model for micro-slip conditions where the ellipsoidal asperities are uniformly distributed. The model shows that anisotropy, material properties and the number of formed contact spots influences the tangential stiffness

at zero displacement, the length of the micro-slip zone and the energy dissipated in the contact.

Elleuch et. al [84] showed that the tangential contact stiffness can also be used as a prediction tool for crack propagation. Testing an aluminium alloy, a significant increase of the tangential contact stiffness was observed during the initial phase of fretting. No cracking was observed in this phase and the increase is linked to the evolution of the contact interface due to wear and contact area extension. Multigrain crack propagation is linked to a sudden drop of contact stiffness from which a cracking life time parameter was derived.

An alternative way to measure the tangential contact stiffness is by ultrasound measurements. An ultrasonic pulse is sent into the assembly in a direction normal to the interface. The incident wave eventually hits the interface where part of the wave is reflected, part of it is transmitted. The amplitude of the reflected wave divided by the amplitude of the incident wave gives the amplitude of the reflection coefficient which is correlated to the stiffness per unit area [85]. The relationship between reflection coefficient and contact stiffness per unit area of the interface was first proposed by Tattersall [86]. Fundamental work was performed by Kendall and Tabor [87] who used longitudinal waves and their reflection to correlate to the true area of contact. Using longitudinal waves is limited to low loads which can be circumvented by using shear waves. When using shear ultrasonic waves the normal contact stiffness and the acoustic impedance are replaced by the tangential contact stiffness and the acoustic impedance [88]. The measured stiffness in correlation to the applied normal load increases rapidly at low loads but shows only little change at high loads. For repeated loading cycles Dwyer-Joyce et al. [89] assumes that the remaining plasticity in the asperities is gradually removed and that the asperities reach an elastic state. Additionally at the end of each loading cycle plastic deformation might result in a small increase in the interfacial

stiffness. This last increase is not fully understood but the Gonzales-Valadez et al. [90] suggest that stress relaxation and creep phenomena might contribute to the effects. A small increase of the stiffness can be observed at high pressures which is thought to be related to further conforming between the two surfaces [90].

2.3.5.3 *Energy dissipation*

The area of the fretting loop corresponds to the dissipated energy. For very small displacements, measurements by Mindlin [17] showed a quadratic relationship between displacement and energy dissipation. An elastic model by the same author predicted a cubic relationship [17].

The accumulated dissipated energy has been employed as a measure to predict wear as well as crack nucleation and propagation. It was shown that the total wear volume behaves linearly to the accumulated energy dissipation in the fretting contact. Fretting wear prediction using this approach shows higher stability when compared to Archard's wear law approach which links the wear volume to normal force and the sliding [44]. Extensions of the approach took debris ejection into account [91]. It shows that the majority of the dissipated energy is used up for flow of debris and heat generation rather than plastic deformation[91].

Nowell et al. [92] presented an analytical model which is based on the distribution of dissipated energy within the slip annulus of a partial slip contact. The variation of frictional energy dissipation predicted maxima parallel to the fretting direction. This would be only a poor predictor for crack initiation and the authors suggest that in-plane stresses are involved in the nucleation process. The according empirical combination of the parameters improves the prediction, but lacks in a theoretical justification. The results were confirmed by a numerical approach by Medina et al. [93].

Dini and Hills [94] used an analytical elastic model of a sphere in contact with a ‘bumpy’ surface where each asperity was identical. The authors employed the Cattaneo-Mindlin solution and taking corrective tractions into account to calculate the amount of energy for a range of shear forces. They showed that a very lightly loaded smooth contact absorbs slightly more energy compared to a rough one. This is true as long as the shear tractions stay below 37% of the sliding value. When the shear tractions go above this value the rough contact absorbs more energy when compared to a smooth contact.

2.3.5.4 *Temperatures in fretting*

Part of the dissipated energy in a frictional contact is transferred into heat, which leads to an increase of the local temperatures at the interface. The surface conjunction temperature are short lived and known as flash temperatures. The prediction of these temperatures is important as they can initiate the formation of oxides, metallurgically transformed surface layers, thermal expansion or melting of the interfaces [95]. The flash temperature theory [96] distinguishes between transient and steady-state flash temperatures. Under well lubricated conditions the transient flash temperatures stay small and are added to the relatively big steady state temperatures. Dry friction conditions however can lead to transient flash temperatures which become larger than the steady state temperatures. The generated frictional heat in the contact can be described as a heat source moving over the surface and be treated as a heat transfer problem. A summary of the approach of evaluation is for example given in [97].

Sproles and Duquette [98] investigated the effect of temperatures at the interface on the oxidation behaviour and the mechanical properties during fretting conditions. They showed that the average temperature of the contacting asperities does not increase more than 18 K under their testing condition. Based on sliding measurements they composed a map which

showed the dependence of the temperature rise from the sliding velocity and contact pressure. This was accomplished by extrapolating experimental data from sliding tests to lower sliding velocity, which would be expected for fretting. Only at very high contact pressures would fretting conditions result in a significant temperature effect, as confirmed by [70].

Greenwood and Alliston-Greiner [99] presented an analysis to calculate the steady state as well as the spatial variation of temperature within a Hertzian contact subjected to fretting conditions.

Infra-red imaging systems proved to be useful tools to measure temperature fields within frictional contact interfaces [100] or along cross sections into the material [101]. Later these systems were used and studied by Hwang et al. who were interested in the temperature field caused by surface grinding. The radiation was measured up to and including one pixel below the work piece surface which represents the heat flux into the material. So far the approach has not been applied on a fretting contact.

2.4 Dry friction and friction damping

When a body is sliding over a second body it experiences a resistive force called friction. It can be a desirable process such as in the case of joints, clutches, brakes, but undesirable in other case such as gears and bearings. Friction is a dissipative process and is related to an irreversible energy loss. It is the response of the system and not only dependent on the materials in contact. A distinction is drawn between static and dynamic friction where the first is required to initiate sliding, the second to maintain it. Comprehensive reviews on friction can be found in references [7], [19] and [102].

Based on the historical work by da Vinci, Amontons and Coulomb, empirical laws of friction have been established.

- The friction force Q is proportional to the normal force P via the coefficient of friction μ . Coulomb added a smaller load independent term C .

$$Q = \mu P (+C) \quad (2.30)$$

- The coefficient of friction is independent of the nominal area of contact
- The coefficient of friction is independent of the sliding velocity, a statement which has been disproved by a large volume of data
- Dynamic friction is usually lower or equal to static friction

2.4.1 Friction mechanisms

The first friction theories attributed asperity interlocking the most importance, but as this theory does not provide a source of energy dissipation it has been dropped. Other similar theories utilized e.g. depressed obstacles, bent over springs and hard spheres to explain the origin of friction [103].

Bowden and Tabor [19] attributed adhesion and ploughing the responsibility for friction. The coefficient of friction follows as a sum of the two components.

$$\mu = \mu_a + \mu_p \quad (2.31)$$

High pressures at the summits of the asperities result in their plastic deformation. The resulting true area of contact is proportional to the normal load P via the hardness H of the softer of the surfaces (see also Section 2.2.2). Adhesion, caused by molecular forces, bonds the junctions and before the surfaces can slide, a lateral force equal to the adhesive force Q_a is needed to shear and break these junctions.

$$Q_a = A\tau \quad (2.32)$$

where τ is the shear strength of the softer of the two materials. The coefficient of adhesive friction, based on Amontons' law of friction, follows as

$$\mu_a = \frac{A\tau}{P} = \frac{\tau}{H} \quad (2.33)$$

The predicted values for the coefficient of friction lie around 0.2, far lower than experimental data suggests. This is explained by an increase of the contact area due to the tangential force. The more plastically a material deforms, the greater the area of contact and respectively friction increases. This has been called the plastic junction growth model.

The second contribution to friction in the model by Bowden and Tabor is ploughing. It arises from inelastic, plastic or viscoelastic deformation of the asperities while ploughing into each other. A simplified model of a conical asperity grooving into a softer surface is used to estimate the ploughing component of friction. Due to the small slopes of the asperities in a surface this component often stays quite small. The contribution of this mechanism becomes smaller when repetitive sliding caused the asperities to reach their elastic state as shown by experimental data by Bowden and Tabor.

A combined adhesion roughness model was presented by Ford [104] using the Greenwood and Williamson contact model [23]. The author found that the contribution of roughness to friction is half the elastic contribution when the majority of the asperities deform plastically.

2.4.1.1 Adhesion term of friction

The Bowden and Tabor adhesion model assumes that where there is contact the surface adheres completely. The model remains quite basic as it does not consider the variation of adhesive forces in the normal direction. These surface forces become more and more

important with decreasing surface roughness and at very light loads [105, 106]. The actual contact load N in the true area of contact must be the sum of external applied load P and intermolecular adhesion forces P_a as shown below.

$$N = P + P_a \quad (2.34)$$

This leads to the corrected coefficient of friction as follows.

$$\mu_a = \frac{Q}{N - P_a} \quad (2.35)$$

The study of adhesion forces employs the following two models: the JKR model [107], named after Johnson, Kendall and Roberts and DMT model [108], named after Derjaguin, Muller and Toporov.

2.4.1.2 *The deformation term of friction*

Many researchers did not agree with the predominance of adhesion in friction theories and considered deformation losses more important. A component of friction which is only treated secondary in the classical theory by Bowden and Tabor [19] but already Tabor and Greenwood admitted that where adhesion is not possible, friction is dominated by plastic deformation [109].

It was upon this that Bikerman [110] based his opposition to the theory of adhesion. He concluded that adhesion does neither cause nor influence friction because of the omni-present absorbed layer of contaminants on the surface. This layer would prevent metal on metal contact even during sliding due to the high absorption rate in air.

Rigney and Hirth [103] were looking for a way to quantify the contribution of plastic deformation and proposed a model which calculated the work which was done when

deforming asperities. The deformation was limited to the near-surface region and considered work hardening, recovery and microstructure. This concept is very similar to common wear theories and offers a link between wear and friction.

Others have extended the classical friction theory, e.g. Suh and Sin [111] who added a third contributing part. Next to adhesion and asperity deformation, ploughing by wear particles was taken into account.

2.4.1.3 *Other theories*

Other mechanisms which have been attributed to friction are structural effects such as the crystallographic structure of a material and the corresponding number of slip planes and grain boundary effects [5].

Frictional contact on an atomistic level has been modelled using the Prandtl-Tomlinson model [37, 112] which is also known as the independent oscillator model. A review on the principles of atomic friction is given by Hoelscher [113, 114].

2.4.2 Running-in

The term running-in describes the transition from a non-equilibrium state to a steady-state of friction. Running-in can lead to a desired state of the contact and increase life expectancy and prevent failure. Blau [115] reported several types of transitions for friction whereas Figure 2-16 (a) and (b) show the most likely behaviour for dry metallic contacts.

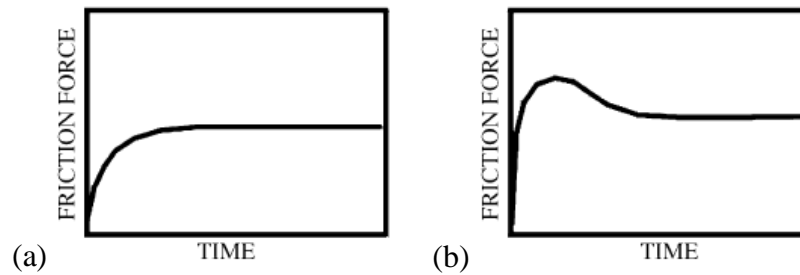


Figure 2-15: Typical running-in behaviour for dry on dry contacts [115].

The first curve, seen in Figure 2-16 (a), is characteristic of a dry clean metal-metal contact. Surface contaminations such as oxide or adsorbed layers are quickly removed and an increase of adhesion increases friction. Figure 2-16 (b) is typical for a non- or boundary lubricated contact. The initial increase of friction is caused by roughness, which is quickly worn-in resulting in conformity and an apparent smoother contact, which reduces friction. Another cause of the initial rise of friction can be surface texturing by shear [115].

Surface roughness and macro-conformity, thermal effects, vibration, microstructural effects such as work-hardening, fatigue damage and third body formation are among the factors affecting running-in [116]. Comprehensive reviews on the subject can be found by Blau [116] and Karpinska [117].

2.4.3 Friction damping

The importance of the frictional behaviour of joints has been recently pointed out by Ewins et al. [52]. Vibration related failures of mechanical assemblies can be avoided by accurate design requiring vibration characteristics of relevant components. Friction dampers are frequently used in bladed disk assemblies and provide additional interfaces at which energy dissipates when slip occurs. Stiffness and damping must be controlled in order to avoid the most severe resonance conditions. If some resonances cannot be avoided the

survivability of the assembly must be guaranteed. Recent models developed to predict the dynamical behaviour of structures divides the contact interface in elements, each attributed friction and stiffness properties. The prediction of vibration properties of separate components is very accurate. However, the accuracy drops significantly when predicting the vibration properties of assembled components where the additional interfaces are ignored. Finite element models which divide the contact interfaces into elements which are assigned friction and stiffness properties improve the predictions. The models predict the frictional response for each element based on this input data. The friction behaviour can be set Coulomb-like as well as modified Coulomb like. Ewins et al. [52] developed a rig which measures the properties on a rig that simulates a modal element of 1 mm^2 .

A review on friction damping and the available methods for vibrational analysis is given by Griffin [118]. Since either stick, slip or separation can occur, the analysis of friction damping is a non-linear problem. Common methods are the Multi Harmonic Balance method, the Equivalent Energy Balance method, the Equivalent Linearization method or the Slowly Varying Parameters method.

Micro-slip is the primary source of friction damping as it modifies the resonant frequencies of the system [80]. Figure 2-16 (a) and (b) show the effect of different values of coefficient of friction and the tangential contact stiffness on the dynamic response of a structure. Under the right conditions it can be seen that the peak displacements can be significantly lowered [119, 120].

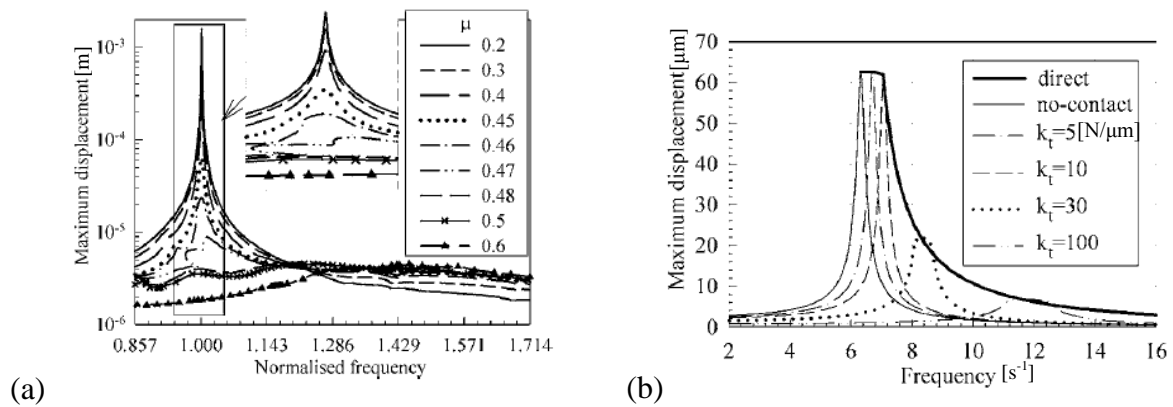


Figure 2-16: Influence of different (a) friction coefficient [119], and (b) tangential contact stiffness [120] values on the dynamic response of a system.

There are two possibilities to describe the frictional phenomenon in models: phenomenological and constitutive. The Coulomb friction model is a phenomenological description of friction and is based on experimental information. The model describes the relation between the tangential force and the relative displacement in a global approach. Constitutive models describe friction as a local problem which can be described as a relation between traction and displacement at the interface. The interface physics become the centre of attention. Moving from the Coulomb model to a constitutive model helps overcoming disadvantages in the case of flexible joints [121].

2.5 Discussion

An overview of contact models, fretting and friction, in particular friction damping, has been given. Both fretting tests and contact models are able to assess the coefficient of friction and the tangential contact stiffness, the values of which are needed for the prediction of the dynamic behaviour of joints.

Knowledge of the surface geometry and contact conditions are essential for the determination of the friction damping as the conditions will affect the resonant response. It has been widely reported that fretting changes the surface topography but a correlation of the surface topography to the change of macroscopic load-displacement loops is still lacking. Also an interpretation of the variable shape of fretting logs is missing in the literature. Further transformations of the fretting interface, such as deformation and oxidation need to be added to a wider understanding.

Latest contact models predicting tangential contact stiffness and energy dissipation distribution within the slip area need validation.

The current contribution is needed in order to provide experimental data for the dynamic prediction of joints, the validation of the latest contact models and to clarify to what extent the material and the surface morphology effect the measurement of fretting logs.

Chapter 3

Friction tests – Materials and methods

Coefficient of friction and tangential contact stiffness are parameters describing the reluctance to sliding and are crucial input parameters when modelling the dynamic response of a structure. These parameters were obtained from friction tests as described in this chapter. The materials which were tested, the methods which have been used to measure these parameters, as well as the methods used for further investigation of the fretting contact are presented in this chapter.

3.1 Materials

Four different materials were chosen to perform friction tests on: the Ti-alloy Ti6Al4V, the Ni-based super-alloy Udimet 720, the stainless steel BS 970 303S31 and the low alloy steel BS 970 EN24T.

3.1.1 Ti6Al4V

Ti6Al4V (MSRR 8672) is a widely used titanium alloy in the aerospace industry. The alloy was designed for high strength applications at temperatures up to 400°C [122] and is, for example, used for fan blades in turbine engines. Its mechanical properties, and also those of all the other materials described here, are summarized in Table 3-1. The microstructure, as shown in Figure 3-1 (a), consists of equiaxed α -Ti grains and an α - β lamellar structure at the

grain boundaries. The crystal structure of the α -phase, which is stable at room temperature, is hexagonal closed packed (HCP). The β -phase has a body centred cubic (BCC) crystal structure.

When deforming Ti6Al4V, the most active slip planes in the α -phase are $\{10\bar{1}0\}$ planes which correspond to the prismatic planes in the hexagonal crystal. The corresponding slip direction is given by $\langle 11\bar{2}0 \rangle$. Slip on $\{10\bar{1}1\}$ first order pyramidal planes and the (0001) basal plane are possible but require favourable orientations [123].

Titanium alloys form a very stable, continuous, extremely adherent, and protective surface oxide layer. The oxide film on titanium forms spontaneously due to the high affinity of the metal to oxygen. If new substrate is exposed due to damage the oxide layer heals itself rapidly. Depending on the environmental conditions, different oxides are formed, including TiO_2 , Ti_2O_3 , and TiO . The oxide scale formed at low temperatures consists of a less crystalline and protective form of TiO_2 called anatase or a mixture of rutile and anatase. An oxide layer consisting of the chemically resistant rutile, TiO_2 , is formed at high temperatures [124].

The testing material was extracted from strips of cross rolled plate which is used in the manufacture of hollow fan blades. It has been subject to a heat treatment cycle at 950°C which simulates the diffusion bond super-plastic formation (DBSPF) process. The samples were supplied by Rolls-Royce.

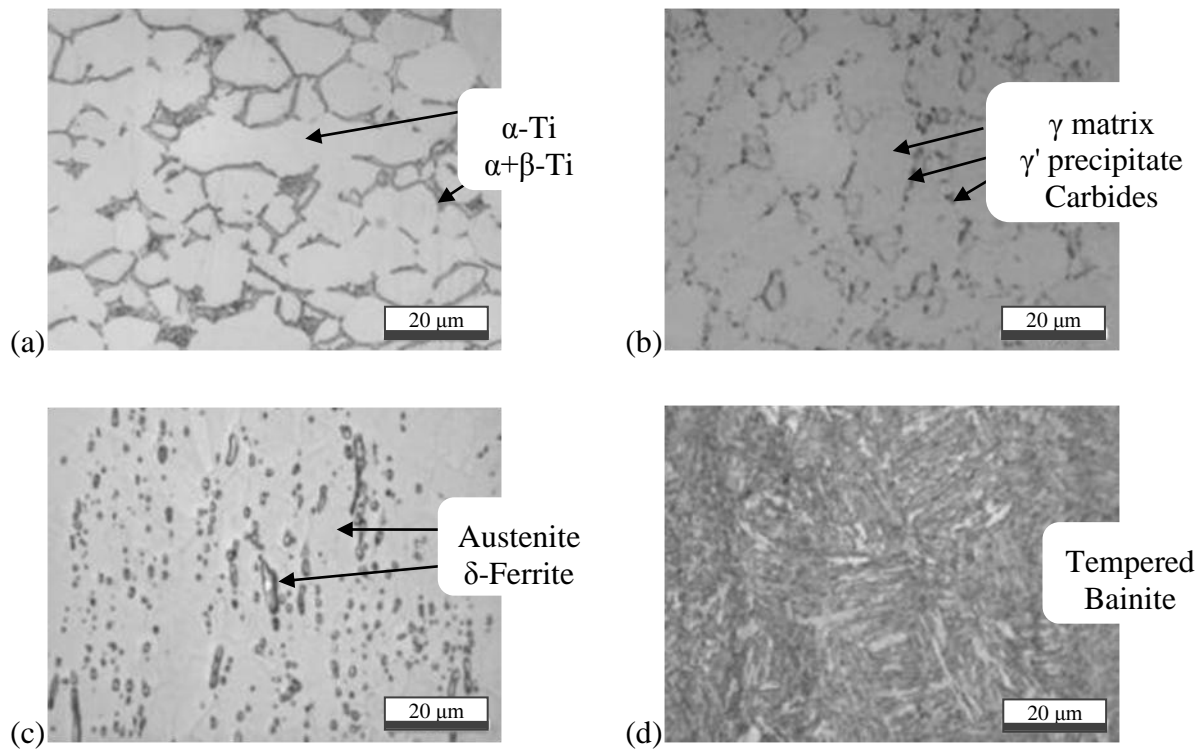


Figure 3-1: Microstructure of (a) $\alpha + \beta$ Ti-alloy Ti6Al4V, (b) Ni-based superalloy Udimet 720, (c) Stainless steel 303S31 and (d) low alloy steel EN24T.

3.1.2 Udimet 720

Udimet 720LI (MSRR 7252), is a multiphase and multi component superalloy based on nickel. The alloy was designed for long time strength at temperatures above 650°C and resistance to hot corrosion and erosion. It is, for example, used turbine discs in gas turbine engines. The microstructure of the alloy consists of a face centred cubic (FCC) γ' precipitate which is embedded in a FCC γ -matrix. The γ' phase has an ordered A3B type structure and improves the strength of the material with increasing volume fraction. Additional phases present are carbides such as MC, M_6C and M_{23}C_6 , and can be recognised as the darkest phase in Figure 3-1 (b). The expected slip system is given by $\{111\}\{1\bar{1}0\}$.

The relevant oxides formed by this material are NiO, Cr_2O_3 , and Al_2O_3 . Of these, Alumina is the most and NiO the least stable oxide. Cr_2O_3 is in between [125]. However, the mechanism

of selective oxidation which takes place in Ni-based superalloys changes this order and NiO forms very rapidly a friable structure [126]. Oxygen can now further diffuse into the material and form a Cr_2O_3 and Al_2O_3 subscale under the external scale.

The hot isostatically pressed casting was forged into a stub using conditions typically for high temperature turbine disc applications and was supplied by Rolls-Royce. The samples used here were extracted from recrystallized material.

3.1.3 Steel selection

For further comparison, two commercially available steels have been added to the selection of materials.

3.1.3.1 *EN24T*

The low alloy steel BS970 817M40 (EN24) was sourced from West York Steel. The nickel chromium molybdenum steel was chosen in a hardened and tempered T condition. The hardening process comprises heating up to 823/850°C until the material is uniformly heated through and followed by quenching in oil. In order to obtain the tempered T condition the material had been uniformly heated to the selected tempering temperature and held at this temperature for 45 minutes for the rod shaped material of a diameter of 9.5 mm.

Low alloy steels show similar high corrosion rates as carbon steels. Different ferrous oxides form: FeO, Fe_3O_4 and Fe_2O_3 . Fe_2O_3 forms an outer layer, whereas FeO is adjacent to the metal. A layer of Fe_3O_4 lies between the other two oxides [127].

3.1.3.2 Stainless steel BS 970 303S31

The austenitic stainless steel BS 970 303S31 (EN58AM) was sourced from RS components as rods with a diameter of 10 mm. The material is non-hardenable by heat treating. The corrosion resistance of stainless steels is based on a thin passive surface layer of chromium oxide which forms as soon as bare material is exposed [127].

Table 3-1: Mechanical properties and chemical composition of materials.

	Young's modulus [GPa]	Yield Stress [MPa] 0.2%	Poisson's ratio ν	Chemical composition
Udimet 720	219	881	0.33	Cr(15.5-16.5), Co(14.0-15.5), Mo(2.8-3.3), W(1.0-1.5), Ti(4.8-5.3), Al(2.3-2.8), C(0.01-0.02), Zr(0.03-0.05), B(0.01-0.02)
Ti6Al4V	115	999	0.31	Al(5.5-6.75), V(3.5-4.5), N(0-0.05), C(0.-0.08), O(0-0.2), Fe(0-0.4), H(0-0.02)
EN24T (BS 970 817 M40)	208.5	834	0.3	Ni(1.31), Cr(1.09), Mn(0.65), C(0.39), Si(0.31), Mo(0.21), P(0.012), S(0.003)
BS 970 303S31	193	190	0.25	Cr(18.0), Ni (9.0), Mn(2.0), Si(1.0), Mo(0.60), P(0.20), S(0.15), C(0.15)

3.2 Methods

3.2.1 Friction tests

Friction tests were performed on two different rigs. Their main difference is the nominal area of contact formed between the specimens. The first rig forms a 1 mm² nominal area of contact, the other an 80 mm² contact area. Results for the 80 mm² rig were supplied by a collaborator and have been previously published by Kartal [49].

3.2.1.1 1 mm^2 contact friction rig

Under standard conditions this rig formed a 1 mm^2 nominal area of contact between two specimens in a flat-on-flat arrangement. Images of the rig and specimens are shown in Figure 3-2. Technical drawings of the specimen with all dimensions are shown in the Appendix, Figure A-1. One specimen was placed on top of a second which was rotated 90° . The bottom sample was mounted onto a static arm which was rigidly attached to the rig. The flat part of the sample was aligned perpendicular to the direction of sliding. The top sample was considered as the moving sample and was mounted to a reciprocating arm which was excited by a sinusoidal shaker at a constant frequency of 100 Hz for all tests. The flat part of the roof was aligned with the direction of sliding. In order to identify the orientation after taking the samples out of the holder the back (B) and the front (F) were labelled accordingly. Whenever a top view of the flat roof or a section of it is here presented, the top of the image corresponds to the back of the specimen and the bottom to the front of the specimen. A detail of the rig showing the mounted samples and the incoming laser beams is shown in Figure 3-2 (c). A dead weight was attached to the top arm to create a nominal pressure of 70 MPa or 45 MPa, depending on the chosen test conditions. The first value represents the maximum testing pressure of the rig, and enables a comparison with the 80 mm^2 rig, which has the same value as a minimum value. The second value was chosen as it represents an average crushing stress value for friction dampers. Crushing stress values depend on the coefficient of friction and lie typically between 5 MPa and 50 MPa for a coefficient of friction of 0.7 for this application. Two force transducers at the end of the static arm captured the time dependent friction force. A Laser Doppler Vibrometer (LDV) pointed alternately at the upper and lower specimen measuring the time dependent velocity of the specimen. The laser was directed as closely as possible to the contact interface. The measured velocity data was then integrated to displacement data. By drawing the measured forces versus the displacement, hysteresis loops

were plotted. To achieve alignment between the two surfaces, a dial test indicator on a stand was used to ensure that the excitation arm sample holder was parallel with the table surface [128, 129].

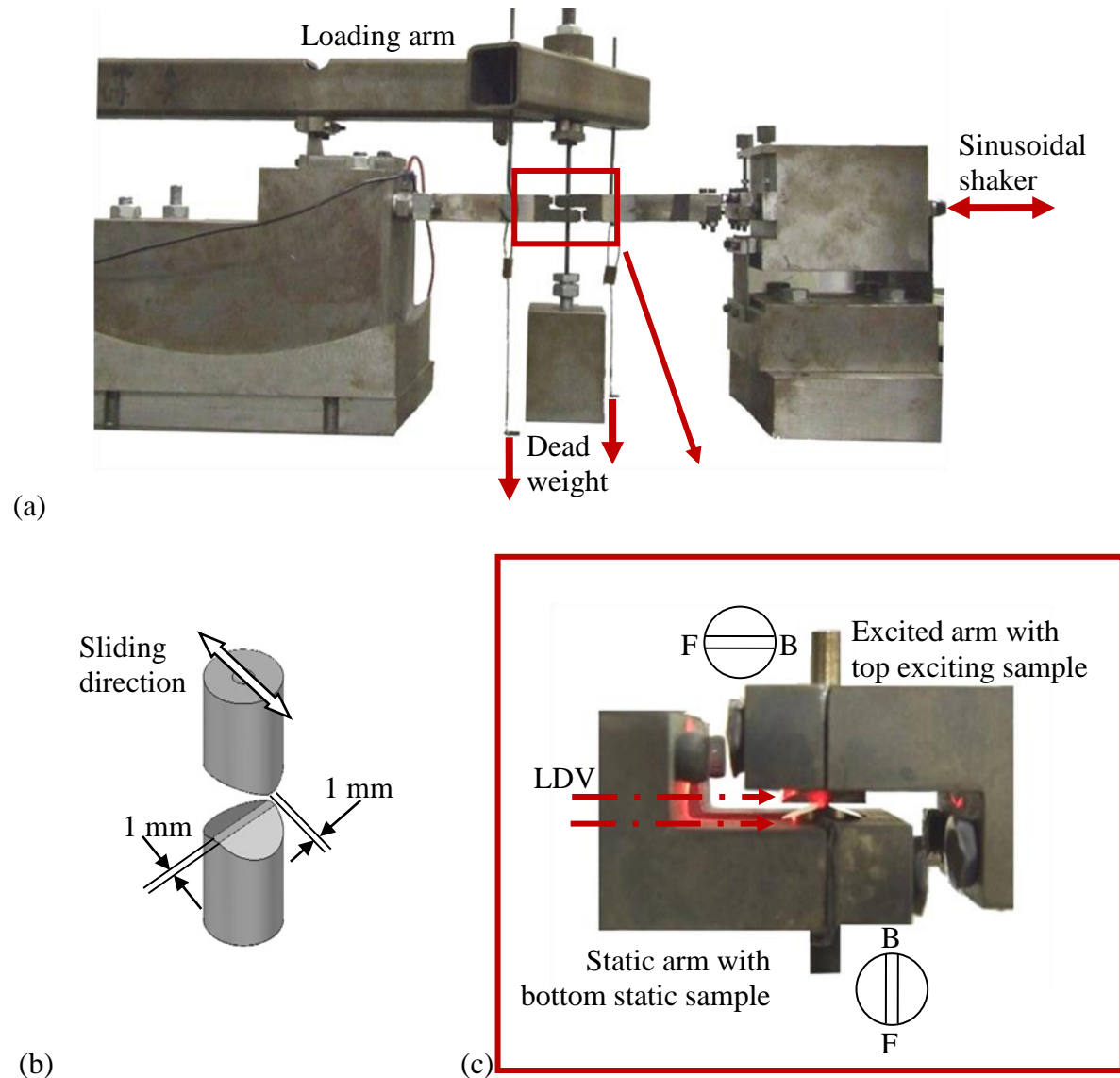


Figure 3-2: (a) 1 mm^2 contact area rig, (b) schematic fretting specimen arrangements forming a 1 mm^2 area of contact [130] and (c) specimens mounted in holders.

Additionally to the flat roof samples sets of specimens forming a cylinder-on-cylinder and a spherical on flat arrangement contact were used. The radius of the cylindrical and spherical

specimens top of the specimens was 33 mm. Under test conditions and a 70 MPa pressure both arrangements formed according to Hertz a 1 mm^2 nominal contact area.

A two-part furnace was used to perform heated tests. The heater halves were positioned around the samples and the loading arms. Great care was taken to ensure that they did not interfere with the laser beams nor touch the rig and dampen the excitation or change the loading of the specimens. Four halogen light bulbs provided the source of heat. A thermocouple was positioned as close to the contact as possible. A second thermocouple was placed away from the heat to provide a room temperature reference. Both thermocouples and heater were connected to a main voltage oven controller where the test temperature was set. An on-off cycle was activated by the controller to reach the required temperature. It required several minutes to reach and keep the temperature stable within a $\pm 20^\circ\text{C}$ frame. The specimen support arms had been designed to withstand the heat but additionally a desk fan was used to keep the heat away from the temperature sensitive force transducers [128, 129].

The procedure of measuring tangential stiffness and friction coefficient is displayed in Figure 3-3. The tangential contact stiffness is the asymptotic value of the inclining slope of the friction loop. Two points were chosen on the inclining slope of the friction hysteresis loop through which a line was drawn. The tangential contact stiffness was read as the slope of this line.

In order to determine the coefficient of friction μ two parallel lines were laid through the bottom and top of the curve. The value of μ could be deducted from the distance between these two lines as they equal $2\mu P$, where P is the normal load [128, 129].

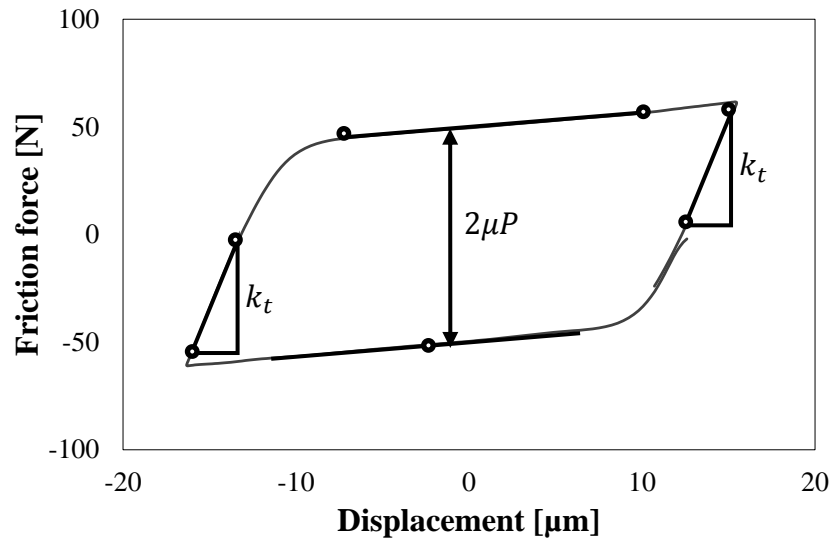
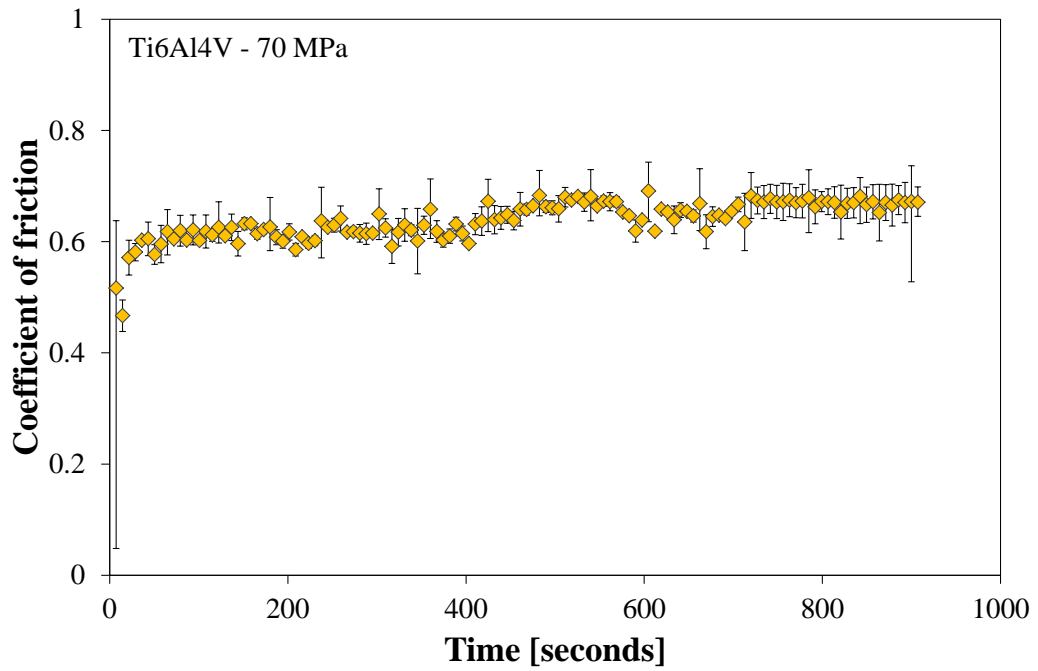


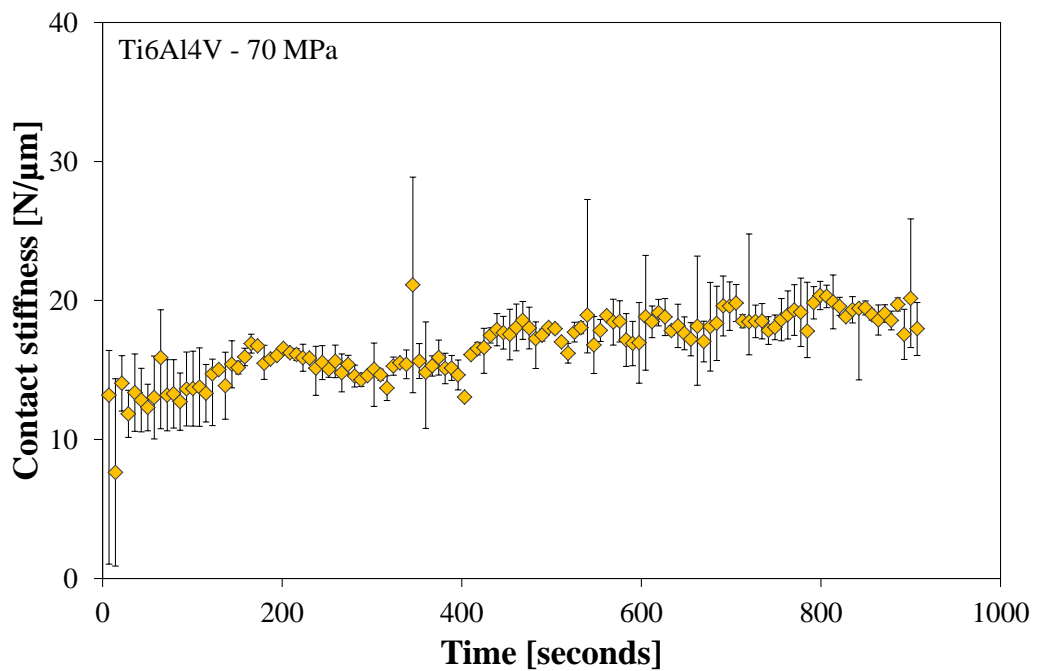
Figure 3-3: Friction hysteresis loop and definition of contact stiffness, k_t , and coefficient of friction, μ .

Properties were first measured with a sampling rate of 1 min. At each minute, including minute zero, 10 loops were extracted. The corresponding contact stiffness and coefficient of friction values were verified and an average final value was determined. For the latest tests the methodology was slightly changed in order to extract a loop and corresponding parameters every 7.2 seconds, which involved rewriting the data retrieving and processing code.

Figure 3-4 shows the repeatability for the measurements for friction coefficient and contact stiffness in the case of 5 different sets of titanium alloy samples with an applied contact pressure of 70 MPa. Friction coefficient results, as shown in Figure 3-4 (a), varied in a range of $\pm 4\%$. Contact stiffness values, as shown in Figure 3-4 (b), varied with a slightly higher value of $\pm 10\%$. The variation was higher for both values at the beginning of tests and decreased after the running-in period. These variation values are representative for all tests performed on the 1 mm^2 contact rig.



(a)



(b)

Figure 3-4: Measurement variation of (a) friction coefficient and (b) contact stiffness.

3.2.1.2 80 mm² contact friction rig

The second friction rig, which has been developed at Oxford University, was substantially bigger. Tests on this rig were not performed by the author of this thesis but by collaboration

partners and results have been previously published by Kartal [49]. A schematic drawing of the friction rig is shown in Figure 3-2 (a). Two pads were symmetrically pressed against a middle specimen and twice a contact area of 80 mm^2 was formed as shown in Figure 3-2 (b). For standard performance, the specimen in the middle was moved up and down with a frequency of 1 Hz and a zero to peak displacement of $200 \text{ }\mu\text{m}$. A recently developed digital image correlation (DIC) method was used to capture displacements and a load cell was used to measure shear forces [49, 131].

DIC enabled the measurement of the displacement at several reference points with different distances from the interface. Because the effect of the compliance of the bulk increases with distance from the interface, the results obtained closest to the surfaces were chosen for comparison. Corresponding friction hysteresis loops could be plotted. Standard settings and a comparison between the two friction rigs are shown in Table 3-2.

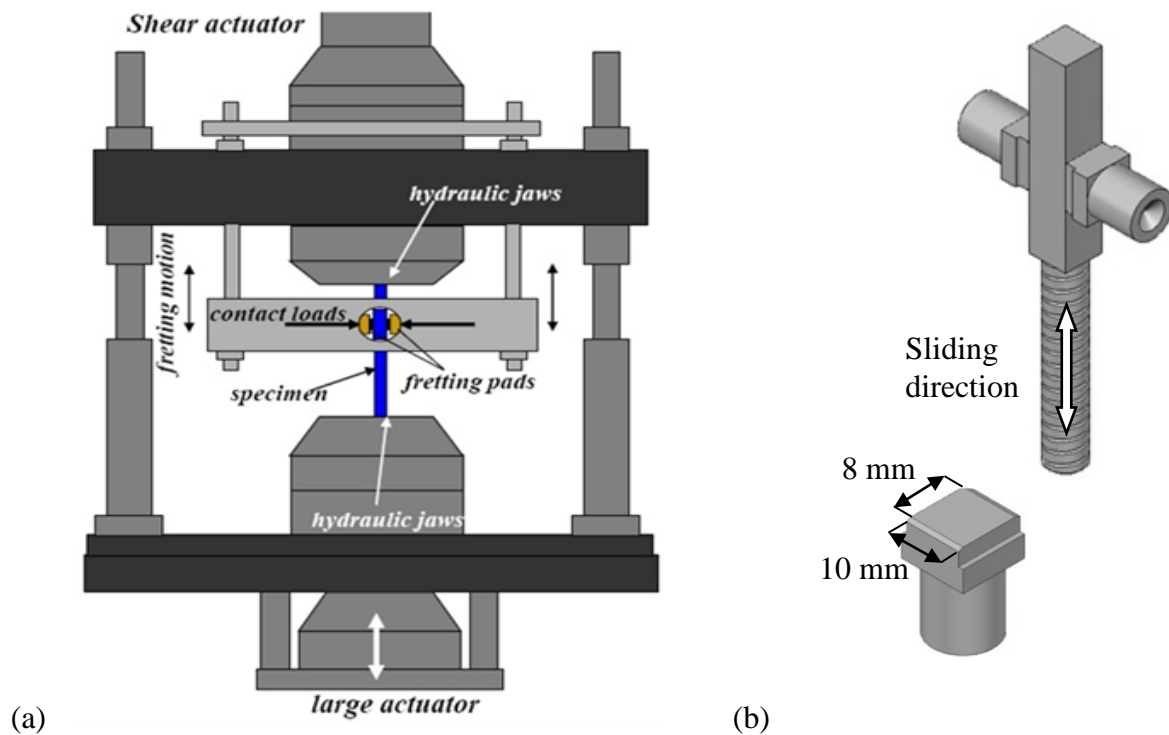


Figure 3-5: Schematic fretting specimen arrangements: (a) 1 mm^2 contact area specimens and (b) 80 mm^2 contact area specimens [130].

3.2.1.3 Comparison between 1 mm² and 80 mm² contact rig

Table 3-2: Standard settings on the 1 mm² and 80 mm² area friction rigs.

	1 mm ² contact rig	80 mm ² contact rig
Contact area	1 mm ²	80 mm ²
Pressure	70 MPa	70 MPa
Frequency	100 Hz	1 Hz
Displacement (0-to-peak)	Not displacement controlled 5-30 μm	200 μm
System	Force controlled	Displacement controlled

3.2.1.4 Sample preparation

Samples were prepared with great care to ensure the least possible surface deformation and negligible oxide layers. The individual machining processes for the standard specimens for the 1 mm² and the 80 mm² contact rig specimens are shown in Table 3-3 to Table 3-5. Prior to all tests and measurements, samples were thoroughly cleaned with Acetone in an ultrasonic bath for 15 minutes.

Table 3-3: Machining processes for 1 mm² rig specimens.

Operation	Machine	Machine tool	Process
Rough band saw	Band saw	High speed steel blade	
Rough square size	Shaper	High speed steel tool	Square pad machined to a collet size that is up on the finish diameter and which is over length
Finish diameter	Lathe	Tip tool	Pad turned to final diameter
Rough length	Lathe	Tip tool	Pad turned to about 0.2 over length
118° angle	Lathe	Carbide tool	Compound slide used to machine the angle
Profile	Diaformer	Green grit wheel	Pad was hold in a 3 jaw chuck to grind the profile, which also created the correct length. The different surface finish on the titanium specimens was accomplished by winding a wheel across by hand with a slightly heavier for only one pass.

Table 3-4: Machining processes for 80 mm² rig specimens.

Operation	Machine	Machine tool	Process
Rough band saw	Band saw	High speed steel blade	
Rough size	Shaper	High speed steel tool	Specimen left 0.5 mm up on dimension
Rough size ensuring square	Mill	High speed steel	Specimen left 0.15 mm up on dimension
Final size	Grind	Green grit wheel	Machined across the length of the components. The different surface finish on the titanium specimens was accomplished by winding a wheel across by hand with a slightly heavier for only one pass.
Threading	Lathe	Tip tool	The specimen was turned around by using a square collet and the thread was screw cut.

Table 3-5: Machining processes for 80 mm² rig pads.

Operation	Machine	Machine tool	Process
Rough band saw	Band saw	High speed steel blade	
Rough size	Shaper	High speed steel tool	Specimen left 0.5 mm up on dimension
Rough length	Mill	High speed steel	Square pad machined to final size
Final size	Lathe	Tip tool	Pad turned to about 0.2 over length
Final diameter	Lathe	Tip tool	Pad turned to final diameter
90° angle	Lathe	Carbide tool	The hole was pilot drilled, followed by machining of the angle using a compound slide.
Machining of steps	Mill	High speed steel	Machining of the two 1 mm steps on pad
Machining on the flats	Mill / Grinder	High speed steel / Green grit wheel	Titanium pads were machined on the mill, nickel pads were machined on a grinder
Profile	Diaformer	Green grit wheel	The different surface finish on the titanium specimens was accomplished by winding a wheel across by hand with a slightly heavier for only one pass.

3.2.2 Surface characterisation

Two surface profiling systems were used which are both based on non-contact interference technology.

3.2.2.1 *Wyko NT9100 profiler*

The Wyko NT9100 (Veeco Instruments Inc.) is an optical non-contact profiler. The system is based on optical interferometry and offers two different measurement options. Vertical

Scanning Interferometry (VSI), which is used to profile rough surfaces and Phase Shifting Interferometry (PSI), which is used for smooth surfaces (see Chapter 6).

In VSI mode, a white light source emits a beam which is split at a beam splitter. One of the two beams is reflected from a reference mirror, the other travels to the samples surface. The beam from the reference mirror unifies again with the light reflected from the surface and will produce interference fringes for the parts of the sample in focus. Additionally a neutral density filter is applied to the beam to preserve the short coherence length of the white light source. This enables the system to measure the coherence rather than the phase of the interference fringes. The light source beam is sampled in definite intervals while the stage moves vertically through the focus which continuously changes the optical path difference (OPD). For each point on the surface, the fringe signal and the corresponding height of the point is recorded. The system automatically applies a low-pass filter to the signals and corrects them by square-law detection; the resolution beyond the sampling interval is improved by using a curve-fitting interpolation technique [132].

The software of the profiler enables visualisation of the surfaces in two and three dimensions and performs calculation of roughness values. Bad data can be removed, tilt or curvature fitted, and sub-regions defined. The height profiles are exported for further editing.

3.2.2.2 Alicona profiler

This profiler uses the InfiniteFocus® method which is based on focus variation. A coaxial white light beam goes through a beam splitter and reflects from the surface of the specimen. The reflected beam goes back through the beam splitter and is delivered to a colour digital sensor. Each position at the surface is differently imaged as the distance between the sample and the objective is changed continuously and the system subsequently calculates the

sharpness for it. From the sharpness data the information of depth for each position can be derived; a 3D plot of the surface can be plot and roughness values extracted [133]. Measurements using this profiler where performed by co-workers and not the author of this thesis.

3.2.2.3 Comparison between Wyko and Alicona

Table 3-6: General specifications.

		Alicona	Wyko NT9100
Magnification		20x	20 x
Vertical Resolution		for 20x 100 nm	3 nm
Horizontal resolution	20x	436.99 nm	487.78 nm
	10x/11x	880 nm	898.31 nm

A preliminary comparison between two measurements performed with each system showed high agreement as shown below. The images appear here slightly different as the Alicona profile is merged with the underlying structure. Only the heights are displayed in the Wyko image. The roughness values of the chosen area of comparison are shown in the table below.

Table 3-7: Comparison of roughness values measured by Wyko and Alicona profiling system.

	S_a [μm]	S_q [μm]	S_z [μm]	S_{ku}	S_{sk}
Wyko	3.60	4.51	29.55	2.91	0.10
Alicona	3.56	4.47	30.76	2.90	0.10

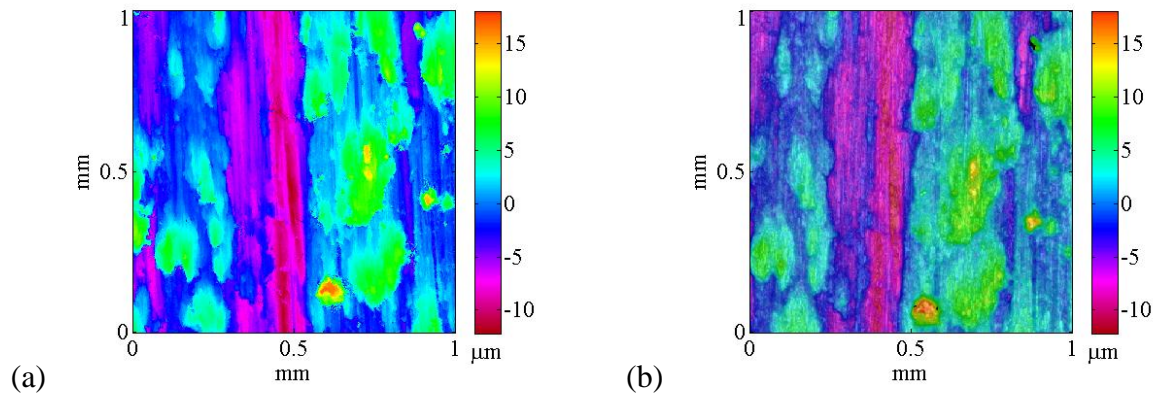


Figure 3-6: Roughness measurements of a 1 mm^2 area using a (a) Wyko system and (b) Alicona system.

3.2.2.4 Measurements

The profiles of all 1 mm^2 friction samples were measured before and after each test with the Wyko NT9100 profiling system. The profiles of the 80 mm^2 contact samples were measured using the Alicona profiler before the tests to ensure that the roughness conditions were similar to the smaller samples. Figure 3-7 (a) indicates the area from which the roughness parameters have been derived.

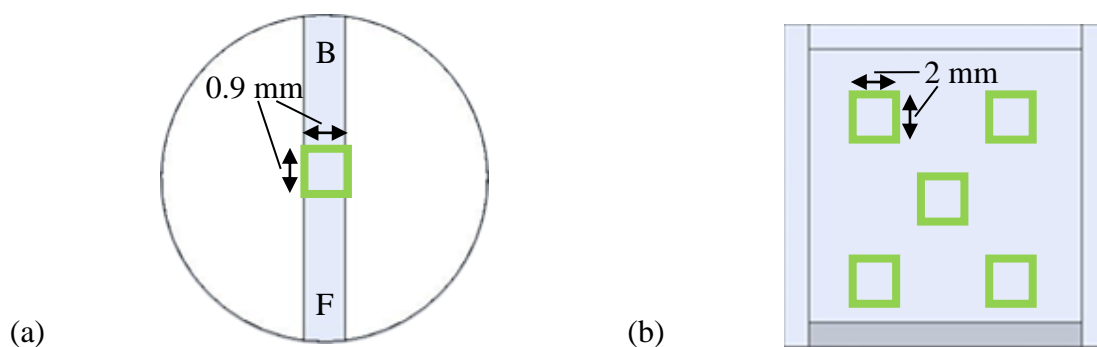


Figure 3-7: Measurement areas for (a) 1 mm^2 contact rig and (b) 80 mm^2 contact rig.

A slightly bigger section than indicated was measured, but a subregion was excluded to ensure that only the flat part of the sample contributed to the roughness calculation. For the evaluation of roughness properties of the 80 mm^2 contact samples, an average of 5 distributed

2x2 mm areas were measured as indicated in Figure 3-7 (b). A summary of surface roughness values for the different specimens is shown in the table below.

Table 3-8: Surface roughness values for 1 mm² and 80 mm² specimens for all materials.

	S_a [μm]	S_q [μm]	S_z [μm]	S_{sk}	S_{ku}
Ti6Al4V rough 1 mm ²	1.87	2.32	14.79	0.07	3.88
Ti6Al4V rough 80 mm ²	2.13	2.74	22.79	0.54	3.49
Ti6Al4V smooth 1 mm ²	1.24	1.60	11.78	-0.54	4.87
Ti6Al4V rough 80 mm ²	1.19	1.49	14.87	-0.01	3.04
Udimet 720 1 mm ²	1.39	1.73	10.08	-0.43	2.86
Udimet 720 80 mm ²	1.54	1.88	16.79	0.04	3.07
EN24T 1 mm ²	1.72	2.05	10.87	0.01	4.55
Stainless steel 1 mm ²	2.39	2.95	18.12	-0.35	3.05

3.2.2.5 Surface wear

Wear volume calculations were performed on the 1 mm² contact samples. After each test, the samples were dismantled from the friction rig, cleaned in an ultrasonic bath in acetone for 15 minutes and then their profiles were measured. The simplest way to calculate the wear volume would be by subtracting the profile of the worn surface after the friction tests, Figure 3-8 (a), from the unworn profile measured before the friction test. If this method were applied

errors occur due to misalignment of the samples caused by the transfer of the samples between the rigs. Samples are moved twice. Before the test, from the profiler to the friction rig, and after the friction test, back to the profiler. This introduces a misalignment between the profiles before and after the friction test. To avoid this misalignment a different methodology has been applied to assess the wear volume. The worn profile is saved as two versions, utilizing the visualisation software Vision. One is kept as a reference. The other version only contains the profile outside of the worn contact and sets the worn region to zero as in Figure 3-8 (b).

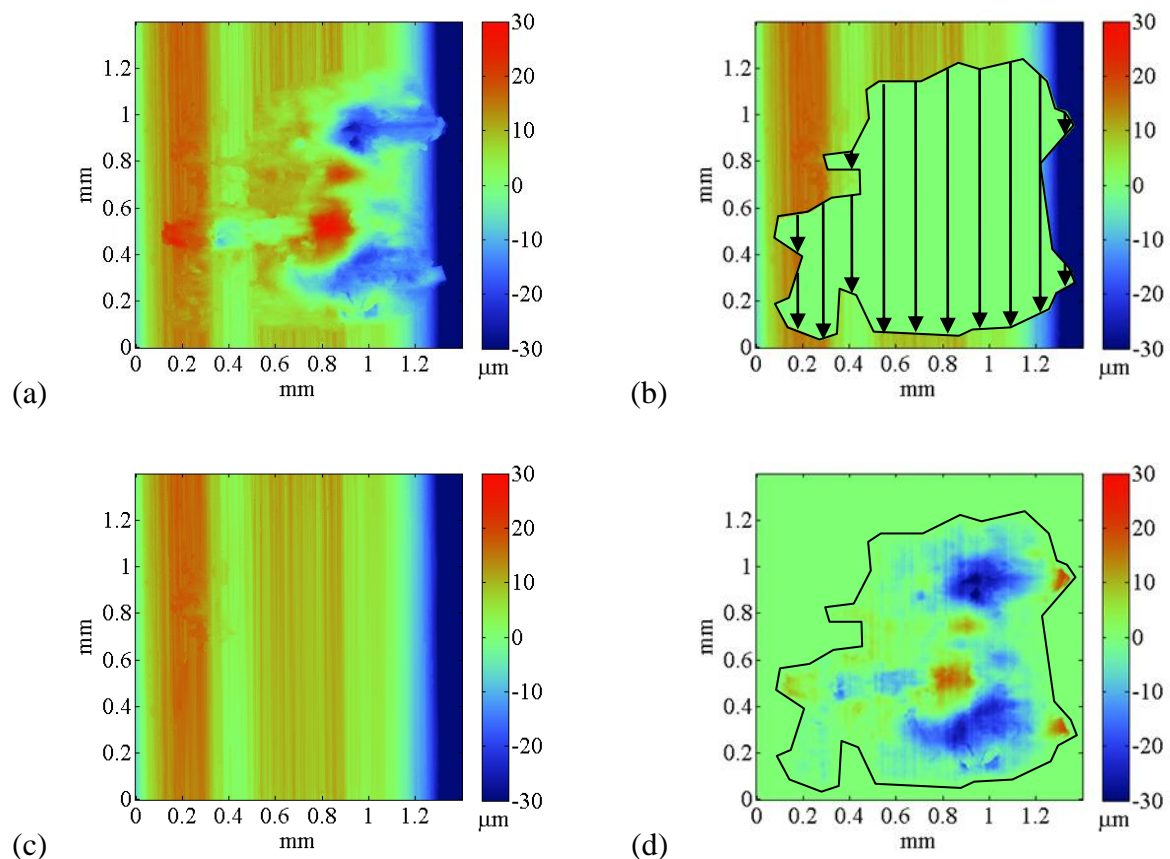


Figure 3-8: Procedure of wear calculation. (a) Worn surface after test. (b) The worn area is set to zero and the grinding structure is extrapolated to give a (c) unworn surface which can be easily subtracted from the original worn surface from which (d) the wear volume can be calculated.

The saved profiles were then opened as an array of heights in a math software program, e.g. Matlab, for further processing. Using the profiles with the worn area set to zero, the original profiles can be estimated based on the ground nature of the surface by interpolating the heights in each column of the zero-set region towards the next available height value unequal to zero. An unworn profile created like this is shown in Figure 3-8 (c) which when subtracted from the worn profile gives the wear, as shown in Figure 3-8 (d). The wear volume was then added up over the area.

3.2.2.6 Profile correlation

Autocorrelation was previously discussed in the literature chapter as a method to highlight reappearing features and self-similarity in one signal. Cross correlation, a derivation of it, can be used to evaluate the similarity between two signals, or in this case two surfaces which have been in fretting contact. The two surfaces were first measured using a profiler described earlier and subsequently exported as arrays of heights for further manipulation. Cross correlation was used for two reasons. First, optimum alignment was sought between the couple, when found the degree of correlation between the two surfaces was compared to other couples. Formula (3.1) shows the discrete three-dimensional version of the cross correlation between the two surface profiles A and B .

$$C(i, j) = \sum_{m=0}^{(Ma-1)} \sum_{n=0}^{(Na-1)} A(m, n) * conj(B(m + i, n + j)) \quad (3.1)$$

Where $0 \leq i < Ma + Mb - 1$ and $0 \leq j < Na + Nb - 1$.

The surface profiles were mathematically represented by matrix A , holding Ma times Na elements and matrix B , Mb times Nb . The procedure required matrix A to be bigger than matrix B . To explain the procedure of the cross correlation calculation one can imagine

Matrix A stable while B moves over it. The position of B is defined by the delay length parameters i and j which is limited by the size of A . At each position of B Matrix A is multiplied by the complex conjugate of B . However the step to define the complex conjugate of B was irrelevant for this purpose as only real parts are expected. The origin of this function lies in signal processing, where imaginary parts are more likely and this step would be necessary. After the multiplication all elements of the product matrix were summed up and assigned to the corresponding position in matrix $C(i, j)$. The maximum in $C(i, j)$ corresponded to the position where the resemblance between B and A was the greatest. In order to compare the correlation of different surface pairs $C(i, j)$ was normalized by the combined variance of heights of the two surfaces. The maximum of the normalized cross correlation matrix was the correlation factor (CCF) which was then used to directly compare the factor of conformity of different surface pairs.

Both specimen couples were measured using the Wyko profiling system and were labelled Profile A , representing the top moving specimen, and Profile B , representing the bottom static specimen. In order to calculate the correlation between Profile A and Profile B , the following methodology, which is presented in a flow chart in Figure 3-9, was applied.

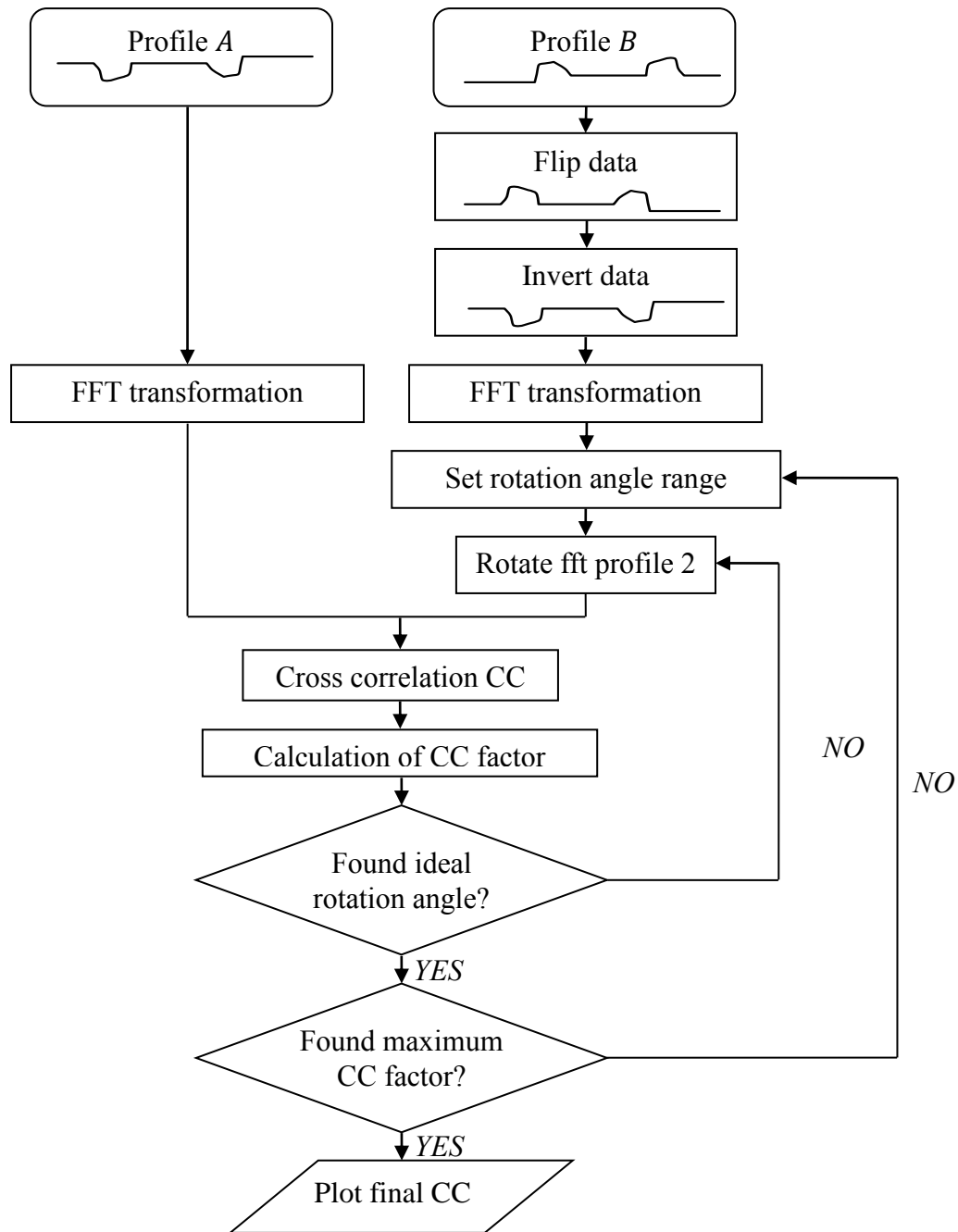


Figure 3-9: Flowchart showing the sequence of operation during image correlation between worn profiles.

Profile A remained in the orientation as it was measured for each test couple. Profile B was mirrored about its y-axis and the height values were inverted about its mean. Both profiles were zero-embedded and transferred into frequency domain using a Fast Fourier transformation (FFT) enabling quicker computation. In order to find the perfect alignment,

rotation steps are performed on Profile B and after each step cross correlation is performed and the CC factor calculated in order to assess the alignment. A series of rotations within a range of angles between -20° and 20° were performed. During the rotation a bilinear interpolation was performed. The step size was 0.5° . The rotation found to have the highest cross correlation factor was assumed to show the best alignment between the two surfaces. An example is shown in Figure 3-10. The area outside the contact was removed, because the inversion of Profile B caused incorrect intersections. The maximum angle of rotation found for the worn surfaces was then applied for the cross correlation of the unworn surfaces. In order to remove the effect of the zero-embedding, the CC factors were normalised by the area of the actual profile area.

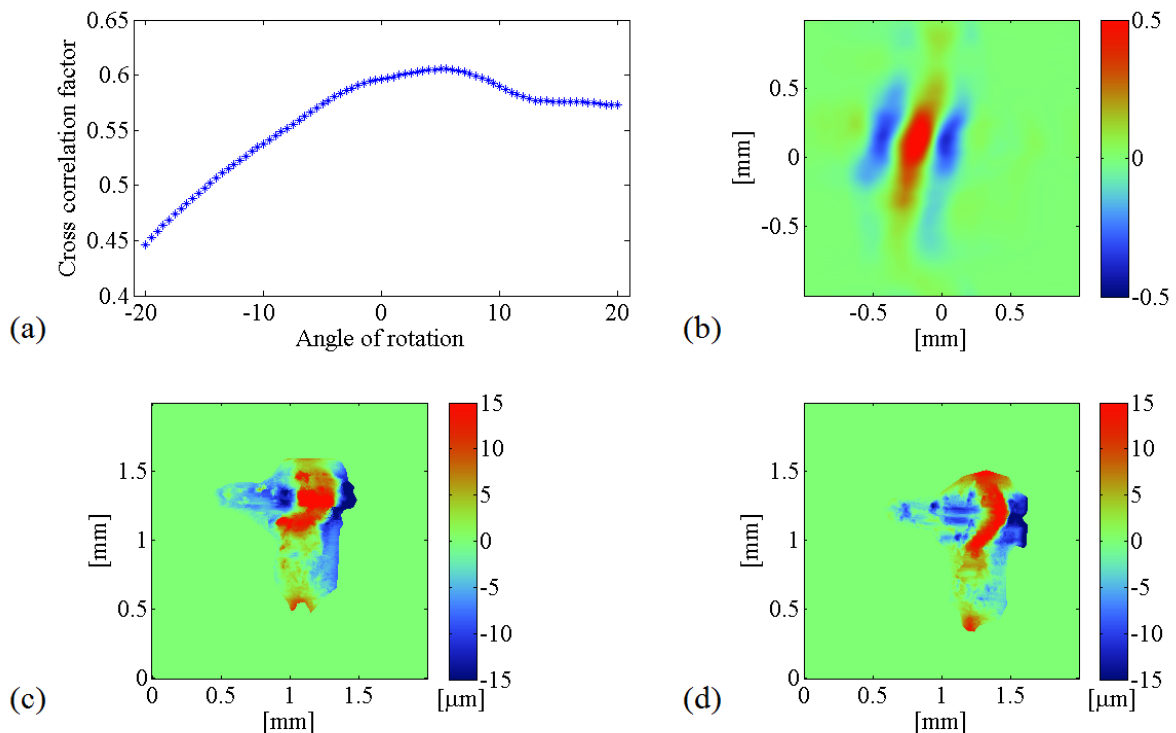


Figure 3-10: Cross correlation of two worn surfaces: (a) Search for best alignment, (b) cross correlation plot for best alignment angle, (c) Profile A and (d) Profile B.

All calculations were performed in Matlab. The cross correlation method is a widely applied method for image correlation and the methodology applied here followed loosely the methodology presented in [134]. A comprehensive review on image registration can be found in [135].

3.2.3 Sample preparation for microscopy

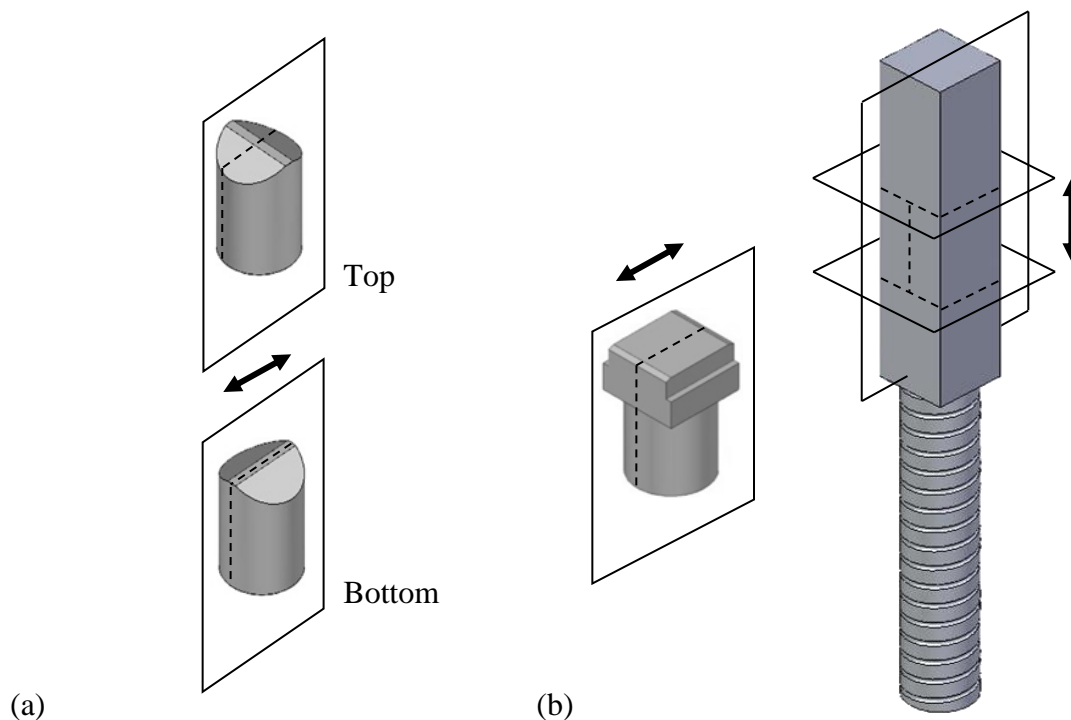


Figure 3-11: Cutting planes for cross sections on (a) 1 mm^2 contact rig specimens and (b) 80 mm^2 contact rig specimens. The direction of sliding is indicated by a double arrow.

Samples were cut into appropriate sizes with precise cutting machines (Struers Accutom, Struers Seccutom) using a diamond abrasive cutting wheel. The feed speed was set to 0.005 mm/s at 3000 rpm. The schematic drawings in Figure 3-11 provide a guide to how cross sections have been extracted from the samples. All cross sections were cut through the centre of the worn contact area with the cut being orientated parallel to the direction of sliding.

3.2.3.1 Grinding and polishing

Before grinding, samples were embedded in Bakelite using a hot mounting process. The grinding and polishing regime prior to microstructural investigations are displayed in Table 3-9. The same grinding regime was followed for all materials. The grinding speed was set to 130 rpm with a 10 N applied load. For polishing, the speed and load were substantially decreased. For the last polishing step of the Ti6Al4V samples, a colloidal silica polishing suspension (OP-S) was chosen which removes fine scratches best for this material [136].

Table 3-9: Grinding and polishing steps.

	Disc	Duration	Lubricant
All materials	SiC paper Grit 180, 320, 800, 1000, 1200, 2000 and 4000.	each step 3 mins	Water
All materials	Struers MD/DP Dac cloth	3 mins	6 μm diamond suspension plus standard lubricant
All except Ti6Al4V	Struers MD/DP Nap cloth	6 mins	1 μm diamond suspension plus standard lubricant
Ti6Al4V	Struers OP Chem cloth	6 mins	OP-S plus standard lubricant

3.2.3.2 Etching

Where not otherwise specified, samples have been etched with the following etching methods in order to reveal the microstructure.

Table 3-10: Etching methods for different materials.

Material	Etchant	Details	Duration
Udimet 720	Kalling 2	100 ml ethanol (96%) 100 ml hydrochloric acid (32%) 5 g copper chloride	5-20 seconds
Ti6Al4V	Kroll	100 ml distilled water 2 ml hydrofluoric acid (40%) 2-6 ml nitric acid (65%)	5-20 seconds
EN24T	Nital	100 ml ethanol (96%) 2 ml nitric acid (65%)	5-20 seconds
Stainless steel	Ammonium persulphate	100 ml distilled water 10g ammonium persulphate	electro chemical etching 6V, 20 seconds

3.2.4 Scanning electron microscopy (SEM)

SEM was used to investigate the oxide layer on the 1 mm² contact area Udimet 720 samples, as the layer was too thin to be observed with optical microscopy. Oxide layers on Udimet 720 and Ti6Al4V 80 mm² fretting pads were also investigated using SEM.

After grinding and polishing, as described in section 3.2.1.4, both materials were electro-polished to ensure a contaminant free surface. Udimet 720 was etched using a Despina solution which consisted of 45 % Butan-1-ol, 43.5% methanol and 4.5 Perchloric acid. To improve the effectiveness of the solution, the sample was cooled to a stable liquid nitrogen temperature. A voltage of 20 V was applied for 15 seconds.

A JSM6400 microscope combined with an INCA Oxford system was used to obtain secondary electron (SE), backscattered electron (BSE) and diffracted backscattered electron

(EBSD) images. A 20kV accelerating voltage was applied and the optimal working distance was found to be between 16 and 18 mm.

3.2.4.1 Electron back scattering diffraction (EBSD)

The deformation of the centre region of an Udimet 720 and a Ti6Al4V pad, both worn and unworn, was investigated. The cross section was taken in the centre of the sample and parallel to the direction of fretting.

The SEM system, which was equipped with a diffraction camera, was used to perform EBSD measurements. This method is based on the inelastic diffraction of electrons; a beam is directed at the surface and scatters on the atomic planes of the crystals in an open angle cone. The characteristic Kikuchi bands are automatically analysed by the Tango© software which labels each diffracted crystal plane with its corresponding Miller indices. A final map is plotted which shows the crystallographic orientation of the material which has been scanned. An angle greater than 10° mis-orientation between two neighbouring grains determined the grain boundaries. The step sizes were approximately the same for all the samples (between 0.1 and 0.25 µm). Any grain below the step size would not have been indexed. Udimet 720 was indexed for its γ phase and Ti6Al4V for its α phase.

3.2.5 Focused ion beam imaging (FIB)

Focused ion beam imaging was used to further investigate the deformation depth of Udimet 720 samples. Ga⁺ ions are shot at the surface and excite secondary electrons which are detected. The method is destructive and causes the surface atoms to sputter. Ion channelling was used to produce highly contrasted images of the microstructure. Images were

taken in secondary electron mode and at various angles with accelerating voltage. The optimal working distance was found to be 17 mm. The images were taken slightly off centre.

3.2.6 Transmission electron microscopy (TEM)

TEM enables highly localised diffraction pattern characterisation and was used to characterise the nature of the deformed area of a Ti6Al4V sample.

For the sample preparation, a dual ion beam ‘lift-out’ technique was used, which combines FIB and SEM techniques. This produces electron transparent, electron beam stable and conducting samples which are required for the TEM analysis. This method allows precise positioning of where the sample is taken from and requires considerable less time than conventional methods. The area of interest was located in the centre of the worn area stretching from the bulk area of material up to the interface. Using a Ga⁺ ion beam two layers of Pt were deposited in order to protect the surface from unwanted ion beam induced damage. The sample cutting process starts by milling two cuts on either side of the deposited Pt layer. This leaves behind a wall of material which is about 2 µm thick at its centre which is subsequently thinned down to about 1 µm using a lower beam current. The method is sped up by milling the trenches in steps. Stepwise decreasing the ion beam current, an ion polishing process reduces the thickness to a final value between 120 to 50 nm. Finally the membrane is completely cut free on both ends and lifted out using a glass needle and a micromanipulator. The sample sticks to the glass needle and can be moved into TEM sample holder grid. More details on this method can be found in [137].

3.2.7 X-ray diffraction (XRD)

XRD was used to study the chemical nature of oxides formed during the fretting process. As XRD diffraction needs a minimum recommended area of 0.5 x 0.5 mm the measurements were only performed on 80 mm² contact area samples. The XRD facilities available required smaller height dimensions and the surface was extracted as shown in Figure 3-12 (a). The scanning process was focused on the centre of the contact interface and covered a range of angles between 10° to 100°.

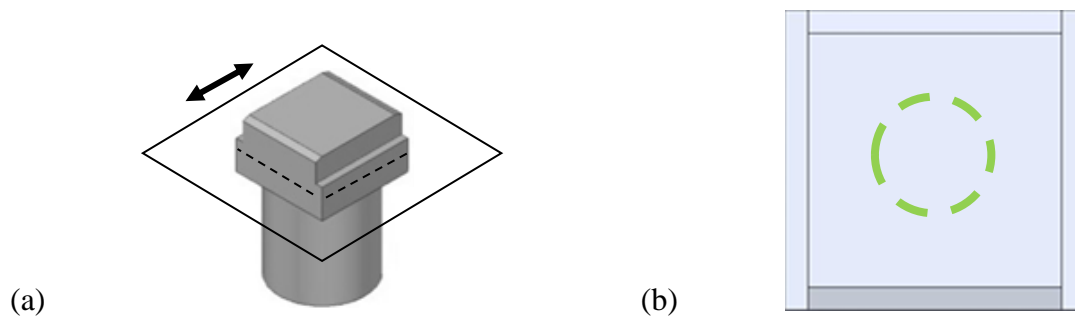


Figure 3-12: Cutting plane for cross section on an 80 mm² contact rig specimen for XRD measurement. (b) Approximate penetration position and area.

Chapter 4

Fretting tests – Results

This chapter presents all experimental results and observations which were obtained from friction tests. Four different materials were tested under various test conditions. The chapter is divided into two parts. The coefficient of friction, μ , and the tangential contact stiffness, k_t , which were directly measured during the friction tests, are shown in the first part. The second part presents the study of the degradation of the surface caused by the friction tests. Interferometric profiling, light and electron microscopy, and image registration techniques were employed to obtain these results. A discussion of the results follows in Chapter 5.

4.1 Coefficient of friction and tangential contact stiffness results

Coefficient of friction and tangential contact stiffness data is presented for different testing conditions.

4.1.1 Influence of the material

The Ni-based superalloy Udimet 720, the Ti-alloy Ti6Al4V, the low alloy steel EN24T and one austenitic stainless steel BS 970 303S31 were chosen to study the influence of different materials on the friction and stiffness behaviour. During all tests a pressure of 70 MPa was applied.

A comparison of the coefficient of friction results over time for all materials is shown in Figure 4-1. The difference in material had only a small effect on the long-term behaviour of the coefficient of friction, as shown in Figure 4-1. Both steels reached a very similar coefficient of friction value after 15 minutes, a value of just above 0.7. Specimens machined from Ti6Al4V and Udimet 720 showed lower coefficient of friction values and reached values just below 0.7.

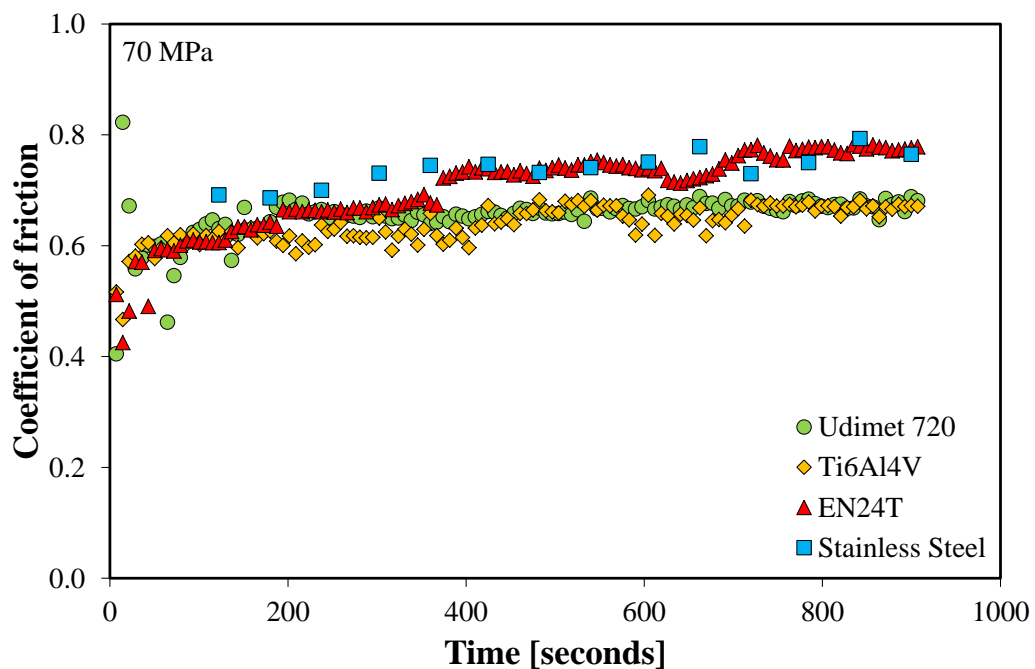


Figure 4-1: Comparison of the coefficient of friction over time for different materials: Udimet 720, Ti6Al4V, EN24T and stainless steel.

The different materials showed a greater effect on the measured tangential contact stiffness, as displayed in Figure 4-2. The highest tangential contact stiffness values were measured for Udimet 720 and the stainless steel which lay just above 30 N/ μm . Tangential contact stiffness values for the Ti6Al4V showed lower values stabilising at around 18 N/ μm and EN24T values stabilising at around 20 N/ μm .

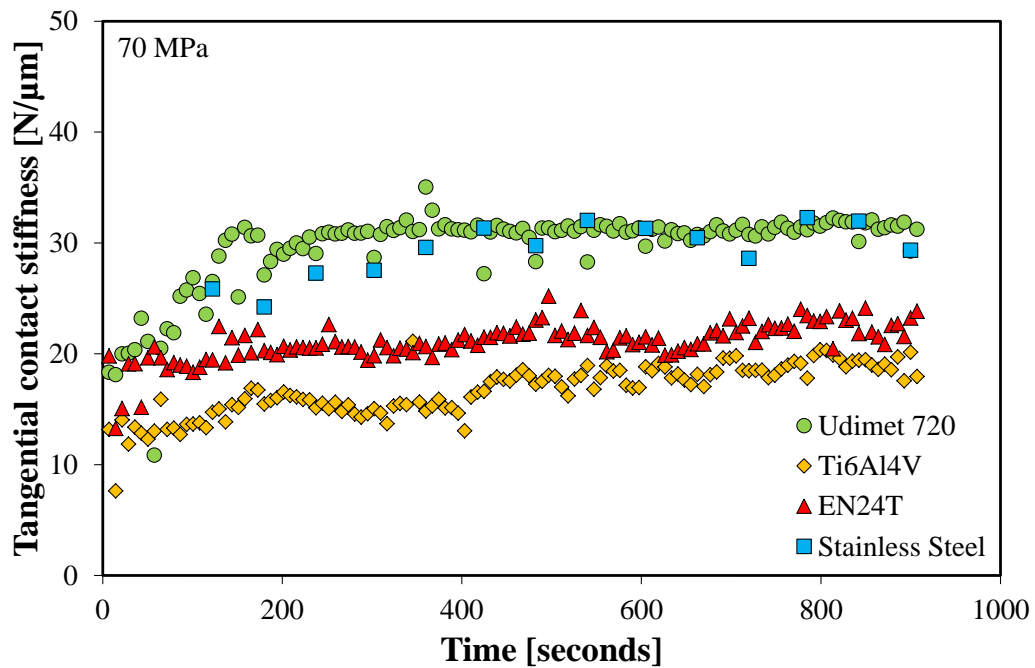
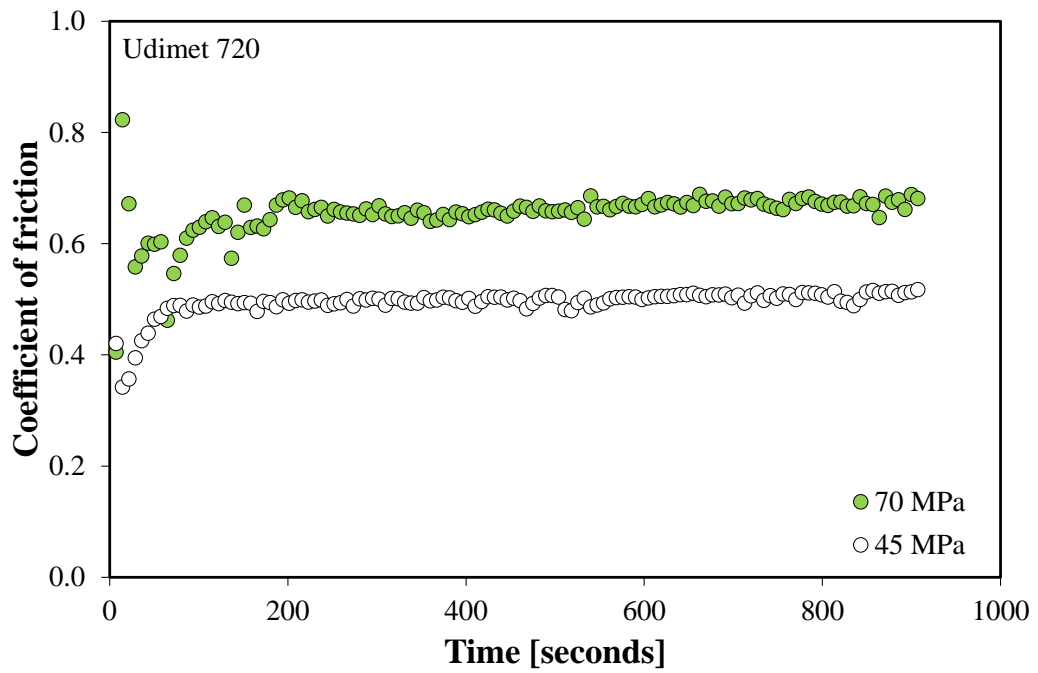


Figure 4-2: Comparison of the tangential contact stiffness over time for different materials: Udimet 720, Ti6Al4V, EN24T and stainless steel.

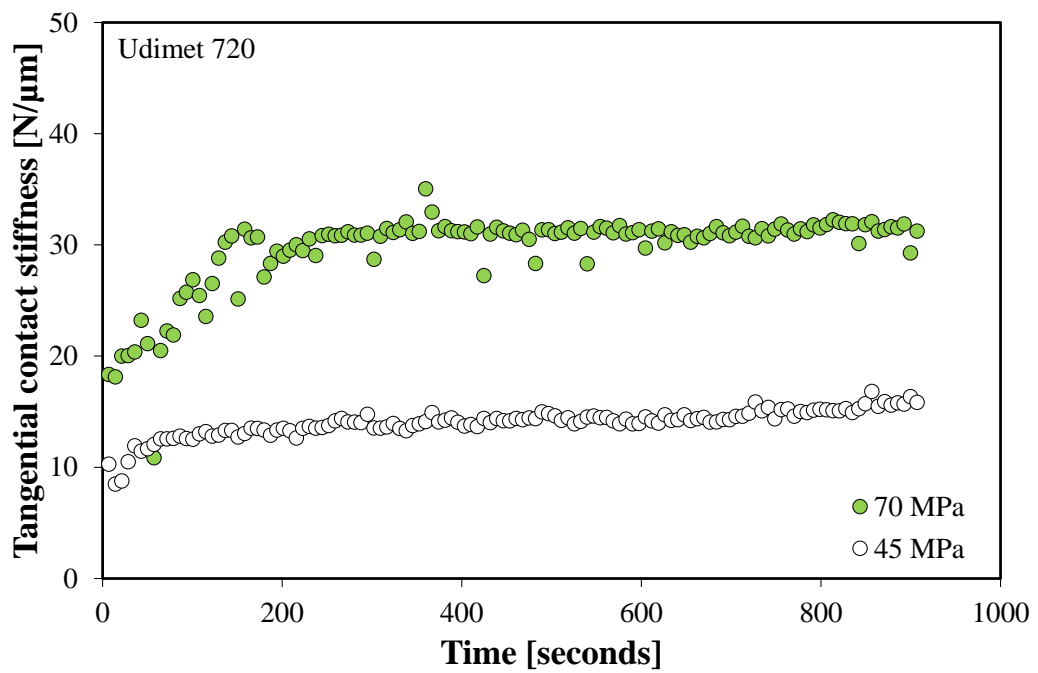
All materials showed a running-in behaviour for the coefficient of friction as well as the tangential contact stiffness during the 15 minutes test time. The values stabilised over this period of time.

4.1.2 Influence of load

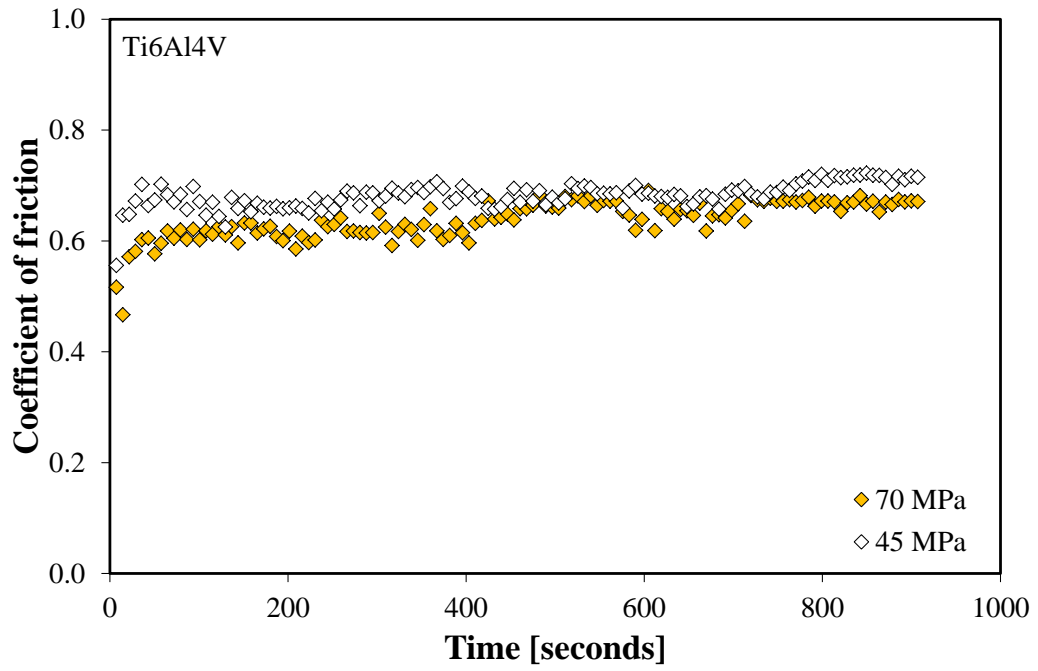
The influence of load on the friction properties was investigated on all four materials. One set of specimens was loaded to produce a pressure of 70 MPa on the 1 mm² contact. A second set of tests was loaded by a nominal pressure of 45 MPa. A comparison of coefficient of friction and tangential contact stiffness results for the two loading conditions is shown in Figure 4-3 (a) to (h) for each material.



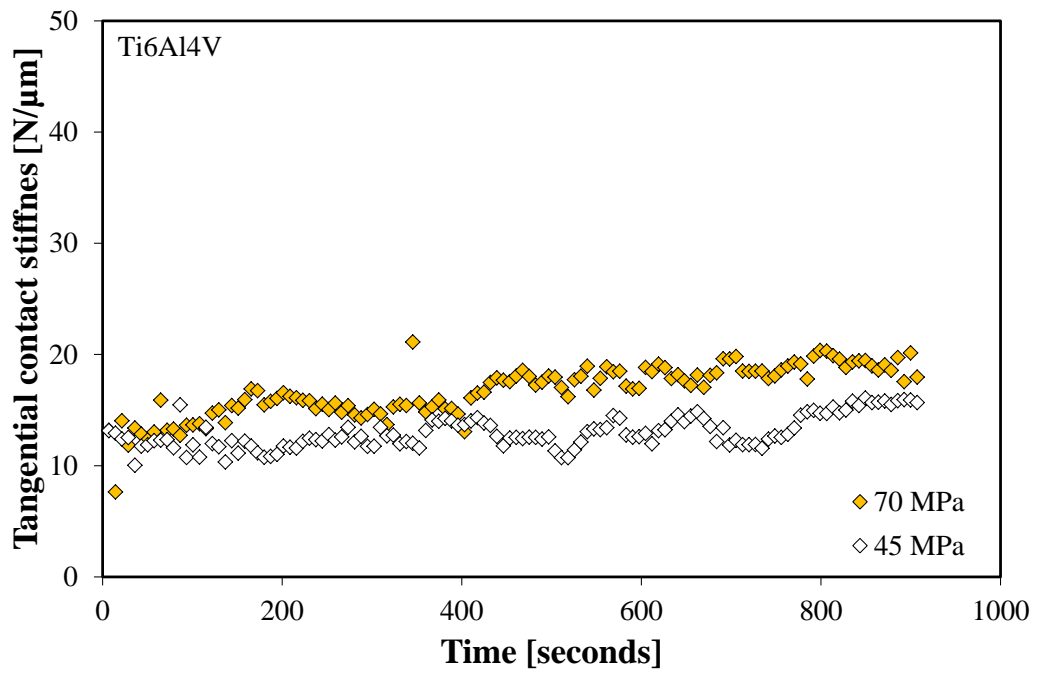
(a)



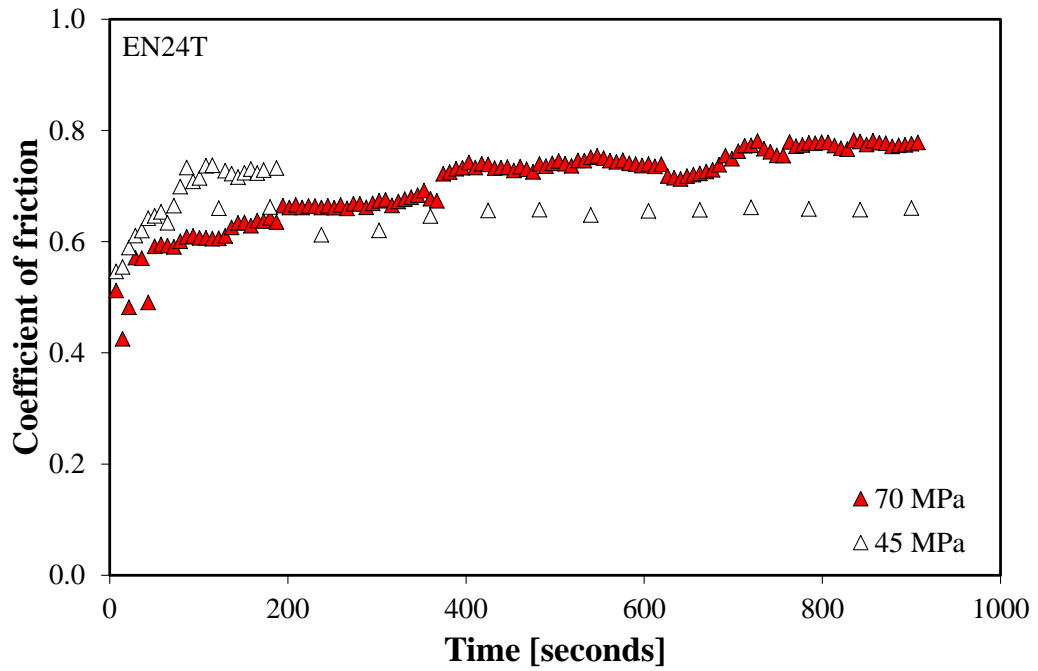
(b)



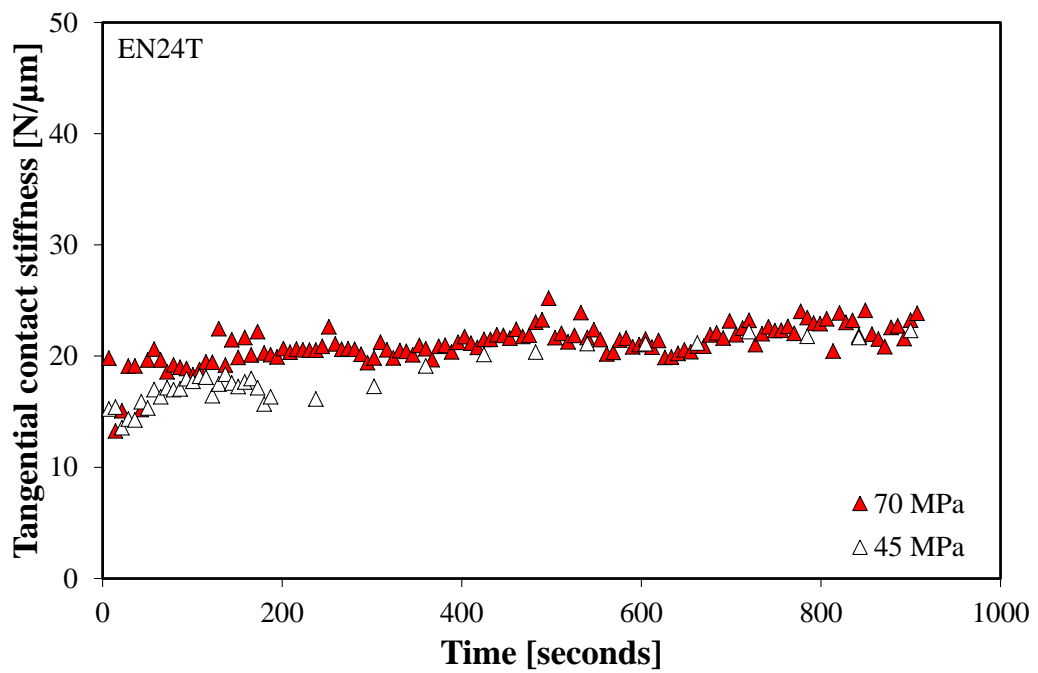
(c)



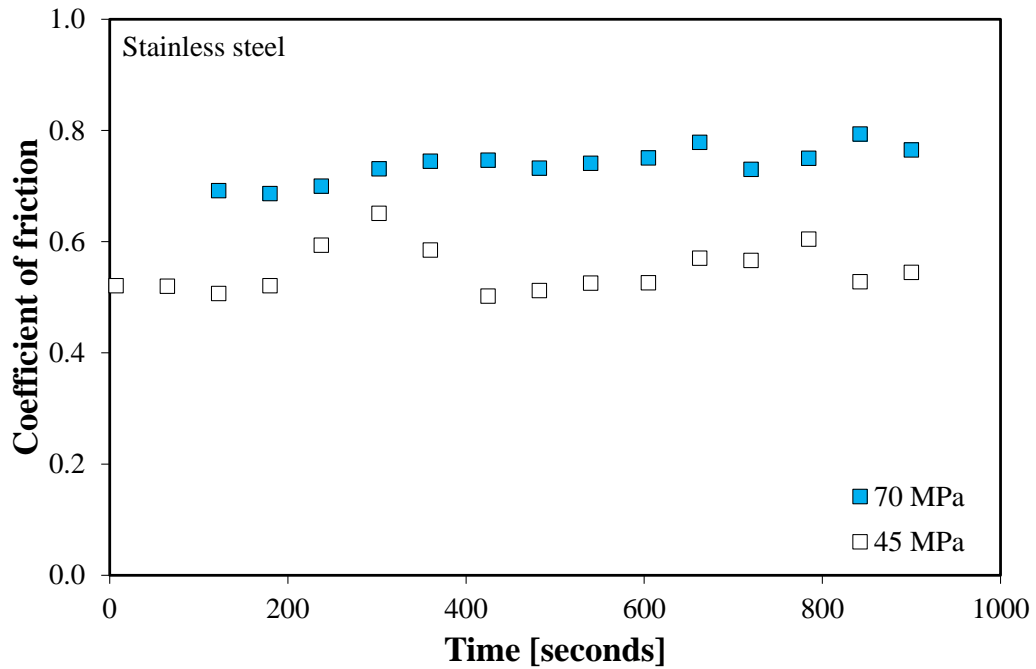
(d)



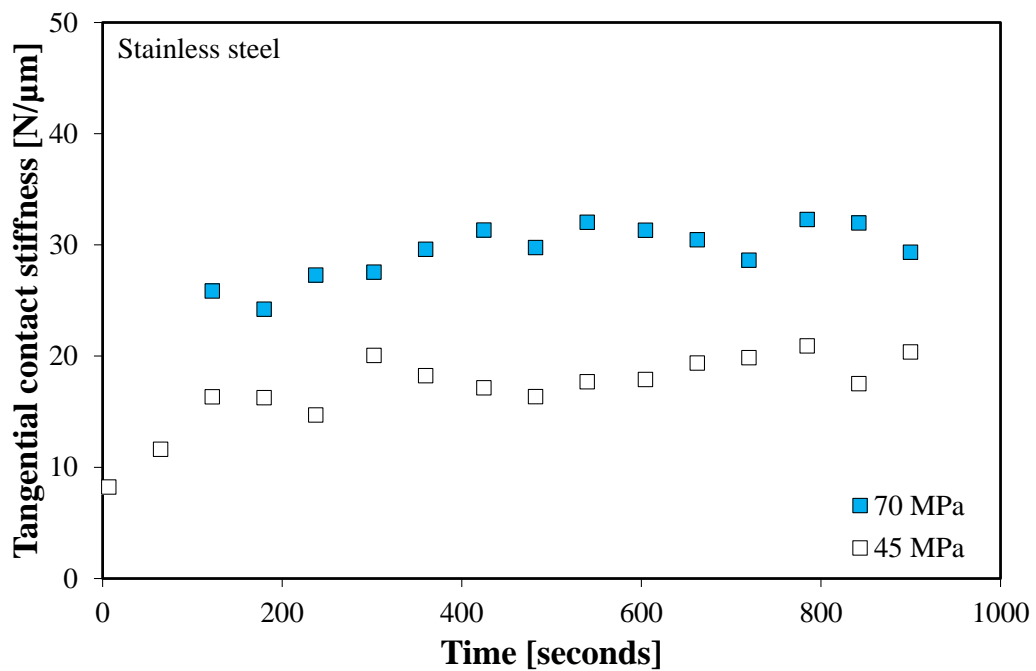
(e)



(f)



(g)



(f)

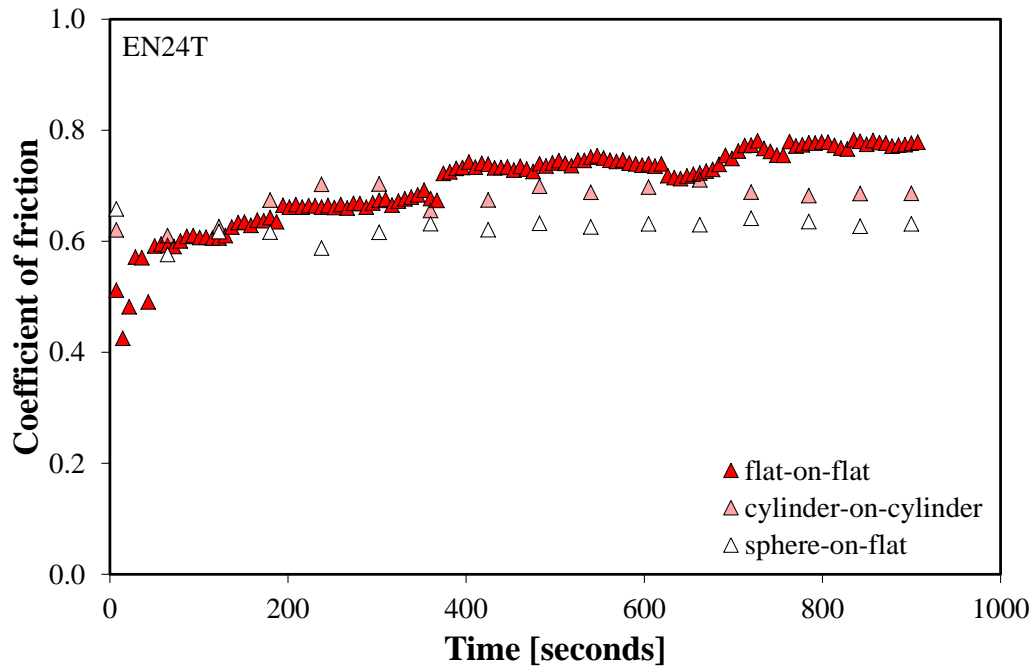
Figure 4-3: Influence of load on the evolution of coefficient of friction and tangential contact stiffness on different materials: Udimet 720 (a) μ and (b) k_t , Ti6Al4V (c) μ and (d) k_t , EN24T (e) μ , and (f) k_t and stainless steel (g) μ and (h) k_t .

Both the coefficient of friction and the tangential contact stiffness of the Ti6Al4V and EN24T samples were indifferent to the change of nominal pressure. The coefficient of friction was

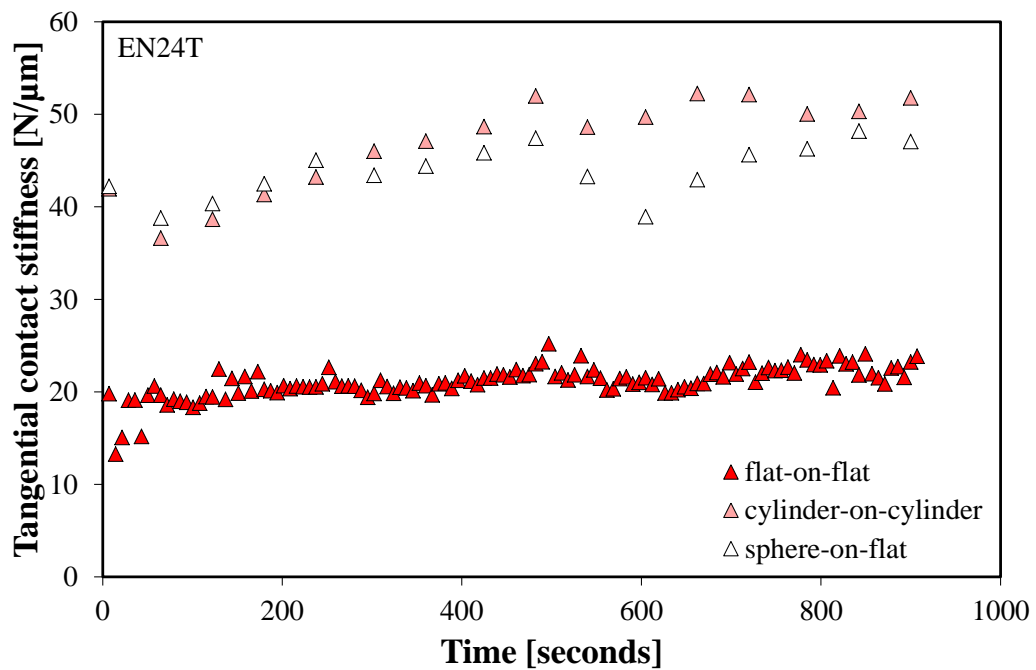
0.7 for both materials and for both pressures. The tangential contact stiffness stabilised at 17 N/ μm for Ti6Al4V and 24 N/ μm for EN24T. A significant effect of the load was seen for Udimet 720 and stainless steel samples. For Udimet 720 samples, the lower load resulted in a 30% lower coefficient of friction, stabilising at around 0.5, and 50% reduced tangential contact stiffness of around 15 N/ μm . The coefficient of friction measured on stainless steel samples showed a decrease from 0.78 to 0.55 for the lower load. The tangential contact stiffness stabilised at 30 N/ μm for the higher load and at 20 N/ μm for the lower load.

4.1.3 Influence of contact shape

Besides using the standard flat-on-flat contact configuration, sphere-on-flat and cylinder-on-cylinder specimens were tested on the 1 mm² contact rig to show their influence on coefficient of friction and tangential contact stiffness measurements. This comparison was done on EN24T steel specimens under the same pressure conditions as for the flat-on-flat contact. Recorded values are shown in Figure 4-4. Coefficient of friction measured on a flat-on-flat arrangement showed the highest coefficient of friction of nearly 0.8 after 15 minutes. The coefficient of friction measured on the cylinder-on-cylinder arrangement was 0.7. The lowest value of just above 0.6 was measured for the sphere-on-flat arrangement. There was a strong effect on the tangential contact stiffness values. For the flat-on-flat arrangement the stabilised tangential contact stiffness value of just above 20 N/ μm had been measured. Tangential contact stiffness values for a cylinder-on-cylinder and sphere-on-flat arrangement were measured at more than double that value, around 50 N/ μm .



(a)



(b)

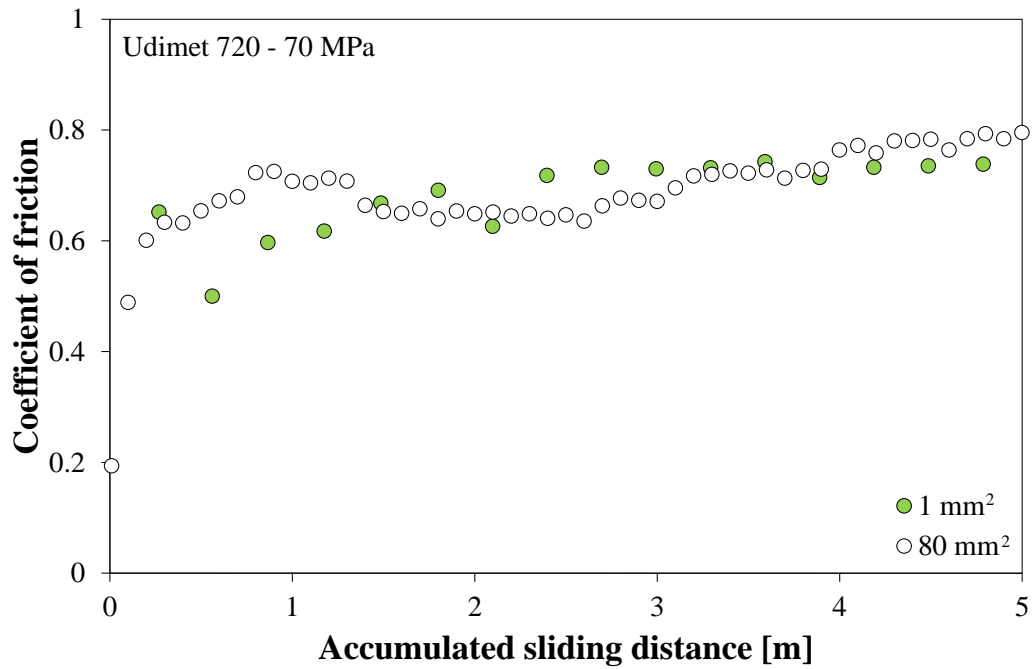
Figure 4-4: Comparison of (a) friction of coefficient and (b) tangential contact stiffness values for different contact conditions: flat-on-flat, cylinder-on-cylinder and sphere-on-flat.

4.1.4 Influence of test rig

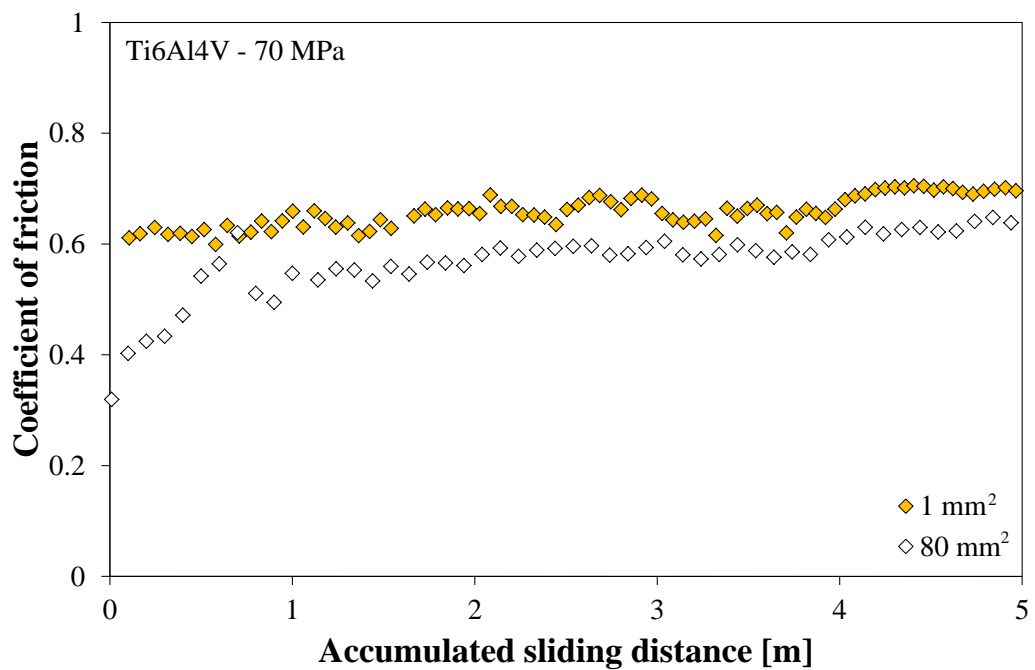
Udimet 720 and Ti6Al4V were tested on two different rigs. The main differences between the two rigs were the areas of contact, 1 mm^2 versus 80 mm^2 , and the operating frequencies, 100 Hz and 1 Hz respectively, as has been explained in more detail in the previous chapter. In order to enable a comparison of the results obtained from the two rigs, the values were plotted against accumulated sliding distance rather than time. For previous plots of coefficient of friction and tangential contact stiffness values the data of at least three tests was averaged. This was not possible when data was plotted against the accumulated sliding distance and one representative set of data is shown in the graphs for the 1 mm^2 contact condition in this section (Figure 4-5 and Figure 4-6). All tests were performed under identical pressure conditions at 70 MPa on a 1 mm^2 and an 80 mm^2 contact rig. The results of the 80 mm^2 measurement have been previously published by Kartal et al [49].

Figure 4-5 (a) shows a comparison of the coefficient of friction for Udimet 720 specimens. Both rigs showed a running-in behaviour. The coefficient of friction measured on the 1 mm^2 contact rig stabilised at around 0.7 compared to 0.8 measured on the 80 mm^2 rig. Figure 4-5 (b) shows a comparison of the coefficient of friction for the Ti6Al4V specimens. The coefficient of friction measured on the 1 mm^2 contact rig stabilised at around 0.6. The same property measured on the 80 mm^2 contact rig stabilised at around 0.7.

Figure 4-6 shows a comparison of the tangential contact stiffness for Udimet 720 and Ti6Al4V specimens measured on each rig. Figure 4-6 (a) compares the results of the Udimet 720 specimens. For the 1 mm^2 contact rig the tangential contact stiffness stabilised around $30 \text{ N}/\mu\text{m}$ after 5 m of accumulated sliding distance. The final value obtained after a similar distance on the 80 mm^2 rig was around $980 \text{ N}/\mu\text{m}$.



(a)

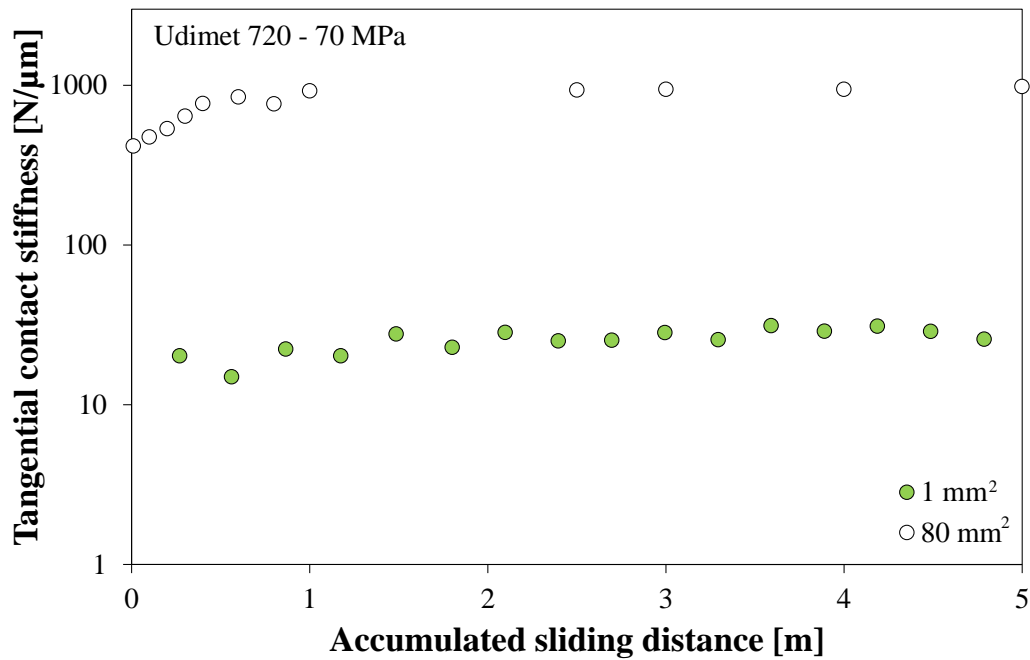


(b)

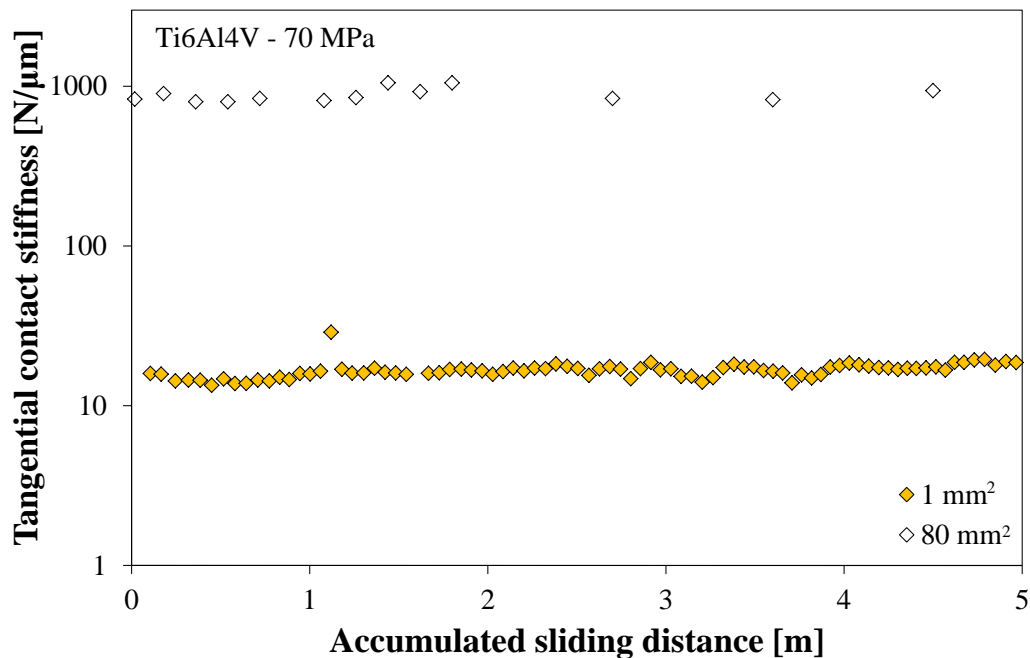
Figure 4-5: Coefficient of friction measured with two different rigs on (a) Udimet 720 specimen and (b) Ti6Al4V specimen.

The behaviour of the tangential contact stiffness measured on Ti6Al4V specimens is shown in Figure 4-6 (b). Again the final value a total accumulated sliding distance of about 5 m is considered. The tangential contact stiffness measured on the 1 mm² contact rig stabilised at

around $18 \text{ N}/\mu\text{m}$. For the 80 mm^2 rig the value stabilised at around $940 \text{ N}/\mu\text{m}$. In order to accommodate the data of both rigs on one graph the tangential contact stiffness is shown on a logarithmic scale.

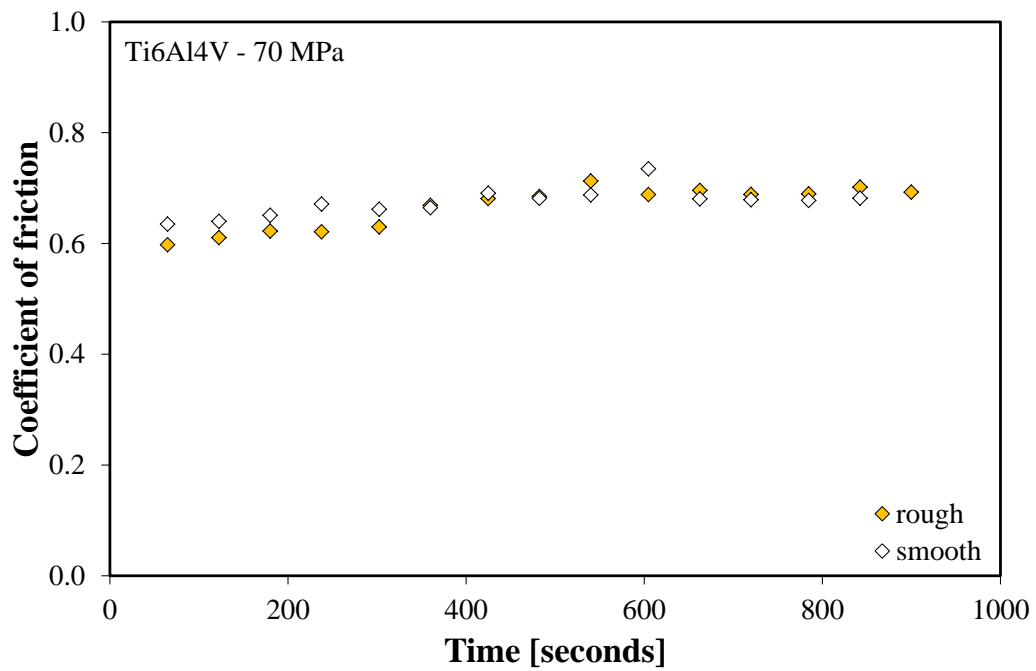


(a)

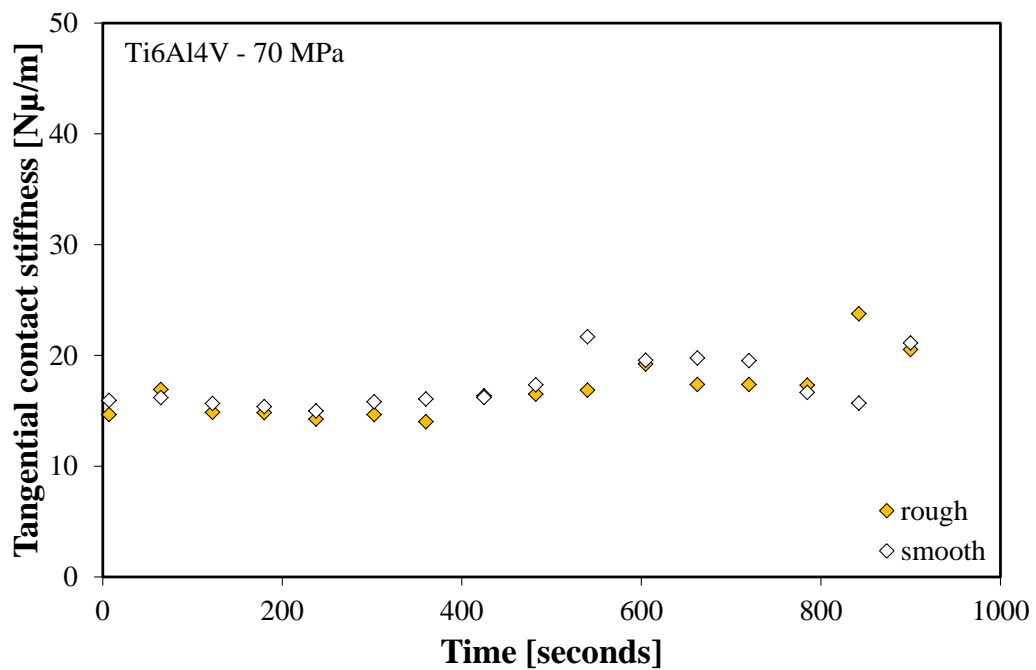


(b)

Figure 4-6: Tangential contact stiffness normalised by the nominal contact area measured with two different rigs on (a) Udimet 720 specimen and (b) Ti6Al4V specimen.

4.1.5 Influence of the surface roughness

(a)



(b)

Figure 4-7: Comparison of (a) μ and (b) k_t results from tests performed on Ti6Al4V samples with smooth and rough surface profiles.

The effect of surface roughness on coefficient of friction and tangential contact stiffness was studied on Ti6Al4V specimens. Two sets of specimens were tested: one with a rough ground surface profile ($S_q \sim 2.3 \mu\text{m}$) and one with a slightly smoother surface roughness ($S_q \sim 1.6 \mu\text{m}$). All tests were performed with an applied normal pressure of 70 MPa. Coefficient of friction and tangential contact stiffness values were extracted every minute for both sets of specimens. Figure 4-7 shows that the behaviour of neither the coefficient of friction nor the tangential contact stiffness was influenced by the initial roughness.

4.2 Surface degradation

The surfaces at the fretting interface underwent a severe transformation and were heavily worn. Figure 4-8 shows the profiles of wear scars of a pair of 1 mm^2 specimens after 15 minutes of testing.

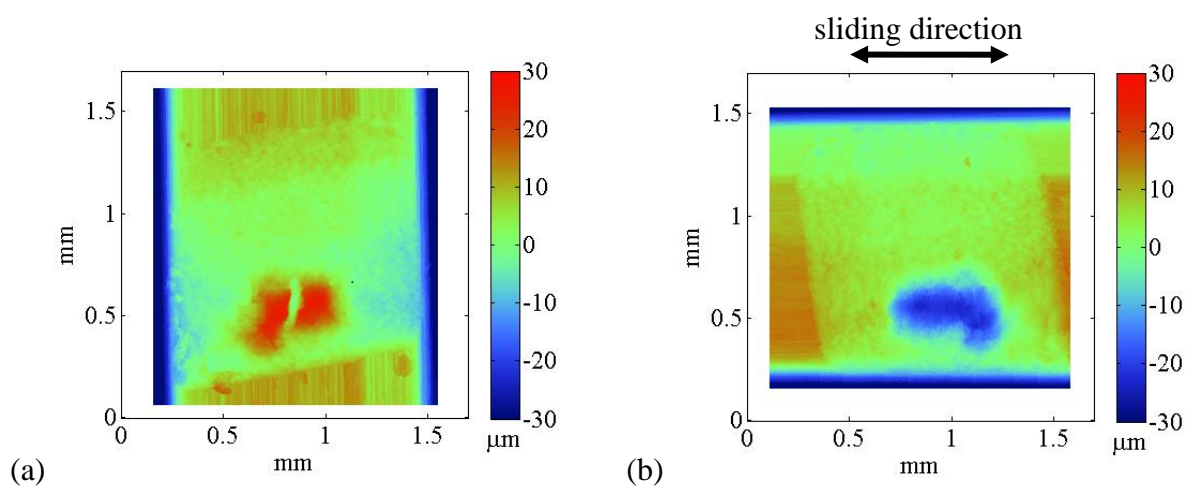


Figure 4-8: Worn contact interface of a (a) bottom and (b) top, moving, Udimet 720 specimen after a test performed at 70 MPa with a maximum displacement amplitude of around $18 \mu\text{m}$. The specimens in contact formed a 1 mm^2 nominal contact.

The left image shows the bottom sample, which had been stationary throughout the test. The right image pictures the wear scar of the top, moving sample. Both samples experienced severe wear. However, the wear scars seemed to mirror each other and where there was a peak in the bottom sample, a matching trough could be found in the top sample. The size of the wear scars was roughly 1 mm^2 . The rig turned out to be slightly prone to misalignment of the samples which can be seen as the wear scar resembles a parallelogram rather than a square. The wear volumes of bottom and top samples were similar and did not show that one sample was more worn than the other. The trend between the materials showed that after 15 minutes Udimet 720 was more severely worn than Ti6Al4V.

The circular wear scars of the cylinder-on-cylinder and the sphere-on-flat arrangement are shown in Figure 4-9 and Figure 4-10. The worn area for both arrangements was roughly 2 mm^2 for the cylinder-on-cylinder and 1.5 mm^2 for the sphere-on-flat arrangement.

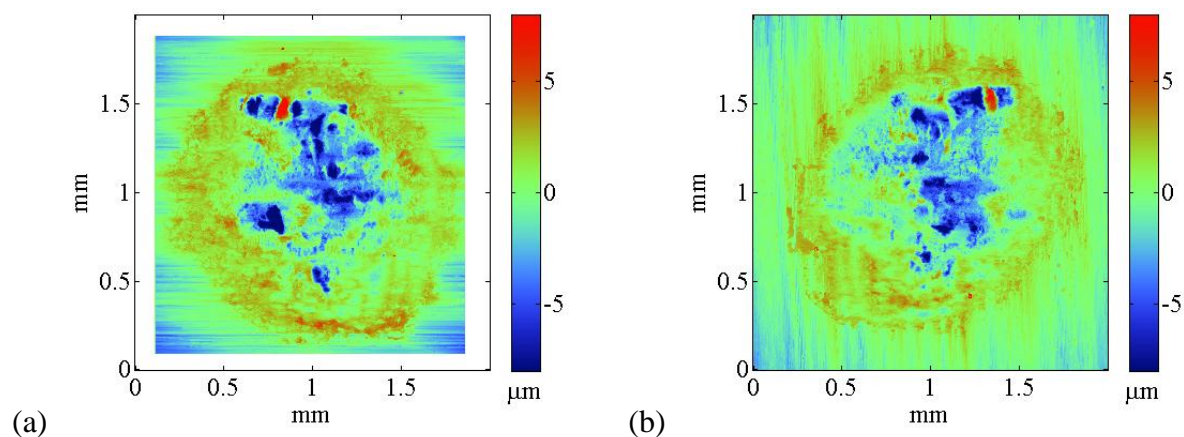


Figure 4-9: Worn contact interface of a (a) bottom and (b) top EN24T specimen of a cylinder-on-cylinder contact. The test was performed at 70MPa with a maximum displacement amplitude of around $18 \mu\text{m}$.

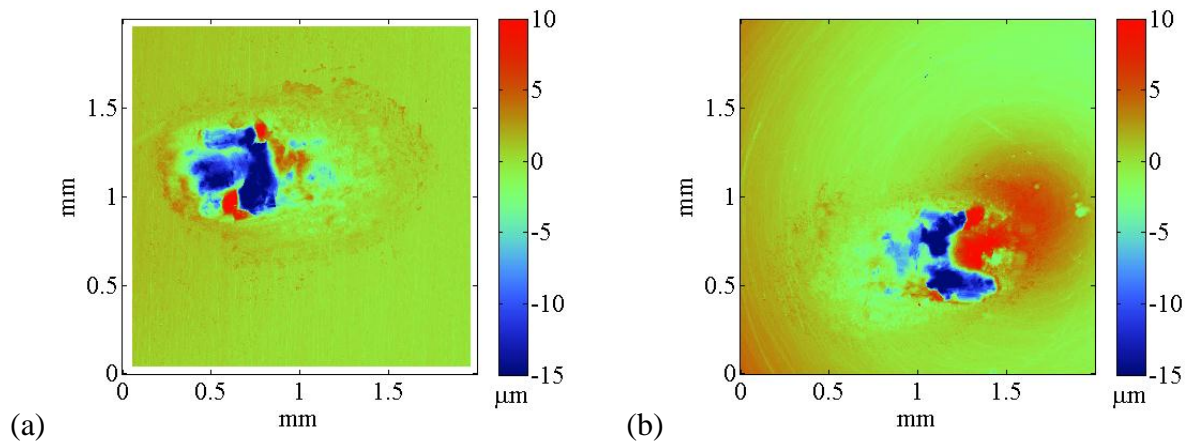
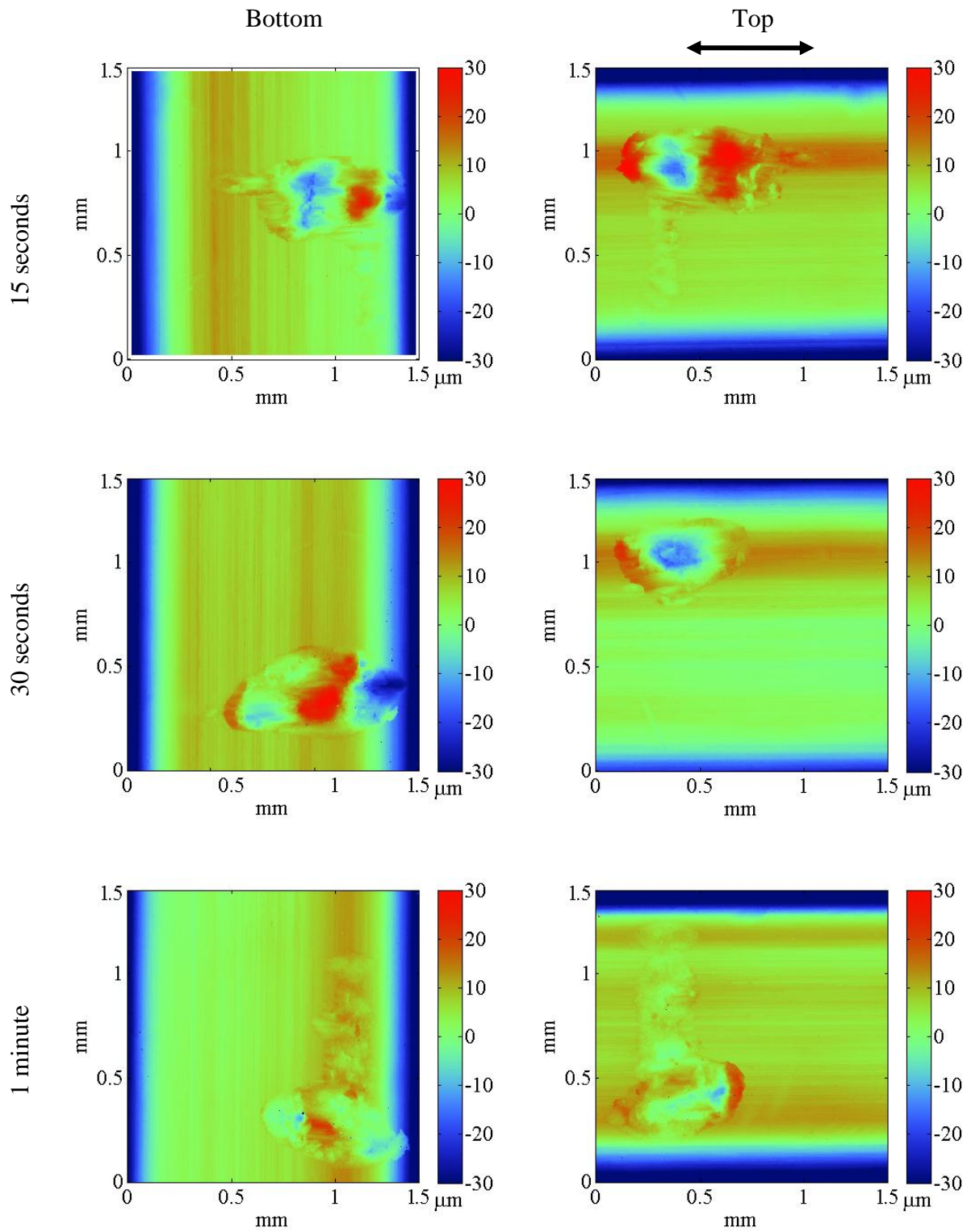
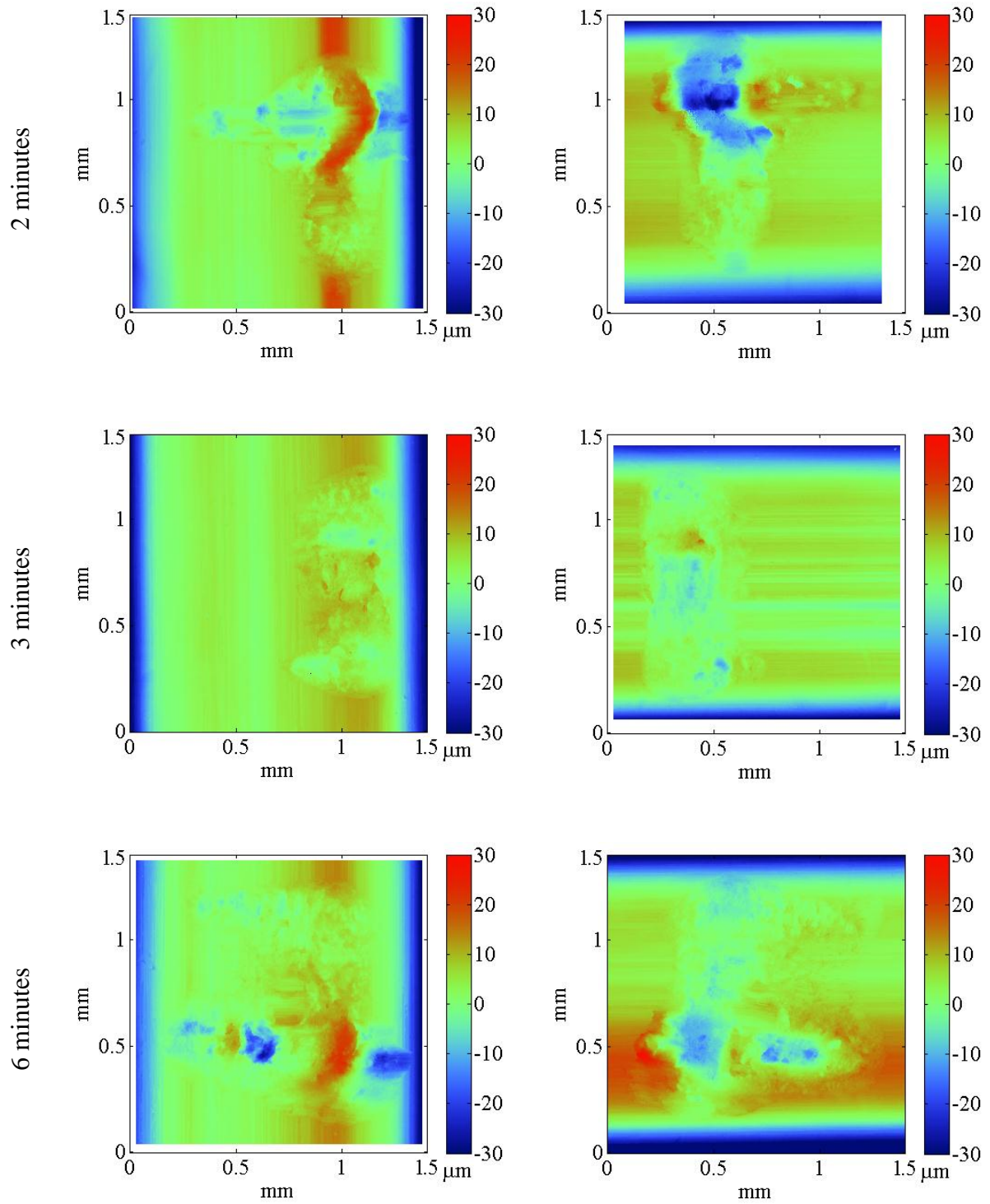


Figure 4-10: Worn contact interface of a (a) bottom and (b) top EN24T specimen of a sphere-on-flat contact. The test was performed at 70MPa with a maximum displacement amplitude of around 18 μm .

4.2.1 Development of correlation

A series of tests were performed to study the time dependent behaviour of the wear scar. This was of interest as the way the tests were interpreted only took the initial state of the specimens and the final value of the coefficient of friction and tangential contact stiffness into account. This series of tests was performed on EN24T specimens. Tests were run for different time periods and shorter than 15 minutes. Worn samples from tests conducted for 15 seconds, 30 seconds, 1, 2, 3, 6 and 9 minutes were compared to samples which were used for 15 minutes. After each test the test was stopped and the samples investigated. Figure 4-11 shows the profiles of wear scars tested for these different testing periods for each couple of top and bottom samples. The time line shows that the idealised 1 mm² contact was not established right at the beginning. It increased over time where it finally reached full nominal contact after 15 minutes.





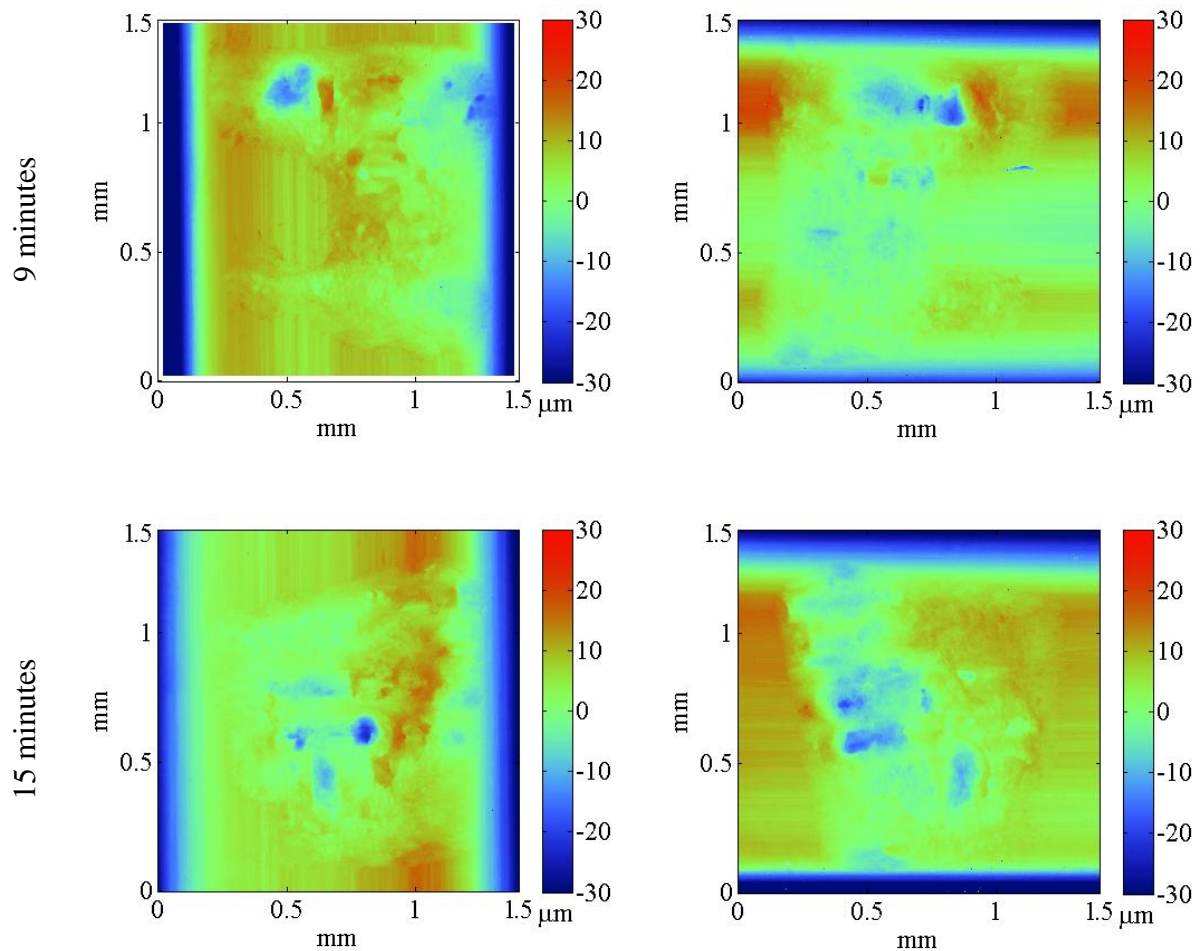


Figure 4-11: Wear scars obtained after (a) 15 seconds, (b) 30 seconds, (c) 1, (d) 2, (e) 3, (f) 6, (g) 9 and (h) 15 minutes. Tests were performed at 70MPa with maximum displacement amplitudes around 30 μm .

The worn interfaces suggested that a high degree of conformity had established after the full running-in period of 15 minutes. The data collected during the tests of different time intervals was further used to study the similarity or conformity between the run-in tests. The initially posed question was: Would the conformity of the two surfaces increase over time and in what fashion? The cross correlation factor served as a measure of conformity. Figure 4-12 shows the cross correlation factor of pairs of specimens which had been tested for different times. The cross correlation factor can take a value between -1 and 1, where the bounds express perfect correlation and 0 no correlation (complete randomness). Here, the cross correlation

factor was plotted from 0 to 1. The first point, at 0 minutes, shows the average correlation factor of an unworn pair of specimens. The average value lies below 0.1. After as little fretting time as a quarter of a minute the value increased to nearly 0.3. Longer durations of testing barely had any effect on the conformity as shown by the dashed trend line in Figure 4-12. For the longest testing time of 15 minutes, the cross correlation factor was just below 0.3.

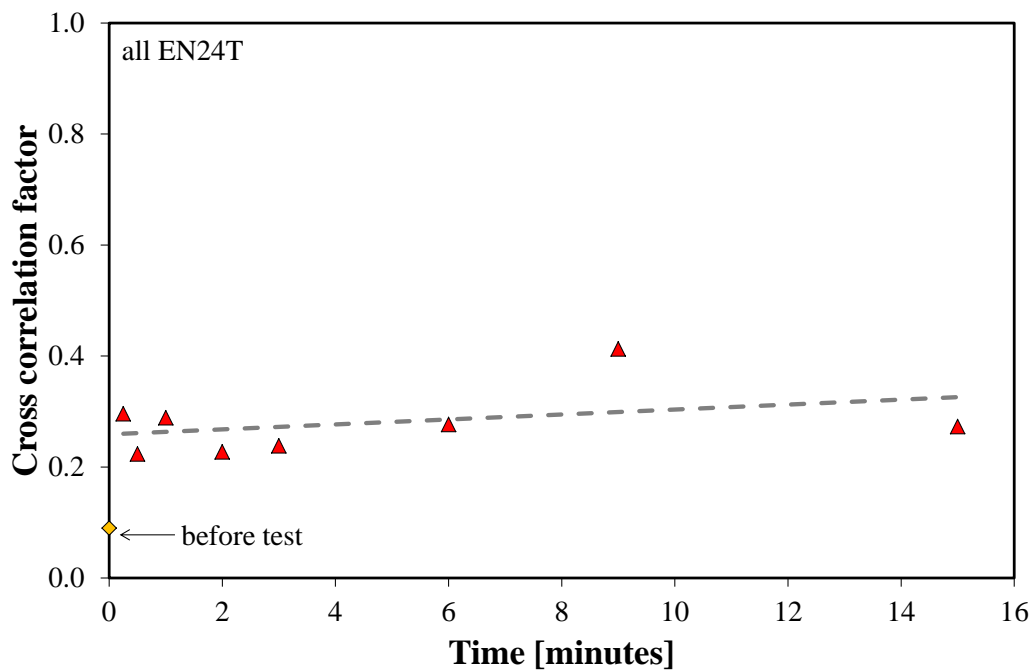


Figure 4-12: Cross correlation factors are assessed for a series of samples which were subjected to fretting for the following time intervals: 0.25, 0.5, 1, 2, 3, 6, 9 and 15 minutes for EN24T samples.

4.2.2 Development of friction loops

Parallel to the development of the interface profiles, the shape of the fretting loop changed considerably during the 15 minutes. The difference between a loop recorded at the beginning of a test and one at the end of a test is shown in Figure 4-13.

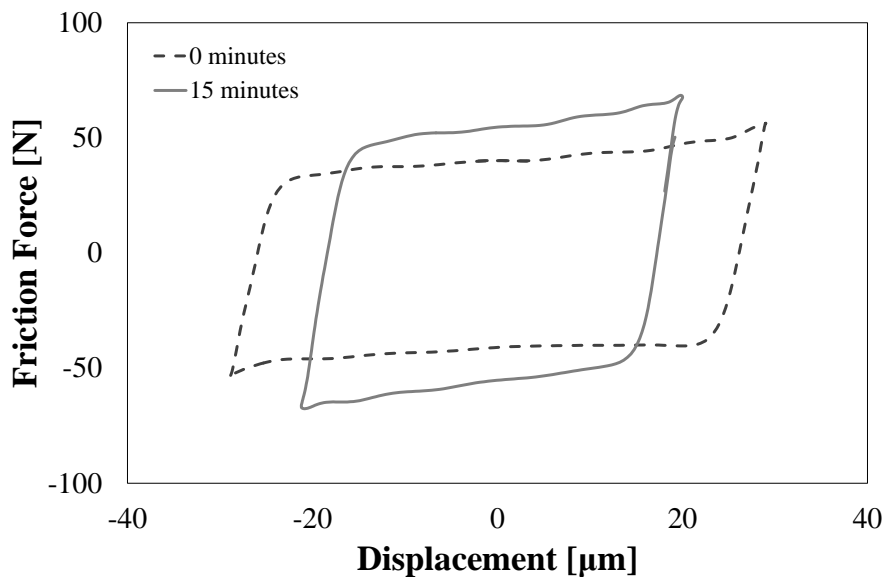


Figure 4-13: Fretting loop at the beginning of a test and 15 minutes into the test for tests performed on the 1 mm^2 contact rig.

The stroke length decreased during the tests, which were controlled by the excitation force. At the same time the measured friction force increased. Both changes directly affected the behaviour of the coefficient of friction. The increase of the initial slope was expressed by the rise of the tangential contact stiffness.

Friction tests performed on the bigger rig and which formed a nominal area of contact of 80 mm^2 , were run displacement controlled. The displacement remained constant and the excitation force was adjusted. These tests showed a different development of the loop shape as seen in Figure 4-14. During these tests the loops developed a hook-like feature. The nature of this feature has been already discussed in [77].

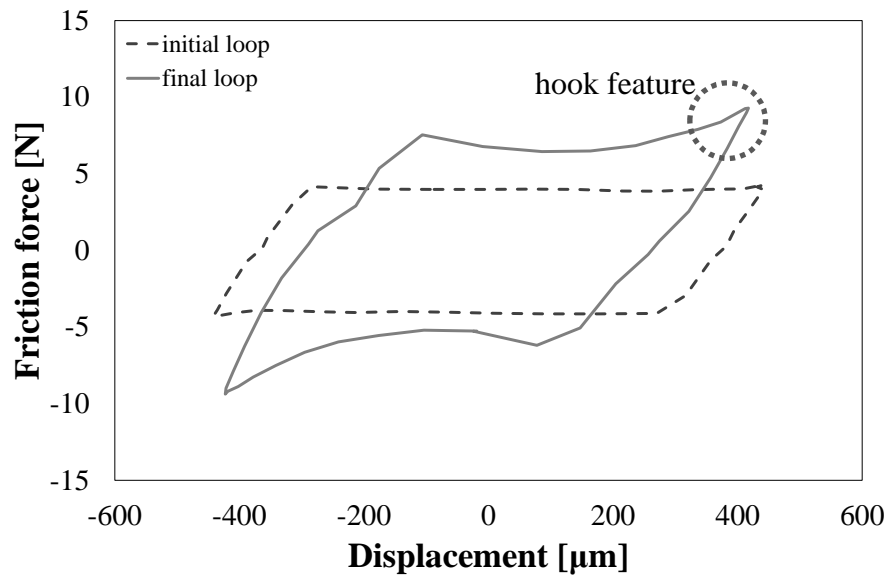


Figure 4-14: Fretting loop at (a) the beginning of a test and (b) after nearly 15 minutes testing time for tests performed on the 80 mm^2 contact rig.

4.2.3 Change of surface constitution

The fretting tests caused significant change to the chemical constitution of the interfaces. After the tests, all four materials revealed oxide scales of different thickness as shown in Figure 4-15. Each material responded differently to the conditions and results are presented below in sub-sections for each material individually. When checking cross sections untested material optical microscopy could not detect any oxide layers or other contaminations which could have been caused by the machining process.

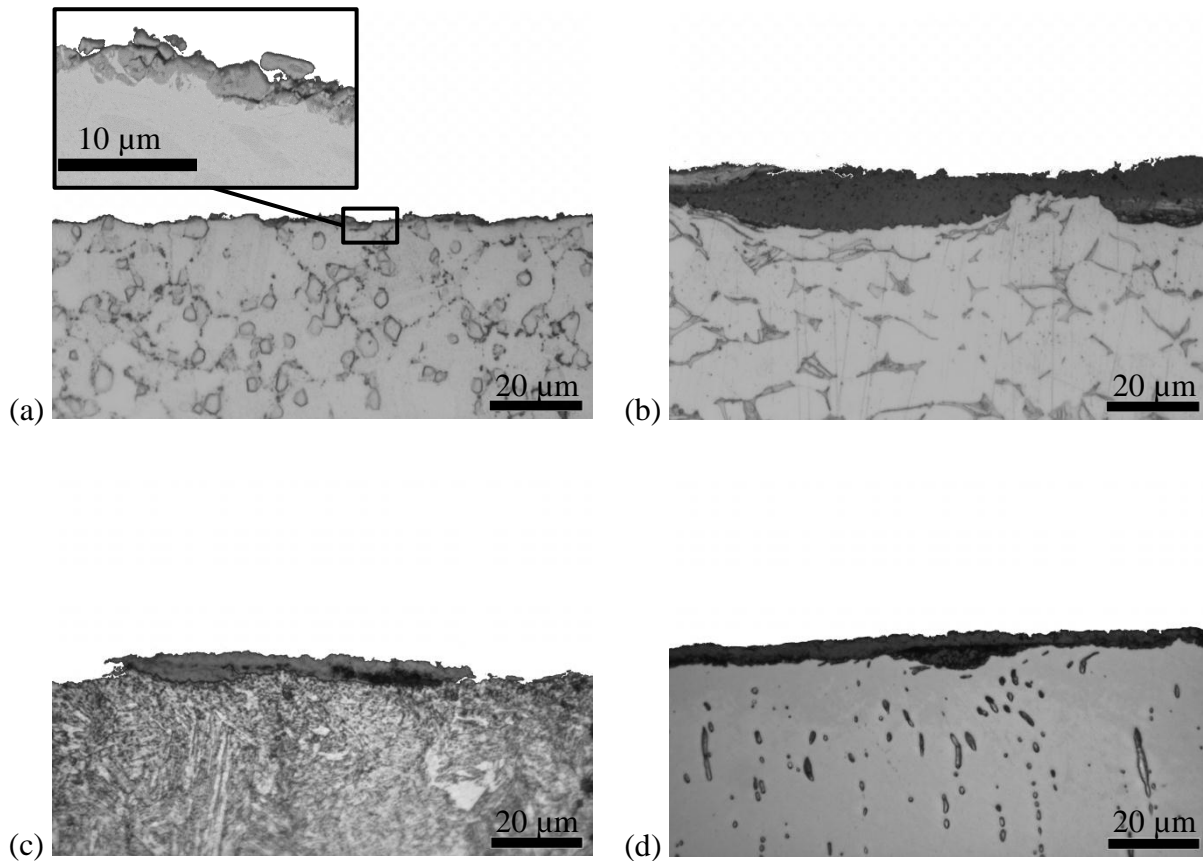


Figure 4-15: Optical micrographs of fretting induced oxide scales on (a) Udimet 720 (small back scattered electron image), (b) Ti6Al4V, (c) EN24T and (d) stainless steel.

4.2.3.1 Oxide scale on Udimet 720

The characterisation of the oxidised scale on Udimet 720 required a higher resolution than optical microscopy and samples were investigated using a SEM. The thickness of the scale reached between 2-5 μm. The scale appeared crumbly but was integrated into the surface and part of it rather than a compressed layer on top of the surface. Only a few cracks appear between the oxidised layer and the bulk material. Figure 4-16 presents a cross section of a worn specimen. The colour contrast in a back scattered electron (BSE) image can be used to detect lighter and heavier elements. The material beneath the surface in Figure 4-16 appears darker which corresponds to a lighter element and an oxygen enriched area is likely. The shading is not continuous and lighter, metallic areas, mix with darker oxygen enriched areas.

This mixture also appears in already partially detached particles. A partially detached particle in more detail is shown in Figure 4-17.

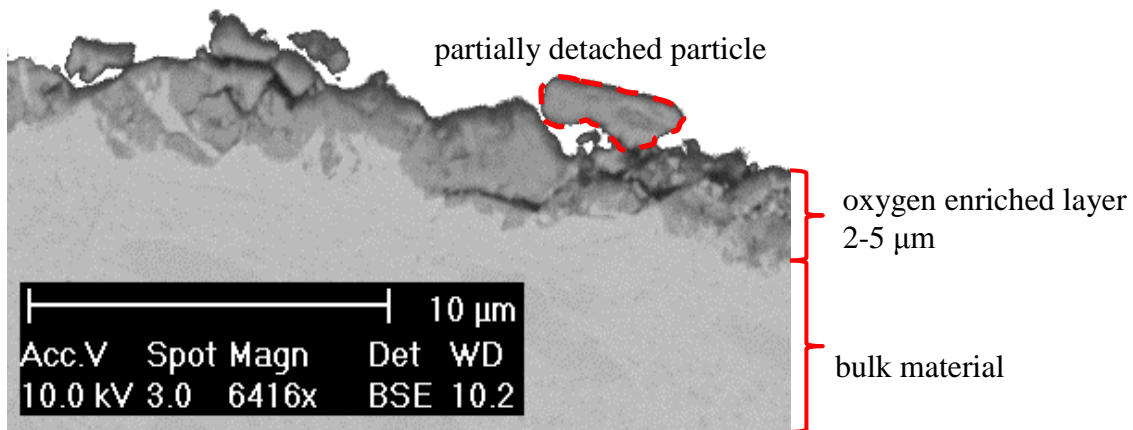


Figure 4-16: Back scattered electron image of fretting induced oxide scale on Udimet 720.

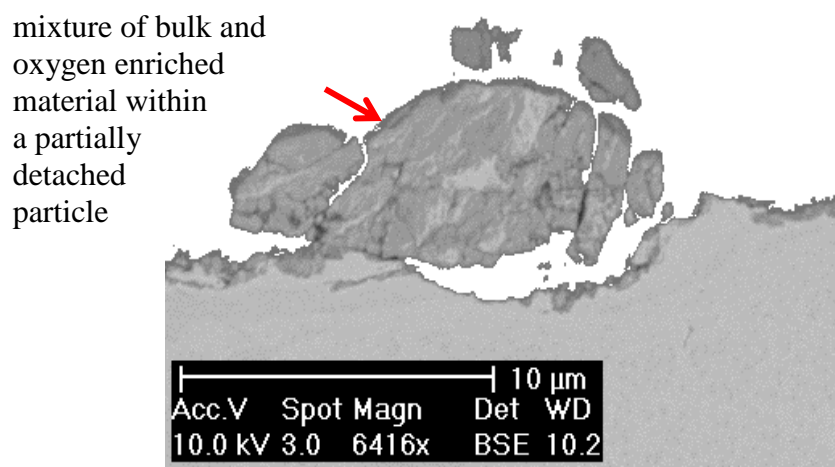


Figure 4-17: Back scattered electron image of details of a partially detached particle on Udimet 720 specimen.

4.2.3.2 Oxide scale on Ti6Al4V

Ti6Al4V formed a thick oxide layer of a thickness between 5-20 μm , which appeared to be nearly continuous, but was of a less dense structure than the bulk material. A representative cross section is shown in Figure 4-18. Within the oxide layer were patches which appeared to be a mixture of oxidised and metallic material.

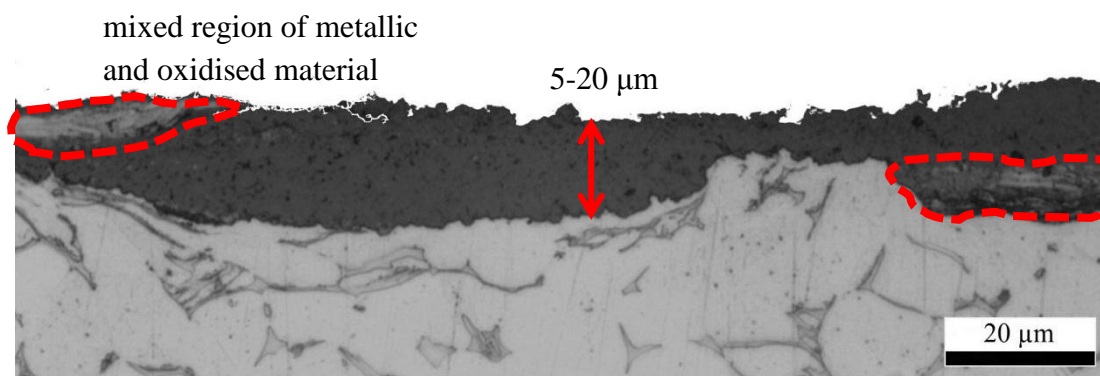


Figure 4-18: Optical micrograph of a fretting induced oxide scale on a Ti6Al4V sample.

The layer was of a crumbly nature as shown in Figure 4-19 and partly separated from the immediate surface. Cracks appeared at several positions.

A comparison of specimens tested at two different pressures showed that a thinner layer was formed at the lower pressure. Even though the 80 mm contact was tested at the same pressure a twice as thick, up to 50 μm , oxide layer was detected on the corresponding samples.

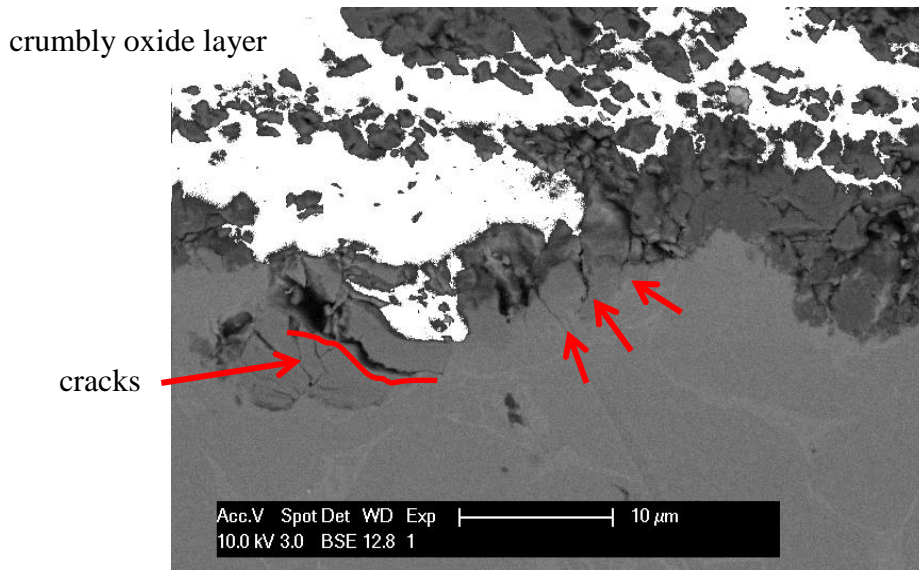


Figure 4-19: Details of immediate interface zone on Ti6Al4V specimen.

4.2.3.3 Oxide scale on EN24T

Oxide scales which formed on EN24T specimens varied in thickness. The thickness of the layer ranged from 5 to 25 μm but some areas were even completely free of oxide. An example of an oxide layer is shown in Figure 4-20. The oxide scale could always be clearly distinguished from the bulk material. The scale appeared dense but longitudinal cracks appeared at numerous locations. Less dense regions displayed a crumbly nature and material flakes were partially detached from the scale as shown in Figure 4-20.

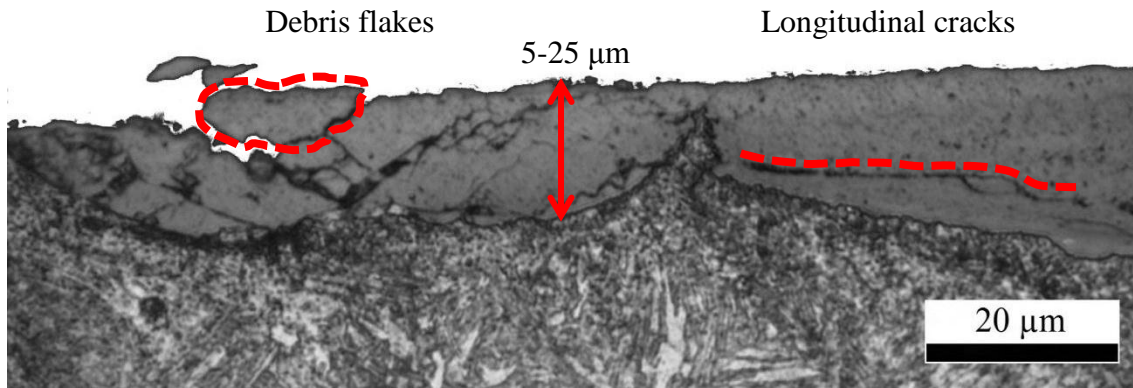


Figure 4-20: Fretting induced oxide scale on an EN24T sample.

An attempt to record the growth of the oxide layer over test duration was less conclusive as shown in Figure 4-21. The thickness of the oxide layer stuck to the bulk material remained around 2-3 μm , whereas from the Figure above a thickness of up to 25 μm was expected. Increasing the test temperature to 200°C showed that it might have an impact on the oxide thickness over time. Whereas the oxide thickness was around 2-3 μm after 30 seconds, it increased to a thickness up to 11 μm when tested at 200°C.

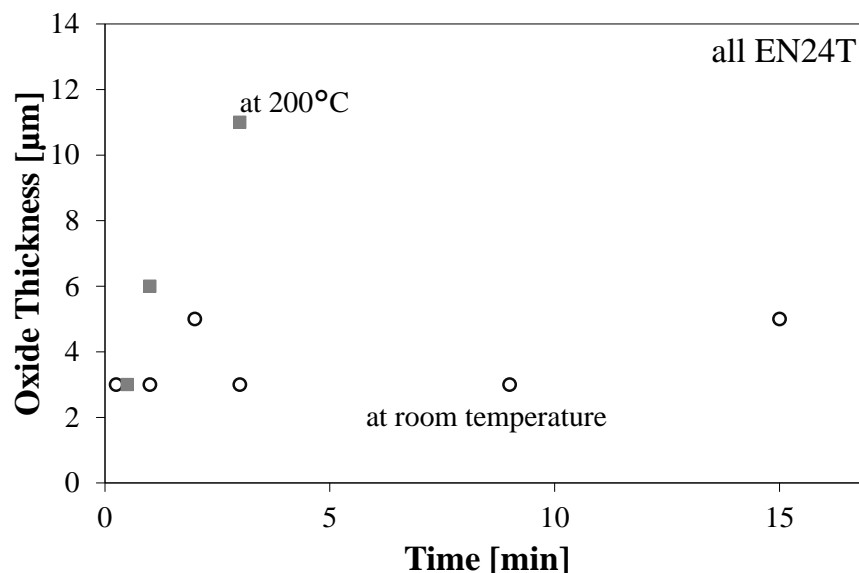


Figure 4-21: Scale thickness observed on EN24T after fretting tests performed at room temperature and 200°C.

4.2.3.4 Oxide scale on stainless steel

On stainless steel samples fretting produced a continuous oxide layer of a thickness around $5\ \mu\text{m}$ as shown in Figure 4-22. The structure of the scale appeared continuous but only loosely compacted with pores and cracks present.

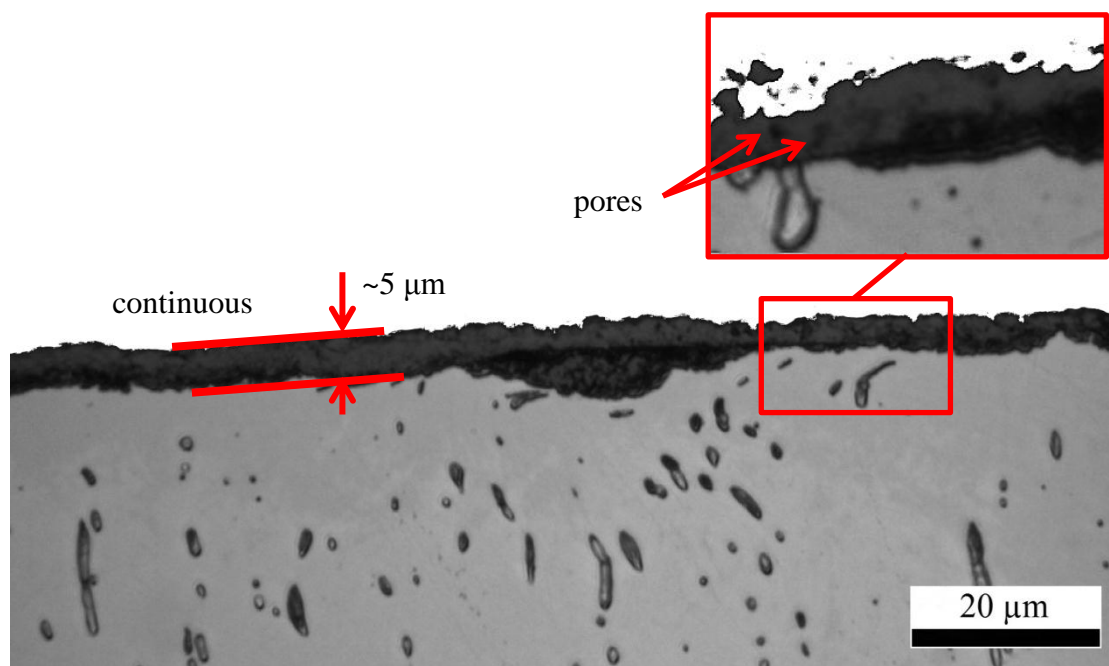


Figure 4-22: Cross section of worn stainless steel specimen.

4.2.3.5 Oxide composition

X-ray diffraction measurements on the $80\ \text{mm}^2$ worn surfaces were carried out on Udimet 720 and Ti6Al4V samples. Only these two materials could be tested as the procedure required a minimum testing area and hence only the $80\ \text{mm}^2$ samples could be used. XRD spectra of an Udimet 720 sample before and after the test are shown in Figure 4-23. The dotted line shows the spectrum of the original unworn surface. The peaks correspond to the expected nickel peaks. The solid darker spectrum corresponds to a measurement on a worn

fretting specimen. New peaks showed up in this spectrum which fit NiO but no other peaks appeared.

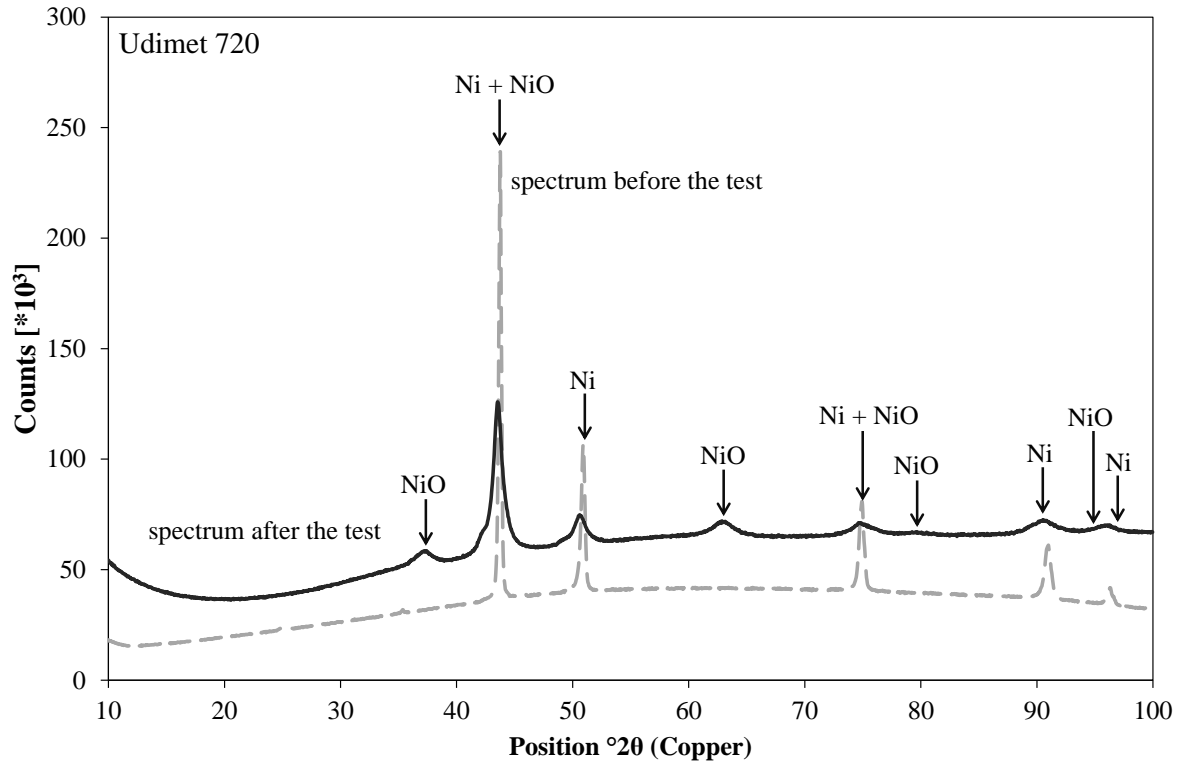


Figure 4-23: XRD spectra of Udimet 720 samples before and after the tests.

The spectra of a Ti6Al4V sample are shown in Figure 4-24. Again the spectrum received from a worn sample (solid line) is compared to an unworn sample (dashed line). The peaks of the unworn spectrum correspond to the expected titanium peaks. Additional peaks in the worn spectrum corresponded to TiO but not rutile or anatase (both TiO_2). Similar to the measurements on the nickel samples peak broadening was observed. Peak broadening was observed on both materials and was therefore caused by the fretting conditions. It can be an indicator for a smaller grain size or a highly stressed material.

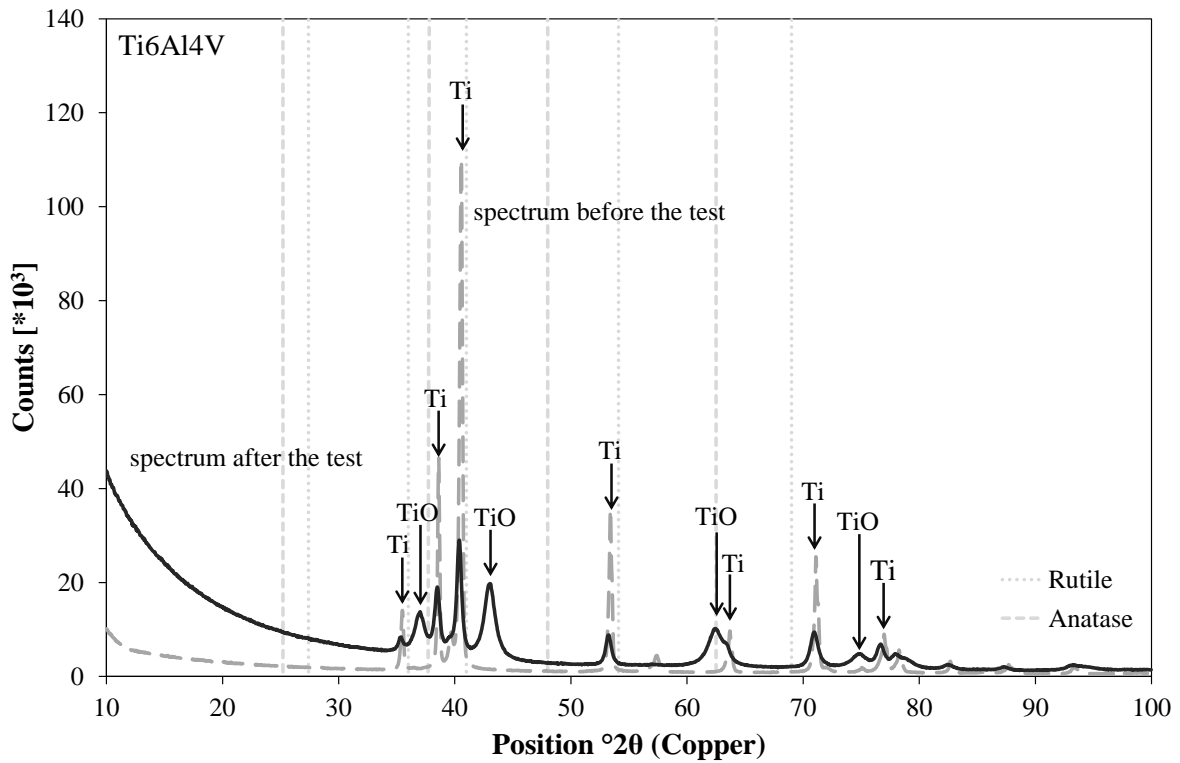


Figure 4-24: XRD spectra of Ti6Al4V samples before and after the tests.

4.2.4 Deformation

Optical microscopy revealed signs of deformation beneath the oxidised scale for all materials except Udimet 720, as shown in Figure 4-25. A variety of methods were employed to further study the degree of deformation in Ti6Al4 specimens and to clarify whether there was truly no deformation in Udimet 720 samples. The effect of the fretting tests on material was highlighted by comparisons with cross sections of untested specimens.

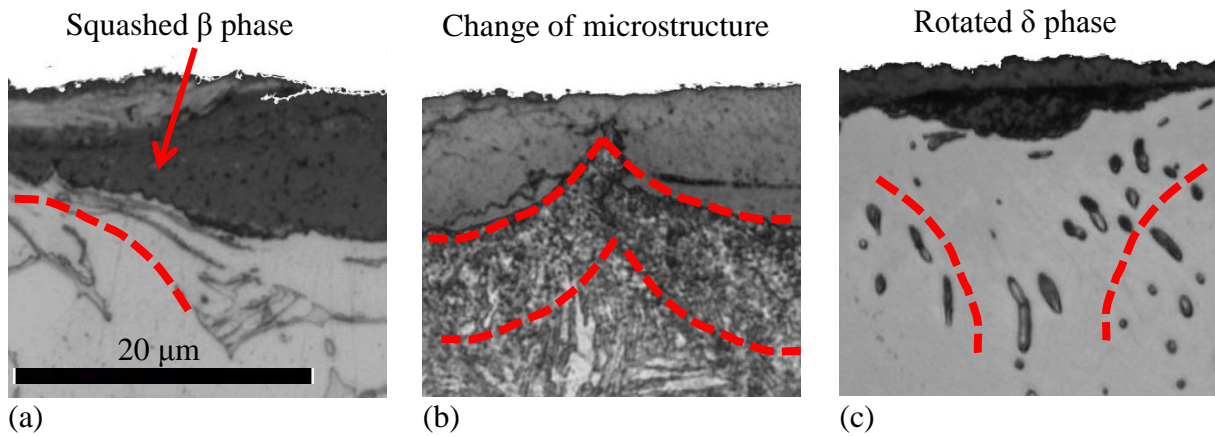


Figure 4-25: Deformation indicated by red lines on (a) Ti6Al4V, (b) EN24T and (c) stainless steel observed with optical microscopy (all images same scale).

4.2.4.1 Sub-surface deformation in Udimet 720

Electron back scattering diffraction was used to index the orientation of the grains of a microstructure. Together with corresponding pole figures the method gave information about preferred orientations and textures. First the results of an unworn specimen are shown. Figure 4-26 shows a back scattered electron images overlaid with the orientation map obtained from EBSD. Each colour represents a different orientation of the lattice within the grains of the FCC material. For the unworn specimen the method could index the grains up to the interface. The edge between the cross section and the contact interfaces is indicated by the dotted line. Two sets of pole figures for 3 different directions are plotted below the orientation map and indicate the degree of orientation within the region. The $\{100\}$, $\{110\}$ and $\{111\}$ planes were chosen which represent planes in a cubic system as indicated in Figure 4-26. The first set of pole figures represents the orientation of grains up to $50\ \mu\text{m}$ below the surface. The second set of pole figures represents the textural orientation of the bulk material, here 50 to $100\ \mu\text{m}$ into the material. Neither of the pole areas indicated texture.

The machining of the interface had not introduced any textural orientation for Udimet 720 samples which could be measured with this technique.

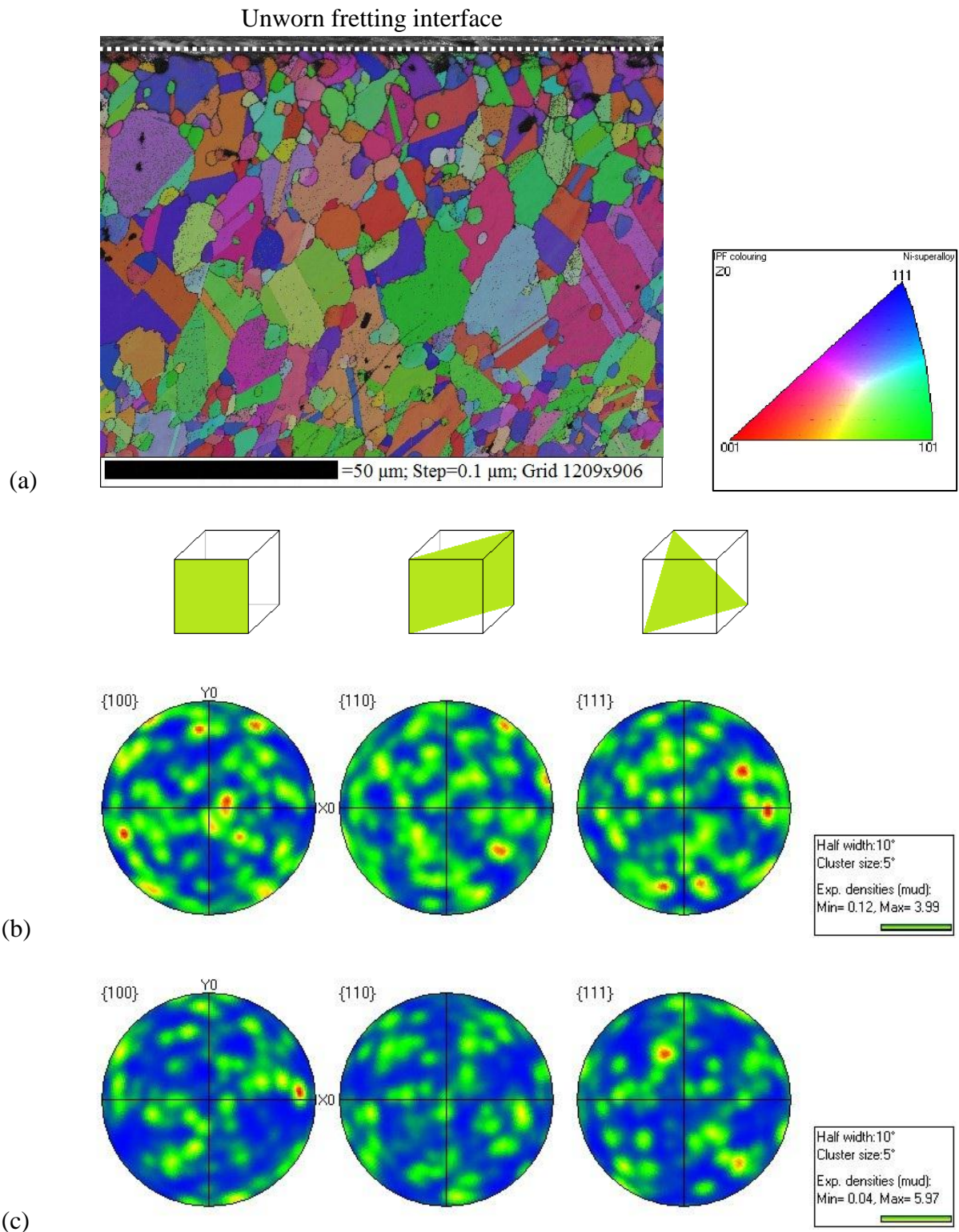


Figure 4-26: Unworn Udimet 720. (a) map (b) subsurface and (c) bulk.

The first image in Figure 4-27 shows an orientation map of an Udimet 720 cross section of a worn specimen. Again the map was laid over an electron back scattered image. From the difference of the two image layers it can be seen that area of the cross section was not fully indexed up to the interface. The edge between interface and cross section is indicated by the dotted line, as the contrast is very weak to the background. A sub-surface layer of a depth of 10 μm remained un-indexed.

The pole figures in Figure 4-27 describe again the frequency of a chosen direction in equal area projection plots. The same planes were chosen as for the unworn material. The direction X0 equals the direction of fretting. The first set of pole figures represents the area between the interface up to 50 μm into the material, which represents the sub-surface region. The second set of pole figures describes the bulk area of the material (50 to 100 μm). Neither of the areas showed preferred orientations. The data did not differ from the data obtained from an unworn cross-section. However, it was unclear whether the region which could not be indexed would have influenced the result. This layer may consist of highly deformed grains, a constitution which is knowingly disadvantageous for being indexed using EBSD. But it could also be the oxide layer which would not be indexed either. The thickness of the layer was bigger than the thickness of the oxide. Therefore it is likely that part of the unindexed region is the oxide and part is deformed material beneath the oxide layer.

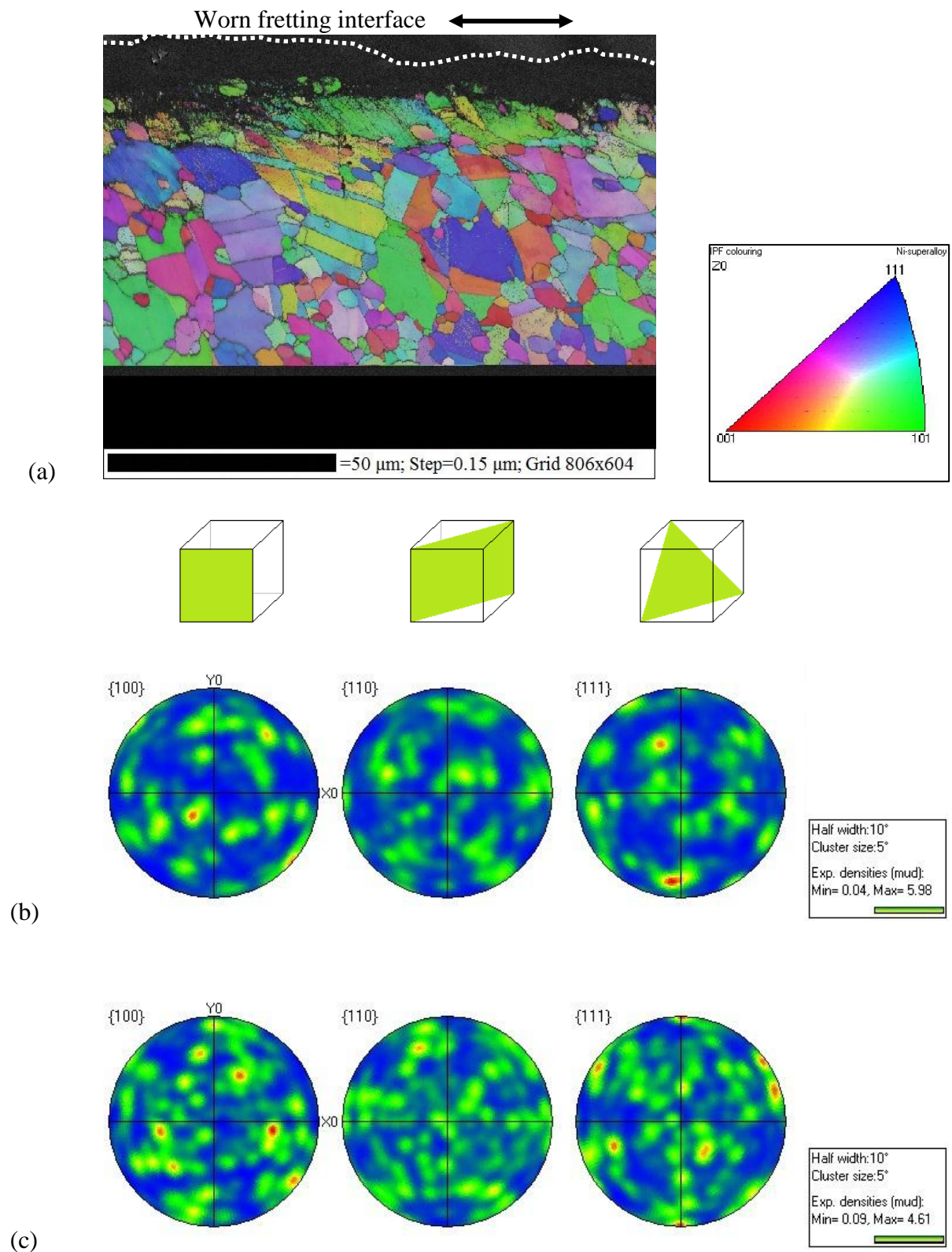


Figure 4-27: Unworn Udimet 720. (a) map, (b) subsurface in 0-50 μm depth and (c) bulk in 50-100 μm depth.

A brief FIB session was undertaken to further investigate this unindexed layer. A series of images were captured at different tilt angles which improves the contrast between the grains. Figure 4-28 shows two pictures, the left at zero tilt, the right taken at a tilt angle of 10° . The fretting interface is for both at the left side. A sub-surface layer of a depth of up to $20\ \mu\text{m}$ appeared of a different constitution. This might correspond to an oxidised area or a microstructure consisting of smaller grains.

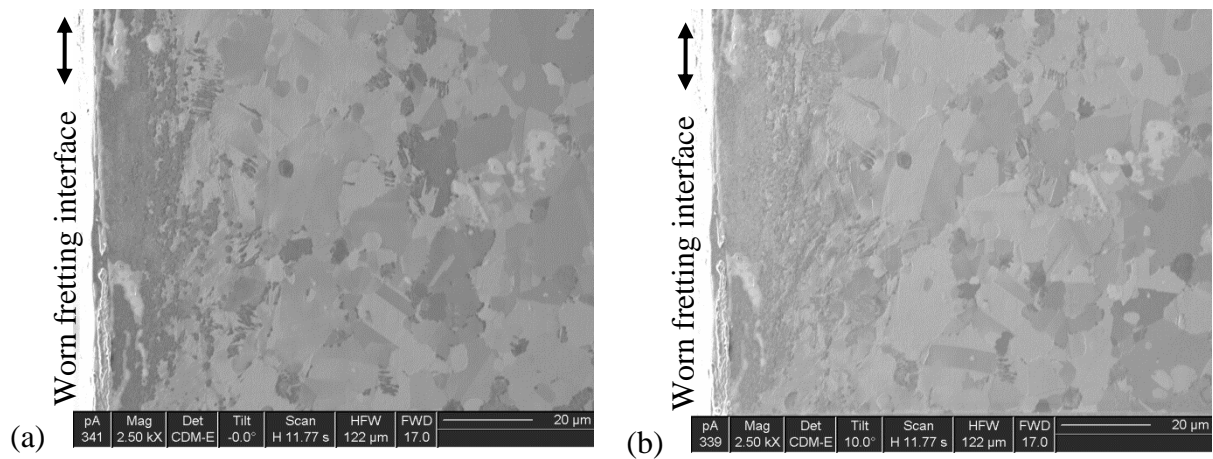


Figure 4-28: Focused ion beam image of (a) bulge and (b) centre area of $80\ \text{mm}^2$ specimen.

4.2.4.2 Sub-surface deformation in Ti6Al4V

The same EBSD study as for Udimet 720 was performed on Ti6Al4V specimens, which have a hexagonal closed packed crystal structure. Figure 4-29 shows the orientation map obtained from an unworn specimen. The interface lies right at the top of the image and is indicated by a dotted line. The material was indexed all the way to the interface. Only the α -phase of the material was indexed and black areas correspond to the β -phase which is mostly located at the grain boundaries and triple-junctions. Large black areas were caused by dirt at the surface. Two sets of pole figures are displayed below the orientation map. The first set represents the subsurface area up to a depth of $50\ \mu\text{m}$. The material appears highly textured as expected for a cross rolled material.

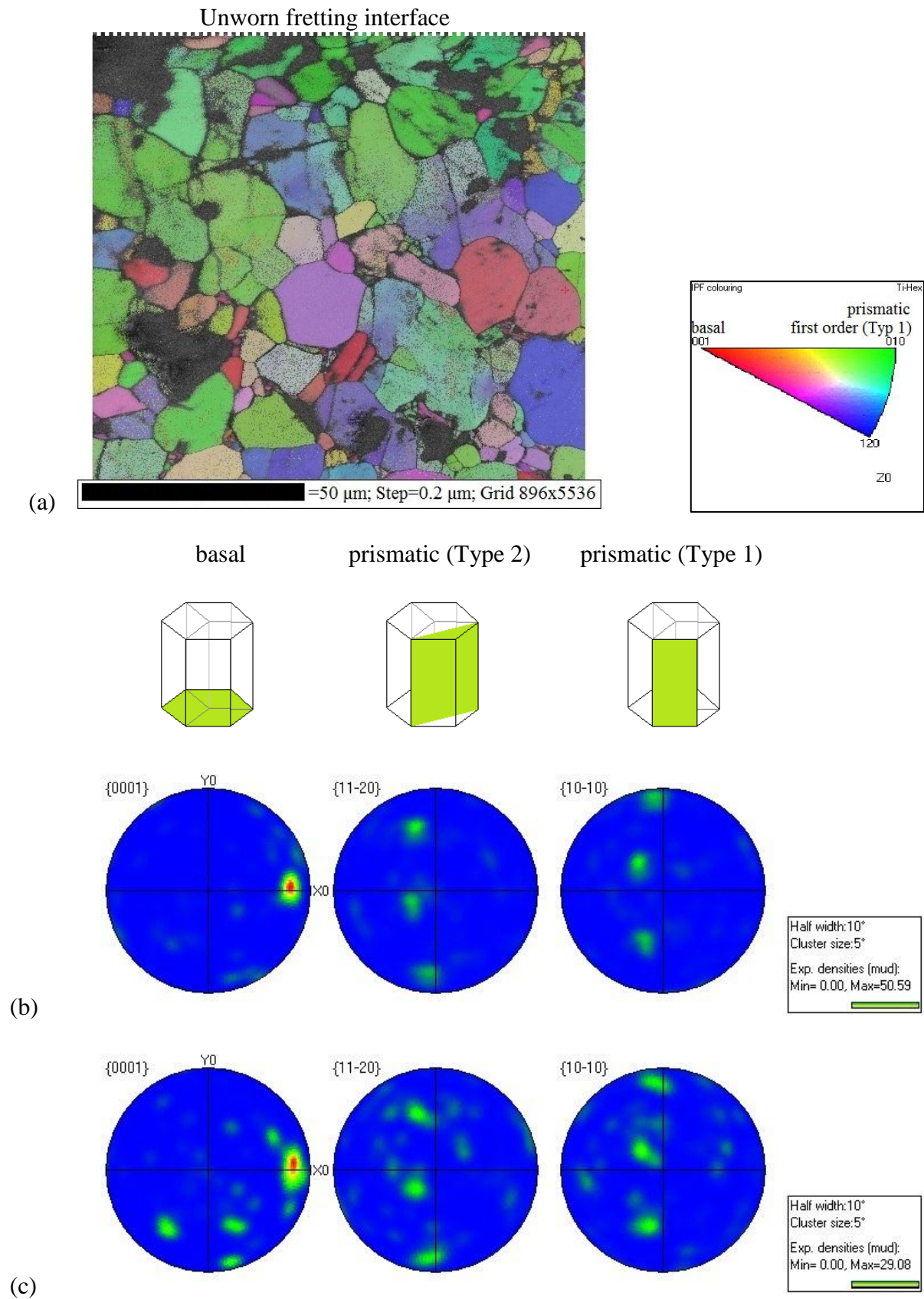
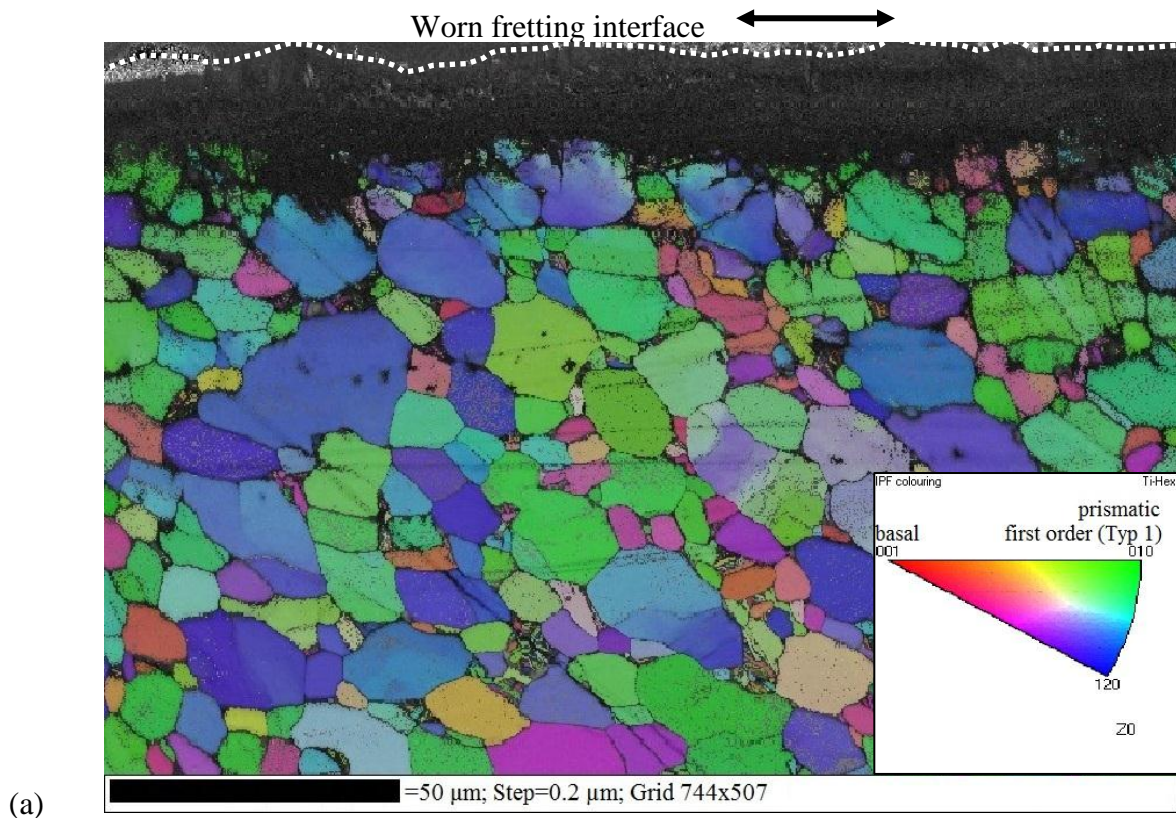


Figure 4-29: Unworn Ti6Al4V specimen: (a) EBSD map, (b) pole figures of subsurface region (0-50 μm depth) and (c) pole figures of bulk region (50-100 μm depth).

The second set of pole figures covers the bulk of the material (50 μm to 100 μm). The material shows still a strong textured orientation. The ability of the method to index the material all the way to the interface suggests a lack of a deformed sub-surface layer caused by the machining procedure of the specimens.

The EBSD orientation map of a worn interface is shown in Figure 4-30. From the backscattered electron image in the background it can be seen that the method was not successful in indexing the material all the way to the interface. The depth of the layer is about of the same thickness as the oxide layer observed in optical imaging.



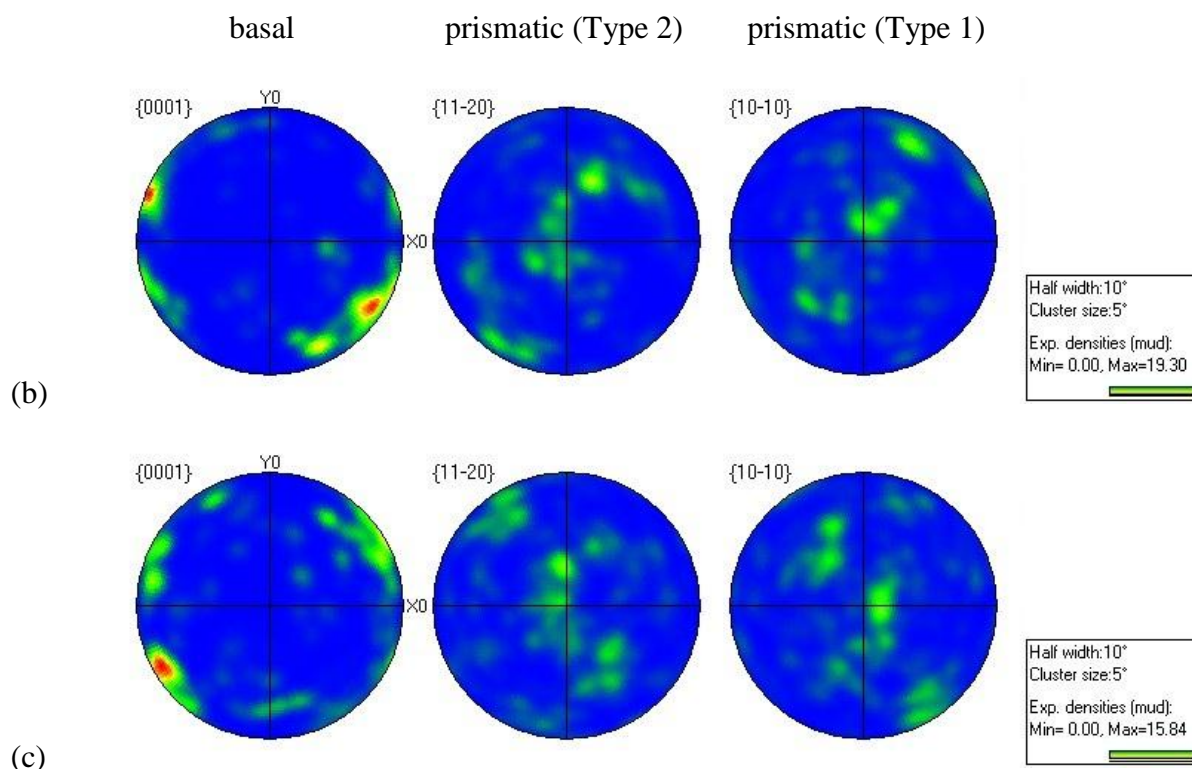


Figure 4-30: Worn Ti6Al4V specimen: (a) EBSD map, (b) pole figures of subsurface region (0-50 μm depth) and (c) pole figures of bulk region (50-100 μm depth).

A brief TEM investigation was performed to further investigate the nature of the sub-surface layer of a worn Ti6Al4V sample as shown in Figure 4-31. Two layers of Platinum at the interface had been deposited to prevent damage from ion milling. The contrast in the image below is a little misleading as it was due to changes of thickness of the sample. No oxide layer was detected and it was thought to have been separated from the bulk material due to the preparation process of the specimen. However, a difference of diffraction patterns was observed. At a point at a distance of about 0.2 μm into the bulk material the measured diffraction patterns were continuous rings, whereas at a point about 1 μm into the bulk material the diffraction patterns appeared as points. This suggested that the grain size increased with distance from the interface.

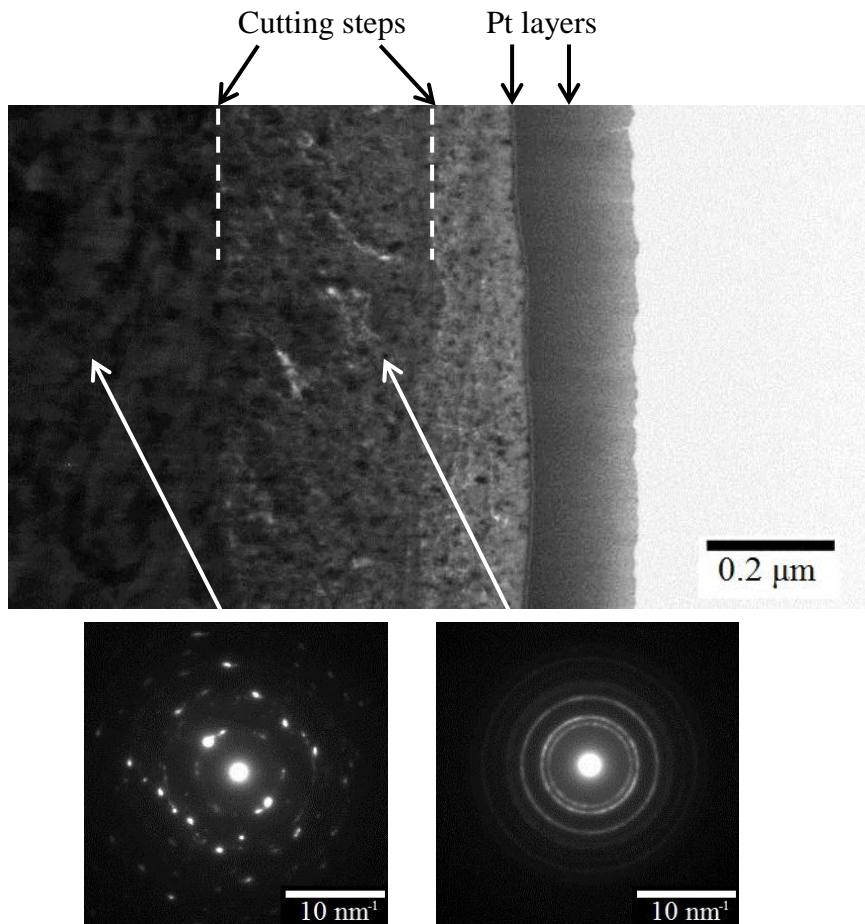


Figure 4-31: TEM investigation of a worn Ti6Al4V specimen.

Chapter 5

Friction tests - Discussion

The coefficient of friction and the tangential contact stiffness were measured for four different materials by performing friction tests under different conditions. This chapter investigates the behaviour of these properties. The experimental findings are compared with contact model predictions and similarities and dissimilarities are interpreted. The importance of surface correlation and surface degradation is discussed.

5.1 Tangential contact stiffness

5.1.1 Comparison of two friction rigs

Chapter 4 compared the tangential contact stiffness values measured on a 1 mm² contact rig and an 80 mm² contact rig. Both tests used the same materials, Udimet 720 and Ti6Al4V, and specimens had been machined in as similar a fashion as possible. Results obtained from the 80 mm² contact rig had been previously published by Kartal et al. [49]. Measured on the 80 mm² rig, the tangential contact stiffness for Udimet 720 was 980 N/μm compared to 30 N/μm measured on the 1 mm² rig. For Ti6Al4V the value stabilised on the 80 mm² contact rig at 940 N/μm compared to 18 N/μm on the 1 mm² rig.

5.1.1.1 Influence of the area of contact

It has not yet been clarified in the literature how the tangential contact stiffness, k_t , is related to the nominal contact area, A_0 . It has been proposed that the tangential contact stiffness is either linear proportional to the nominal contact area, $k_t \propto A_0$, or linear proportional to the square root of the nominal contact area, $k_t \propto \sqrt{A_0}$. Based on experimental results Kartal et al. [49] supported the linear relationship. This was also supported by the results which were obtained on cylinder-on-cylinder and sphere-on-flat EN24T specimens which led to a twice as big contact area after running in. The stiffness values were about twice as high as the values measured on the 1 mm² flat-on-flat configuration, see Figure 4-4 (b). However, an elastic half-space contact predicts the tangential contact stiffness to behave in proportion to the square root of the area of contact or in proportion to the radius of the area of contact [4, 79, 138].

Both types of normalisation were applied to the 80 mm² data for Udimet 720 in Figure 5-1 in comparison with the data collected on the 1 mm² rig. The data measured on the 1 mm² rig did not change except for its units which became either N/μm/mm² or N/μm/mm depending on the chosen normalisation.

When normalised by A_0 the bigger contact appears only slightly more compliant than the 1 mm² contact. Contrary to that, the stiffness on the larger contact rig appears to be a lot higher if the value is normalised by $\sqrt{A_0}$. Because it is assumed that both rigs are supposed to measure the same contact stiffness, Figure 5-1 supports a linear relationship between the tangential contact stiffness and the area of contact. For Udimet 720 the stabilised tangential contact stiffness normalised by the area of contact lies at around 12 N/μm/mm² compared to 20 N/μm/mm² measured on the 1 mm² rig. For Ti6Al4V the values lie around 10 N/μm/mm² measured on the 80 mm² rig compared to 30 N/μm/mm² on the 1 mm² rig. The origin of the

variance between the measured values could be down e.g. to different processes occurring in the rigs or differences in the processing of the data.

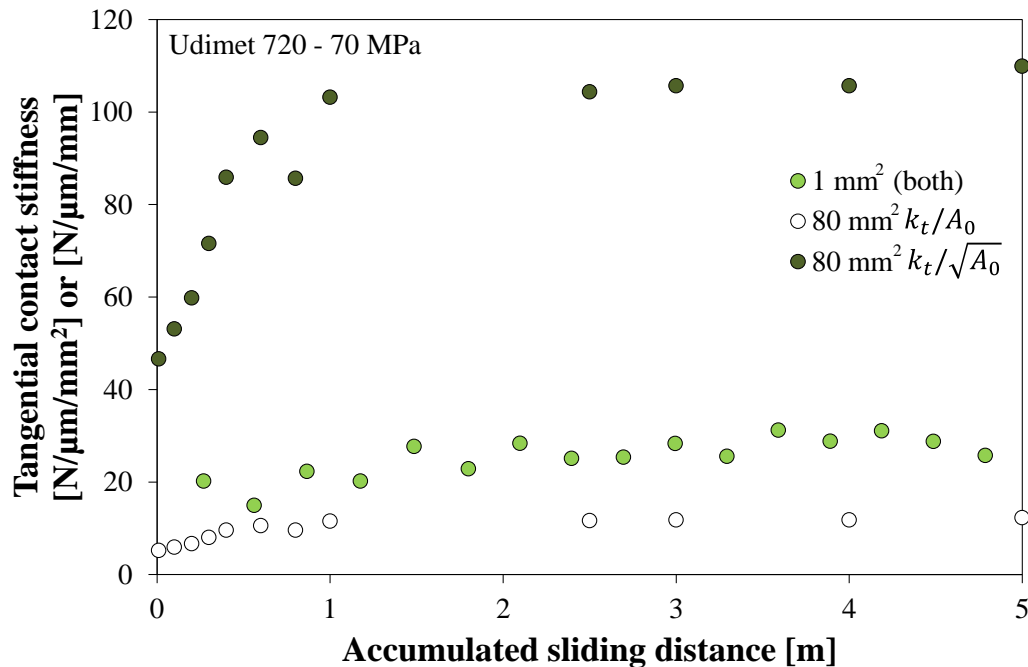


Figure 5-1: Comparison of tangential contact stiffness values for Udimet 720 normalised either by A_0 or by $\sqrt{A_0}$.

5.1.1.2 Location of the stiffness measurements

Based on experimental results, Kartal et al. [49] showed that the tangential contact stiffness varies with the distance from the interface to where the measurement was taken. The authors reported that the measured value of tangential contact stiffness increased linearly with decreasing distance of the measurement points to the interface. The stiffness value of the interface was extracted by the extrapolation to zero distance to the interface. If the tangential contact stiffness measured on the 1 mm² contact rig had been measured closer to the surface than the 80 mm² contact rig, it could explain why the former appeared to be slightly stiffer after the normalisation by the contact area.

This is not the case as the visual comparison of the two techniques shows in Figure 5-2. The 1 mm^2 contact rig uses a Laser Doppler Vibrometer (LDV) technique. The 80 mm^2 contact rig uses a Digital Image Correlation (DIC) approach. Both techniques are limited to how close to the interface they can measure the displacement. For the 80 mm^2 the distances between the measuring points were 0.3 mm for Udimet 720 and 0.5 mm for Ti6Al4V. On the 1 mm^2 contact rig the measurement points were as far as 1.2 mm separated from each other. The comparison of the techniques did not clarify why the 1 mm^2 contact could be slightly stiffer.

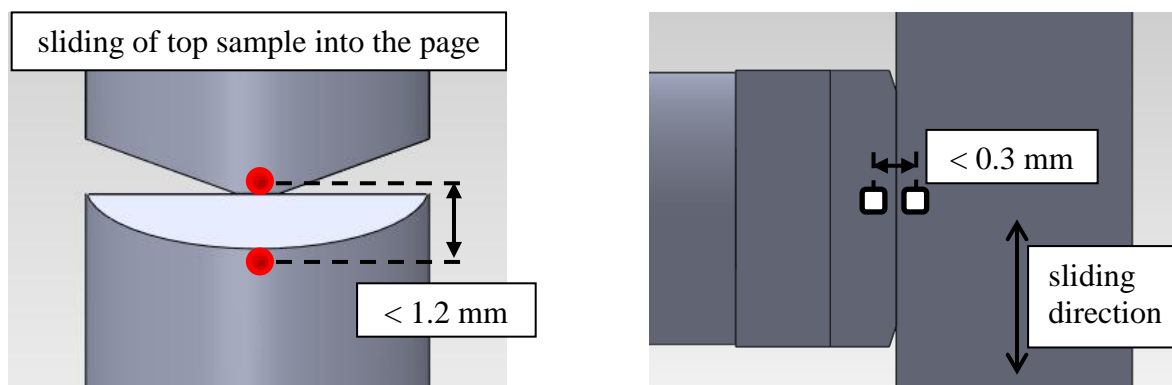


Figure 5-2: Comparison of measurement methods for the tangential contact stiffness for the 1 mm^2 and 80 mm^2 contact rig. (Schematic drawings not to scale).

If the tangential contact stiffness is normalised by the square root of the nominal area of contact the stiffness measured on the 80 mm^2 rig is a lot higher for which again an explanation must be found.

Figure 5-3 revisits a graph from Chapter 2. Figure 2-4 showed two displacement curves expected in a partial slip contact. An advanced numerical contact model such as the one developed by Medina et al. [93] enabled the display of a two-dimensional map of the displacements of every point beneath a contact for a smooth surface, as shown in Figure 5-3 (a), as well as for a rough surface, as shown in Figure 5-3 (b). The contact

interface is at the bottom of the graph. A sphere-on-flat contact geometry was chosen to calculate the smooth contact. To show the rough contact, where the cross section shows three asperities in contact, the sphere was replaced by a rough punch with rounded edges.

The maximum tangential displacement is reached at remote points where it is the same over the whole contact and behaves equally through both stick and slip regions. The total value is caused by the influence of the compliance of the interface plus the bulk compliance.

$$c_{tremote} = c_{interface} + c_{bulk} \quad (5.1)$$

As there are more gaps in the rough contact, the interface is less stiff which also affects the remote stiffness which is lower than that of the smooth contact.

Figure 5-3 (a) and (d) consider three points at the surface and the distribution of the displacements into the material. In the smooth contact one curve is chosen beneath a point in the stick zone, one in the slip zone and one outside the contact. In the rough contact, where the cross section goes through three areas of contact, one curve is chosen beneath a point in a stick zone, one between two stick zones inside a gap and one outside the contact.

At the very interface the stiffness is only influenced by the stiffness of the interface and not by the bulk. However stick and slip or non-contact regions significantly influence the values and the compliance of the interface follows as function of the compliance of gaps and the compliance of the regions in stick.

$$c_{tinterface} = f(c_{non-contact} + c_{stick}) \quad (5.2)$$

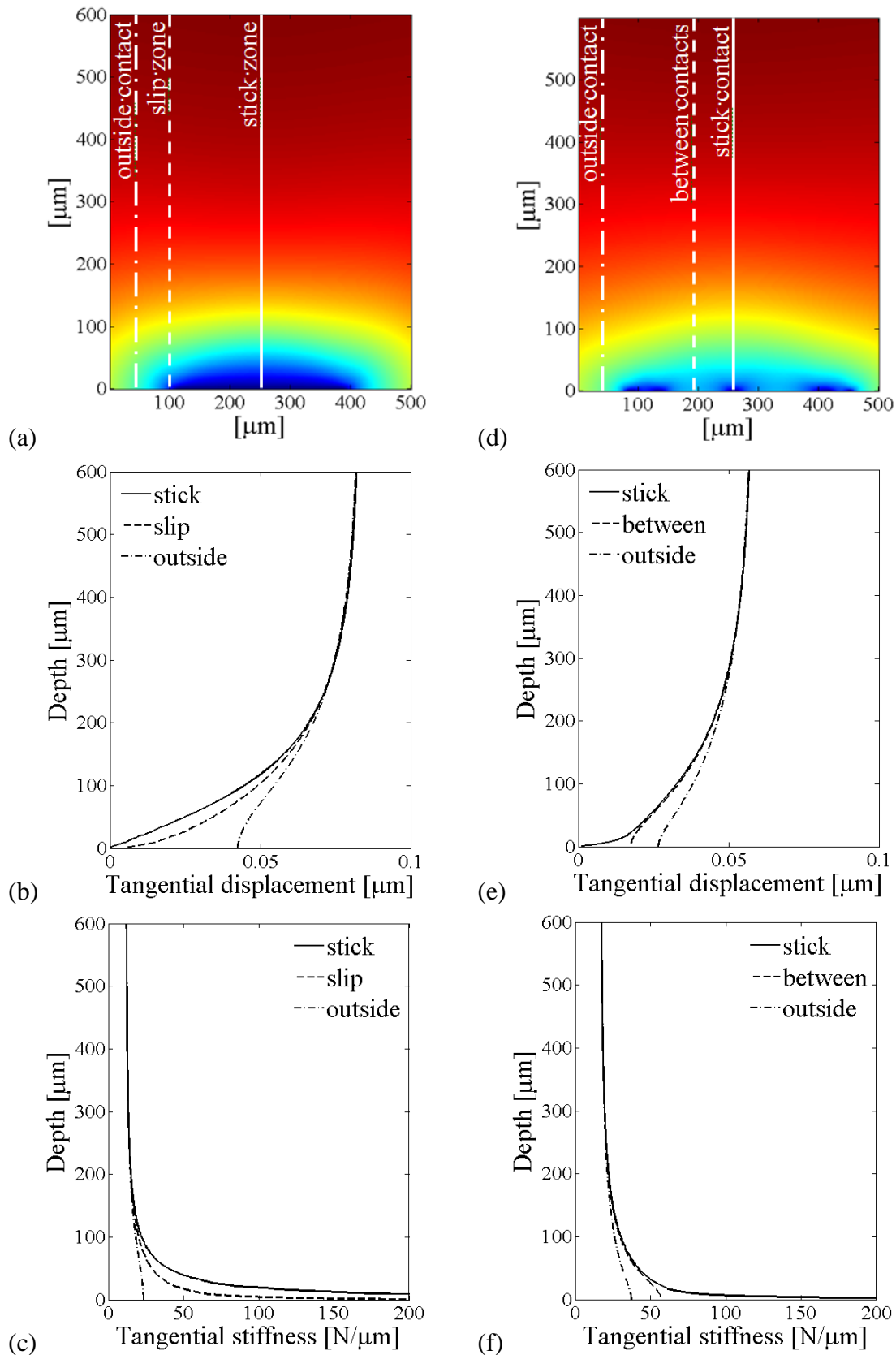


Figure 5-3: Predicted displacement and stiffness behaviour for a smooth, (a), (b) and (c), and a rough contact (d), (e) and (f) using a half-space model.

At the stick regions the displacement and compliance are zero which makes the stiffness infinite. In regions where opposing points are free to move or separated the stiffness reaches a finite value. Under test conditions a complete contact would consist of a mixture of these conditions and the stiffness value for the whole contact would lie between the finite value and infinity. The effect of the points in stick decreases when going into the material away from the immediate interface. The stiffness curves of the points in stick and slip or separation are similar and show the same dependence on the distance to the interface. However, the stiffness does not appear to decrease linearly with distance and the assumption by Kartal et al. [49] could be considered incorrect for a half-space configuration.

Kartal et al. [49] showed for the 80 mm^2 contact rig that the tangential contact stiffness was dependent on the distance to the interface. But even if the measurement was taken so close to the interface that it would have been significantly influenced by the interface it would not explain why the measured stiffness should be so much higher than the stiffness measured on 1 mm^2 contact rig. If the relatively large distance to the interface is taken into account the normalisation by the square root of the nominal area of contact becomes plausible.

5.1.2 Comparison of measured and predicted behaviour of the tangential contact stiffness

Medina et al. [138] used an analytical half-space contact model to show the behaviour of the tangential contact dependent on the applied load. The approach divides the loading in two areas: a low load and a high load region. The definition of the predicted stiffness for each region differs. At low loads an analytical model is used to describe the behaviour for sparse contact, where the formed contact areas cannot influence each other. The analytical rough surface model is based on the Greenwood and Williamson model and assumes an exponential distribution of asperity heights. The model proposes a linear proportionality between the

tangential contact stiffness and the normal load as shown below. The area of contact is approximately proportional to the load.

$$k_{t_{sparse}} = \frac{4(1-\nu) P}{(2-\nu)\sqrt{\pi} \sigma^*} \quad (5.3)$$

where σ^* is the standard deviation of peak heights. This suggests that at low loads the tangential contact stiffness is not dependent on the Young's modulus and therefore independent of the material. However, the inverse proportionality to the standard deviation of peak heights introduces a dependence on the roughness of the surfaces in contact. At low loads the tangential contact stiffness increases in proportion to load for sparse contact. The real area of contact is approximately proportional to the load. This confirmed the findings of Berthoud and Baumberger [81] who also showed that the tangential contact stiffness did not show a strong dependence on the Young's Modulus. It also agrees with Dwyer-Joyce [89] who had shown experimentally a rapid increase of the tangential contact stiffness at low loads.

When two elastic rough surfaces are placed into contact and a high normal load is applied, the asperities will deform up to the point where the surfaces are completely pressed against each other. At this upper limit complete contact occurs where the true area of contact equals the nominal area of contact. A further increase in load would have no effect on the gap-free interface. Under these conditions the tangential contact stiffness reaches a maximum limit. This limit can be calculated using a Hertzian approach as follows. Both surfaces deform elastically and the tangential contact stiffness is given by the normal load divided by the displacement as shown in (2.27). It is assumed that no slip occurs. For this case the traction distribution can be found in (2.14) in Chapter 2. The local and remote displacements can then be found according to (2.15) and (2.16). From this k_t is expressed as follows

$$k_{t\text{limit}} = 2a \left(\frac{E}{(1 + \nu)(2 - \nu)} \right) \quad (5.4)$$

At high loads complete contact occurs and tangential contact stiffness depends on the Young's modulus E but not on roughness. The stiffness depends only on the bulk deformation. An alternative way to calculate this limit would be by finite element modelling, which can use the actual geometry of two specimens in contact. However it was found that this calculation strongly depends on where the specimens are fastened or locked against deformation. By changing the locked position on the sample a wide range of possible values for tangential stiffness could be calculated [138].

The combination of the high and low load equation of k_t is shown in Figure 5-4. The relationship between k_t and the normal load at low loads is indicated by two slopes. The black solid slope represents two relatively smooth surfaces in contact. The grey striped slope stands for two relatively rough surfaces in contact. The continuous curve is a combination of the contact stiffness regions as shown in Equation (5.5). The curves agree very well with predicted curves by the numerical elastic model by Medina [93] which was based on a multi-level multi integration approach. The numerical model can generate surfaces which can take on any shape, from being smooth, based on the surface model by Greenwood and Williamson or random.

$$\frac{1}{k_t} = \frac{1}{k_{t\text{sparse}}} + \frac{1}{k_{t\text{limit}}} \quad (5.5)$$

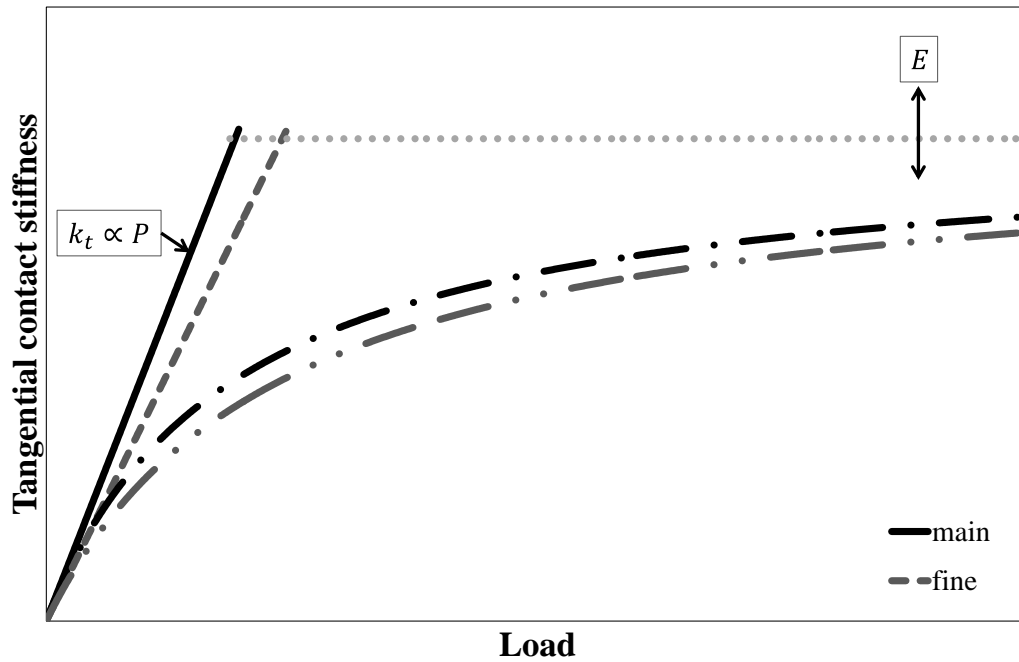


Figure 5-4: The relationship between the tangential contact stiffness and load, as predicted by analytical models (straight lines) and a numerical model (continuous curved lines). Roughness influences the tangential contact stiffness at low loads, whereas the Young's modulus affects it at high loads.

The model also showed that the stiffness should neither be normalised by the nominal area of contact nor the square root of the nominal area. The curve at low loads could be normalised by the nominal area of contact and the limit could be normalised by the square root of the nominal area of contact. But a measured value which lies in between the limiting options cannot be normalised by either but must be discussed in relation to the authentic contact dimensions.

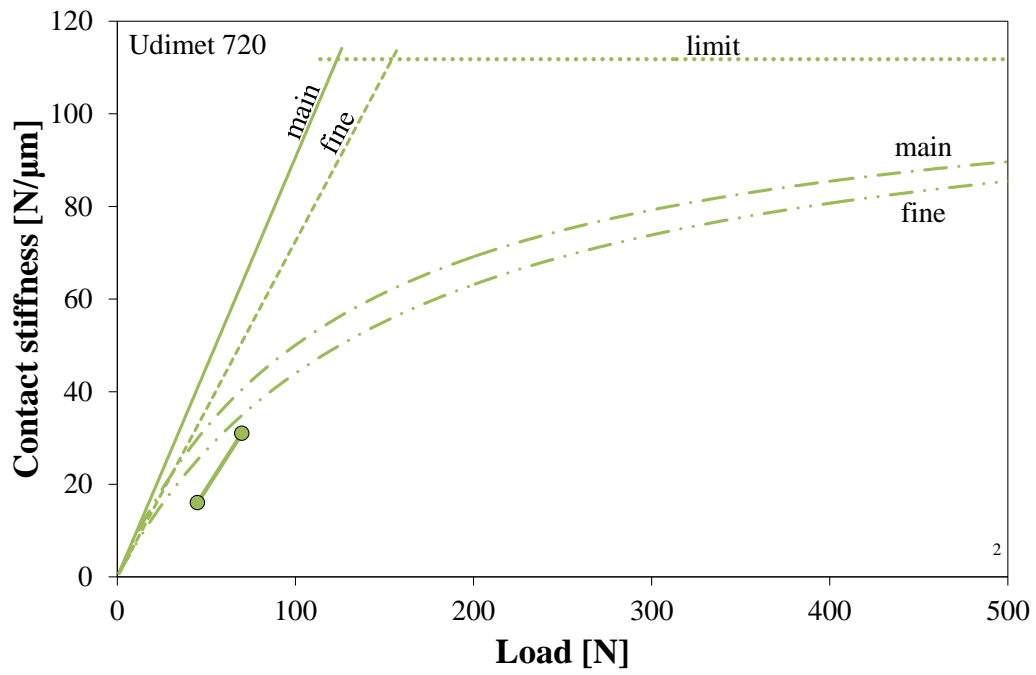
5.1.2.1 The effect of material and load on the tangential contact stiffness

A numerical evaluation of k_t for all materials and a nominal contact of 1 mm^2 is presented in Figure 5-5. The corresponding graphs for an 80 mm^2 contact for Udimet 720 and Ti6Al4V

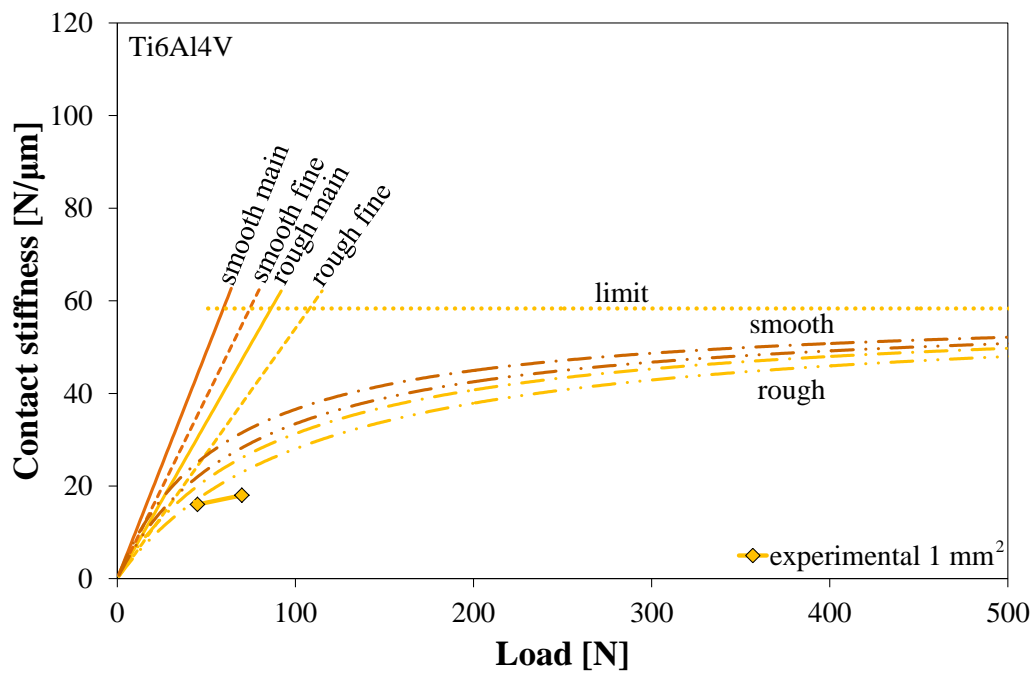
specimens are shown in Figure 5-6. For a given nominal area of contact of 1 mm^2 , the radius of an equivalent circular contact area is $1/\sqrt{\pi}$ mm. Material properties were used as stated in Table 3-1 and roughness conditions as determined in Table 3-8. Whitehouse and Archard [25] predicted a value for σ^* for a main structure as 0.71σ where σ is the standard deviation of surface heights. For a fine structure reference [25] predicted a proportionality factor of 0.9. The main structure consists only of the bigger features of the surface, whereas the fine structure also takes fine features into account hence the higher proportionality factor. Both options were calculated. In the case of Ti6Al4V, Figure 5-5 (b), both roughness conditions were considered.

The curves of the theoretical model are meant to produce a limiting envelope for the tangential contact stiffness (since any unconsidered factors will increase compliance). The experimental 1 mm^2 values support this as all data points lie within these limits for both pressures, 70 MPa and 45 MPa. But the comparison also shows that the model, except for stainless steel, overestimates the tangential contact stiffness. The real contacts seem to be more compliant than expected.

The comparison in Figure 5-5 shows that the effect of load for the different metals seems to reflect different parts of the theoretical curves, the load dependent region and load independent region. An increase in the nominal contact pressure affected the experimentally determined tangential contact stiffness of Udimet 720 and stainless steel, but not of Ti6Al4V and EN24T. For these two materials the measured tangential contact stiffness did not increase at all or only slightly with the higher load. The curves generated by the contact model show that Udimet 720 and Ti6Al4V were still expected to be in the load dependent region and agree with the experimental results. For Ti6Al4V the model predicts the approach of the load independent region which was as well validated by the experimental results.



(a)



(b)

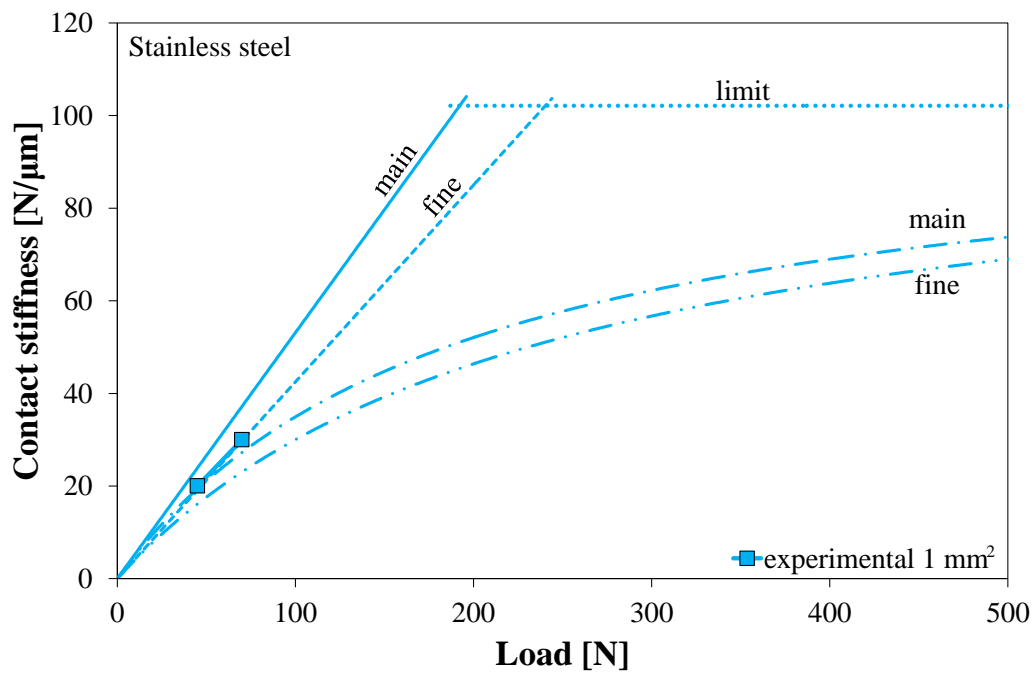
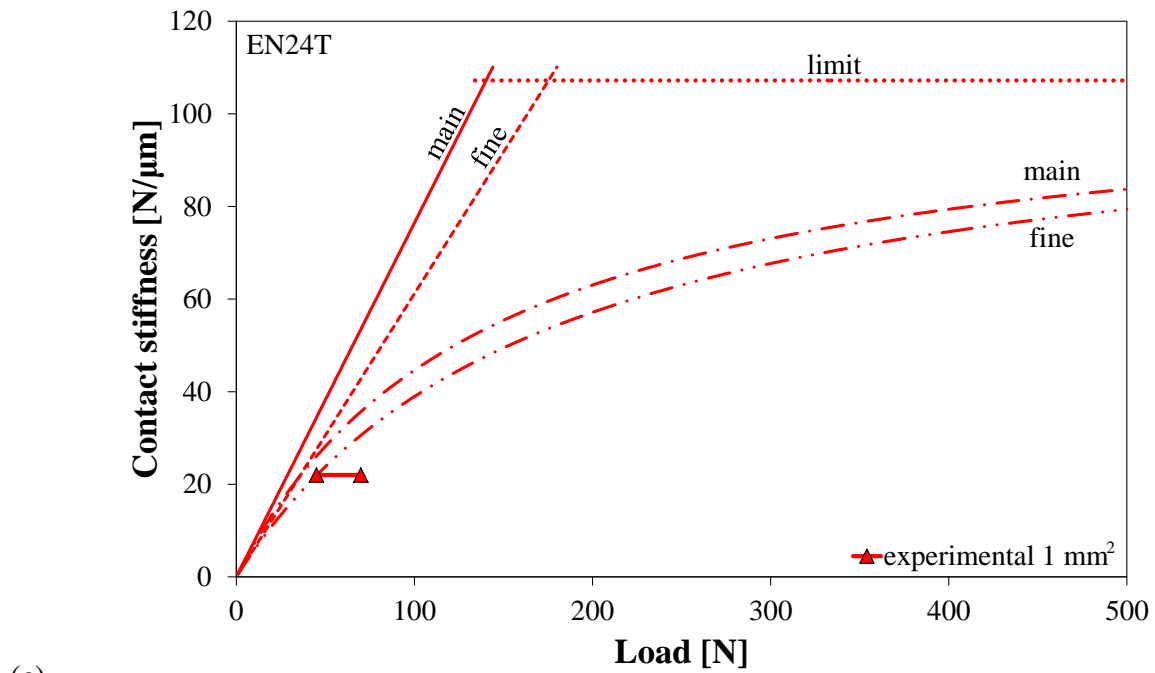
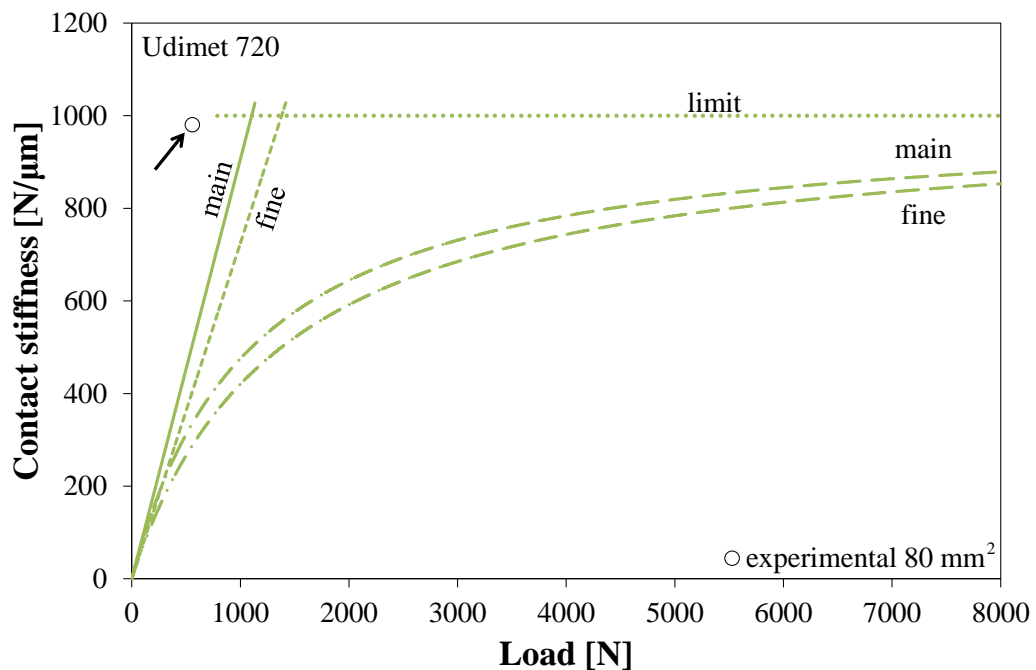


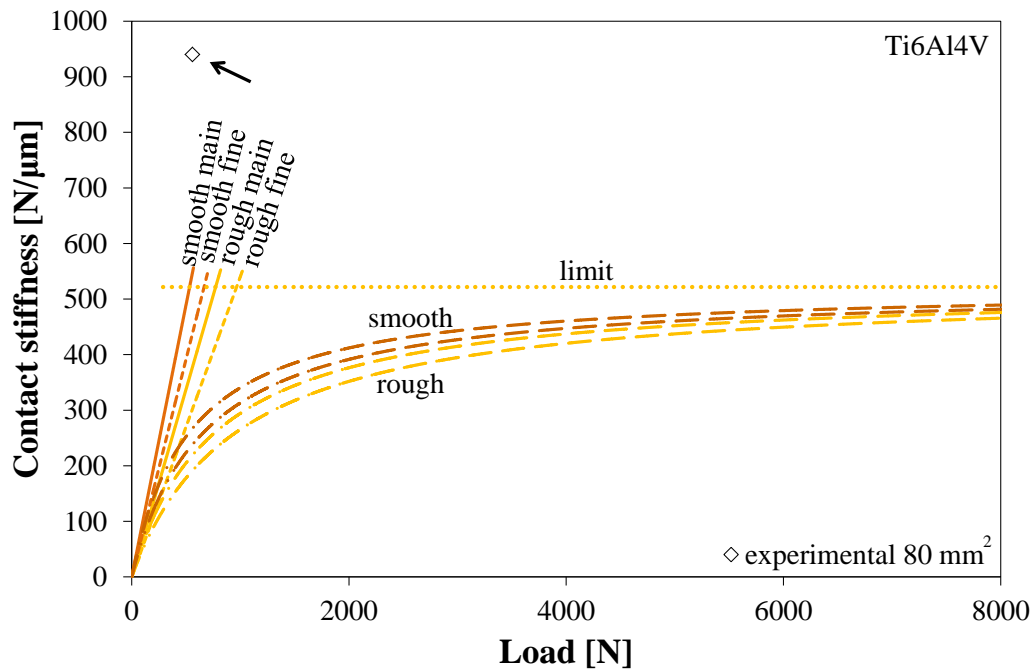
Figure 5-5: Comparison of 1 mm^2 experimental value with predicted curves for (a) Udimet 720, (b) Ti6Al4V, (c) EN24T and (d) stainless steel. At low loads two options are given for a main structure and for a fine structure of the surface as explained in the text.

However for EN24T the model predicted that the stiffness should be still load dependent, but the behaviour was not confirmed by the experimental results. The material must have reached the maximum limit for the tangential contact stiffness a lot earlier than predicted by the contact model. Explanations must be found for the general underestimation of the stiffness and in case of EN24T the premature approach of the load independent region.

The bigger contact area changes the curves of the model and the experimental results must be compared with the contact model separately. For both materials, Udimet 720, shown in Figure 5-6 (a), and Ti6Al4V, shown in Figure 5-6 (b), the experimental values lie outside the envelope of the prediction by the elastic contact model. This discrepancy must have been caused by the different contact geometries and the half-space model is not applicable for the 80 mm^2 rig conditions.



(a)



(b)

Figure 5-6: Comparison of 80 mm^2 experimental values with predicted curves for (a) Udimet 720 and (b) Ti6Al4V.

5.1.2.2 Contributions to the compliance of the contact

The contact models either overestimated the tangential contact stiffness, as in the case of the 1 mm^2 contact, or underestimated the stiffness as in the case of the 80 mm^2 . Where the models overestimated the contact stiffness, something must contribute towards the compliance of the real contact.

There are several major differences between the experiments and the models. The models are solely dependent on the elastic properties of the material and expect a two-body contact. In an elastic contact model the compliance of the contact only originates from the interface or the bulk.

In a real contact the authors of [49] attributed the surface roughness, the formed oxide layer and the compacted wear debris, if not fully dense, the most importance to contributing

additionally to the compliance of the contact. These components of compliance contribute to the total compliance as shown in the Figure 5-7 below.

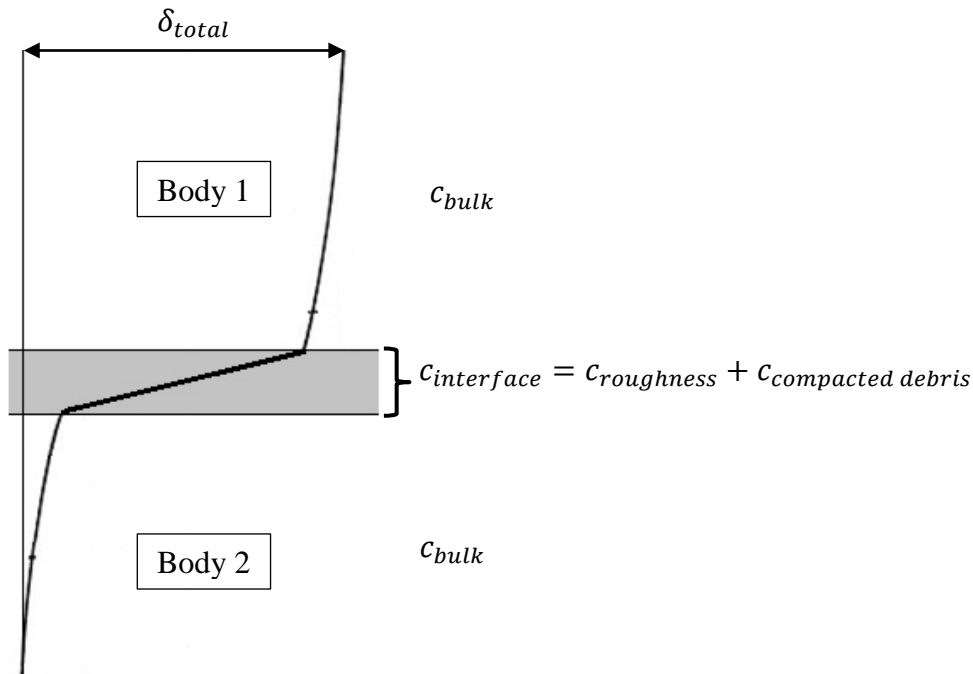


Figure 5-7: Components of the total compliance inside the contact [49].

Initial surface roughness did not seem to play an important role, as it changed with the first stroke. The numerical contact model by Medina et al. [138] predicted an influence of the roughness as follows. For similar roughness conditions as for the test specimens, low skewness (around 0) and a low/medium kurtosis (around 3) the increase of the R_q value from $1.5\ \mu\text{m}$ to $2.5\ \mu\text{m}$ predicted a slight decrease of the tangential contact stiffness. In case of Ti6Al4V two different roughness conditions were tested. Experimentally there was no difference which would agree with the minimal effect predicted by the contact model. Additionally, and more importantly, the investigation of the specimens after the tests showed that the initial contact roughness was no longer present due to severe wear at the contact.

All materials formed an oxide layer which prohibited a direct metal-metal contact. More-so the debris was e.g. for EN24T, Ti6Al4V and stainless steel compacted into a thick layer which was thought to be a source for extra compliance in the contact. Full contact might have been reached at lower loads but most definitely did not occur towards the end of the tests.

The load independency of EN24T can be explained by the increase of the conformity due to plasticity and oxidation, and not just due to elasticity as in the model.

Even though there is a surprisingly good agreement between the model and the experimental results of the 1 mm² contact it must be expected that the elastic contact models oversimplify the problem. The division of the compliance into its contributing parts, as done by [49], showed that most of the components were not considered in the contact model.

5.2 The time dependent behaviour of friction properties

Tangential contact stiffness as well as the coefficient of friction showed a time dependent running-in behaviour. Chapter 4.2.1 showed that parallel to the measured properties the contact interface changed and evolved over time significantly.

5.2.1 A wear scar interaction model

A model was sought which could explain the interaction between two worn-in surfaces. The model aims to characterise the effect of the change of the surface profile upon the friction loop. A successful model was created by collaborators and first presented by Mulvihill et al. [77], where it was used to explain the continuous increase of friction during gross slip caused by the interaction of the worn surfaces. The model shall be reviewed here again but tailored to the conditions of the wear scar of a 1 mm² rig friction test.

The model assumes two bodies in fretting contact. The surfaces had a considerable amount of time to run-in. A local peak on the bottom surface has formed which at the same time caused a trough in the top surface, shown in Figure 5-8 (a). The top surface has the weight m and is additionally loaded by P . The profile of the wear scar is described by the following power law

$$z(x) = z_0 \left(\frac{x}{x_0} \right)^n \quad (5.6)$$

where x_0 and z_0 are the semi-width and depth of the wear scar. The wear scar is deepest in the centre where $x = 0$. The steepness of the edges of the wear scar is defined by the exponent n . It is assumed that the material from the centre of the wear scar has been moved to the edges. Three different exponents, $n = 2, 4$ and 6 were studied. The corresponding wear scar shapes are shown in Figure 5-8 (b). The edges of the $n = 6$ wear scar has steeper edges than when $n = 2$.

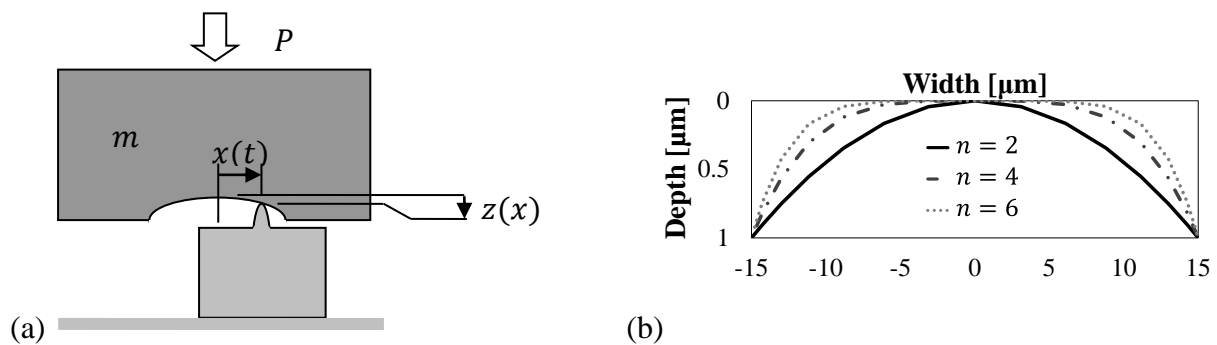


Figure 5-8: Schematic illustration of the wear scar interaction model.

The local slope of the wear scar is given by

$$\frac{dz}{dx} = \frac{z_0}{x_0^n} nx^{n-1} \quad (5.7)$$

The tangential motion with time t of the upper body is described by the sinusoidal function $x(t)$ shown below.

$$x(t) = x_0 \sin \omega t \quad (5.8)$$

where x_0 is the maximum amplitude of the displacement and ω the angular frequency. The vertical speed and acceleration are shown in (5.9) and (5.10).

$$\dot{z}(t) = \dot{x} \frac{dz}{dx} = \dot{x} \frac{z_0}{x_0^n} nx^{n-1} \quad (5.9)$$

$$\ddot{z}(t) = \frac{z_0}{x_0^n} n \left[\frac{d^2x}{dt^2} x^{n-1} + (n-1)x^{n-2} \left(\frac{dx}{dt} \right)^2 \right] \quad (5.10)$$

The equilibrium of the force in the contact is schematically displayed in Figure 5-9 with the definitions of the vertical force V and the horizontal force Q shown below.

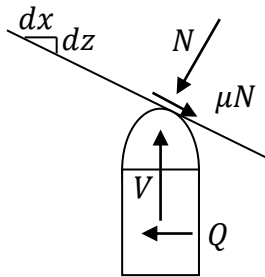


Figure 5-9: Schematic equilibrium of the forces in the interaction model.

If the contact is rigid the vertical force N and the horizontal force Q are defined as follows

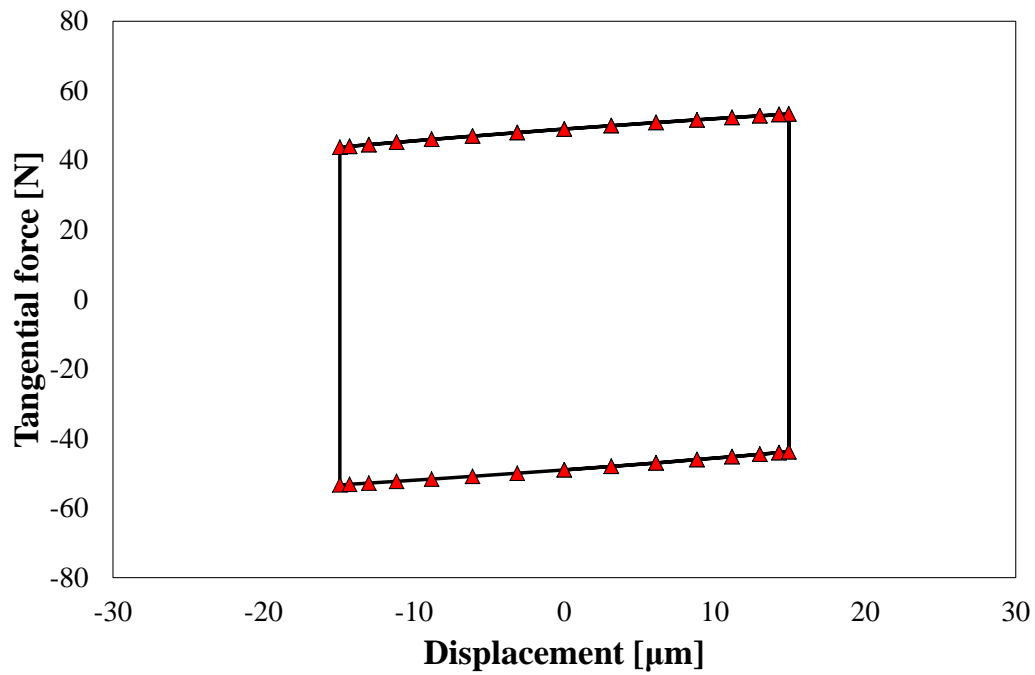
$$V = N + \mu N \frac{dz}{dx} = F + m\ddot{z} \quad (5.11)$$

$$H = N \left(\frac{dz}{dx} - \mu \frac{|\dot{x}|}{\dot{x}} \right) \quad (5.12)$$

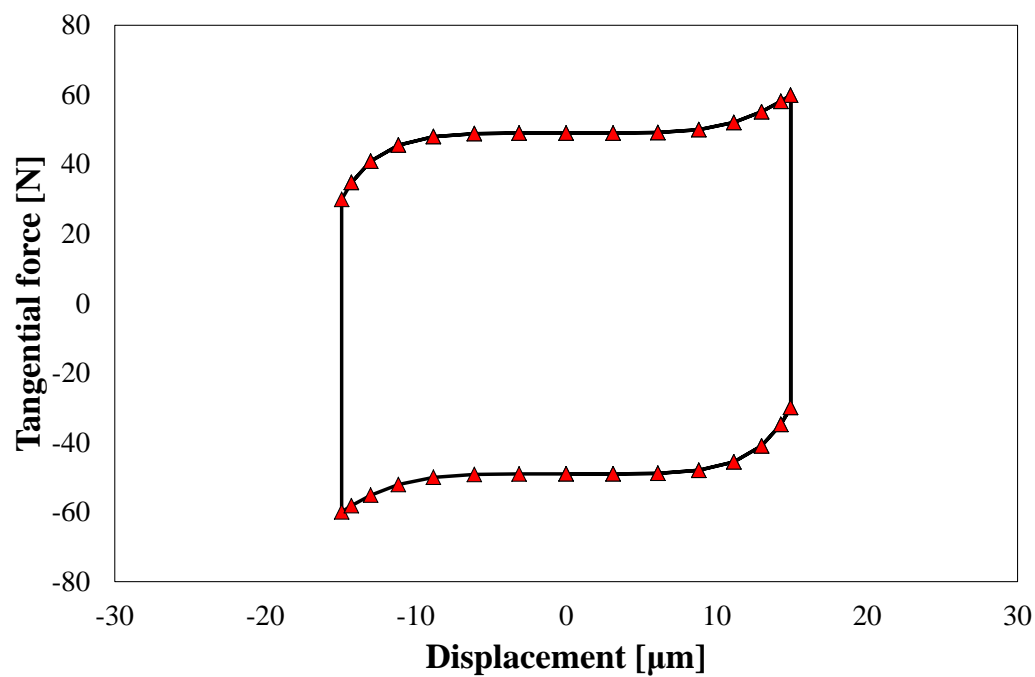
This fully defines the proposed interaction model. Conditions similar to the real friction tests were chosen with the coefficient of friction of 0.7, a 0-to-peak displacement of 15 μm and the depth of the wear scar set to 1 μm . For an applied force of 70 N, where $m = 0$ and therefore $V = N$ the resulting friction loop is shown in Figure 5-10 (a).

The model helps to envision what happens during the test in the interface and how the wear scar affects the friction loop. In the case of a parabolic wear scar, the friction increases linearly in the region of gross slip. A loop like this is typical for the 1 mm^2 contact rig which was not displacement controlled. A surface peak forms an initial parabolic scar. The next stroke is constrained by the result of the previous stroke and continuously decreases but the wear scar keeps a parabolic shape.

Figure 5-10 (b) displays a loop caused by a more shallow wear scar with $n = 6$. The loop features a hook similar to the one seen in loops obtained from the 80 mm^2 contact rig. The rig is displacement controlled and the hook feature is regularly discovered after a certain amount of time. The shallow wear scar causes the friction to increase at the beginning and the end of gross slip. As the peak has to move along the whole length of x_0 the shape of the wear scar will resemble more the case of $n = 6$ where the resulting friction loop displays the hook feature as seen in the real tests.



(a)



(b)

Figure 5-10: Friction loops produced by the interaction contact model, where (a) $n = 2$ and (b) $n = 6$.

Figure 5-11 (a) shows a wear scar evolution which could be expected for the 1 mm^2 rig specimens. The wear scar depth increases, while the displacement amplitude decreases with

time from 30 μm to 20 μm . The exponent of the power law which describes the shape of the wear scar remains $n = 2$. Three loops from different times are shown Figure 5-11 (b). The graph shows that for such a wear scar evolution the slope of the gross slip region of the loop increases with time. The same behaviour was seen on the loops which were measured on the 1 mm^2 contact rig.

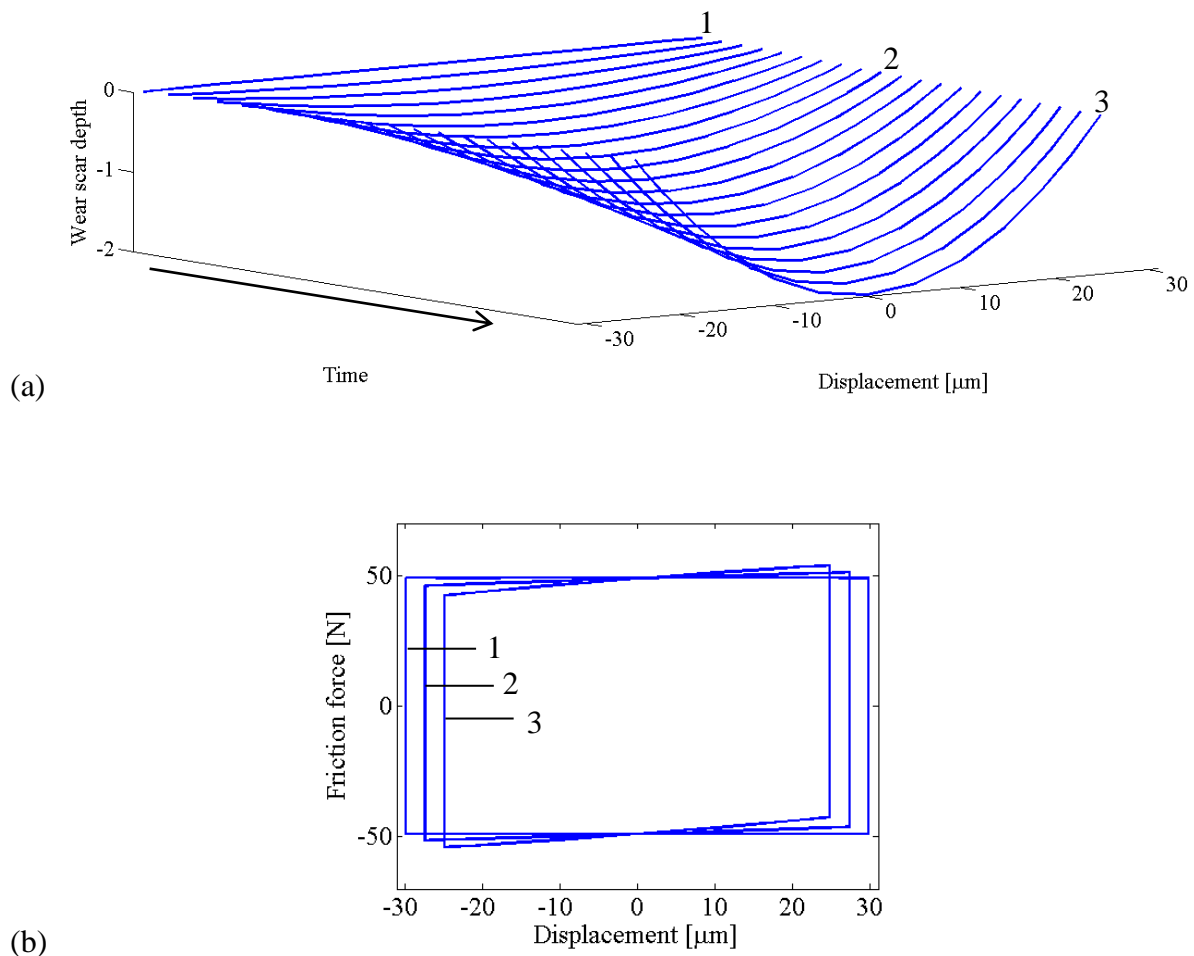


Figure 5-11: (a) Expected wear scar evolution in a 1 mm^2 contact without controlled displacement, (b) predicted loops corresponding to wear scars at three different times.

In Figure 5-12 (a) the initial and final loop of a test are shown. The displacement decreased from around 29 μm to 20 μm and the coefficient of friction increased from 0.68 to 0.78 during the test. According to the wear scar evolution shown in Figure 5-11 the wear scar

shape exponent remains $n = 2$. With the additional information of coefficient of friction and displacement amplitude the model produced the loops in Figure 5-12 (b). The initial slopes of the loops were adjusted to correspond to the measured tangential contact stiffness.

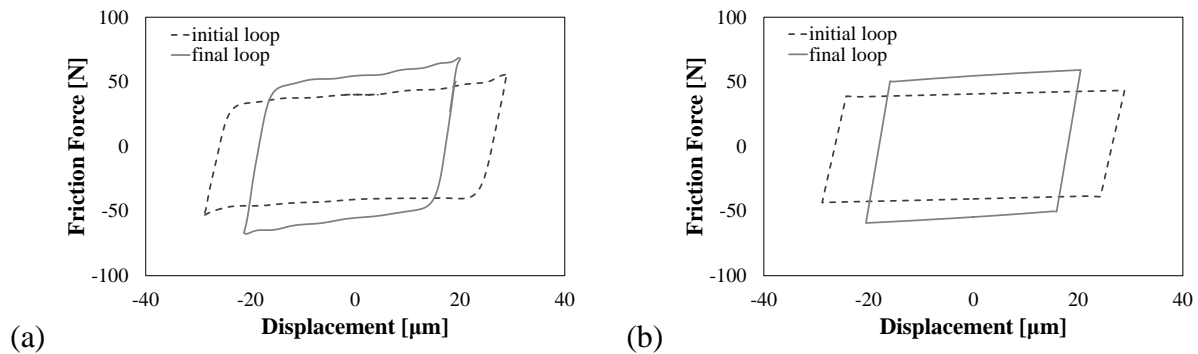


Figure 5-12: (a) Measured initial and final loop of a 1 mm^2 contact, (b) predicted initial and final loop based on the same changes in displacement amplitude and coefficient of friction. The initial slopes of the predicted loops were adjusted additionally to correspond to the measured tangential contact stiffness.

A similar comparison was done for loops measured on the 80 mm^2 contact rig. Figure 5-13 shows the wear scar evolution as it would be expected for a displacement controlled contact. While the depth of the wear scar increases with time, the displacement remains constant. To take the change of the wear scar roughly into account the initial exponent of the wear scar shape is chosen $n = 2$ but increases with every fifth wear scar by 2. The resulting wear scar evolution is shown in Figure 5-13 (a). Three times were chosen to show the corresponding friction loops, Figure 5-13 (b). The loops show that for such a wear scar evolution a hook feature develops with time. The same feature was seen on the loops which were measured on the 80 mm^2 contact rig.

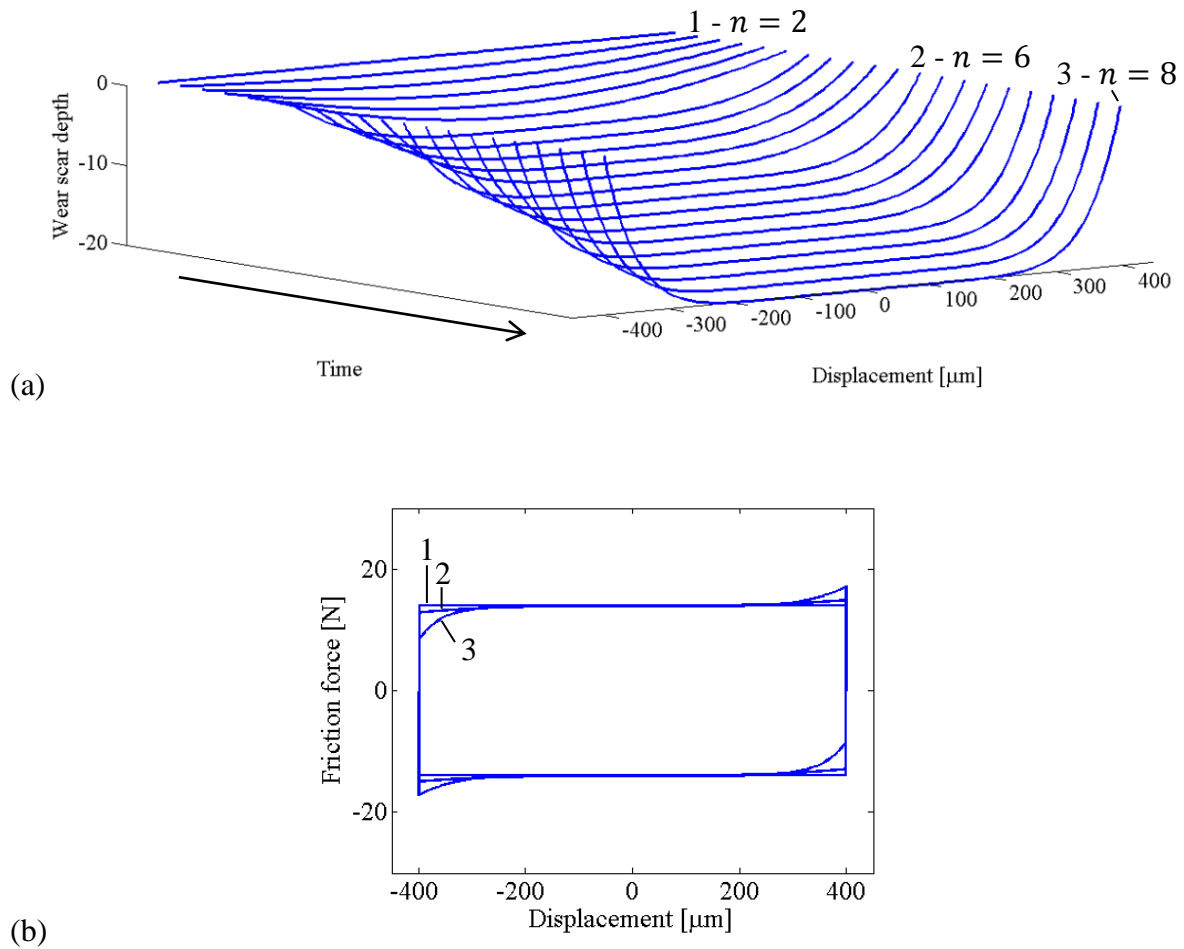


Figure 5-13: (a) Expected wear scar evolution in a 80 mm^2 contact with controlled displacement, (b) predicted loops corresponding to wear scars at three different times.

Figure 5-13 (a) displays typical initial and final loops obtained from the 80 mm^2 contact rig which was run displacement controlled. The coefficient of friction increased from 0.38 to 0.58 during the test. The wear scar shape exponent was chosen to be $n = 2$ for the initial loop and $n = 8$ for the final loop. With this information the model was able to produce loops as shown in Figure 5-12 (b). The initial slopes of the loops were adjusted to correspond to the measured tangential contact stiffness.

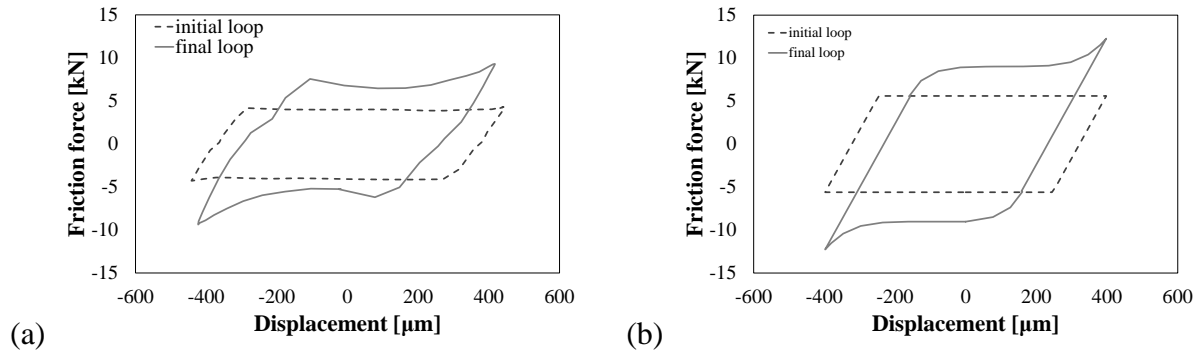


Figure 5-14: (a) Measured initial and final loop of a 80 mm^2 contact, (b) predicted initial and final loop based on the same changes in displacement amplitude and coefficient of friction. The initial slopes of the predicted loops were adjusted additionally to correspond to the measured tangential contact stiffness.

The model would also be able to visualize dynamic effects, in which case $m > 0$ and $P \neq N$. Under these conditions the apparent friction decreases at the beginning and the end of a stroke as shown in the figure below. An effect which was also observed on the 80 mm^2 rig.

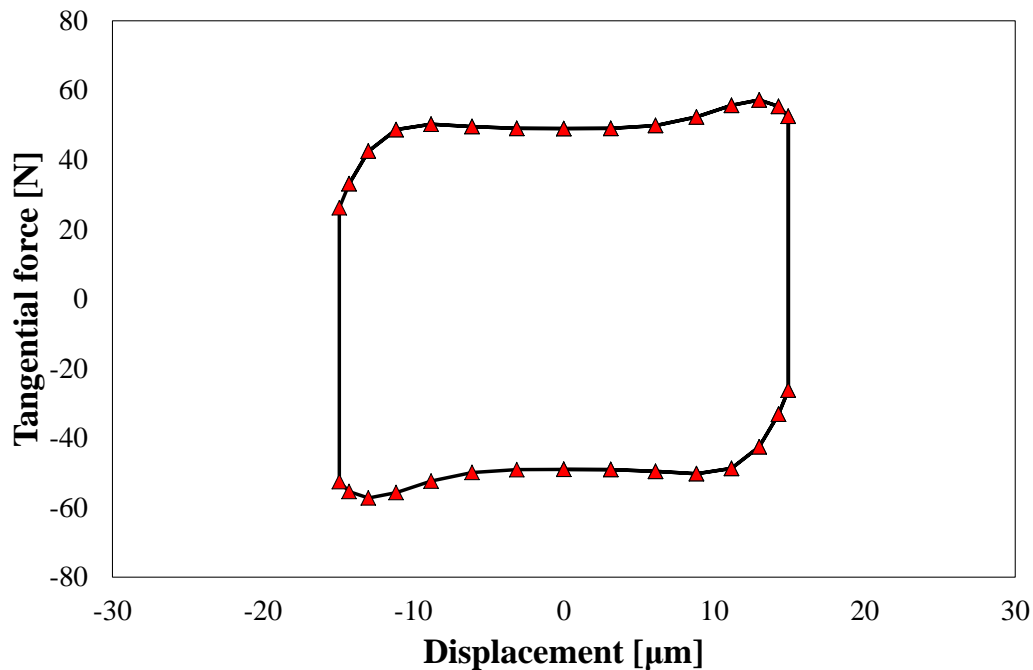


Figure 5-15: Effect of acceleration where m and $n = 4$.

5.3 Nature of the surface degradation

Cross sections of all materials were investigated to gain additional information about the surface and subsurface changes of the contact. All materials showed changes of the chemical constitution of the interface and signs of deformation in the subsurface material.

5.3.1 Oxide layers

The fretting conditions, caused on all materials the formation of an oxide layer. The thickness of the layers differed depending on the individual material. Pressure, testing temperature and test duration seemed to have an effect on the oxide layer as well.

If the contact models overestimate the stiffness, a compliant layer can be introduced to account for the additional needed compliance. The observed oxide layers which if not fully dense could act as the source for the compliance, and if introduced to contact models, needed further characterisation.

5.3.1.1 *Thickness of oxide layer*

The thickness of the layers differed depending on the tested materials. This might be down to various reasons such as the wear behaviour of the materials and the production of debris, the adherence of the compressed layer on to the bulk material and how much of the wear debris was transported out of the contact. However if the layer is acting as a compliant layer, a thinner layer, such as in the case of Udimet 720 would contribute less to the compliance of the contact than the thick layers, such as observed on EN24T and Ti6Al4V.

The reasons for why the layer was not preserved through the preparation of the fretting samples for microscopy are numerous. Many steps were involved in the process such as separation of the specimens, cutting and mounting under pressure which could have caused

the separation of parts of the oxide layer from the bulk material. As the oxide layers appeared quite friable and crumbly this is even more likely. This was a particular problem when trying determining the thickness of the oxide layers over time. The process chosen could not reproduce the measurements.

5.3.1.2 *Chemical composition*

X-ray diffraction was used to characterise the chemical composition of Udimet 720 and Ti6Al4V. The layer on Udimet 720 was found to be NiO. The expected oxides were NiO, Al₂O₃ and Cr₂O₃ whereas according to the selective oxidation process taking place in Ni-based superalloys, NiO would form a top layer with a friable structure. This agreed very well with what has been found on the tested specimens. It is likely that selective oxidation is still taking place under fretting conditions.

The relevant oxides formed on a Ti alloy are TiO₂, Ti₂O₃ and TiO. Due to the reciprocating movement and the resulting wear, the top-layer is continuously removed. This removing process might be in balance with re-healing nature of titanium. Oxide scales on titanium alloys after reciprocating sliding have been shown before in the literature [45] but the chemical composition had not been determined.

5.3.2 Formation of oxide layer

Based on the observations a general discussion can be made about the origin of the formation of the oxide layer. Two processes are suggested, diffusion driven oxidation or mechanical stirring.

Higher temperatures can increase the oxidation process in metals. The following analysis based on equations by Jäger [96, 97] was used to predict the maximum flash and average

temperatures within a square contact for steel specimens to see whether they could be a source for a diffusion driven oxidation.

The value of the Peclet number L_p determines whether the contact moves at low, intermediate or high speed and is defined as follows.

$$L_p = Ua/2\chi \quad (5.13)$$

where U is the velocity of one of the two solids, b is the half width of the square and χ is the thermal diffusivity of the material. For the given conditions the Peclet number is smaller than 0.1 and resembles a low speed case. The following formulas were used to calculate the average and maximum flash temperatures respectively [97].

$$T_{f_{average}} = 0.946 \frac{qb}{\chi} \quad (5.14)$$

$$T_{f_{max}} = 1.112 \frac{qb}{\chi} \quad (5.15)$$

where q is the rate of the heat supply per unit area and defined as follows

$$q = \frac{\mu p_m U}{4b^2} \quad (5.16)$$

where p_m is the nominal average pressure. For fretting conditions as given above where the nominal contact area is assumed as 1 mm^2 , the velocity is given by 5 mm/s , the pressure is 70 MPa the average flash temperature was calculated as 2.27°C and the maximum flash temperature reaches 2.67°C . K the thermal conductivity was given as 46 W/mK . It is unlikely that these low temperatures would significantly support diffusion driven oxidation.

Signs of mechanical stirring have been observed in the cross section images of the worn samples, where parts of the oxide layer were not fully oxidised but consisted of a mixture of

bulk material and oxidised material. A mechanical stirring process is very likely to be the driving process of oxidation in the fretting contacts.

Chapter 6

Infrared energy dissipation

This chapter covers all details related to measuring frictional energy dissipation in a partial slip fretting contact using an infrared temperature mapping system. A brief retrospective introduction shows how the two methods have been used before. Both the HFR test rig and the infrared system were modified to enable temperature mapping. Methods, modifications and testing parameters are described.

6.1 Introduction

The reciprocating friction test rig and an infrared imaging system have been used before separately. The proposed method to map energy dissipation in a fretting contact combines the two systems.

6.1.1 Optical investigation of fretting wear

Baker and Olver [58] optically investigated the fretting wear behaviour of a ball-on-flat arrangement using a High Frequency Reciprocating (HFR) rig. In the original set up, as suggested by the manufacturer of the rig, PCS instruments, a metal ball is rubbed against the flat side of a metal disc which lies beneath. In this study the metal disc was replaced by a sapphire disc and the ball-on-flat arrangement was turned up-side down. This allowed a visual investigation of fretting wear, from above, through the transparent sapphire window.

Videos of the fretting process were recorded through which particle movement and oxidation could be traced.

6.1.2 Infrared temperature mapping

An infrared capturing system was used by Reddyhoff et al. [139] to record temperature maps to study the rheology of elastohydrodynamic contacts. Since energy dissipation is mainly caused by shear and thus friction of the fluid film within a rolling-sliding contact it can be linked to the measured temperature rise.

A ball was in rolling-sliding contact with a sapphire disc, which had been divided in three sections as shown in Figure 6-1. One third of the disc remained uncoated; the second third had been coated with a Cr layer and the last third with an Al layer. The layers were applied on the side of the disc which was in contact with the ball.

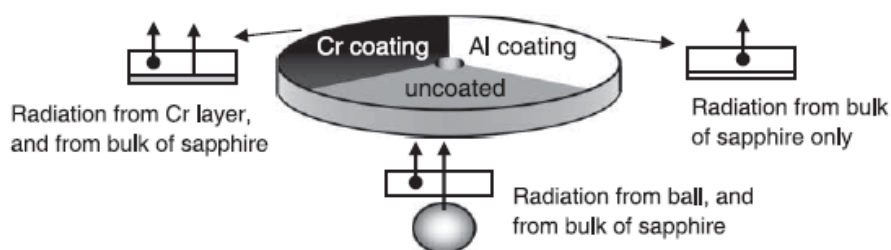


Figure 6-1: Infrared measurement as used by Reddyhoff [139].

The infrared measuring system is placed above the contact and radiation is emitted from the ball surface, from the oil, the sapphire surface and the bulk of the sapphire. The uncoated area was used to measure the temperature of the ball. The Cr coated area was used to measure the temperature of the contacting disc. The Al layer, which is a very low IR emitter, allowed subtracting any unwanted radiation from the bulk of the sapphire. Because the Aluminium

layer tends to wear off easily, emission readings from this sector were taken at several positions about one half Hertz diameter outside of the contact. Calibration was performed in pure rolling. While gradually increasing the temperature, radiation measurements were conducted for each of the three disc section. This resulted in a calibration curve of camera reading (counts) versus temperature.

6.1.3 Proposed combination of techniques

Temperature mapping in fretting contacts combines the HFR rig setup by Baker and Olver [58] with the infrared temperature mapping system by Redyhoff et al. [139]. The infrared system captures a top view of the fretting contact, which allows the temperature mapping within the area of contact. Slight modifications of the HFR rig specimen set up were needed in order to meet the requirements of the infrared measuring system and are described in detail below.

6.2 Methods

6.2.1 High frequency reciprocating rig

The High Frequency Reciprocating (HFR) rig has been widely used in the study of reciprocating and fretting contacts [58, 140]. The standard set up of the rig is shown in Figure 6-2. The upper specimen is loaded against the lower specimen and excited by an oscillating electromagnetic vibrator which is connected to the upper specimen holder via a pushrod. A linear variable differential transformer (LVDT), which is positioned at the front of the vibrator, is connected to the electronic unit of the rig. It monitors the displacement of the excited arm and can adjust the frequency and amplitude of the vibrator. The rig allows

testing in the both the fretting and reciprocating sliding regimes. In order to stiffen the system and to increase the accuracy of measurements below 100 μm the fretting flexure lock must be screwed into the housing. The upper specimen, normally a 6 mm diameter steel ball, is mounted in the upper specimen holder. A rod which is connected to the specimen holder provides the attachment points for a dead load. Two pins secure alignment between the sample holder and the pushrod. A M3 socket head cap screw keeps the holder in place. The standard lower specimen is a 3 mm high and 10 mm diameter disc and is clamped into a little recess of the lower specimen holder. If desired, the sample holder can be filled with a lubricant. The sample holder is mounted to the rig with two M3 socket head cap screws. A piezoelectric force transducer measures the friction force between the two specimens during sliding. Platinum resistance temperature devices are available to measure the ambient temperature.

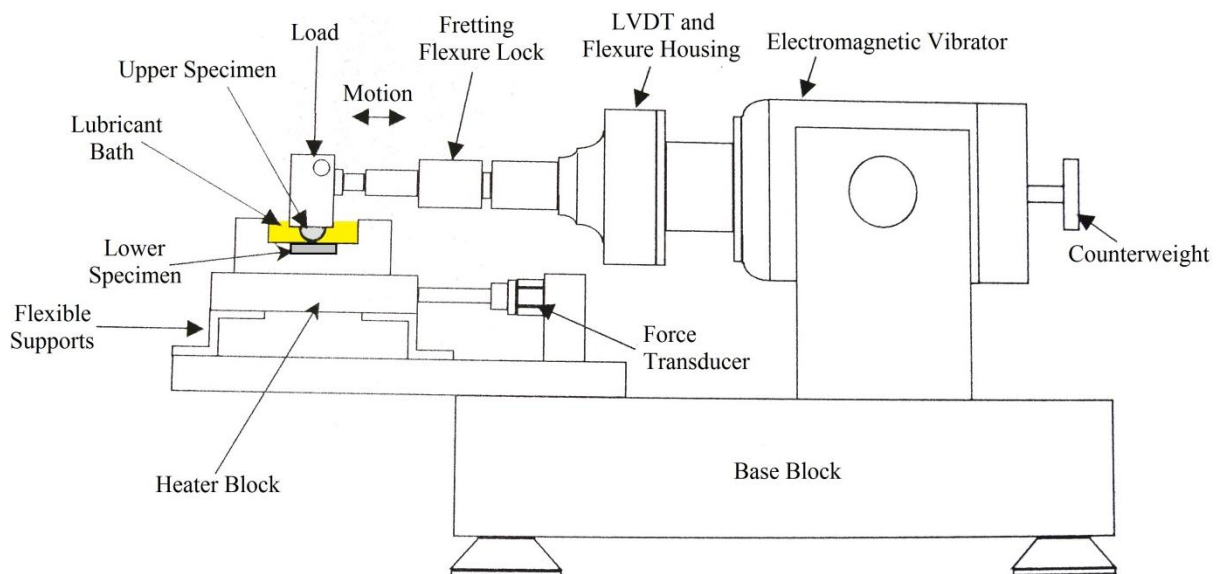


Figure 6-2: Schematic drawing of general HFR rig set up [140].

A PC, which is connected to the rig, controls and stores all instrument functions using provided software tools. It generates frequency signals for the vibrator and processes

temperature, force, LVDT and signals from the force transducer. The range of standard test parameters is shown in the table below.

Table 6-1: Standard parameter range of HFR rig.

Stroke length (0 to peak)	20 μm – 2 mm
Frequency of oscillations	20 Hz – 200 Hz
Applied load	100-1000 g
Time intervals	1 minute steps
Temperature	up to 200°C

6.2.1.1 Modifications of HFR rig

Both, the upper and lower specimen holder were replaced by newly designed holders. Technical drawings of the specimen holders are shown in the Appendix. The upper specimen holder could now hold a 4 mm high and 10 mm diameter sapphire disc. The bottom specimen, a 6 mm diameter steel ball is mounted in the new bottom specimen holder. A cross section of the holders with mounted specimens is shown in Figure 6-3. The table below shows the specifications of the specimen. Two bars were attached to the left and right of upper specimen holder where a dead weight was attached for loading. The maximum loading of the rig was limited by the manufacturer to 1000 g, but, because it was the aim to cause partial slip conditions, loads up to 1200 g were applied. The design of the specimen holders allowed the discs, and balls, to be re-used for several measurements. All specimens were cleaned before and after tests in isopropanol in an ultrasonic bath.

Table 6-2: Dimensions and material properties of specimens.

	Lower specimen – Ball	Upper specimen – Disc
Material	Steel (AISI 52100)	Sapphire (Al_2O_3)
Dimensions [mm]	$\phi 6$	$\phi 10$ 4 (thickness)
Young's Modulus E [GPa]	210	345
Poisson's ratio ν	0.3	0.25
Yield strength σ_y [MPa]	2034	1900
Thermal diffusivity χ [$10^{-6} \text{ m}^2/\text{s}$]	13.93	8.00
Thermal conductivity K [W/mK]	46	24
Roughness R_a	50 nm	2 nm

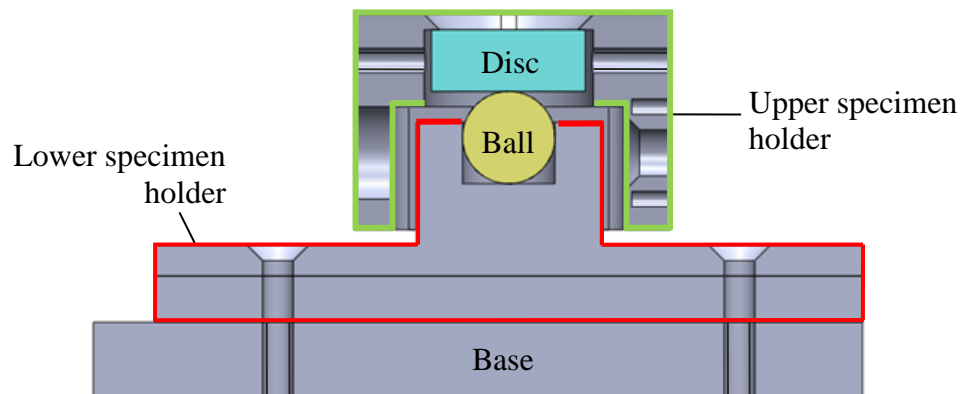


Figure 6-3: Cross section of sapphire disc and steel ball mounted in new sample holders.

6.2.2 Infrared measurement

The same infrared camera system was employed as in [139]. The InSb detector of the camera is sensitive to IR radiation of a wavelength from 3 μm to 5 μm . The 320x256 elements focal plane array of the camera was combined with an objective lens, which is limited to a maximum magnification of 5x due to the divergence limit of IR radiation. This results in a resolution of 6.3 $\mu\text{m}/\text{pixel}$.

6.2.2.1 *Modifications of the infrared system*

The camera is placed on top of the loaded contact, formed between the mounted specimens in the HFR rig. According to Hertz, the ball-on-flat arrangement, with the above given geometry and material specifications, forms a 107 μm diameter circular contact when loaded with 1000g. 18x18 temperature readings were possible within the Hertzian contact area, as shown in Figure 6-4 (a) with the given resolution. Each temperature measurement covered a 2.016 x 1.606 mm rectangular area but which was subsequently cropped during the data processing routine. The sapphire discs remained either completely uncoated or one side was completely coated with a Cr layer as shown in Figure 6-4 (b).

Uncoated discs were used to measure the radiation from the ball. Coated discs were used to measure the radiation from the disc. The Cr coating had a thickness of 120 nm and had been applied using an ion sputtering technique. The Cr coating presented full opaqueness to the IR beam. Figure 6-4 (b) shows how the incident infrared beam is reflected from a coated disc. One part is reflected from the Cr layer, which represents the contact interface. A second, smaller part is reflected from the bulk.

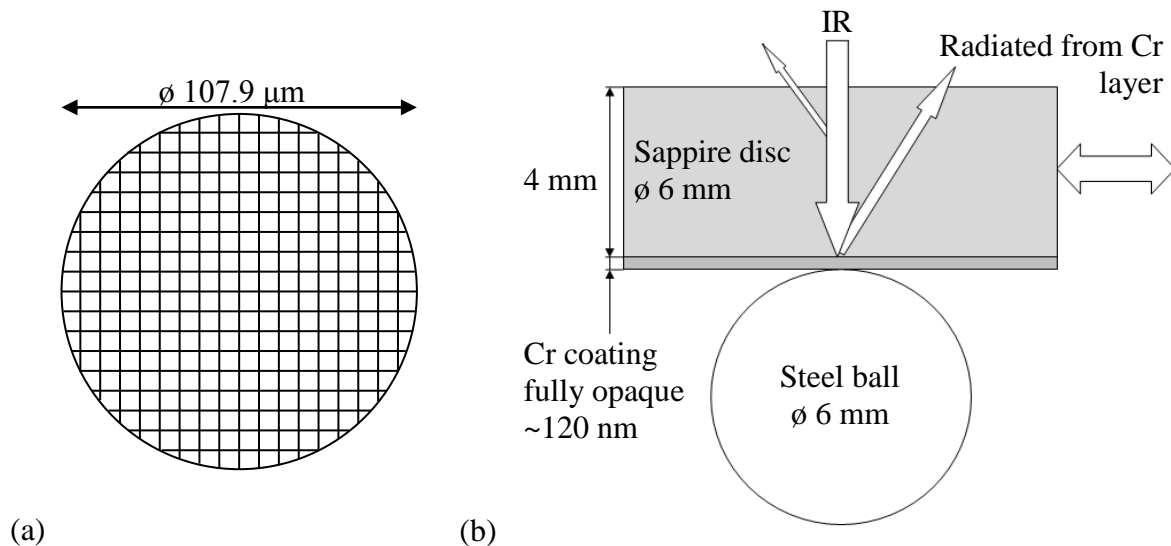


Figure 6-4: (a) Hertzian contact area, when loaded with 1 kg, with measuring grid, where one square equals one pixel of $6.3 \times 6.3 \mu\text{m}$.

6.2.3 Testing methodology

The HFR rig and the infrared camera were positioned on two separate tables in order to avoid vibrations and to keep the image of the contact as stationary as possible. A complete arrangement of the testing equipment is shown in Figure 6-5. The infrared camera was mounted to a stage which was horizontally and vertically controlled by an x-, y- and z-stage. The base of the bottom stage was clamped to the table. A foam mat, placed underneath decreased further vibrations. The objective, which was attached to the camera as shown in Figure 6-5, was roughly aligned with the contact using the x-, y- and z-stage. A foam cushion was wedged between the objective and the stage to dampen any vibrations of the long objective.

The precise alignment of the camera with the centre of the contact was achieved by using an uncoated sapphire disc under loaded conditions. The radiation reflected from the curvature of the ball creates circular fringes. At the middle of those fringes lies the centre of the contact.

The z-stage is used to set the focus on the contact area, which leads to approximately a 5 mm distance between the objective and the specimen holder. To allow enough space to exchange the uncoated for a coated disc, the camera system was moved from the contact along the y-axis for a recorded distance and moved back again.

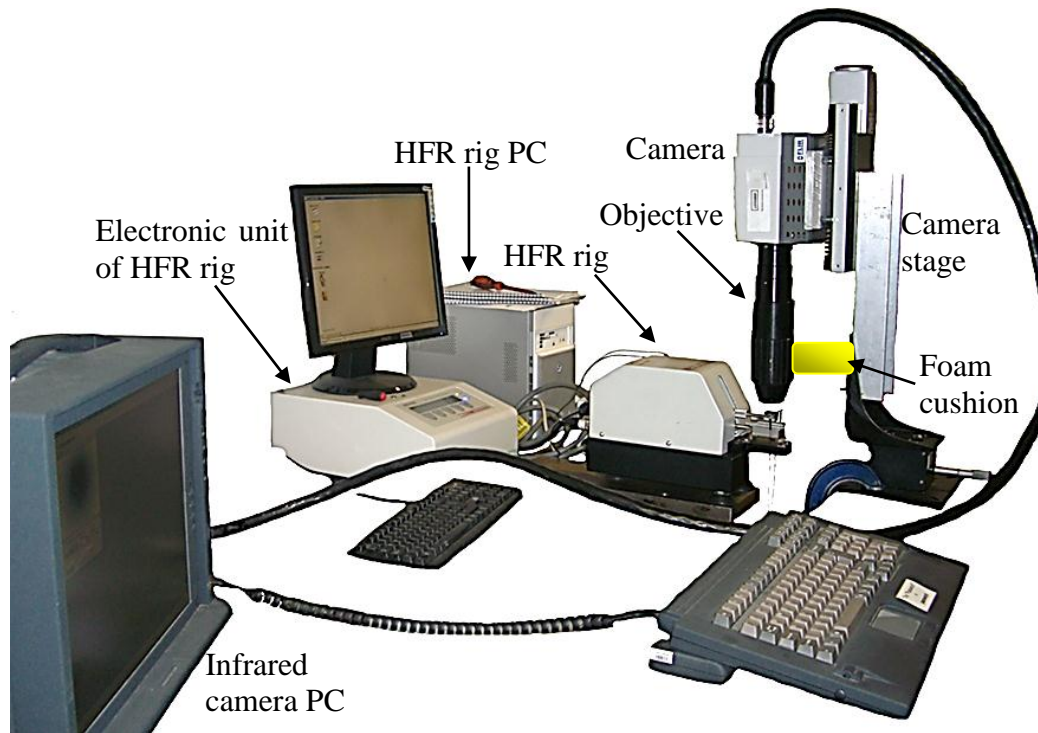


Figure 6-5: Testing arrangement.

Data was acquired under three different conditions for each test. First, the loading was removed and one data acquisition of the unloaded and stationary contact was performed. This can be useful when considering the deformation effect due to the loading. Second, data was acquired of the loaded and stationary contact. Finally the fretting test is started and data is acquired every 2 seconds. Each separate data acquisition contains 100 frames. The integration time (exposure time) of the camera was set to 4 ms for all tests. Previous to each measurement a NUC, non-uniformity correction, was performed.

The conversion of camera readings (counts) into temperature data was done using data kindly provided by Reddyhoff et al. [139]. The data had been originally obtained from pure rolling tests under lubricated conditions, where the oil was gradually heated up to increase the temperature at the contact. From this a calibration curve of counts versus contact temperature could be obtained as shown in Figure 6-6. Data was only available for 2 ms and 6 ms integration times and an approximate conversion value lying in between was used for 4 ms. The calibration factor for Cr-coated disc was 114 and 106 for uncoated discs.

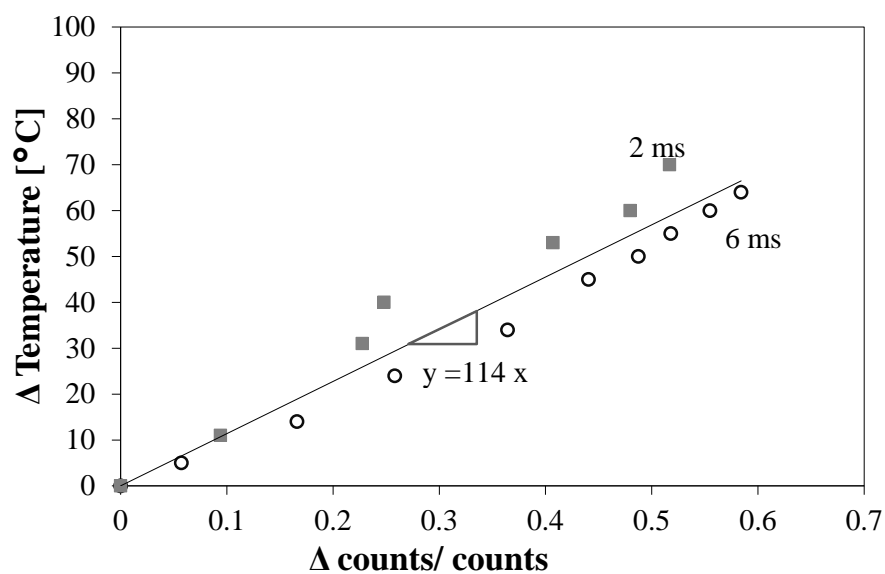


Figure 6-6: Derivation of conversion parameter from kindly provided data [139].

6.2.4 Data processing

The radiation counts are saved in data files which can be accessed as binary 16bit image data and subsequently modified via a mathematics program such as Matlab. The routine in Matlab was based on codes kindly provided by [139]. Each acquisition array contains all 100 frames. Each dynamic data acquisition is dealt with separately. The program reads in the frames of the dynamic acquisition, the related static acquisition and the corresponding NUC files. All one hundred frames of both the static and dynamic acquisition are averaged to one frame

each. The averaged frames are then corrected by the NUC. The static and the dynamic array were then minimized to a 100 x 100 pixels square (630 x 630 μm) in which centre the contact was located. The dynamic array, from which the static array was subtracted, was finally multiplied by the calibration factor given above. This procedure resulted in an array which contains the temperature difference ΔT for each point of the contact and its neighbourhood.

6.2.5 Specimen surface characterisation

The Wyko NT9100 profiler, as described in Chapter 3, Section 3.2.2.1, was used to characterise initial roughness and post-test damage. Because of their smoothness, the measurements of the undamaged discs were performed in the phase shift interferometry (PSI) mode of the profiler. The PSI mode uses a filtered light source, which has a nominal wavelength of 633 nm, and calculates the surface heights based on the intensity variations. The PSI mode is limited to a maximum roughness peak difference of 160 nm ($\frac{1}{4}$ of a wavelength) and has a vertical resolution of less than 0.1 nm.

Chapter 7

Infrared energy dissipation – Results and discussion

This chapter presents the results obtained with the newly introduced infrared temperature mapping system. The study assumed that the temperature rise distribution in a partial slip contact correlates with the position of maximum energy dissipation. Little research has been done to directly measure the energy dissipation in terms of temperature rise and the results will fill this gap. Various predicted energy dissipation maps have been proposed in the literature and a comparison of predicted and measured maps follows.

7.1 Adjustment of test settings

The HFR rig was originally designed for gross slip fretting and reciprocal sliding tests. Various settings had to be tried out to achieve partial slip conditions. For all tests the frequency was kept to 100 Hz which mirrored the conditions in Chapters 3 to 5. Whether a contact experienced stick, partial or gross slip conditions, was initially determined after each test by characterising the wear scars of ball and disc.

A contact which experienced mostly stick conditions is shown in Figure 7-1 (a). The contact was subjected to a 1200 g load and a 20 μm stroke length. The wear scar which was observed on the ball was circular and only minor wear appeared at the circumference of the area of contact. No part of the area of contact slid for the set length of stroke. The diameter of the thin worn circle equaled the initial contact area and roughly the expected Hertzian diameter

of contact, which was 115 μm for the given load. No temperature rise was expected to be seen under these contact conditions. The corresponding wear scar of the coated disc is shown in Figure 7-1 (b). It revealed that the contact slipped at one point during the test. Two thin annuli were observed which had the same diameter as the wear scar of the ball. But other than that the contact remained at both positions stuck. At both times a thin annulus had been affected.

The wear scars of ball and disc shown in Figure 7-1 (c) and (d) infer that the contact experienced mostly partial slip conditions. A 1000 g load and a 100 μm stroke length were applied to obtain these wear scar. The annulus of slip of the wear scar of the ball is somewhat interrupted due to wear but nonetheless distinguishable as a round groove. The contact area had remained circular but grew in diameter compared to the initial diameter of the Hertzian contact, which was 107 μm for the given load. In a theoretical model of a contact in partial slip, the centre area is only elastically deformed and does not experience any slip. However, the partial slip contacts investigated here have all experienced gross slip at some point during the test duration. This caused minor wear within the stick area. The wear scars obtained from the coated disc was not as clear as its counterparts. The measured profiles presented a circular affected area but did not have a distinguishable stick or slip zone. The surface profile appeared raised rather than worn. In order to clarify if this was an artefact due to the sapphire or the coating, the worn surface was coated with a very thin layer of gold, as used for the preparation of SEM samples. The measured troughs and peaks remained the same after being coated; therefore the additional height was real and must have accumulated due to material transfer from the steel surface on to the disc.

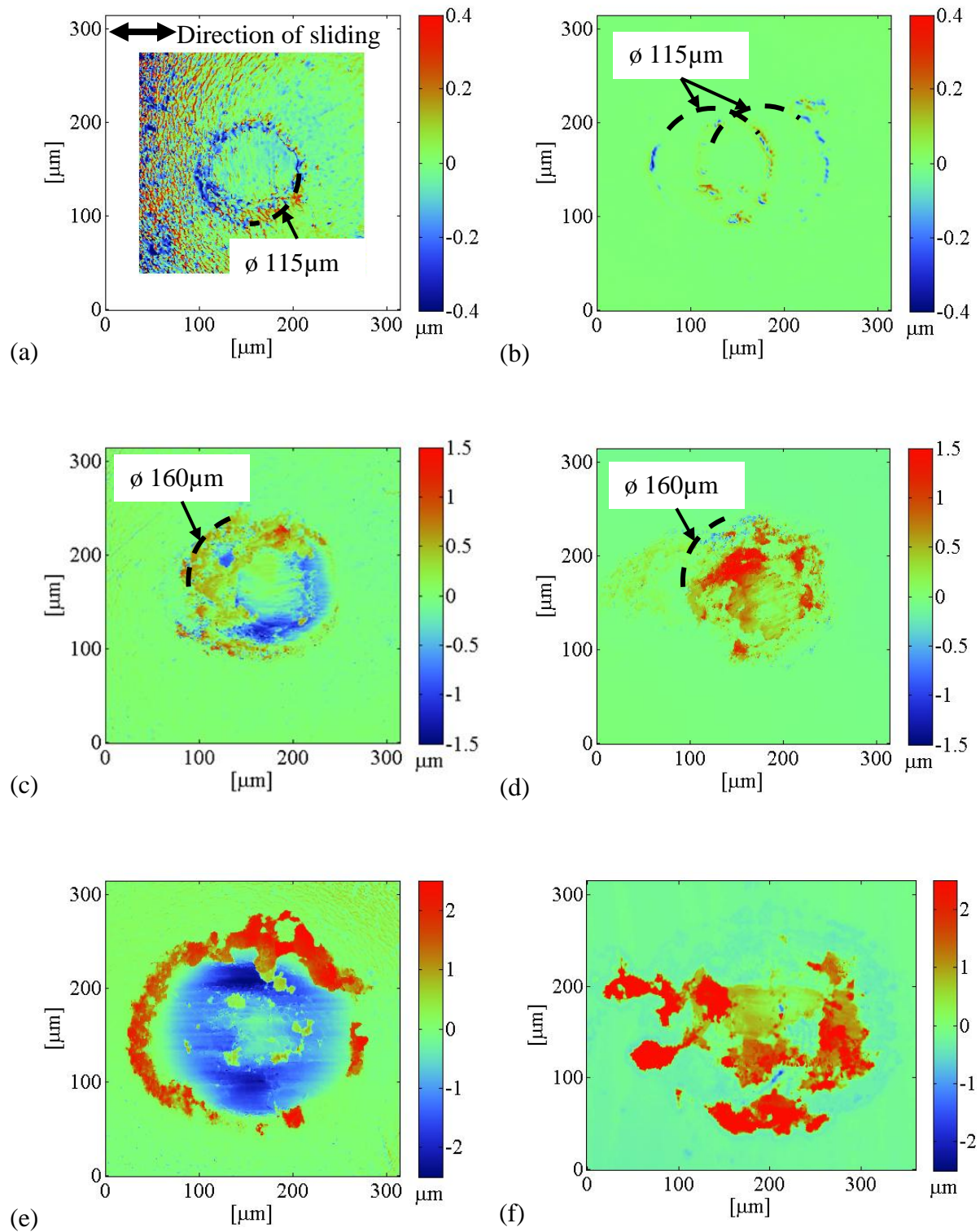















Figure 7-1: Fretting damage as observed for different fretting regimes. (a) ball and (b) disc stuck, (c) ball and (d) disc in partial slip and (e) ball and (f) disc in gross slip.

The wear scars shown in Figure 7-1 (e) and (f), respectively for ball and disc, were measured on specimens which experienced mostly gross slip. The test was conducted under the same loading and stroke length conditions as the previous example, but the observed wear scars were oval shaped and elongated in the direction of sliding. Whilst there was still a trace of a slip and stick zone in the wear scar of the ball, which suggests that the contact was at one point in partial slip, the wear scar on the disc is elongated and clearly inferred gross slip.

Table 7-1 shows a summary of conditions under which mostly partial slip was achieved. By reducing the stroke length and increasing the load, the likelihood of partial slip was increased. But the combination of maximum load and minimum stroke length led to a contact which was fully stuck, as expected.

Table 7-1: Stuck , partial slip , and gross slip  conditions were achieved with the following combinations of load and stroke length.

		Maximal Stroke length [μm] (0-peak)			
		20	50	100	200
Load [g]	900			 	
	1000			 	
	1200				

7.2 Test results from coated discs

The following results were obtained applying a 1000 g load and a 50 μm stroke length for one minute. The results were representative of other tests carried out under similar conditions. The wear scars on both ball and disc appeared circular and agreed with the theoretical idea of a partial slip contact. The wear scar of the ball, as shown in Figure 7-2 (a), displayed a stick zone which spanned a circular area of diameter of 116 μm and a slip annulus which reached a diameter of 189 μm . The diameter of the annulus had grown from the initial 107 μm diameter Hertzian contact to roughly twice the size.

Figure 7-2 (b) shows a height profile of a cross-section through the centre of the wear profile. It was oriented parallel to the direction of sliding and the profile outside the contact had been levelled to zero. The maximum depth of the slip annulus reached 2.5 μm beneath the unworn surface level. Grinding marks inside the stick zone in the direction of sliding showed that the contact was not in partial slip for the entire length of the fretting test and the fretting wear had appeared over the whole contact. Wear debris was found piled up mostly outside of the contact. The wear scar on the disc is shown in Figure 7-2 (b) and shows circular affected area. The profile is raised which must have been caused by material transfer triggered by adhesion. A cross section of the profile is shown beneath.

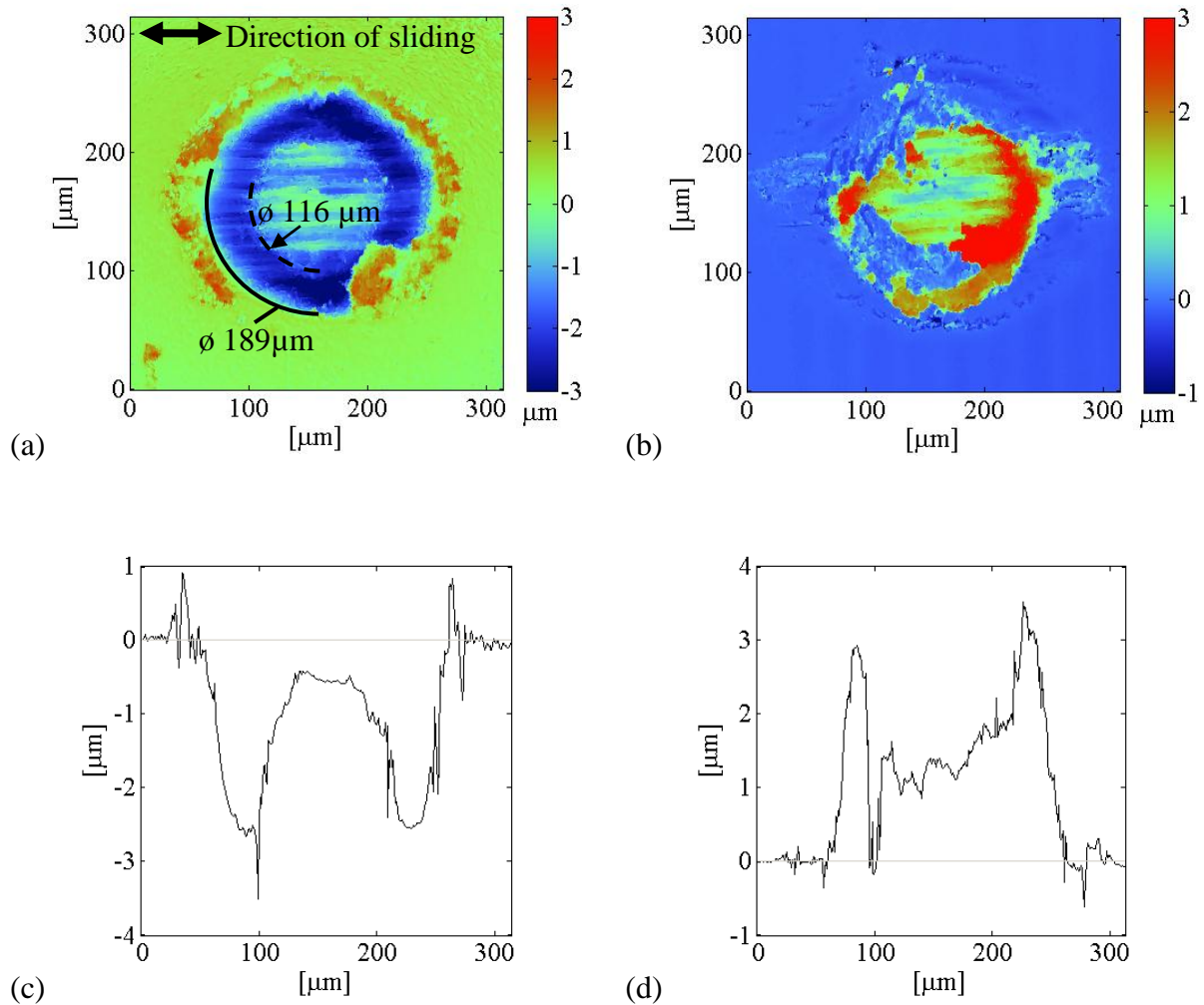


Figure 7-2: Surface profiles of worn (a) ball and (b) disc and corresponding cross sections (c) and (d).

The images presented in Figure 7-3 show the same $315 \times 315 \mu\text{m}$ section of the total recorded area, featuring the contact area in the centre. The maps show the temperature increase, ΔT , where the dark blue areas indicate no temperature increase and dark red areas show a maximum temperature increase of up to 8.6°C . First signs of a temperature increase were detected halfway through the test, as seen in Figure 7-3 (a). The area of temperature rise was sickle shaped, positioned around the centre of the contact and extending perpendicular to the direction of friction. After 40 seconds, the temperature reading appeared blurred, as shown in Figure 7-3 (b). The sickle shaped temperature rise appeared doubled on each side, which is

more clearly seen at the right of the contact as indicated. The contact must have moved and the radiation was captured at two positions during the acquisition. This movement indicates that the contact left the partial slip regime and operated in the gross slip regime. The contact returned again into partial slip conditions, as the last recorded temperature map in Figure 7-3 (c) shows. The last map shows the temperature rise recorded 5 minutes after the fretting excitation had been stopped. Temperatures have dropped by around 2°C within this time.

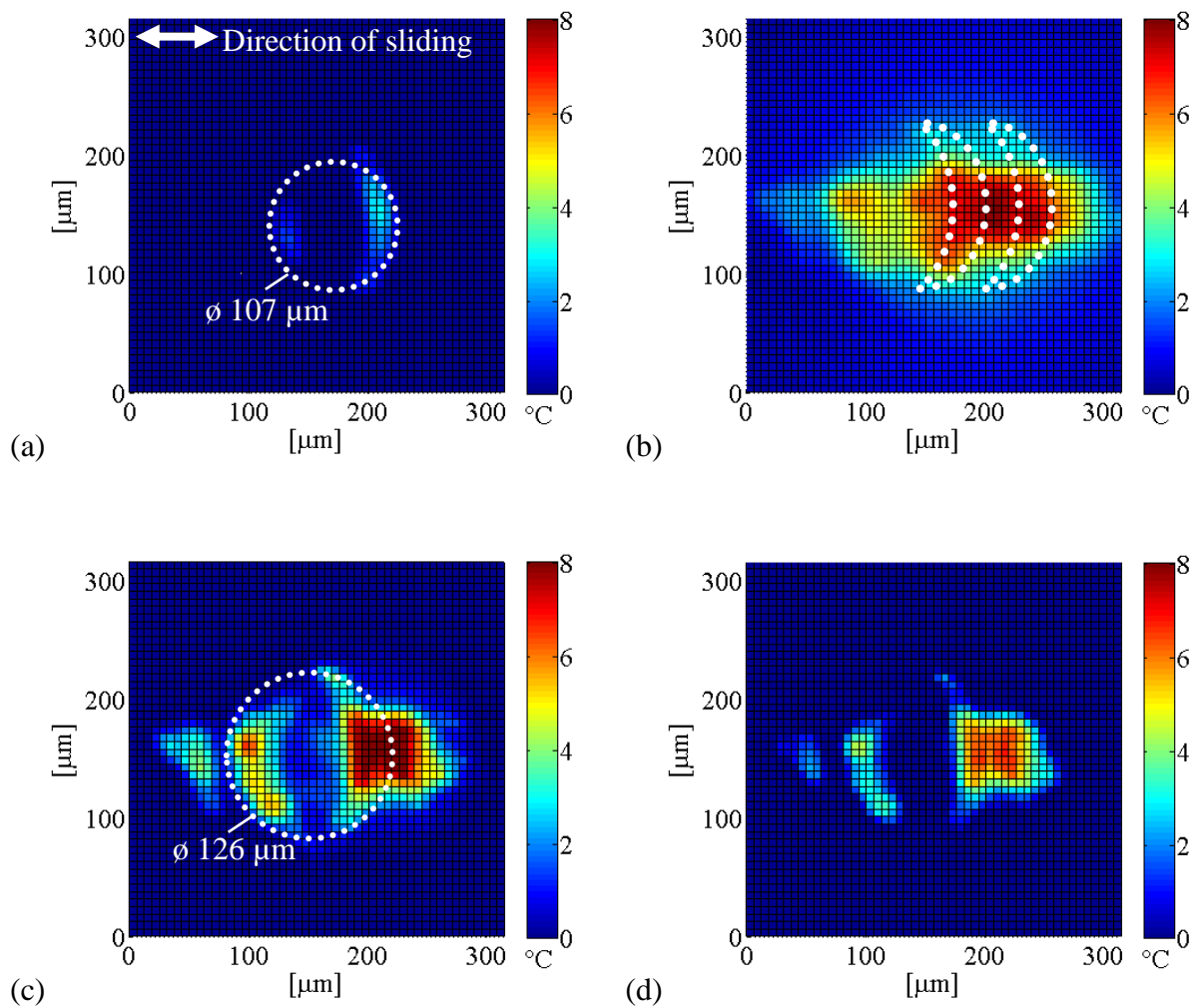


Figure 7-3: Temperature increase maps ΔT maps after (a) 30 seconds, (b) 40 seconds, (c) 1 minute and (d) 5 minutes after test has finished. The radius of contact is indicated in (a) and (c). The moving sickle shaped maxima of the contact in gross slip are indicated.

If the Cr-coating had been scratched during the test than the removal of it would have laid bare the sapphire disc beneath it. Sapphire has a higher emissivity and would appear 'hotter' in the temperature maps. Consulting the wear profiles of the disc in Figure 7-2 (b) and (d) removed this concern because there were no scratches corresponding to the positions of the maximum temperature rise. Uncertainties whether such bare sapphire would also cause an artificial profile for the vertical scanning interferometry had already been addressed by an applied gold film.

Figure 7-4 below compares the fretting condition of the contact, as deduced from ΔT maps, with the frictional behaviour and the maximum temperature rise in the contact. In the first period of the test (0 to 26 seconds) no radiation could be detected. The maximum temperature rise stayed on a constant level just below 0. The fact that it was not zero (or above) indicated the limitations in accuracy of the method. The coefficient of friction rose steadily during this period. As the rig is displacement controlled and designed for gross slip, the rig kept on increasing the excitation force in order to reach this regime, which resulted in an equally increasing coefficient of friction for as long as the contact remained stuck. The lack of a temperature rise during this period of time supports that the contact was indeed stuck.

In the second stage of the test (26-36 seconds) an increase of radiation is detected and its distribution showed that the contact operated in the partial slip regime. The value of the maximum temperature rise started increasing and by the end of this phase reached a value of 8°C. The coefficient of friction continued its rise. The rig had increased the tangential force above the threshold to cause slip inside the contact. The coefficient of friction further rose, as gross slip was aimed for – at least by the rig.

A period of gross slip followed (36-44 seconds) in which the coefficient of friction reached its maximum at 1.2 and started to drop again at point (b). With the transition from partial to

gross slip, the maximum temperature rise stopped its sharp increase and climbed only slightly above 8°C.

The contact returned into the partial slip regime in the last stage of the test. The coefficient of friction dropped to 1.0 but rose again to a final value of 1.1 by the time the test was stopped. The temperature rise reached its maximum value of 8.6°C and stayed at a value just over 8°C. As soon as the test was stopped, the temperature started decreasing. After 5 minutes the maximum temperature rise had dropped by 2°C.

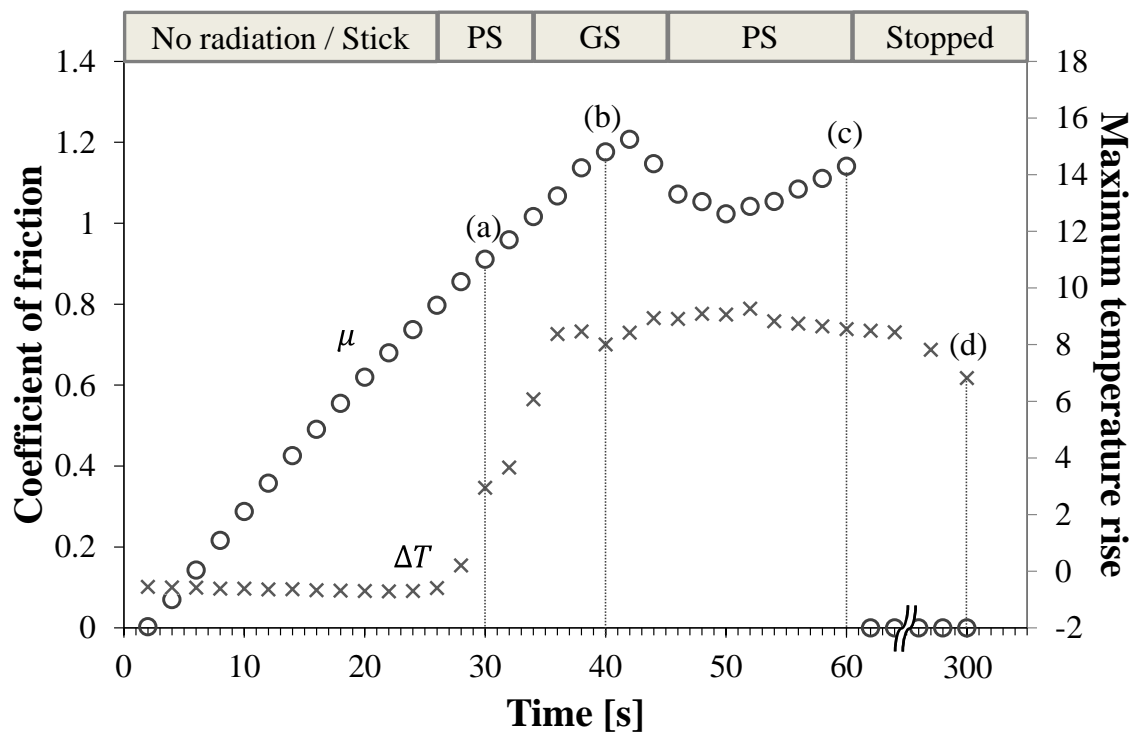


Figure 7-4: Comparison of fretting regime, frictional behaviour of contact and maximum temperature rise during a test. (PS – partial slip, GS – gross slip).

7.3 Test results from an uncoated disc

The following results were obtained applying a 1000 g load and a 100 μm stroke length for one minute. The results were representative of other tests carried out under similar conditions. The wear scars on the ball appeared circular, but the disc also showed clear signs of gross slip. From the tests results discussed in the previous section it is clear that the specimen must have gone through the partial slip regime due to the settings of the rig. Results were examined accordingly.

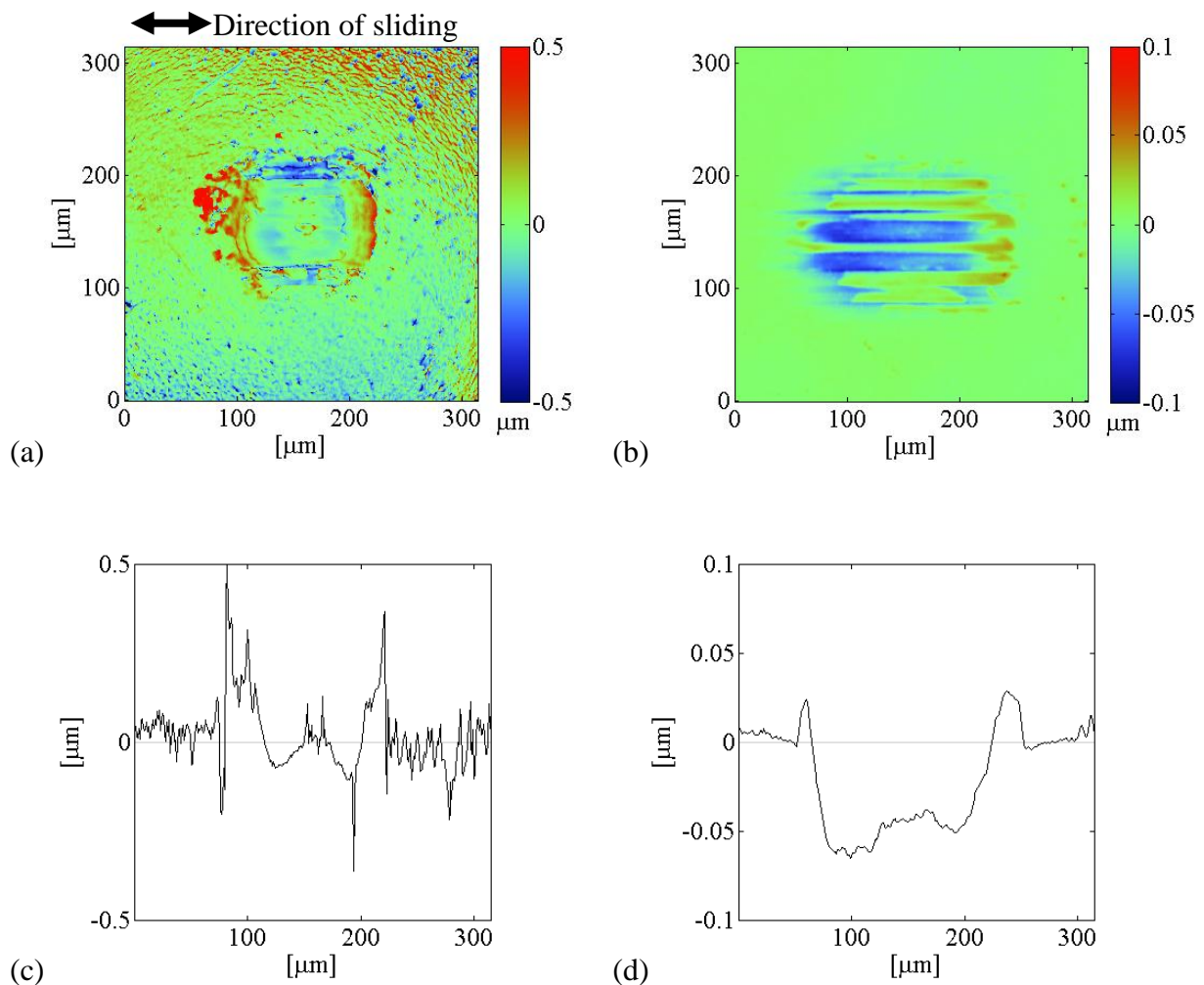


Figure 7-5: Surface profiles of (a) coated disc and (b) ball after test.

The corresponding temperature maps are shown in Figure 7-6. Due to the transparency of the disc, the curvature of the ball produced circular fringes. The contact was found at the centre of the fringes. Within seconds, as seen in Figure 7-6 (a), a sickle shaped temperature rise was observed within the contact. A temperature rise in the right hand top corner however had to be attributed to an irregularity of the surface, possibly a small scratch.

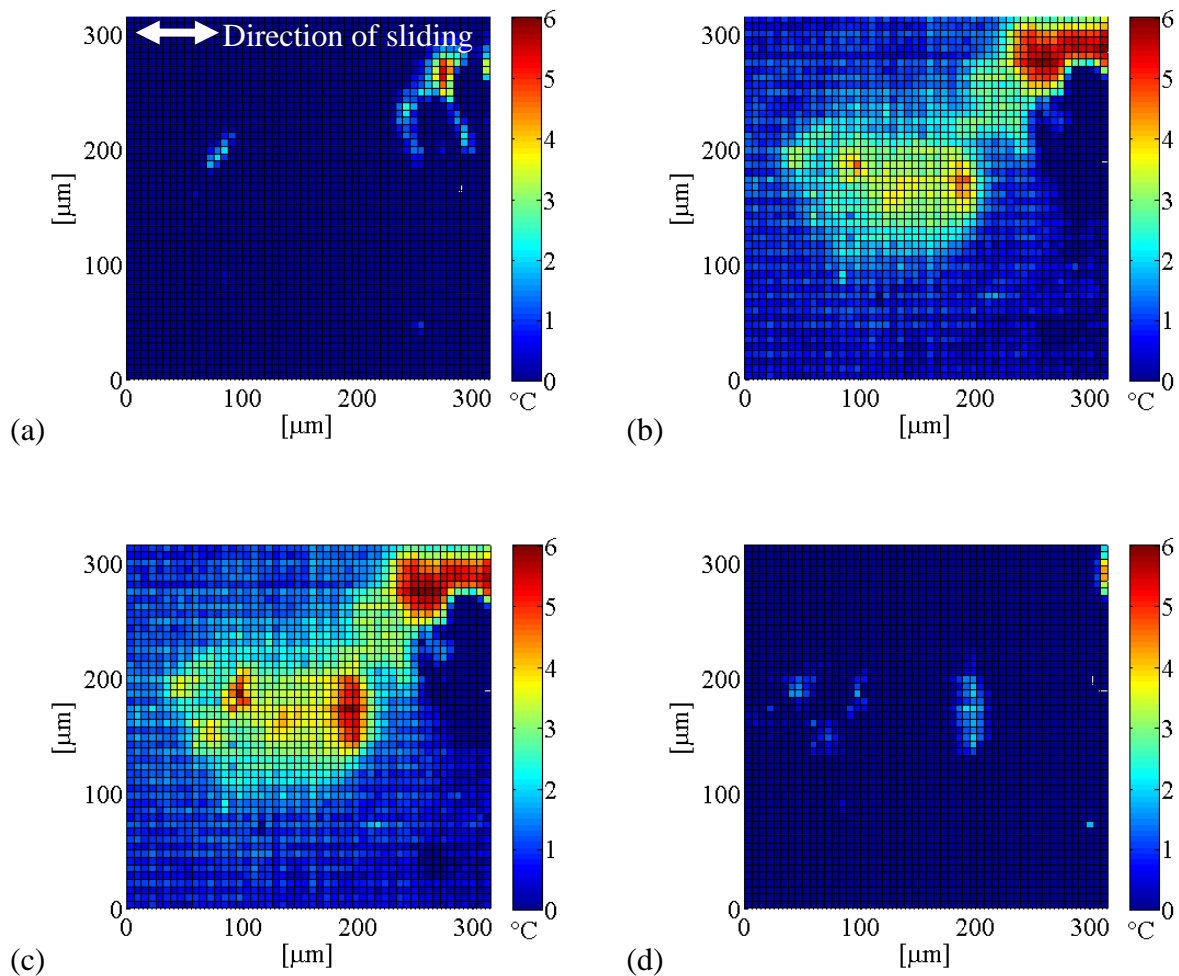


Figure 7-6: Radiation maps after 4 seconds, 34 seconds, 1 minute and 30 seconds after the test had finished.

Halfway through the test, the temperature rise was no longer localised and the whole area of contact appeared heated up. The temperature rise started to drop immediately after the test had been stopped and reached a value of 2.0°C after 30 seconds.

Attention must be also drawn to the scratch in the right hand corner. Radiation is falsely emitted from it and showing a non-existent temperature rise. This scratch and any other irregularity on the surfaces, which includes the curvature of the ball cause additional interference and corrupt the measurement.

Figure 7-7 shows a comparison of the coefficient of friction and the maximum temperature rise. Similar behaviour was observed as for tests carried out with a coated disc. However the contact appeared to be in the partial slip regime right from the beginning. The temperature rise gradually increased over the whole span of the test. Temperature rise readings were possible right from the beginning, which suggests that the contact had been in partial or gross slip from right at the beginning. The temperature rise curve between second 6 and second 18 followed the trend of the coefficient of friction. A steep rise in the coefficient of friction suggested that the rig was trying to reach the gross slip regime. After second 20 the coefficient of friction was nearly stable at a value just over 0.8. This suggests that the contact performed in the gross slip regime for the rest of the testing period. The maximum temperature rise within the contact increased further. It reached its maximum at the end of the test with a value of 6.1°C. The temperature rise was observed over the whole area of contact. After the test was stopped the maximum temperature rise of the contact immediately dropped by 4°C.

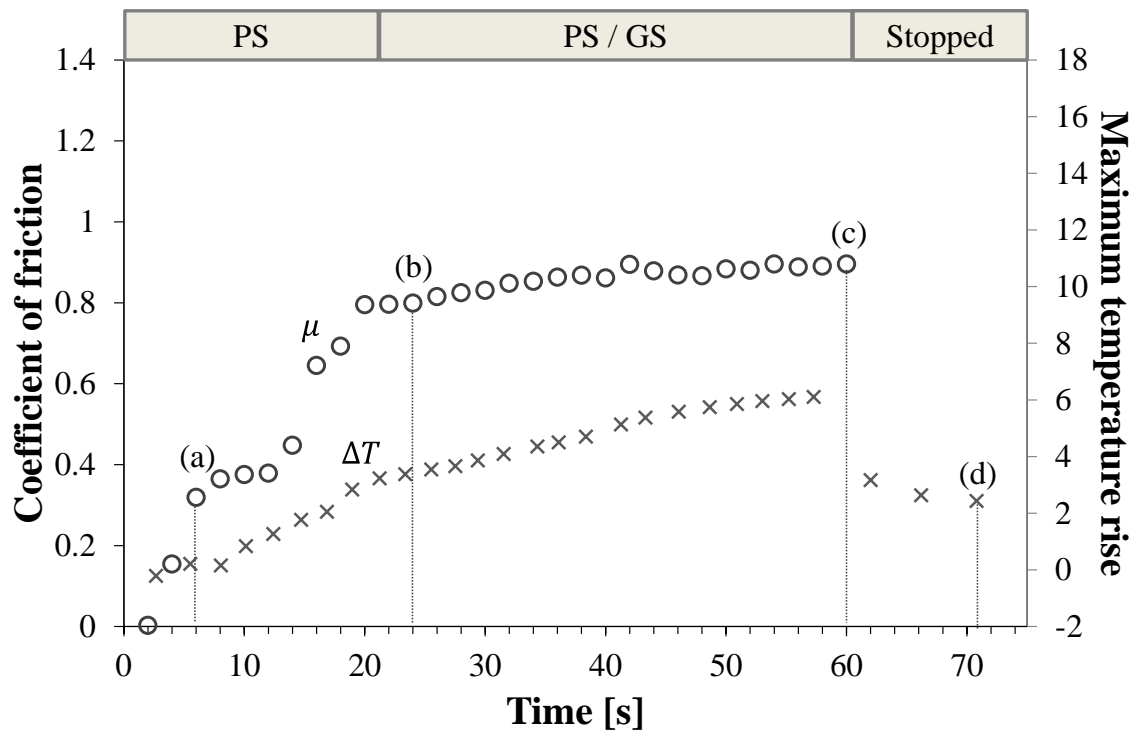


Figure 7-7: Comparison of fretting regime, frictional behaviour of contact and maximum temperature rise during a test. (PS – partial slip, GS – gross slip).

The tests on uncoated discs were initially performed with the intention of correcting the measurements from the Cr-coated discs, by the amount of radiation from the bulk of the disc, as explained in Chapter 6. This could not be done, as with the current test settings the tests were not repetitive enough. Even though the measurements with the uncoated discs lacked in clarity due to additional interference, the results confirmed the findings of the coated tests.

7.4 Distribution of temperature rise – A comparison to contact models

In a fretting contact the dissipated energy due to friction is expected to cause a temperature rise. This experimental study was based on the assumption that distribution of the temperature rise would match with the distribution of the dissipated energy. For partial slip

the measured temperature maps showed temperature rise maxima in the direction of sliding, which displayed a characteristic sickle shape. This shape should be mirrored in predictions of energy dissipation plots produced by various contact models. Three of these contact models were considered below and compared with the experimental results.

The solution by Mindlin [15] for the dissipated energy over a circular contact is shown in Figure 7-8 (a). The solution does not show any circumferential variation of the dissipated energy. The axial distribution of dissipated energy, as shown in Figure 7-8 (b) is the same all the way around.

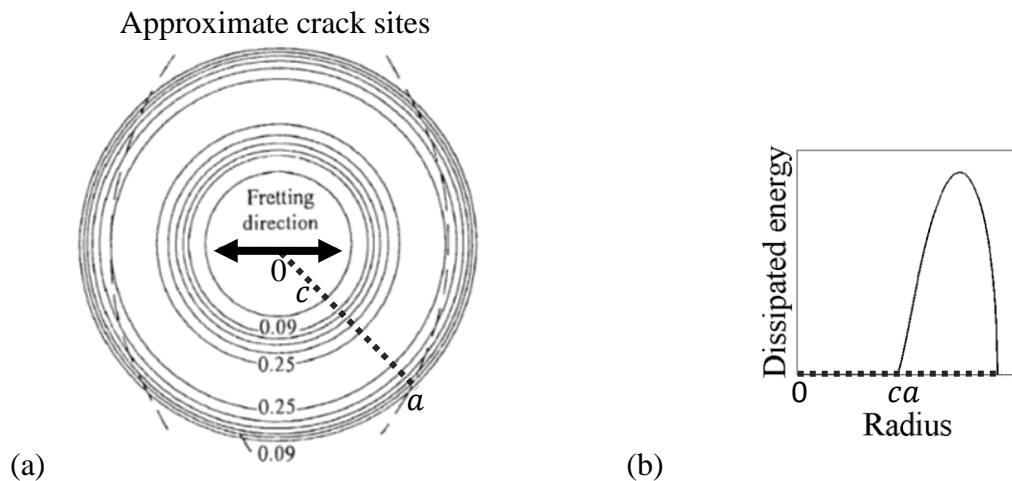


Figure 7-8: (a) Solution by Mindlin for the distribution of dissipated energy within a Hertzian contact [92]. (b) Cross section at a random angle of Mindlin's solution.

It has long been well known that Mindlin's solution was not fully correct as it did not take the effect of the Poisson's ratio into account [92]. Figure 7-9 (a) shows the solution for the dissipated energy within a smooth contact, as given by a numerical contact model by Munisamy et al. [141] which overcame this omission. This distribution shows sickle shaped maxima of dissipated energy. But instead of a perpendicular orientation to the direction of sliding, the maxima lie parallel to it. This paper related the maximum energy dissipation to

the sites of crack nucleation and Ruiz et al. [142] continued to argue that for crack nucleation in-plane stresses must play a crucial part. The authors went on to propose a crack initiation parameter which was the product of the stresses and the dissipated energy at each point of the contact. A map of this parameter is shown in Figure 7-9 (b). The distribution of the parameter is similar to the initial energy dissipation distribution but rotated by 90° . However the distribution is now comparable to the maximum temperature rise maps obtained from the experiments. Nevertheless the authors found the justification of the multiplication of the energy dissipation by the in-plane stresses arbitrary.

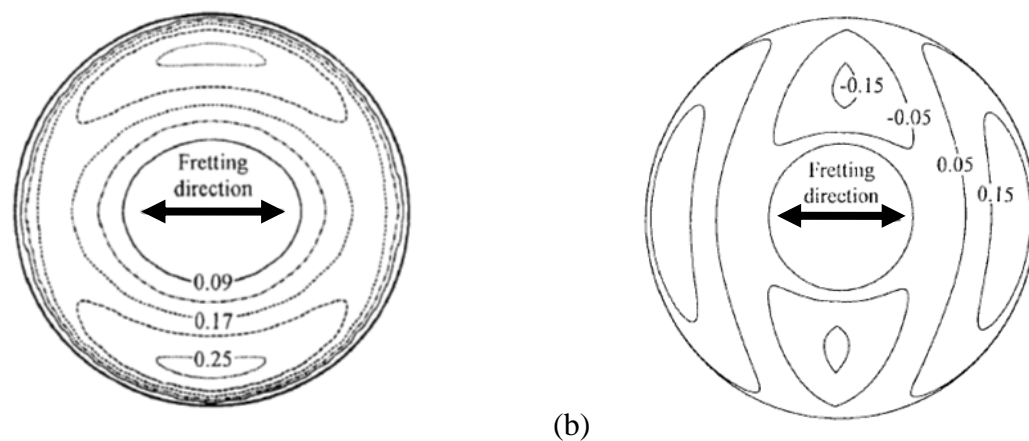


Figure 7-9: (a) Energy dissipation as predicted by an analytical model presented by Nowell and Hills [92]. (b) Variation of the Ruiz initiation parameter over a circular contact.

A more recent model by Medina et al. [93] used a numerical model based on a multi-level multi integration approach to calculate the tractions and subsequently the energy dissipation in a contact of rough surfaces. The solution of the tangential shear tractions employed the theory of Ciavarella [143] and Jäger [144].

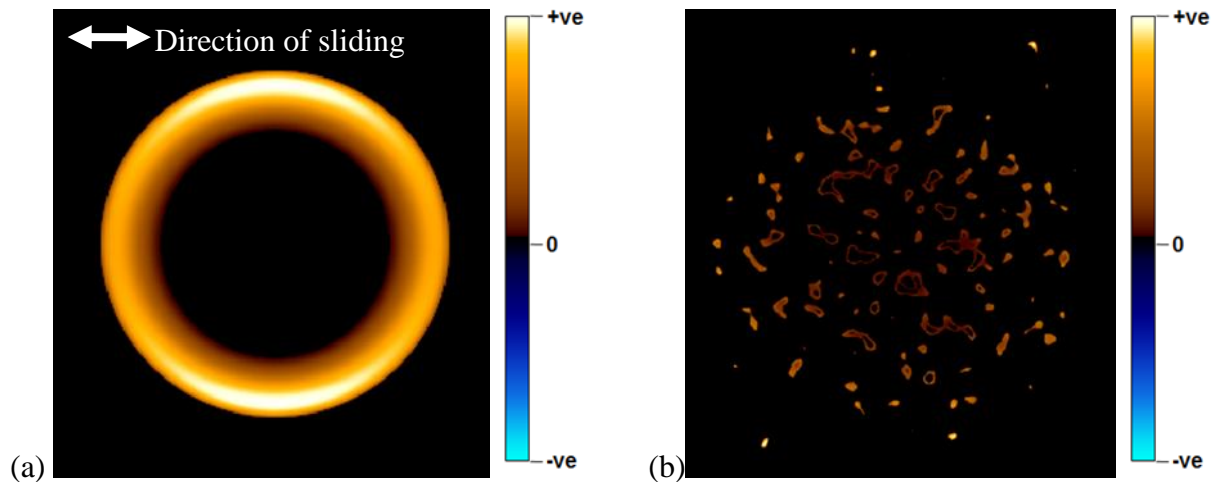


Figure 7-10: (a) Predicted energy dissipation using a numerical contact model, for (a) a smooth and (b) a rough circular contact, as shown by Medina [93].

The predicted energy dissipation map for a smooth contact, as shown in Figure 7-10 (a), is similar to the one shown by Munisamy [141]. The maxima lie parallel to the direction of friction. Figure 7-10 (b) shows the prediction for a rough surface. Whereas it is not as clearly visible from the plot shown here, the maxima lie in the same direction as for the smooth contact, a gradual change in roughness confirms that the position does not change by 90° .

None of these models predict the energy dissipation maxima in the direction of sliding. Whereas Mindlin [15] does not show a variation of energy dissipation in the circumferential direction at all, the maxima predicted by Nowell and Hills [92] and Medina et al. [93] lie parallel to the direction of sliding rather than perpendicular to it. Therefore the disagreement between the prediction of the available models and the experimental results must lie in the differences between the assumptions in the model and the experimental conditions.

In the experiment the energy dissipated in the fretting contact was thought to result in an increase of temperature. The distribution of the temperature rise was expected to be related to the distribution of energy dissipation. But not all of the dissipated energy is turned into heat

but wear as well as cracking, even if not observed here, have been reported for these conditions. The models do not take into account the change of geometry. In the experiment the contact area grows and the wear debris penetrates the surface surrounding the initial contact. Due to the change in the profile and the design of the rig the contacts undergo both partial slip and gross slip conditions during different stages of testing.

Additionally, none of the above models considered the Cr layer used in this experiment. But since both, coated and uncoated experiments showed the maxima of energy dissipation arise in the same regions the presence of the layer was of less importance for this comparison.

7.5 Discussion of the technique

The presented method provides a tool to map the maximum temperature rise and compares it to the dissipated energy within a contact in partial slip. Both uncoated and Cr-coated discs have been tested. The initial thought was to correct the radiation obtained from the coated discs by the radiation emitted by the uncoated discs, as proposed by Reddyhoff et. al [139]. However, the radiation maps obtained from experiments with uncoated discs caused additional interference, in and around the contact, which distorted the measurements and the correction was abandoned.

Previous methods to study fretting did not offer the opportunity to study the change of the contact while the test is still running. The typical investigation of a fretting sample is post-testing and is a static investigation. The infrared radiation measurement offers a dynamic investigation. The maps of maximum temperature rise enabled a distinction of the partial and gross slip regime, and the method allowed one to study the fretting regime history of a contact.

If the investigation of the partial slip regime is of importance the current set up can be improved by performing similar tests on a rig which had been designed for partial slip or which could be operated under force controlled conditions.

The improvement over previous methods which had employed infrared radiation to study fretting contacts [101] was the direct measurement of the temperature within the contact rather than the heat flux into the material.

Chapter 8

Discussion

This chapter reviews the results and main achievements of the current work. The chapter intends to address the initial aims of the project posted in Chapter 1 and 2 and to analyse to what extent they have been accomplished. Where insufficient data was gathered to contribute to open questions, a discussion of the reasons is given and a proposal of how those questions can be tackled in the future.

8.1 Review of conducted work and results

Fretting tests were conducted in order to collect results which could be used in dynamic models and to gather data for comparison with contact models. The tests were conducted on four different materials (Ti6Al4V, Udimet 720, EN24T and stainless steel) at two different pressures (45 MPa and 70 MPa). Friction loops were recorded and the tangential contact stiffness and the coefficient of friction were determined. The nominal area of contact used in the experiments was 1 mm² but results from 80 mm² contacts were provided by collaborators for comparison.

The experimental results showed that the bulk material properties did not show a significant effect on the coefficient of friction but did affect the tangential contact stiffness when keeping the normal load constant. An increase in normal load did not necessarily mean an increase of

the tangential contact stiffness; Udimet 720 and stainless steel showed an apparent effect, whereas Ti6Al4V and EN24T did not.

Elastic contact models predicted a rapid increase of the stiffness with low normal loads. At high normal loads the predicted stiffness reached a plateau which was limited by the material properties. A comparison of the predicted stiffness values with the 1 mm^2 experimental results suggested that the measured data represented different parts of the predicted curves. Udimet 720 and stainless steel were still in the load-dependent region. EN24T and Ti6Al4V had already reached the load independent zone.

Predictions used fixed roughness values. The stiffness of smoother surfaces in contact is higher than of rougher contacts in the load-dependent region. However, the roughness under experimental conditions changed and the correlation between the surfaces evolved over time. This contributed to an effectively smoother composite roughness of the contact.

Tangential contact stiffness values obtained from a larger contact area, 80 mm^2 , were significantly higher than these measured on a smaller contact area 1 mm^2 . Experimental results suggested that the stiffness varies in proportion to the area of contact. In contact models this proportionality only applied to the low load region, whereas at high loads the stiffness behaved in proportion to the square root of the contact area. However this only applied for the chosen nominal contact geometry. In the current model a ball was in contact with a semi-infinite half plane whereas two finite bodies were in contact in the experiments.

It was shown that the distance between the reference points at which the displacement measurements were taken had a significant effect on the stiffness values. The stiffness increased with decreasing measurement distance to the interface, but not linearly as suggested by literature [145].

It was shown that the assumption of an interface layer between the two surfaces could introduce extra compliance to the contact. On the other hand, the conformity between the two surfaces could move the load at which maximum contact stiffness is reached to lower values, as observed on 1 mm² EN24T contacts and 80 mm² contacts. Conformity effectively reduces the composite roughness of the two surfaces and so increases the gradient of the asperity controlled stiffness asymptote as shown in Figure 5-5 (b).

X-ray diffraction, light and electron microscopy were used to characterise the worn interface. All specimens developed a significant layer of metal oxide. The change of the topography was studied on surface profiles measured with interferometric instruments. Cross correlation was employed to study the evolution of conformity (Figure 4-12) and metallography was used to monitor the development of surface oxide layers (Figure 4-21). The oxidation appeared to be driven by mechanical deformation arising from the interacting rough surfaces (mechanical stirring) rather than by thermal diffusion of oxygen. Since the bulk material properties seemed to have little or negligible influence on the frictional properties, it is possible that those of the oxide layer control the surface behaviour.

An infrared temperature mapping system was successfully employed to record the temperature change within a fretting contact. Based on the assumption that the dissipated energy in a contact would mirror the temperature rise in a contact, a reciprocating rig was modified to measure the temperature. The comparison of the temperature maps with predicted energy dissipation maps showed that the respective maxima were 90° rotated from each other. Possible explanations for this included the change of contact conditions, wear and debris formation in the contact.

8.2 Initial objectives of the project

The 1 mm² area of contact friction rig has been used in the past to measure the coefficient of friction and the tangential contact stiffness to be used in dynamic models of frictional joints [128]. In finite element models the contact area of joints were divided into elements. The measured coefficient of friction and the tangential contact stiffness were then applied to each element and the model would predict the dynamic behaviour depending on the frictional properties assigned. Three questions of particular interest arose regarding this procedure:

- Was the procedure of applying the measured friction properties to elements of different sizes of area correct?
- Could the experimental tests which are used to determine the frictional properties be avoided by predicting the frictional properties with elastic contact models?
- Could the dissipated energy be predicted using an elastic contact model?

During experimental measurements the frictional properties showed a time-dependent behaviour. The values which had been used for the dynamic prediction were measured 15 minutes after the test was started and when the values had stabilised. From this procedure two further questions arose.

- What affects the time-dependent behaviour of the friction loop?
- Which processes take place in a real contact?

8.2.1 Experiments vs. predictions: Frictional properties

The work presented here concerned the possibility to replace the experimental evaluation of the coefficient of friction and the tangential contact stiffness by values predicted by contact models. This is of particular interest as experiments are time and material consuming. Despite

the contact models developed by collaborators, the prediction of the coefficient of friction has not been realised yet. The models were restricted to Coulomb friction behaviour and rather uninteresting in the gross slip part of the predicted loop. Only the tangential contact stiffness could be truly predicted. Therefore the current project mainly focused on whether the predicted values of the tangential stiffness would match and could be used in the dynamic models.

8.2.1.1 Contact area

The comparison of the 1 mm² and the 80 mm² tests was used to assess the validity of the practice of applying the measured friction properties on individual elements in the dynamic model. This methodology is based on the belief that the contact stiffness is linearly proportional to the area of contact. Based on experimental results this seemed to be the appropriate normalisation for the stiffness values but theoretically the normalisation was dependent on the load regime. At low loads the predicted stiffness behaves proportional to the area of contact, at high loads proportional to the square root of the area of contact but both only applies for the contact geometry considered in the contact model. It would not be possible to apply this differentiation on experimental results. The procedure of applying the frictional properties to individual elements of the contact in a finite element seems to be acceptable from an experimental perspective.

8.2.1.2 Use of tangential contact stiffness in dynamic models

Analytical as well as numerical models were provided by collaborators to model the contact between smooth and rough surfaces. The results of the 1 mm² area of contact rig showed surprisingly good agreement with the predicted values. If at all the experimental contact was slightly more compliant, which could be explained with the presence of a compliant layer. Experimental and predicted stiffness values did not agree for the 80 mm² where the models

underestimated the experimental stiffness for reasons which could be explained by their neglect of conformity (see section 5.1.2).

Nonetheless it is crucial to predict the contact stiffness accurately. If the correct shape of the frequency response function (FRF) is unknown, very little or no energy might be dissipated in the contact. Figure 8-1 below illustrates the effect of wrongly predicted tangential contact stiffness values. Figure 8-1 (a) shows the FRFs of a single degree of freedom system, (b), for different contact stiffness values [120].

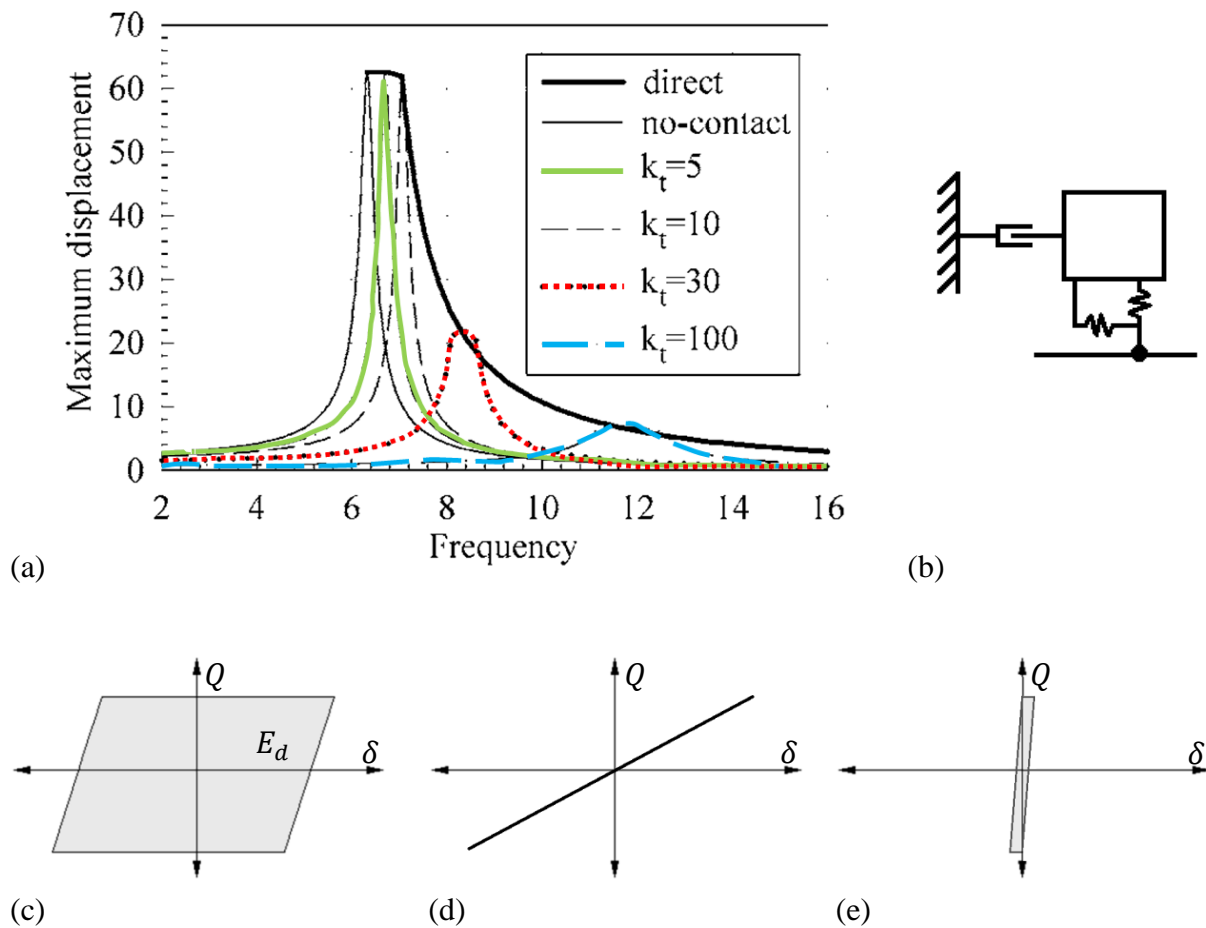


Figure 8-1: (a) Predicted frequency response curves of (b) a single degree of freedom system [120], and friction loops for different stiffness and displacement conditions (b), (c) and (d).

A change in stiffness causes an amplitude shift as well as a frequency shift of the resonance frequency of the system. If damping is wanted energy must be dissipated in the contact for which Figure 8-1 (c) shows the ideal friction loop. The loops in (d) and (e) illustrate cases where a forcing frequency was chosen which due to a wrongly predicted FRF would cause undesirable conditions. If the frequency response curve for a very compliant contact is predicted wrongly and the system is run at a high maximum displacement, as shown in Figure 8-1 (d), no slip will occur. Therefore also no energy is dissipated in the contact and the joint has no damping effect. Similar conditions are caused if a very stiff system is excited at frequency causing very little displacement as shown in Figure 8-1 (e).

The examples showed the influence of the tangential contact stiffness and the consequence of an incorrect frequency response curve. The incorrect stiffness would lead to an erroneous value of the natural frequency. Hence, the response would be entirely wrongly predicted.

8.2.2 Experiments vs. predictions: Dissipated energy

An infrared temperature mapping technique was employed to measure the radiated heat of a partial slip contact and to see whether it correlated with the maxima of a dissipated energy map predicted by the contact model. In this case no comparison of actual values of the same unit was possible but simply a comparison of the location of eventual maxima. The temperature maps showed maxima, however they were at different positions to the dissipated energy maps. Explanations included wear and debris production within the contact as discussed in Chapter 7.

8.2.3 Experiments vs. predictions: Summary of main differences

The two techniques which were employed to validate different parameters predicted by elastic contact models differed significantly from the contact model conditions. Especially the

complementary characterisation of the worn specimens highlighted the differences between the contact model and the real contact. The presence of plastic deformation, material transformation, a compacted oxide layer and increased surface conformity were revealed. This adds a number of parameters which might need to be considered in one way or another in a more accurate contact model.

Differences between the contact models and the experiments are summarised in Table 8-1. These points seem to be the determining factors why the experimental values deviate from the predictions. In fact with the presence of the layer of compacted and partly oxidised wear debris between the bodies the experiments might measure the behaviour of something completely different from that modelled.

Table 8-1: Main differences between contact models and experiments.

Prediction	vs.	Experiment
elastic deformation		elastic and plastic deformation
semi-infinite half plane		finite body
rigid body support		test rig of finite stiffness
parallel surfaces		specimens which can tilt and misalign
time independent		time dependent
two body contact		three body contact
homogenous material		oxide layer
combined roughness		two rough surfaces
fixed roughness		evolving roughness

8.2.4 Time dependent behaviour of the contact

The experiments to measure the frictional properties were run for 15 minutes as this time has previously proved to be sufficient to stabilize the values of the coefficient of friction and the tangential contact stiffness. It was successfully shown that the wear scar geometry can have a significant effect on the measured friction loop.

The investigation of the contacts after the tests was very useful in helping to understand the formation mechanism of the oxide layers but the knowledge gathered was still not sufficient to fully characterise the oxide layer. The study provided further insight in the chemical composition of the layer for Ti6Al4V and Udimet 720. The measurement of thickness of the layers was less conclusive and suggested that the sample handling caused detachment of some of the layers.

8.3 Application of findings to frictional joints

Chapter 1 pointed out the importance of this project to aero-engines applications, but joints are omni-present in mechanical structures and important for any industry dealing with mechanical structures e.g. automotive, power plants, marine industry. Ewins [146] presented a roadmap, shown in Figure 8-2, which illustrated different points of interest which could lead towards a better understanding of frictional joints and wear. Some of these points, highlighted in green, were addressed in this work.

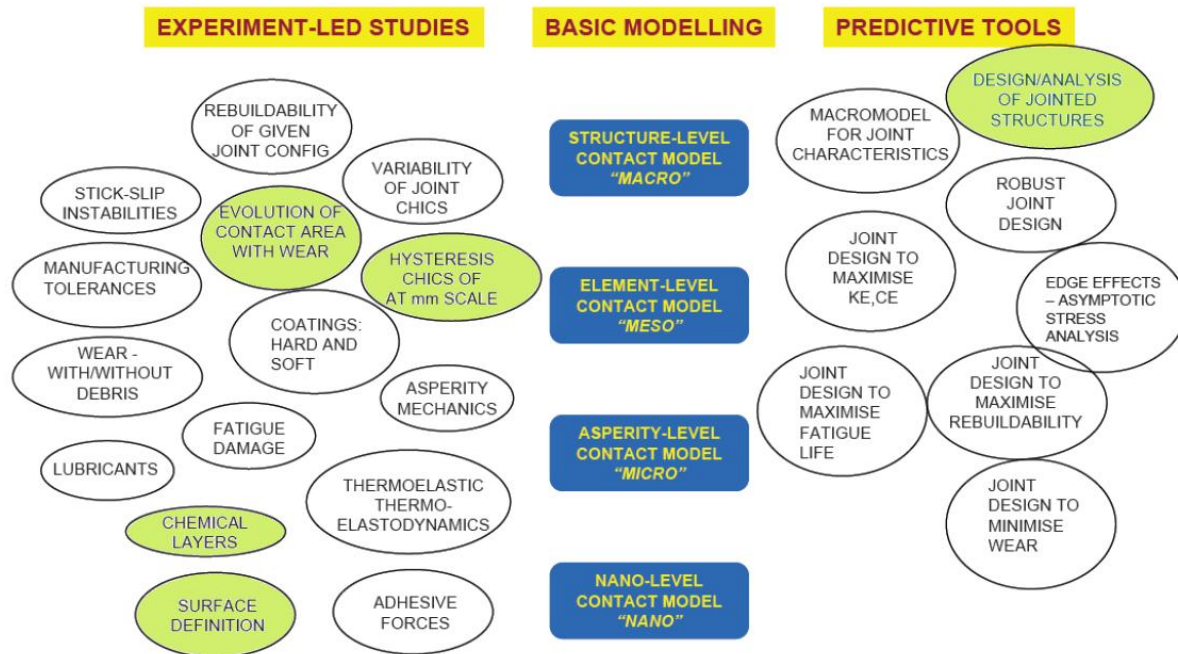


Figure 8-2: Roadmap for research for friction contact and wear in structures adapted from Ewins [146]. Topics to which the current work contributed are highlighted green.

8.3.1 Evolution of contact area with wear

The project contributed towards this point by recording the evolution of the wear scar for different testing time intervals. An analysis of the conformity between two contacts followed. It showed that the conformity increased over time which had direct influence on the contact stiffness.

8.3.2 Hysteresis characteristics at mm scale

The proposed wear scar interaction model in combination with the analysis of the two different rigs attempted to explain different shapes of the hysteresis loops. It successfully showed how different wear scar geometries affected the hysteresis loop. This also contributed towards the previous point.

8.3.3 Chemical layers

The project characterised the chemical composition for Ti6Al4V and Udimet 720 as well as the thickness of the oxide layers of these two materials as well as EN24T and stainless steel under specific conditions. The work also characterised the deformed subsurface layer using electron microscopy to show the effect of the fretting conditions on the material. An explanation for the mechanism of oxide formation was given and mechanical stirring for tests performed at room temperature was considered.

8.3.4 Surface definition

The project studied the effect of roughness and showed that the initial surface definition in terms of roughness had changed within seconds of the start of the test. On the other hand conformity increased between the two surfaces with time leading to an effective reduction in the composite roughness.

8.3.5 Design/Analysis of jointed structures

The generation of tangential contact stiffness and coefficient of friction results provided data which could be immediately used in dynamic models. However, the data could also be used to validate predictive contact models. This helped to point out where the predictive tools need improvement and if successful could make experiments unnecessary.

8.4 Suggested improvements and future work

The road map by Ewins [146] shown in the previous section offers many other points for a continuation of this project and to work towards the goal of understanding frictional joints better. However immediate points for future work are shown below.

8.4.1 Friction test conditions

A wide range of conditions needs to be studied to gain more understanding about the influence of contacts on the friction and damping behaviour. This includes

- wider range of contact areas
- wider range of loads
- elevated temperatures
- controlled amplitudes
- frequencies.

8.4.2 Further characterisation of the compliant layer

The compliant layer, which could be introduced in a contact model for extra compliance, is an approximation for the actual contact region. Part of this region is the formed oxide layer which, if not fully dense and homogenous, will add extra compliance to the contact.

In order to implement such a layer in a contact model it would be necessary to characterise the properties of the oxides fully. The oxide layers must be characterised in terms of material properties, density, and homogeneity and improved techniques must be found to assess the thickness of the layer correctly without the breakup of the layer.

Chapter 9

Conclusions

This chapter presents the main conclusions of this thesis.

9.1 Experimental results

This thesis has presented research concerning the effects of surface topography, surface chemistry, and material properties on the friction, stiffness and temperature distribution behaviour of fretting contacts.

Fretting tests were conducted on four different materials (Ti6Al4V, Udimet 720, EN24T and stainless steel) at two different pressures (45 MPa and 70 MPa). The coefficient of friction and the tangential contact stiffness were extracted from the recorded friction loops. The specimens used formed a nominal area of contact of 1 mm² but results from 80 mm² contacts were provided by collaborators for comparison.

The results of the fretting tests were used to show the influence of the material properties, contact pressures and the area of contact. Further influence of the distance of measurement points to the contact surface was discussed. The experimental results were compared to predictions of half-space elastic contact models. This allowed to validate the predictive models and highlighted points for improvement for better contact models.

Surface profiles were measured using interferometric instruments in order to study the change of topography. Cross correlation was employed to study the evolution of conformity. A wear scar interaction model was introduced to explain the evolution of fretting loops based on the evolution of the wear scar shape. X-ray diffraction, light and electron microscopy were used to characterise the worn interface and to study formed oxide layers. Deformation in the sub-surface layer of fretting specimens was investigated by using electron back scattering diffraction.

The temperature distribution within a fretting contact was successfully measured by modifying a high frequency reciprocating rig. Based on the assumption that the dissipated energy in a contact would mirror the temperature rise the temperature maps were compared with predicted energy dissipation maps.

9.2 Experimental results vs. theories

Comparison of the experimental results with predictions of simple two-body elastic contact models showed major discrepancies between the two.

Large plastic strains were observed in the cross sections of worn samples. This contradicts the basic assumption of contact models considered which only allowed elastic deformation.

Experiments showed an evolving roughness and an increase of conformity between the two surfaces in contact. In contact models the roughness is fixed and no change of the contact geometry is considered, neither can any such change easily be predicted.

The specimens all developed oxide layers during the test. Oxidation changes the material properties and hence differs from those assumed in the models. Further, layers of oxidised

debris of lower density and loose debris were observed. This extra material could be regarded as a third body whereas the contacts in the models only considered two bodies in contact.

The investigation of the oxide layers showed that they consisted of a mixture of metallic material, oxides metal parts and gaps or pores. This inhomogeneity is quite different to the homogeneous material considered in the models.

The measured maxima of temperature in a fretting contact did not correspond to the predicted maxima of dissipated energy.

9.3 Considerations for development of contact models

The elastic theory which is used in the current models has the advantage of being fully understood and being very mature. Some parts of a frictional contact can be explained by using the elastic theory, such as the tangential contact stiffness, but others, such as friction itself, debris production and the transport of debris cannot.

In order to overcome this and to resolve the major discrepancies mentioned above the following points must be considered in coming models:

- oxidation
- evolving roughness and conformity
- third body effects, such as debris
- plasticity and inhomogeneity.

The work presented in this thesis helped to identify the above points which are crucial for improved contact models.

References

1. Panning, L., *Symmetric and Asymmetric Underplatform Dampers for Turbine Blades*. PAMM, 2006. **6**(1): p. 251-252.
2. Thomas, T.R., *Rough Surfaces*. 2nd ed 1999, London: Imperial College Press.
3. Abbott, E.J. and F.A. Firestone, *Specifying surface quality: a method based on accurate measurement and comparison*. Mechanical Engineering, 1933. **55**: p. 569–572.
4. Johnson, K.L., ed. *Contact Mechanics*. 9th ed. 2003, Cambridge University Press.
5. Bhushan, B., ed. *Introduction to Tribology*. 1 ed. 2002, John Wiley and Sons.
6. Sayles, R.S. and T.R. Thomas, *Spatial representation of surface roughness by means of the structure function: A practical alternative to correlation*. Wear, 1977. **42**(2): p. 263-276.
7. Oden, J.T. and J.A.C. Martins, *Models and computational methods for dynamic friction phenomena*. Computer Methods in Applied Mechanics and Engineering, 1985. **52**(1-3): p. 527-634.
8. Bhushan, B., *Contact mechanics of rough surfaces in tribology: multiple asperity contact*. Tribology Letters, 1998. **4**(1): p. 1-35.
9. Hills, D.A., D. Nowell, and A. Sackfield, *Mechanics of elastic contacts* 1993, Oxford: Butterworth-Heinemann.
10. Hertz, H., *Über die Berührung fester elastischer Körper*. J. reine und angewandte Mathematik, 1882a. **93**: p. 156-171.
11. Boussinesq, J., ed. *Application des Potentials à l'étude de l'équilibre et du mouvement des solides élastiques*. 1885, Gauthier-Villars: Paris.
12. Cerruti, V., ed. Mem. fis. mat. 1882, Acc. Lincei: Roma.
13. Love, A.E.H., ed. *A Treatise on the Mathematical Theory of Elasticity*. 4th ed. 1952, University Press: Cambridge.
14. Cattaneo, C., *Sul contatto di due corpi elastic: distribuzione locale degli sforzi*. Academia del Lincei, Rendiconti, 1938. **27**(6): p. 342-348.
15. Mindlin, R.D., *Compliance of elastic bodies in contact*. ASME J App Mech, 1949. **16**: p. 259-268.
16. Johnson, K.L., *Energy dissipation at spherical surfaces in contact transmitting oscillating forces*. Proceedings of the Institution of Mechanical Engineers; Part C; Journal of mechanical engineering science, 1961. **3**(4): p. 362-368.
17. Mindlin, R.D., et al. *Effects of an oscillating tangential force on the contact surfaces of elastic spheres*. in *1st US National Congress of Applied Mechanics*. 1952. New York: ASME.
18. Ödfalk, M. and O. Vingsbo, *An elastic-plastic model for fretting contact*. Wear, 1992. **157**(2): p. 435-444.
19. Bowden, F.P. and D. Tabor, *Mechanism of Metallic Friction*, in *The Friction and Lubrication of Solids* 1950, Clarendon: Oxford p. 90-121.

20. Courtney-Pratt, J.S. and E. Eisner, *The Effect of a Tangential Force on the Contact of Metallic Bodies*. Proceedings of the Royal Society of London. Series A, Mathematical and Physical Sciences, 1957. **Vol. 238, No. 1215**: p. 529-550.
21. Archard, J.F., *Elastic Deformation and the Laws of Friction*. Proceedings of the Royal Society of London. Series A, Mathematical and Physical Sciences 1957. **243**(1233): p. 190-205.
22. Greenwood, J.A. and J.H. Tripp, *The contact of two nominally flat rough surfaces*. Proceedings of the Institution of Mechanical Engineers, 1970. **185**(1970-71): p. 625-633.
23. Greenwood, J.A. and J.B.P. Williamson, *Contact of Nominally Flat Surfaces* Proceedings of the Royal Society of London. Series A, Mathematical and Physical Sciences, 1966. **295**(1442): p. 300-319.
24. Greenwood, J.A. and J.H. Tripp, *The elastic contact of rough spheres*. ASME J App Mech, 1967. **34**: p. 153-159.
25. Whitehouse, D.J. and J.F. Archard, *The properties of random surfaces of significance in their contact*. Proceedings of the Royal Society of London. Series A, Mathematical and Physical Sciences (1934-1990), 1970. **316**(1524): p. 97-121.
26. Nayak, P.R., *Random Process Model of Rough Surfaces*. Journal of Lubrication Technology, 1971. **93**(3): p. 398-407.
27. Bush, A.W., R.D. Gibson, and T.R. Thomas, *The elastic contact of a rough surface*. Wear, 1975. **35**(1): p. 87-111.
28. Pullen, J. and J.B.P. Williamson, *On the Plastic Contact of Rough Surfaces*. Proceedings of the Royal Society of London. Series A, Mathematical and Physical Sciences, 1972. **327**(1569): p. 159-173.
29. Chang, W.R., I. Etsion, and D.B. Bogy, *An elastic-plastic model for the contact of rough surfaces*. Journal of tribology, 1987. **109**(2): p. 257-63.
30. Abdo, J.A. and K. Farhang, *Elastic-plastic contact model for rough surfaces based on plastic asperity concept*. International Journal of Non-Linear Mechanics, 2005. **40**(4): p. 495-506.
31. Webster, M.N. and R.S. Sayles, *A numerical model for the elastic frictionless contact of real rough surfaces*. Journal of tribology, 1986. **108**(3): p. 314-320.
32. West, M.A. and R.S. Sayles, *A 3-dimensional method of studying 3-body contact geometry and stress on real rough surfaces*, in *Tribology Series*, D. Dowson, et al., Editors. 1987, Elsevier. p. 195-200.
33. Ren, N. and S.C. Lee, *Contact Simulation of Three-Dimensional Rough Surfaces Using Moving Grid Method*. Journal of tribology, 1993. **115**(4): p. 597-601.
34. Francis, H.A., *The accuracy of plane strain models for the elastic contact of three-dimensional rough surfaces*. Wear, 1983. **85**(2): p. 239-256.
35. Komvopoulos, K. and D.H. Choi, *Elastic Finite Element Analysis of Multi-Asperity Contacts*. Journal of tribology, 1992. **114**(4): p. 823-831.
36. Majumdar, A. and B. Bhushan, *Fractal Model of Elastic-Plastic Contact Between Rough Surfaces*. Journal of tribology, 1991. **113**(1): p. 1-11.
37. Tomlinson, G.A., *A molecular theory of friction*. Philos. Mag. Ser. 7, 1929: p. 905-939.
38. Waterhouse, R.B., ed. *Fretting Fatigue*. 1981, Applied Science Publishers: UK.
39. Waterhouse, R.B., *ASM International Vol.18 - Wear*, 2002.
40. Waterhouse, R.B., *Fretting wear*. Wear, 1984. **100**(1-3): p. 107-118.
41. Dini, D., *Studies in fretting fatigue with particular application to almost complete contacts*, in *Department of engineering science* 2004, University of Oxford: Oxford.

42. Leen, S.B., et al., *An investigation of the fatigue and fretting performance of a representative aero-engine spline coupling*. The Journal of strain analysis for engineering design, 2002. **37**(6): p. 565-583.
43. Farris, T.N., H. Murthy, and J.F. Matlik, *Fretting Fatigue*, in *Comprehensive Structural Integrity* 2003. p. pp. 281–326.
44. Fouvry, S., P. Kapsa, and L. Vincent, *Quantification of fretting damage*. Wear, 1996. **200**(1-2): p. 186-205.
45. Vingsbo, O. and S. Söderberg, *On fretting maps*. Wear, 1988. **126**(2): p. 131-147.
46. Ding, J., et al., *Experimental characterisation and numerical simulation of contact evolution effect on fretting crack nucleation for Ti-6Al-4V*. Tribology International, 2009. **42**(11-12): p. 1651-1662.
47. Fouvry, S., P. Duó, and P. Perruchaut, *A quantitative approach of Ti-6Al-4V fretting damage: friction, wear and crack nucleation*. Wear, 2004. **257**(9-10): p. 916-929.
48. Elleuch, K. and S. Fouvry, *Experimental and modelling aspects of abrasive wear of a A357 aluminium alloy under gross slip fretting conditions*. Wear, 2005. **258**(1-4 SPEC. ISS.): p. 40-49.
49. Kartal, M., et al., *Determination of the Frictional Properties of Titanium and Nickel Alloys Using the Digital Image Correlation Method*. Experimental Mechanics, 2010: p. 1-13.
50. Yoon, Y., I. Etsion, and F.E. Talke, *The evolution of fretting wear in a micro-spherical contact*. Wear, 2011. **270**(9-10): p. 567-575.
51. Everitt, N.M., et al., *Characterisation of fretting-induced wear debris for Ti-6Al-4 V*. Wear, 2009. **267**(1-4): p. 283-291.
52. Ewins, D.J., et al., *Experimental Contributions to the Prediction of the Dynamics of Structures with Contact Interfaces*, in *Symposium of Advances in Contact Mechanics: a tribute to Prof. J.J. Kalker* 2008: Delft, The Netherlands.
53. Nowell, D. and D.A. Hills, *Crack initiation criteria in fretting fatigue*. Wear, 1990. **136**(2): p. 329-343.
54. Johnson, K.L., *Surface Interaction between Elastically Loaded Bodies under Tangential Forces* Proceedings of the Royal Society of London. Series A, Mathematical and Physical Sciences, 1955. **230**(1183): p. 531-548
55. Zhou, Z.R. and L. Vincent, *Mixed fretting regime*. Wear, 1995. **181-183, Part 2**(0): p. 531-536.
56. Stachowiak, G.W., ed. *Engineering Tribology*. 2nd ed. 2000, Butterworth-Heinemann.
57. Bryggman, U. and S. Söderberg, *Contact conditions in fretting*. Wear, 1986. **110**(1): p. 1-17.
58. Baker, R.F. and A.V. Olver, *Direct observations of fretting wear of steel*. Wear, 1997. **203-204**: p. 425-433.
59. Varenberg, M., I. Etsion, and G. Halperin, *Slip Index: A New Unified Approach to Fretting*. Tribology Letters, 2004. **17**(3): p. 569-573.
60. Nowell, D., D. Dini, and D.A. Hills, *Recent developments in the understanding of fretting fatigue*. Engineering fracture mechanics, 2006. **73**(2): p. 207-222.
61. Tomlinson, G.A., *An investigation of the fretting corrosion of closely fitting surfaces*. Proceedings of the Institution of Mechanical Engineers 1847-1982, 1939. **141**(1939): p. 223-249.
62. Hurricks, P.L., *The mechanism of fretting - A review*. Wear, 1970. **15**(6): p. 389-409.
63. Suh, P.N., *The delamination theory of wear*. Wear, 1973. **25**(1): p. 111-124.
64. Jahanmir, S., N.P. Suh, and E.P. Abrahamson, *Microscopic observations of the wear sheet formation by delamination*. Wear, 1974. **28**(2): p. 235-249.

65. Waterhouse, R.B. and D.E. Taylor, *Fretting debris and delamination theory of wear*. Wear, 1974. **29**(3): p. 337-344.
66. Kapoor, A. and K.L. Johnson, *Plastic ratchetting as a mechanism of metallic wear*. Proceedings. Mathematical and physical sciences, 1994. **445**(1924): p. 367-384.
67. Sauger, E., et al., *Tribologically Transformed Structure in Fretting*. Wear, 2000. **245**: p. 39-52.
68. Fouvry, S., P. Kapsa, and L. Vincent, *An elastic-plastic shakedown analysis of fretting wear*. Wear, 2001. **247**(1): p. 41-54.
69. Mohd Tobi, A.L., et al., *A study on the interaction between fretting wear and cyclic plasticity for Ti-6Al-4V*. Wear, 2009. **267**(1-4): p. 270-282.
70. Kalin, M. and J. Vizintin, *A tentative explanation for the tribochemical effects in fretting wear*. Wear, 2001. **250**(1-12): p. 681-689.
71. Uhlig, H.H., *Mechanism of fretting corrosion*. Journal of Applied Mechanics, 1954. **21**: p. 401-407.
72. Godet, M., *The third-body approach: A mechanical view of wear*. Wear, 1984. **100**(1-3437-452.): p. 437-452.
73. Godet, M., *Third-bodies in Tribology*. Wear, 1990. **136**(1): p. 29-45.
74. Waterhouse, R.B., *Role of adhesion and delamination in fretting wear of metallic materials*. Wear, 1977. **45**(3): p. 355-364.
75. Stachowiak, G.W., ed. *Wear - Materials, Mechanisms and Practice*. Tribology in Practice Series 2005, John Wiley & Sons, Ltd: The Atrium, Southern Gate, Chichester.
76. Swalla, D.R., R.W. Neu, and D.L. McDowell, *Microstructural Characterization of Ti-6Al-4V Subjected to Fretting*. Journal of tribology, 2004. **126**(4): p. 809-816.
77. Mulvihill, D.M., et al., *Investigation of non-Coulomb friction behaviour in reciprocating sliding*. Wear, 2011. **271**(5-6): p. 802-816.
78. Dini, D., *UTC Report No. 172 - Investigation of Coefficient Of Friction: fretting behaviour of low friction coatings*, 2002, University Technology Centre for Solid Mechanics: Oxford.
79. Popov, V.L., *Contact mechanics and friction: physical principles and applications*, 2010, Springer: London.
80. Filippi, S., A. Akay, and M.M. Gola, *Measurement of tangential contact hysteresis during microslip*. Journal of tribology, 2004. **126**(3): p. 482-489.
81. Berthoud, P. and T. Baumberger, *Shear Stiffness of a Solid-Solid Multicontact Interface*. Proceedings: Mathematical, Physical and Engineering Sciences, 1998. **454**(1974): p. 1615-1634.
82. Olofsson, U. and L. Hagman, *A model for micro-slip between flat surfaces based on deformation of ellipsoidal elastic bodies*. Tribology International, 1997. **30**(8): p. 599-603.
83. Hagman, L.A. and U. Olofsson, *A model for micro-slip between flat surfaces based on deformation of ellipsoidal elastic asperities--parametric study and experimental investigation*. Tribology International, 1998. **31**(4): p. 209-217.
84. Elleuch, K., et al., *Development of a contact compliance method to detect the crack propagation under fretting*. Tribology International, 2006. **39**(10): p. 1262-1270.
85. Drinkwater, B.W., R.S. Dwyer-Joyce, and P. Cawley, *A Study of the Interaction between Ultrasound and a Partially Contacting Solid--Solid Interface*. Proceedings: Mathematical, Physical and Engineering Sciences, 1996. **452**(1955): p. 2613-2628.
86. Tattersall, H.G., *The ultrasonic pulse-echo technique as applied to adhesion testing*. Journal of physics. D, applied physics, 1973. **6**(7): p. 819-832.

87. Kendall, K. and D. Tabor, *An Ultrasonic Study of the Area of Contact between Stationary and Sliding Surfaces*. Proceedings of the Royal Society of London. Series A, Mathematical and Physical Sciences, 1971. **323**(1554): p. 321-340.
88. Królikowski, J. and J. Szczepek, *Assessment of tangential and normal stiffness of contact between rough surfaces using ultrasonic method*. Wear, 1993. **160**(2): p. 253-258.
89. Dwyer-Joyce, R.S., B.W. Drinkwater, and A.M. Quinn, *The Use of Ultrasound in the Investigation of Rough Surface Interfaces*. Journal of tribology, 2001. **123**(1): p. 8-16.
90. Gonzalez-Valadez, M., A. Baltazar, and R.S. Dwyer-Joyce, *Study of interfacial stiffness ratio of a rough surface in contact using a spring model*. Wear, 2010. **268**(3-4): p. 373-379.
91. Fouvry, S., *An energy description of wear mechanisms and its applications to oscillating sliding contacts*. Wear, 2003. **255**(1-6): p. 287-298.
92. Nowell, D., D.A. Hills, and D.N. Dai, *Energy dissipation and crack initiation in fretting fatigue*, in *Tribology Series*, D. Dowson, et al., Editors. 1994, Elsevier. p. 389-396.
93. Medina, S., et al. *Fast computation of frictional energy dissipation in rough contacts under partial slip*. in *IJTC*. 2008. Miami.
94. Dini, D., *Frictional Energy Dissipation in a Rough Hertzian Contact*. Journal of tribology, 2009. **131**(2): p. 21401.
95. Archard, J.F. and R.A. Rowntree, *The temperature of rubbing bodies; part 2, the distribution of temperatures*. Wear, 1988. **128**(1): p. 1-17.
96. Jäger, J.C., *Moving sources of heat and temperature at sliding contacts*. Journal and proceedings of the Royal Society of New South Wales, 1942. **76**(Part 3): p. 203-224.
97. Stachowiak, G.W., *Surface temperature at the conjunction between contacting solids and its effect on EHL*, in *Engineering Tribology*, G.W. Stachowiak, Editor 2000, Butterworth-Heinemann. p. 327-343.
98. Sproles Jr, E.S. and D.J. Duquette, *Interface temperature measurements in the fretting of a medium carbon steel*. Wear, 1978. **47**(2): p. 387-396.
99. Greenwood, J.A. and A.F. Alliston-Greiner, *Surface temperatures in a fretting contact*. Wear, 1992. **155**(2): p. 269-275.
100. Spikes, H.A., V. Anghel, and R. Glovnea, *Measurement of the rheology of lubricant films in elastohydrodynamic contacts*. Tribology Letters, 2004. **17**(3): p. 593-605.
101. Hwang, J., et al., *Measurement of temperature field in surface grinding using Infra-Red (IR) imaging system*. Journal of tribology, 2003. **125**(2): p. 377-383.
102. Tabor, D., *Friction - The present state of our understanding*. Journal of Lubrication Technology, 1981. **103**: p. 169-179.
103. Rigney, D.A. and J.P. Hirth, *Plastic deformation and sliding friction of metals*. Wear, 1979. **53**(2): p. 345-370.
104. Ford, I.J., *Roughness effect on friction for multi-asperity contact between surfaces*. Journal of Physics D: Applied Physics, 1993. **26**(12): p. 2219-2225.
105. Gane, N., P.F. Pfaelzer, and D. Tabor, *Adhesion between Clean Surfaces at Light Loads*. Proceedings of the Royal Society of London. Series A, Mathematical and Physical Sciences, 1974. **340**(1623): p. 495-517.
106. Fuller, K.N.G. and D. Tabor, *The Effect of Surface Roughness on the Adhesion of Elastic Solids*. Proceedings of the Royal Society of London. A. Mathematical and Physical Sciences, 1975. **345**(1642): p. 327-342.
107. Johnson, K.L., K. Kendall, and A.D. Roberts, *Surface Energy and the Contact of Elastic Solids*. Proceedings of the Royal Society of London. A. Mathematical and Physical Sciences, 1971. **324**(1558): p. 301-313.

108. Derjaguin, B.V., V.M. Muller, and Y.P. Toporov, *Effect of contact deformations on the adhesion of particles*. Journal of Colloid and Interface Science, 1975. **53**(2): p. 314-326.
109. Greenwood, J.A., *The friction of hard sliders on lubricated rubber: the importance of deformation losses*. Proceedings of the Physical Society, 1958. **71**: p. 989-1001.
110. Bikerman, J.J., *Adhesion in friction*. Wear, 1976. **39**(1): p. 1-13.
111. Suh, N.P. and H.C. Sin, *The genesis of friction*. Wear, 1981. **69**(1): p. 91-114.
112. Prandtl, L., *Ein Gedankenmodell zur kinetischen Theorie der festen Koerper (Hypothetical model for the kinetic theory of solid bodies)*. 2, 1928. **8**(2): p. 85-106.
113. Hölscher, H., *Principles of atomic friction: from sticking atoms to superlubric sliding*. Philosophical transactions. Mathematical, physical, and engineering sciences, 2008. **366**(1869): p. 1383-1404.
114. Johnson, K.L., *The contribution of micro/nano-tribology to the interpretation of dry friction*. Proceedings of the Institution of Mechanical Engineers; Part C; Journal of mechanical engineering science, 2000. **214**(1): p. 11.
115. Blau, P.J., *On the nature of running-in*. Tribology International, 2005. **38**(11-12): p. 1007-1012.
116. Blau, P.J., *Friction and wear transitions of materials : break-in, run-in, wear-in*1989, Park Ridge, New Jersey, USA: Noyes Publications.
117. Karpinska, A., *Running-in and the evolution of metallic surfaces subjected to sliding and rolling contact*, in *Department of Mechanical Engineering 2010* Imperial College: London.
118. Griffin, J.H., *A Review of Friction Damping of Turbine Blade Vibration*. International Journal of Turbo and Jet Engines, 1990. **7**: p. 297-307.
119. Petrov, E.P., *Direct parametric analysis of resonance regimes for nonlinear vibrations of bladed disks*. Journal of Turbomachinery, 2007. **129**: p. 495-502.
120. Petrov, E.P. and D.J. Ewins, *Advanced modeling of underplatform friction dampers for analysis of bladed disk vibration*. Journal of turbomachinery, 2007. **129**(1): p. 143-150.
121. Gaul, L. and R. Nitsche, *The Role of Friction in Mechanical Joints*. Applied Mechanics Reviews, 2001. **54**(2): p. 93-106.
122. Boyer, R., G. Welsch, and E.W. Collings, *Materials properties handbook: titanium alloys* 1994: Materials Park, OH : ASM International.
123. Feaugas, X., P.H. Pilvin, and M. Clavel, *Cyclic deformation behaviour of an α/β titanium alloy -II. Internal stresses and micromechanic modelling*. Acta materialia, 1997. **45**(7): p. 2703-2714.
124. Schutz, R.W., *Corrosion of Titanium and Titanium Alloys*, in *Corrosion: Materials, ASM Handbook*2005, ASM International. p. 252-299.
125. Reed, R.C., ed. *The Superalloys - Fundamentals and Applications*. 2006, Cambridge University Press: New York.
126. Giggins, C.S. and F.S. Pettit, *Oxidation of Ni-Cr-Al Alloys Between 1000[degree] and 1200[degree]C*. Journal of The Electrochemical Society, 1971. **118**(11): p. 1782-1790.
127. Trethewey, K.R.C., J., *Corrosion for students of science and engineering*1988, Harlow: Longman Scientific & Technical
128. Stanbridge, A.B., *Measurement of friction damper contact characteristics - The High-Temperature Friction Damper Test Rig*, 1999, Centre of Vibration Engineering: London.
129. Stanbridge, A.B., *Technical Note: The CUTC Friction-Contact Test Rig - A Users Guide*, 2001, Centre of Vibration Engineering: London.

130. SolidWorks®, *Student Design Kit* 2009-2011.
131. Dini, D. and D.A. Hills, *Energy Dissipation in Rough Contacts Under Partial Slip*, in *34th Leeds-Lyon Symposium on Tribology* 2007: Leeds-Lyon.
132. Lamb, C. and M. Zecchino, *WYKO Surface Profilers Technical Reference Manual*. Verion 2.2.1 ed, ed. V.M. Group 1990, Tuscon, Arizona.
133. Alicona. *Optische 3D Oberflaechenmesstechnik* 2008 [cited 2008 December]; Available from: http://www.alicon.com/cms/upload/pdf/if/de/IFM_Broschuere.pdf.
134. De Castro, E. and C. Morandi, *Registration of Translated and Rotated Images Using Finite Fourier Transforms*. IEEE transactions on pattern analysis and machine intelligence, 1987. **PAMI-9**(5): p. 700-703.
135. Zitová, B. and J. Flusser, *Image registration methods: a survey*. Image and Vision Computing, 2003. **21**(11): p. 977-1000.
136. Taylor, B. and E. Weidmann. *Metallographic preparation of titanium* Struers Application Notes 2010 [cited 2010 15.02.2010]; Available from: <http://www.struers.de/resources/elements/12/105280/Application%20Notes%20titanium%20English.pdf>.
137. Fibics-Incorporated. *Steps in TEM sample preparation using the 'Lift-Out' Method*. 2011 [cited 2011 November]; Available from: <http://www.fibics.com/fib/application/steps-in-tem-specimens-preparation-by-lift-out-method-/24/>.
138. Medina, S., D. Nowell, and D. Dini, *Analytical and Numerical Models for Tangential Stiffness of Rough Elastic Contacts*. Proceedings of the Royal Society of London. A. Mathematical and Physical Sciences, 2011. **Submitted for publication**.
139. Reddyhoff, T., H.A. Spikes, and A.V. Olver, *Improved Infrared Temperature Mapping of Elastohydrodynamic Contacts*. Proc. I.Mech.E. part J: Journal of Engineering Tribology, 2009. **223**.
140. Baker, R.F., *Durability of steel spline couplings*, in *Department of mechanical engineering* 2005, Imperial College of Science: London.
141. Munisamy, R.L., D.A. Hills, and D. Nowell. *Contact of similar and dissimilar elastic spheres under tangential loading*. in *Contact Mechanics International Symposium*. 1992. Lausanne: Presses Polytechniques et Universitaires Romandes.
142. Ruiz, C. and K.C. Chen. *Life assessment of dovetail joints between blades and discs in aereengines*. in *Int. Conf. Fatigue*. 1986. Sheffield.
143. Ciavarella, M., *The generalized Cattaneo partial slip plane contact problem. Part I - Theory*. International journal of solids and structures, 1998. **35**(18): p. 2349-2362.
144. Jäger, J.C., *A new principle in contact mechanics*. ASME J Tribology, 1998. **120**: p. 677-684.
145. Kartal, M.E., et al., *Measurements of pressure and area dependent tangential contact stiffness between rough surfaces using digital image correlation*. Tribology International, 2011. **44**(10): p. 1188-1198.
146. Ewins, D.J. *Friction contact roadmap v 6.4*. in *NSF-Sandia Joints Modelling Workshop*. 2006. Arlington, USA.

Appendix

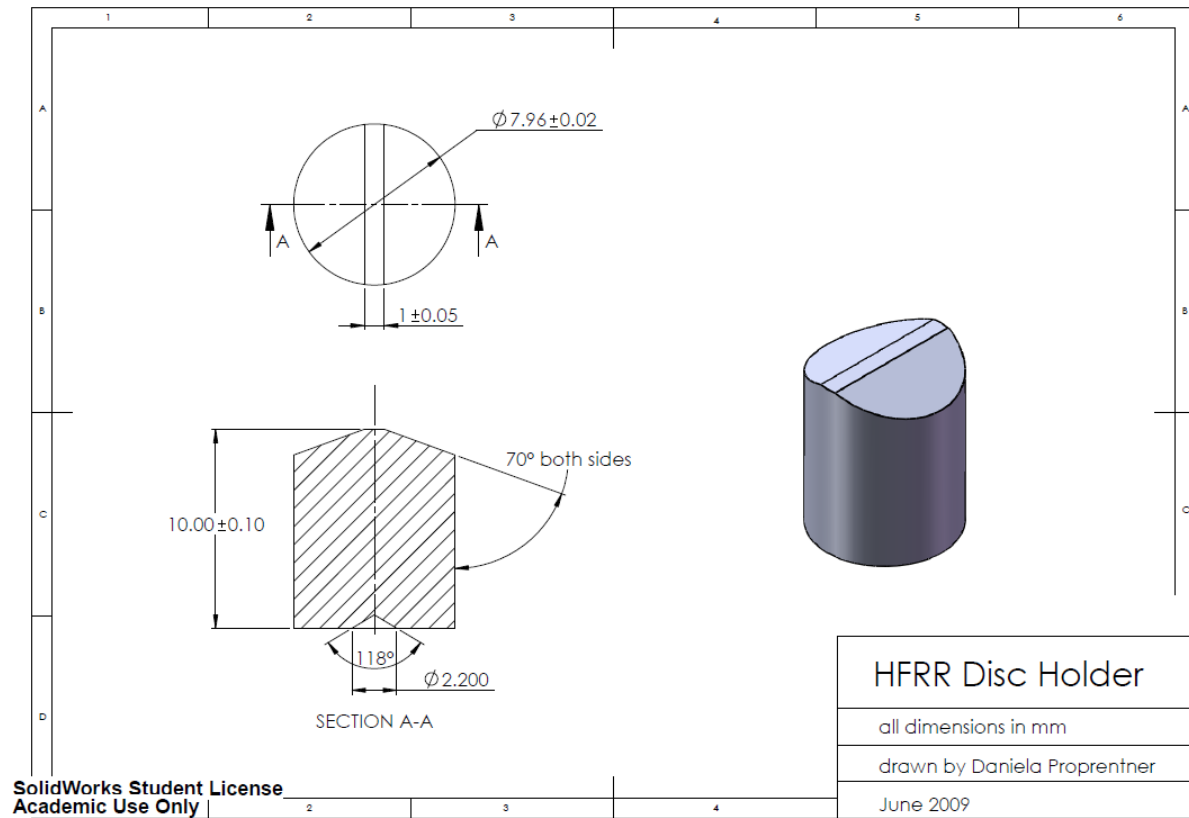


Figure A-1: Technical drawings of friction specimens for 1 mm^2 rig.

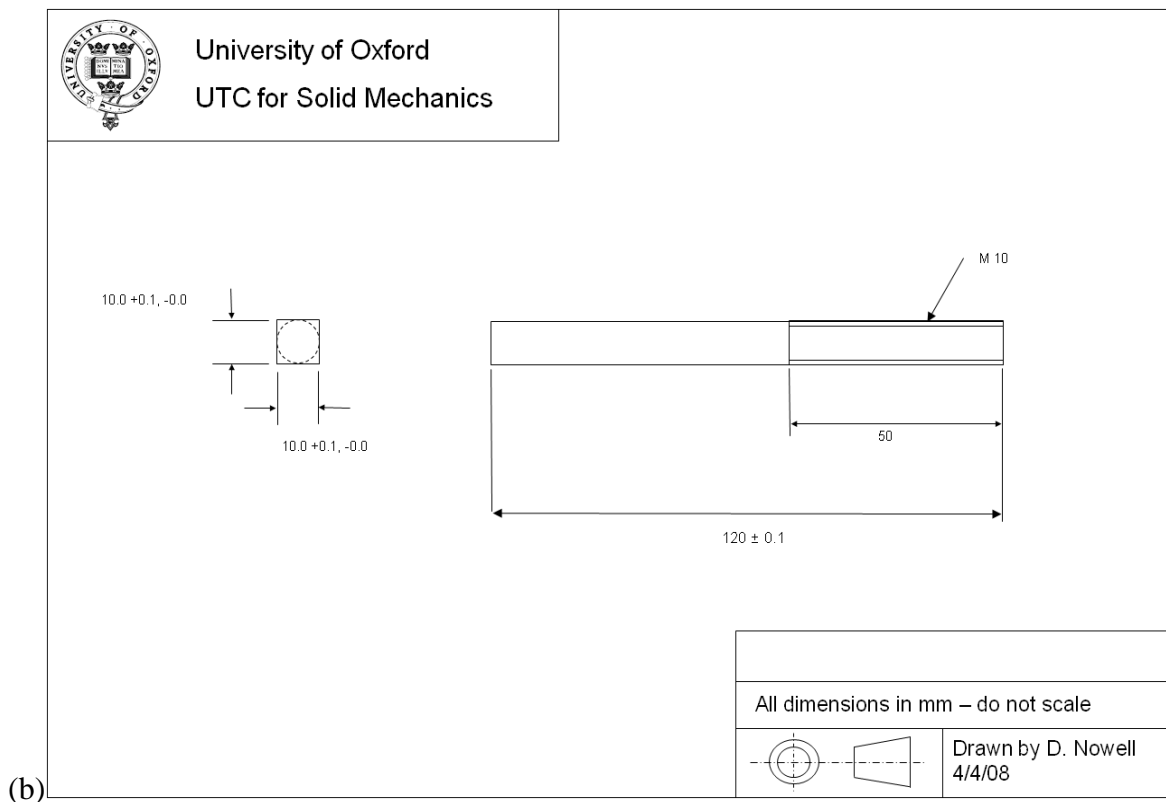
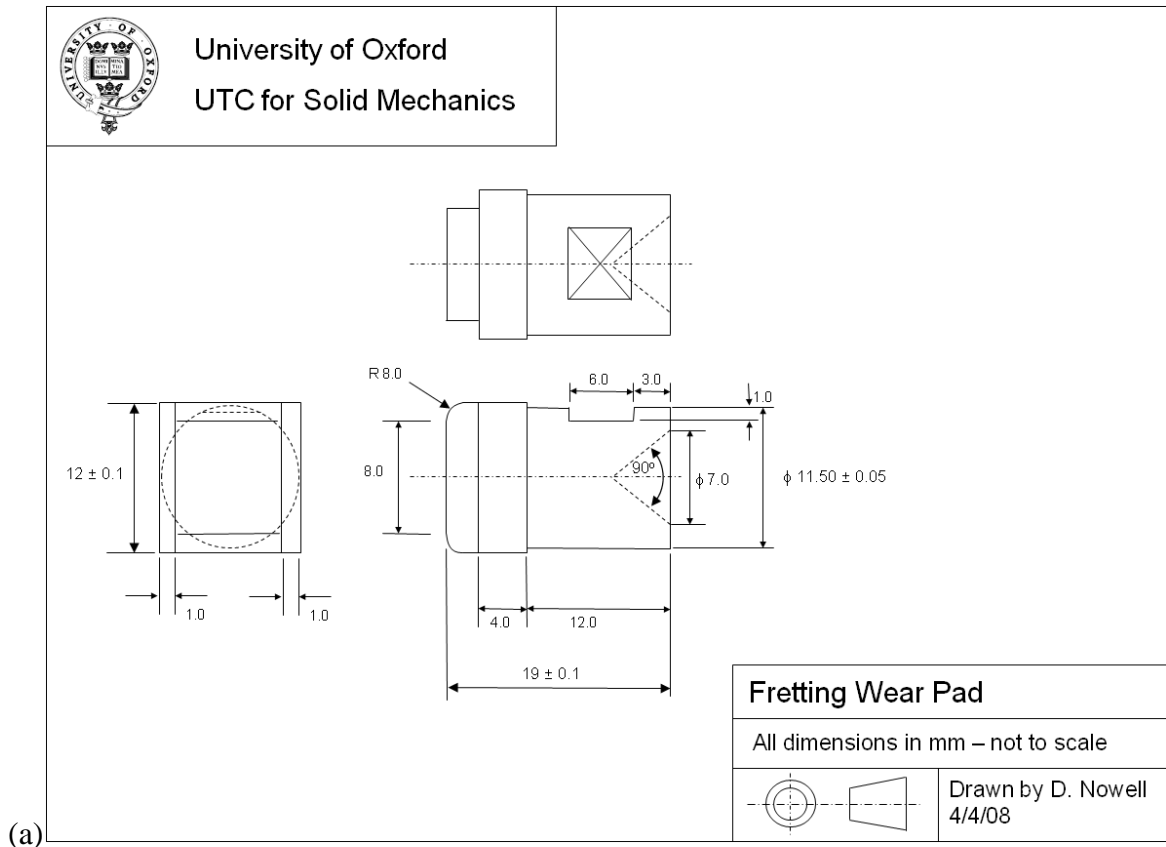


Figure A-2: Technical drawings of (a) pads and (b) specimens for 80 mm² contact rig.

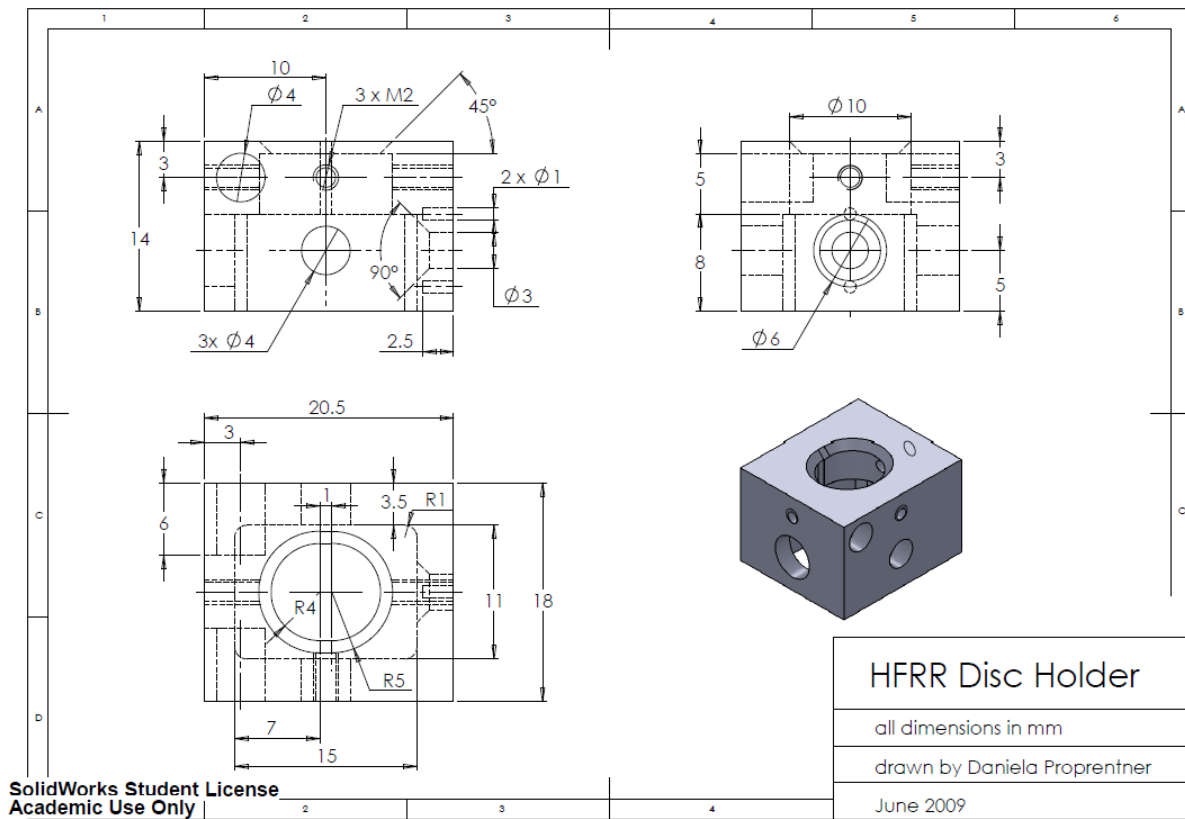


Figure A-3: Newly designed upper HFRR sample holder for the sapphire disc.

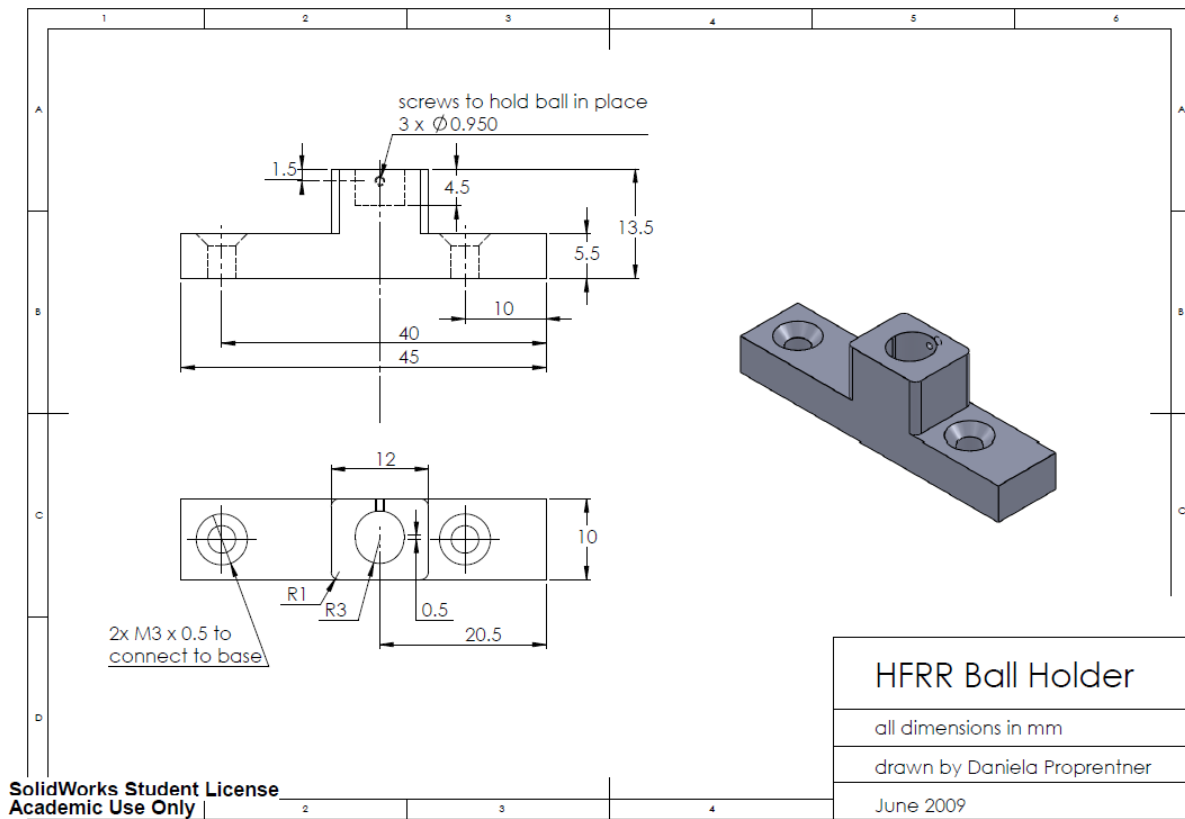


Figure A-4: Newly designed lower HFRR sample holder for a steel ball.